

# Fabrication and integration of metallic nano and micro cones for on-chip electron field emitters

**Erzeugung und Integration von metallischen Nano- und Mikrokonen für On-Chip Elektronenfeldemitter**

Zur Erlangung des akademischen Grades Doktor-Ingenieur (Dr.-Ing.)

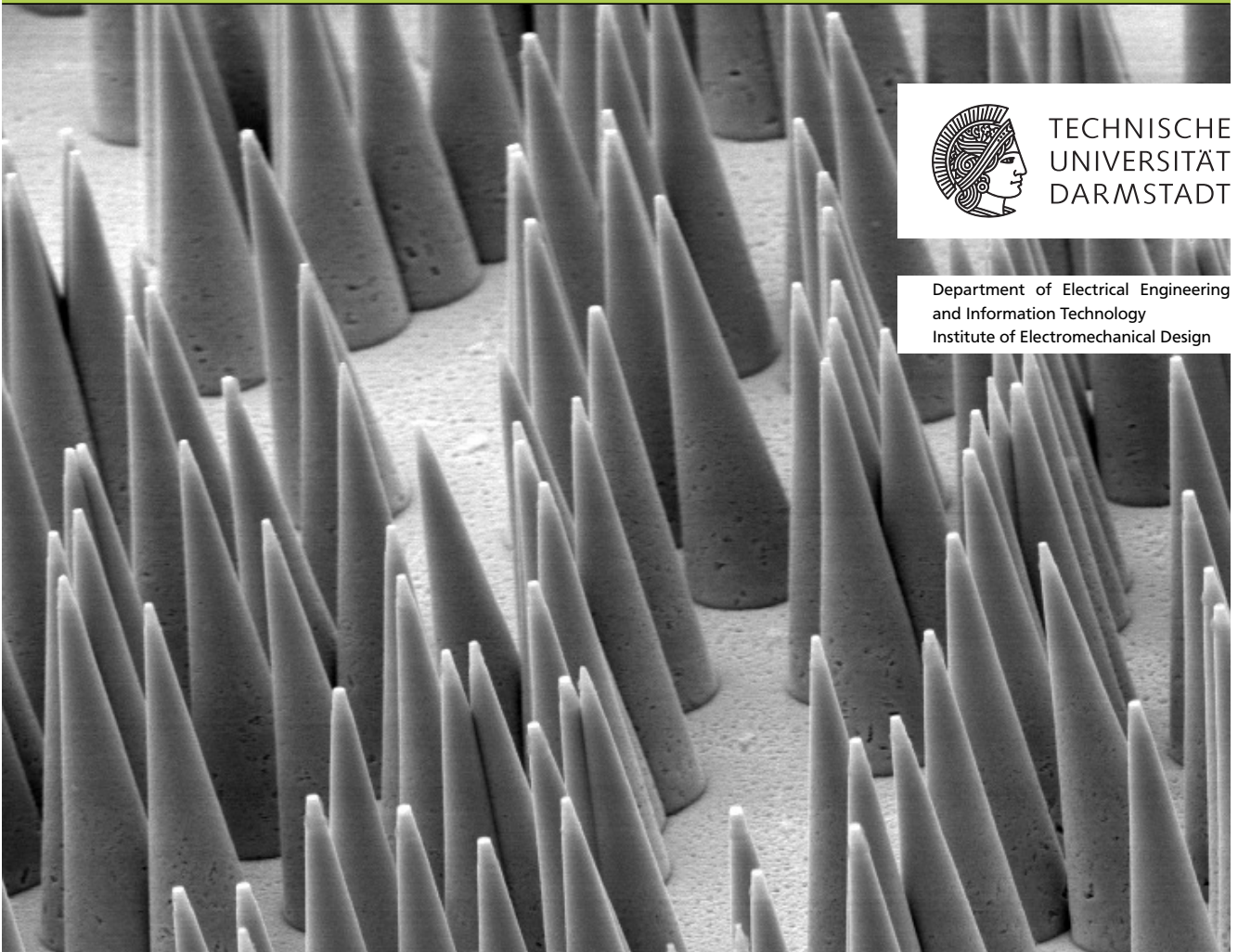
genehmigte Dissertation von Farough Roustaie aus Esfahan / Iran

Tag der Einreichung: 30. November 2021, Tag der Prüfung: 15. Juni 2022

Darmstadt — D 17

1. Gutachten: Prof. Dr.-Ing. Helmut F. Schlaak

2. Gutachten: Prof. Dr.-Ing. Martin Hoffmann



TECHNISCHE  
UNIVERSITÄT  
DARMSTADT

Department of Electrical Engineering  
and Information Technology  
Institute of Electromechanical Design

Fabrication and integration of metallic nano and micro cones for on-chip electron field emitters  
Erzeugung und Integration von metallischen Nano- und Mikrokonen für On-Chip Elektronenfeldemitter

Genehmigte Dissertation von Farough Roustaei aus Esfahan / Iran

1. Gutachten: Prof. Dr.-Ing. Helmut F. Schlaak
2. Gutachten: Prof. Dr.-Ing. Martin Hoffmann

Tag der Einreichung: 30. November 2021

Tag der Prüfung: 15. Juni 2022

Darmstadt — D 17



---

# **Fabrication and integration of metallic nano and micro cones for on-chip electron field emitters**

Vom Fachbereich  
Elektrotechnik und Informationstechnik  
der Technischen Universität Darmstadt  
zur Erlangung des akademischen Grades eines  
Doktor-Ingenieurs (Dr.-Ing.)  
genehmigte Dissertation

von

**Dipl.-Ing. Farough Roustae**

geboren am 18. Mai 1980  
in Esfahan/Iran

Referent: Prof. Dr.-Ing. Helmut F. Schlaak

Korreferent: Prof. Dr.-Ing. Martin Hoffmann

Tag der Einreichung: 30. November 2021

Tag der mündlichen Prüfung: 15. Juni 2022

D 17  
Darmstadt 2022

---

---

Bitte zitieren Sie dieses Dokument als:

URN: urn:nbn:de:tuda-tuprints-220340

URL: <https://tuprints.ulb.tu-darmstadt.de/id/eprint/22034>

Dieses Dokument wird bereitgestellt von tuprints, E-Publishing-Service der TU-Darmstadt

<http://tuprints.ulb.tu-darmstadt.de>

[tuprints@ulb.tu-darmstadt.de](mailto:tuprints@ulb.tu-darmstadt.de)

Die Veröffentlichung steht unter folgender Creative Commons Lizenzvertrag:

*Namensnennung - Nicht kommerziell - Keine Bearbeitungen 4.0 International Lizenz*



<http://creativecommons.org/licenses/by-nc-nd/4.0/>

---

---

## Erklärungen laut Promotionsordnung

---

### §8 Abs.1 lit. c PromO

Ich versichere hiermit, dass die elektronische Version meiner Dissertation mit der schriftlichen Version übereinstimmt.

### §8 Abs.1 lit. c PromO

Ich versichere hiermit, dass zu einem vorherigen Zeitpunkt noch keine Promotion versucht wurde. In diesem Fall sind nähere Angaben über Zeitpunkt, Hochschule, Dissertationsthema und Ergebnis dieses Versuchs mitzuteilen.

### §9 Abs.1 lit. c PromO

Ich versichere hiermit, dass die vorliegende Dissertation selbstständig und nur unter Verwendung der angegebenen Quellen verfasst wurde.

### §89 Abs.1 lit. c PromO

Die Arbeit hat bisher noch nicht zu Prüfungszwecken gedient.

Darmstadt, den 30.11.2021

---

(Farough Roustaie)

---



---

## Acknowledgment

---

The following thesis is done in context of a scientific project at the Technische Universität Darmstadt in cooperation with GSI Helmholtzzentrum für Schwerionenforschung (Project 500475) and the support program of the German Federal Ministry for Economic Affairs and Energy (BMWi) for improving the entrepreneurial environment at universities and research institutes.

This has been a long way and I have many people to thank for their help, support, and encouragement.

With a sense of deep regards, I express my sincere thanks to my supervisor Prof. Dr.-Ing. Helmut F. Schlaak, for his inspiring guidance and support during this research work. His keen interest in research and regular discussion and the great freedom at the institute for performing different experiments were helpful to enhance my scientific knowledge and it was an opportunity for my personal development.

I thank Prof. Dr.-Ing. Martin Hoffmann for his interest in my work and accepting the second referee. My thanks also go to Prof. Dr.-Ing. habil. Dr. h.c. Andreas Binder, Prof. Dr.-Ing. Klaus Hofmann and Prof. Dr. rer. nat. Sascha Preu for their participation in thesis exam committee.

I thank Dr. Stefan Wilfert from GSI for his encouragement and very instructive discussions and time to time feedbacks during his supervision.

I would like to thank all my colleagues from institute EMK for their kindness, supports and discussions, who have created a creative and collaborative environment at the institute. Especially I thank Bernhard Jochem for his technical support in clean room during my thesis and his friendliness. I was grateful to work in the Micro-Nano-Integration group of institute EMK with my colleagues Dr. Sebastian Quednau, Florian Weißenborn and Felix Greiner. I would like to thank my students, Stefan Kunz, Andreas Humbert, Hamed Soltanishirazi, Rojda Cicek, and Tobias Wähner, who helped me in my research work during their theses.

I want to thank Yashar kouhi and Soroush Kouhi for proofreading.

On Personal level, i would like to thank my family, Especially my parent Faeze Firooze and Farhang Roostaei for their affection, support and encouragement. I am blessed with the siblings giving me a wonderful family and great childhood.

Finally, i would like to thank my best friend and wife Yalda Kouhi Anbaran for her unrestricted supports and understanding and patience during my research work. She always motivated me to do my best. Last but not least, my son Artin gave me the power to finish this thesis. I hope that now I can spend more time with them.

Mannheim, Juni 2022

Farough Roustaie





---

## Zusammenfassung

---

Die Nanotechnologie eröffnet den Zugang zu einer Vielzahl neuer Materialeigenschaften und -verhaltensweisen, die über die klassischen physikalischen Eigenschaften der Materialien weit hinaus gehen. Metallische Drähte mit einem Durchmesser von weniger als  $1\,\mu\text{m}$  und einer Länge von  $10\,\mu\text{m}$  bis  $50\,\mu\text{m}$  zeigen ein großes Aspektverhältnis. Insbesondere eine hohe Dichte solcher Drähte führt zu einem sehr großen Verhältnis von Oberfläche zu Volumen und zu neuen mechanischen, elektrischen, thermischen und chemischen Eigenschaften der mit Nano- und Mikrodrähten bedeckten Oberflächen. Diese neuen physikalischen und chemischen Effekte ermöglichen eine neue Entwicklungsstufe hochempfindlicher Sensoren wie chemische, biologische, Gasfluss-, Kraft- und Trägheitssensoren. Darüber hinaus ermöglicht der Einsatz von Nano- und Mikrodrähten die Herstellung von Schaltkontakten mit äußerst geringem elektrischem Widerstand. Zudem können effizientere thermische Schnittstellen und Verbindungen bei Raumtemperatur hergestellt werden. Durch das hohe Aspektverhältnis eignen sich Nanodrähte als Hochleistungselektronenfeldemitter. Um all diese Anwendungen zu realisieren, muss insbesondere eine wesentliche Hürde überwunden werden: Die vertikale Integration der metallischen Nanodrähte in ein 3D-Mikrosystem.

In dieser Arbeit wird eine Technik zur vor-Ort-Erzeugung und Integration von Nanodrähten in Mikrosysteme mit Fokus auf eine Anwendung in der Sensorik und ihre kommerzialisierbare, industrietaugliche Herstellung vorgestellt. Das Ziel dieser Arbeit ist die Entwicklung eines On-Chip-Elektronenfeldemitters, basierend auf metallischen Nanodrähten, zur Messung von Vakuumdrücken kleiner  $10^{-12}$  mbar in kryogenen Systemen bei Temperaturen unter 6 K. Aufsetzend auf einem Überblick zum Stand der Technik in der Vakuummesstechnik werden Möglichkeiten diskutiert, Probleme von Feldemitter-basierten Messgeräten zu eliminieren bzw. zu minimieren. Es wird theoretisch abgeleitet, dass die Verwendung von metallischen Nanodrähten mit hohem Oberflächenverhältnis und scharfen Spitzen als Elektronenfeldemitter zu einer großen lokalen elektrischen Feldverstärkung und damit zu einer höheren Stromemission führt.

Zur Herstellung der Drähte wird das sogenannte Ionenspur-Ätzverfahren verwendet. Solche Nanodrähte werden auch als Templat-gewachsene Drähte bezeichnet, da die Nanodrähte elektrochemisch in den Poren der ionenspurgeätzten Templat-Membranen synthetisiert werden. Mit diesem Verfahren können Nanodrähte mit einem Durchmesser von 30 nm bis zu einigen  $\mu\text{m}$  und einer Länge von  $2\,\mu\text{m}$  bis  $100\,\mu\text{m}$  mit unterschiedlichen Dichten im Bereich von  $10^4\,\text{cm}^{-2}$  bis  $10^9\,\text{cm}^{-2}$  realisiert werden. Die Entwicklung eines Verfahrens zur in-situ-Integration der Drähte in einer  $10\,\text{mm} \times 30\,\text{mm}$  großen Fläche (als  $16 \times 50$  Pad-Array) und die hierfür entwickelten Bauelemente und Techniken werden ausführlich erläutert. Um die Abdeckung breiter Flächen mit Nanodrähten zu ermöglichen, wurden der Prozess und die elektrochemische Abscheidungsanordnung optimiert. Mit dieser Optimierung können die Nanodrähte über die gesamte Oberfläche mit einer Abmessung von  $300\,\text{mm} \times 300\,\text{mm}$  sowie in industrielle 12-Zoll-Wafer integriert werden.

Im Vergleich zu zylindrischen Nanodrähten zeigen konische Strukturen ein deutlich besseres thermo-

---

mechanisches Verhalten. Aus diesem Grund wurde die Struktur der Drähte in eine konische Form gebracht. Hierfür wurde für die Ionenspur-Templates eine Vorrichtung zum asymmetrischen Ätzen entwickelt inklusive eines elektrischen Messverfahrens zur Steuerung des Scheitelwinkels der konischen Poren. Durch die konische Struktur kann theoretisch eine stabile, für die Vakuumdruckmessung ausreichende Stromemission mit einer deutlich längeren Lebensdauer der emittierenden Konen erreicht werden. Diese Effekte wurden mit einer großen Zahl unterschiedlicher Proben nachgewiesen.

Die Feldemissionscharakteristik der Nanokonen in einem Dioden- und Triodenaufbau werden detailliert beschrieben. In einer Langzeitmessung zeigt ein stabiler Feldemissionsstrom von  $31\mu\text{A}$  bei einer angelegten Spannung von  $290\text{V}$  für  $50\text{h}$  und über  $100\mu\text{A}$  bei einer angelegten Spannung von  $338\text{V}$  für  $12.5\text{h}$  das Potenzial dieser Emitterstruktur für eine ausreichend stabile Stromemission für XHV-Vakuumdruckmessungen.

Um den Aufbau eines On-Chip-Emitters zu vervollständigen, muss über den Nanokonen ein Extraktionsgitter zum Anlegen der Extraktionsspannung sowie zur Übertragung des emittierten Stroms angebracht werden. Ein Konzept für eine XHV-gerechte Integration des Extraktionsgitters wurde entwickelt. Das Konzept verfolgt die Idee, die metallischen Nanodrähte vergleichbar zu einem Klettverschluss einzusetzen. Bei dieser Anwendung werden zwei Flächen mit Nanodrähten belegt. Durch Aufeinanderpressen dieser Flächen werden beide Flächen bei Raumtemperatur miteinander verbunden. Dieser Prozess findet durch Verschränkung und Diffusion der Nanodrähte ineinander statt. Die Entwicklung dieses Raumtemperatur-Verbindungsprozesses und die Untersuchung der mechanischen und elektrischen Eigenschaften der Verbindungen werden detailliert ausgeführt. Diese neue Technologie wird am Einsatzbeispiel für das wärmefreie Verbinden von Halbleitern auf Pads bis zu  $3\mu\text{m}$  und Pitches kleiner als  $5\mu\text{m}$  erklärt. Sie hat das Potenzial für den Einsatz in der Massenproduktion von Wafer-Wafer- und Die-Wafer-Verbindungen bei Temperaturen deutlich unter  $230^\circ\text{C}$  oder bei Raumtemperatur.

Im Rahmen dieser Arbeiten wurde die Firma NanoWired GmbH gegründet. Diese Firma hat die entwickelte Technologie zur Anwendung in der Halbleiter-, Automobil-, Sensor- und Lichtbranche auf den Markt gebracht. Verschiedene konventionelle Methoden wie Kleben, Schweißen, Löten oder Schrauben können durch diese Technologie ersetzt werden.

---

## Abstract

---

Nanotechnology enables a diversity of new effects compared to the classical physical properties of the material. The metallic wires with a dimension of less than  $1\mu\text{m}$  and a length between  $10\mu\text{m}$  to  $50\mu\text{m}$  exhibit a great aspect ratio. A high density of such wires particularly gives a great surface to volume ratio, which results in new mechanical, electrical, thermal, and chemical properties of the surfaces covered with them. These new physical and chemical effects enable a new level of more sensitive sensors like chemical, biological, gas flow, force, and inertial sensors. Also, low resistance micro switches, more efficient thermal interface materials, and room-temperature interconnects can be enabled with nanowired surfaces. The high aspect ratio of the wires enables them to be applied as a high-performance electron field emitter. For realizing these applications there is an obstacle to overcome: Vertical integration of the metallic nanowires into a 3D microsystem.

This work introduces a technique for in-situ integration of nanowires into microsystems with a focus on an application in sensor technology and commercial and industry suitable fabrication. The objective of this work is to develop an on-chip electron field emitter, based on metallic nanowires, for measuring vacuum pressures less than  $10^{-12}$  mbar in cryogenic systems at temperatures below 6 K.

A review of state-of-the-art technologies in vacuum measurement sets the basis for discussing possibilities to eliminate or minimize the problems of the field emitter based gauges. It is shown theoretically that using the metallic nanowires with high aspect ratio and sharp tips as an electron field emitter results in a great local electrical field enhancement, thus, a higher current emission.

For fabricating the wires the so-called ion-track etch process is used. Such nanowires are also known as template grown wires because the nanowires are electrochemically synthesized in the pores of the ion-track etched template membranes. With this process, nanowires with a diameter from 30 nm to some  $\mu\text{m}$  and a length of  $2\mu\text{m}$  to  $100\mu\text{m}$  with different densities in the range of  $10^4\text{ cm}^{-2}$  to  $10^9\text{ cm}^{-2}$  can be realized. The development of a process for in-situ integration of the wires into a  $10\text{ mm} \times 30\text{ mm}$  surface (as  $16 \times 50$  array of pads) and the developed devices and techniques are explained in detail. The process and the electrochemical deposition device are optimized to enable covering broad surfaces with nanowires. With the optimization, the nanowires can be integrated into the whole surface with  $300\text{ mm} \times 300\text{ mm}$  dimensions and also industrial 12-inch wafers.

Compared to cylindrical nanowires, conical structures show a much better thermomechanical performance. Therefore, the used ion-track templates are etched asymmetrically in an etching device, developed in this work including an electrical measurement process to control the apex angle of the conical pores. Theoretically, with the conical structure a stable current emission, sufficient for vacuum pressure measurement, with a significantly longer lifetime of the emitting cones is expected. These effects are experimentally explored with a large variety of samples.

The field emission characteristics of the nanocones in a diode and triode setup are measured and de-

---

scribed in detail. In a long term measurement a stable field emission current of  $31\text{ }\mu\text{A}$  at an applied voltage of 290 V for 50 h and above  $100\text{ }\mu\text{A}$  at an applied voltage of 338 V for 12.5 h shows the potential of this emitter structure for enough stable current emission for XHV vacuum pressure measurement.

To complete the structure of an on-chip emitter, an extraction grid for applying the extraction voltage as well as transmission of the emitted current must be attached over the nanocones. A concept for an XHV suitable integration of the extraction grid is designed. This concept is pursued by the idea, which is to use nanowires as a hook and loop fastener. In this application, two surfaces are covered with nanowires. By pressing these surfaces on top of each other both surfaces are bonded at room temperature. This process takes place by entanglement and diffusion of the nanowires into each other. The development of this room temperature bonding technology and exploring the mechanical and electrical properties of the connections are discussed in detail. This new technology is presented for a heat-free bonding of semiconductors on pads down to  $3\text{ }\mu\text{m}$  and pitches lower than  $5\text{ }\mu\text{m}$ . Also, this technology has the potential of a wafer-wafer and die-wafer bonding in large scales and with temperatures far below  $230\text{ }^{\circ}\text{C}$  or at room temperature.

In the context of this work, the company NanoWired GmbH was founded. This company transfers the developed technology to the market for applications in semiconductor, automotive, sensor, and light segments. Different conventional methods like glueing, welding, soldering, or screws can be substituted with this technology.

---

## Table of Contents

---

<b>1</b>	<b>Introduction</b>	<b>1</b>
1.1	XHV measurement, the gateway toward undiscovered scientific areas . . . . .	1
1.2	Gas pressure measurement and ionization gauges: a brief review . . . . .	2
1.3	Motivation: Improving the specifications of electron emitters . . . . .	5
1.4	Dissertation outline . . . . .	6
<b>2</b>	<b>Field emitter-based cathodes in ionization vacuum gauges</b>	<b>7</b>
2.1	Basic theory of field emission . . . . .	8
2.2	State-of-the-art field emitter-based cathodes . . . . .	12
2.3	Metallic nanowire arrays as field emitter . . . . .	15
<b>3</b>	<b>In-situ synthesis of metallic nanowires and nanocones</b>	<b>19</b>
3.1	A short review of nanowires fabrication processes . . . . .	19
3.2	State-of-the-art methods for the assembly and manipulation of the nanowires . . . . .	21
3.2.1	Requirements for the integration of the nanowires . . . . .	21
3.2.2	Strategies for the assembly and manipulation of the nanowires . . . . .	22
3.2.2.1	Self-assembly of the nanowires . . . . .	22
3.2.2.2	Patterned growth of the nanowires . . . . .	25
3.3	Template grown nanowires . . . . .	28
3.3.1	Porous anodic aluminum oxide template membrane . . . . .	29
3.3.2	Ion-track etch template membrane . . . . .	29
3.3.3	Ion-track etch process for the synthesis of nanowires . . . . .	29
3.3.4	Removing the ion-track etch membrane . . . . .	30
3.4	In-situ synthesis and integration of metallic nanowires fabricated by ion-track etch process	32
3.4.1	Patterning the arrays . . . . .	33
3.4.2	Fixing the template membrane on the substrate . . . . .	36
3.4.2.1	Thermal lamination of the membrane . . . . .	36
3.5	Electrochemical deposition of nanowires . . . . .	40
3.5.1	Electrochemical deposition device for the synthesis of nanowires . . . . .	43
3.5.2	Wetting the template membranes . . . . .	45
3.5.3	Parameters for the synthesis of nanowires inside porous templates . . . . .	47
3.5.4	Different phases in the deposition of nanowires . . . . .	50
3.6	Results and discussion . . . . .	51
<b>4</b>	<b>Optimizing the deposition process and upscaling the nanowiring surface area</b>	<b>53</b>
4.1	Fixing the membrane with a spongy material . . . . .	53
4.2	Design and structuring an optimized deposition bath . . . . .	54
4.3	Deposition results with spring deposition bath . . . . .	55

4.4	Upscaling the spring deposition device	58
<b>5</b>	<b>Fabrication of metallic nanocones with controllable tip diameter and apex angle</b>	<b>61</b>
5.1	Electron field emission of metallic emitters	61
5.1.1	Nottingham effect	61
5.2	Asymmetric etching of ion-tracked polymer templates	63
5.2.1	Heavy ion irradiation of template membrane	64
5.2.2	Cylindrical and conical channels in a template membrane	65
5.2.3	Experimental setup and methodology for chemical etching of the polymer membrane	66
5.3	Geometry control of micro cones	67
5.4	Fabrication of micro cones	73
5.5	Conclusion and outlook	76
<b>6</b>	<b>Field emission of micro cones and nanowires</b>	<b>77</b>
6.1	Optimizing the nanowire structures and preparing the samples	77
6.1.1	Fabricated samples	78
6.1.2	Profilometry of samples	80
6.2	FE properties of high density cones	82
6.3	Measurements on low density cones array	89
6.4	Summary and outlook	93
<b>7</b>	<b>A new concept for the integration of extraction grid</b>	<b>95</b>
7.1	Methods for integrating the extraction grid	96
7.2	A new concept for the integration of the extraction grid	97
7.2.1	Fabrication process of the spacers	98
7.2.2	Nanowires as a hook-and-loop fastener for joining dies	99
7.3	Summary and outlook	101
<b>8</b>	<b>New room temperature bonding technology based on metallic nanowires</b>	<b>103</b>
8.1	Investigation on strength of nanowired connections	104
8.1.1	Experiment setup	104
8.1.2	Results and specifications: shear strength of NanoWired connections	106
8.2	Progress in nanowires based bonding technique: KlettWelding, KlettSintering, KlettGlueing	108
8.3	Summary and outlook	110
<b>9</b>	<b>Conclusion and outlook</b>	<b>111</b>
9.1	Synthesis and integration of the nanowires	111
9.2	Field emission properties of nanocones	113
9.3	Room temperature KlettWelding bonding technology	114

<b>Bibliography</b>	<b>116</b>
---------------------	------------



<b>Appendix</b>	<b>129</b>
<b>A Prescription</b>	<b>129</b>
A.1 Gold Etchant . . . . .	129
A.2 Chromium Etchant . . . . .	129
A.3 Copper electrolyte . . . . .	129
A.4 Nickel electrolyte . . . . .	129
<b>B Datasheets</b>	<b>130</b>
B.1 ma-P 1215 for etching and lamination processes . . . . .	130
B.2 Ti-Prime adhesion promoter . . . . .	131
B.3 AZ9260 Positive photo resist . . . . .	132
B.4 Potentiostat Bank Scholar T . . . . .	133
B.5 Gold electroplating bath . . . . .	134
B.6 Gold electroplating bath . . . . .	135
B.7 AZ40XT Positive photo resist . . . . .	136
<b>C Technical Drawings</b>	<b>137</b>
C.1 Electro chemical deposition bath . . . . .	137
C.2 Formic acid chamber . . . . .	148



---

## List of abbreviations

---

Abbreviations	Description
2D	Two Dimensional
2DEG	Two Dimensional Electron Gas
3D	Three Dimensional
AAO	Aluminum Anodic Oxide
BGA	Ball Grid Arrays
CNT	Carbon Nano Tubes
CMP	Chemical Mechanical Polishing
CVD	Chemical Vapor Deposition
D2W	Die to Wafer
DI-Water	Deionized Water
e-beam	Electron beam
FCCSP	Flip-Chip Chip Scale Packaging
FCBGA	Flip-Chip Ball Grid Arrays
FEC	Field Emitter-based Cathode
FE	Field Emitter
FEA	Field Emitter Array
FESM	Field Emission Scanning Microscope
FN	Fowler and Nordheim
FOPLAP	Fan-Out Packaging on Panel Level
HMA	Hot-Melt Adhesive
HCP	Hexagonal Close-Packed
IC	Integrated Circuit
IMLS	Integral Measurement System with Luminescent Screen
KWT	KlettWelding-Tape
LGA	Land Grid Array
LHC	The Large Hadron Collider
LHe	Liquid Helium
MNI	Micro-Nano-Integration
NEG	Non Evaporable Getter
NMP	N-Methyl-2-pyrrolidone
PC	Poly Carbonate
PCB	Printed Circuit Board

Abbreviations	Description
PE	Polyethylene
PET	polyethylene terephthalate
PI	Polyimide
PVD	Physical Vapor Deposition
PVP	Polyvinylpyrrolidone
RDL	Redistribution Layer
RIE	Reactive Ion Etch
SDS	Sodium Dodecyl Sulfate
SE	Secondary Electron
SEM	Scanning Electron Microscope
SHE	Standard Hydrogene Electrode
SIS100	Schwerionensynchrotron 100 (In Eng.: Heavy Ion Synchrotron 100)
UHV	Ultra High Vacuum
UV	Ultra Violet
VLS	Vapor Liquid Solid
W2W	Wafer to Wafer
WL-CSP	Wafer Level Chip Scale Packaging
XHV	Extreme High Vacuum

---

## List of symbols

---

Symbol	Description	Unit
$A$	Richardson constant	$1.201\,73\,\text{A m}^{-2}\,\text{K}^{-2}$
$A$	Area	m
$B$	Amplitudes of transmitted electron waves for a rectangular potential barrier	m
$C$	Amplitudes of incident electron waves for a rectangular potential barrier	m
$D$	Amplitudes of reflected electron waves for a rectangular potential barrier	m
$E$	Electrical field	$\text{V m}^{-1}$
$E_{\text{on}}$	Onset electrical field	$\text{V m}^{-1}$
$E_{\text{L}}$	Local Electrical field	$\text{V m}^{-1}$
$F$	Faraday constant	$96\,485\,\text{C mol}^{-1}$
$F$	Force	N
$I_{-}$	Electron current in an vacuum ionization gauge	A
$I_{+}$	Ion current in an vacuum ionization gauge	A
$I_{\text{A}}$	Emitter anode current	A
$I_{\text{C}}$	Emitter cathode current	A
$I_{\text{G}}$	Emitter gate current	A
$I_{\text{M}}$	Electrodeposition current	A
$I_{\text{T}}$	Thershold emission current	A
$J$	electrical current densiy	$\text{A m}^{-2}$
$J_{\text{th}}$	Thermionic emission current density	$\text{A m}^{-2}$
$J_{\text{FN}}$	Fowler Nordheim field emission current densiy	$\text{A m}^{-2}$
$M$	Molar mass	$\text{kg mol}^{-1}$
$N(W)$	Number of incident electrons per second incident on $100\,\text{mm}^2$	
$P$	Pressure	mbar
$P_{\text{H}_2}$	Hydrogen pressure	mbar
$Q$	Electrical charge	C
$R_{\text{s}}$	Serial connected resistor	$\Omega$
$S$	Particle transmission probability function	
$S_{\text{tri}}$	Particle transmission probability function for triangle potential barrier	
$S_{\text{rect}}$	Particle transmission probability function for rectangle potential barrier	
$S_{\text{FN}}$	Particle transmission probability function for abrupt potential step	
$T$	Temperature	K
$T^{*}$	Inversion temperature	K

---

Symbol	Description	Unit
$U_t$	Transmembrane voltage	V
$U_{on}$	Upper pulse voltage	V
$U_{off}$	Lower pulse voltage	V
$V_{cell}$	Electrochemical cell potential	V
$V_t$	Transversal etch rate	$\text{m s}^{-1}$
$V_b$	Bulk etch rate	$\text{m s}^{-1}$
$V_l$	Lateral etch rate	$\text{m s}^{-1}$
$W_{Kin}$	Kinetic energy	J, eV
$W_{state}$	Electron state energy	J, eV
$W$	Energy	J, eV
$\bar{W}$	Analytically calculated function of intertube distance and enhancement factor	
$Z$	Atomic number	
$a$	Potential barrier thickness	Å
$d$	Gap size	m
$e$	Elementary charge	$1.602 \times 10^{-19} \text{ C}$
$e\phi_W$	Work function	eV
$h$	Height of Whiskers	m
$i$	Photo emission current	A
$k_B$	Boltzmann constant	$1.380\,649 \times 10^{-23} \text{ J K}^{-1}$
$\nu$	Particle velocity	$\text{m s}^{-1}$
$\hbar$	Planck constant	$1.054\,57 \times 10^{-34} \text{ J s}$
$m_e$	electron mass	$9.109 \times 10^{-31} \text{ kg}$
$n$	Gas molecule density	$\text{cm}^{-3}$
$n_W$	Number of occupied states by electrons per unit energy per unit volume	
$n_{H_2}$	Hydrogen density	$\text{cm}^{-3}$
$p$	Momentum	$\text{kg m s}^{-1}$
$t_b$	Breakthrough time	s
$t_{on}$	Upper pulse width	s
$t_{off}$	Lower pulse width	s
$t(y)$	FE correction factor	
$z$	valency number of ions	
$\Delta\phi$	Shotkey potential barrier	V
$\Delta\phi_M$	Electrode potential compared to SHE	V
$\Delta\phi_{ext}$	Electrochemical cell potential	V
$\Delta\phi_{WE}$	Working electrode potential compared to SHE	V
$\Delta\phi_{REF}$	Reference electrode potential compared to SHE	V



Symbol	Description	Unit
$\Theta$	Apex angle	$^{\circ}$
$\Phi_{\text{tip}}$	Apex Diameter of the cones	m
$\Phi_{\text{base}}$	Base Diameter of the cones	m
$\alpha$	Angle	$^{\circ}$
$\beta$	Field enhancement factor	
$\beta_{\infty}$	Field enhancement factor for a very large gap	
$\epsilon_0$	Vacuum permittivity	$8.854 \times 10^{-12} \text{ F m}^{-1}$
$\epsilon_f$	Fermi level	eV
$\eta$	Over Potential	V
$\theta$	Temperature	$^{\circ}\text{C}$
$\nu$	Frequency	Hz
$\rho$	Wire tip radius	m
$\phi(x)$	Electrostatic potentia	V
$\phi_{\text{W}}$	electroctatic potential in the vacuum nearby the surface	V
$\phi_{\text{eff}}$	Effective work function potential	V
$\phi_f$	Fermie level potential	V
$\phi_{\text{im}}$	Image potential	V
$\phi_{\text{M}}$	Electrode potential at electrode-electrolyte interface	V
$\phi_{\text{H}}$	Standard hydrogene electrode potential	V
$\psi(x)$	Probability distribution function	



---

## 1 Introduction

---

In this thesis, the development and fabrication of cylindrical and conical metallic micro and nano-objects and their integration in 3D complex microsystems will be explored. The basic motivation for this investigation is an idea to improve the performance of ionization vacuum gauges for measuring vacuum pressures less than  $10^{-12}$  mbar<sup>1</sup> in a cryogenic regime. In this chapter, the motivation will be discussed and the segmentation of the work will be introduced.

---

### 1.1 XHV measurement, the gateway toward undiscovered scientific areas

---

New generations of particle accelerators that enable high precision experiments are needed to solve the puzzle of universe evolution and to find out the missing building blocks of the matter structure. These accelerators such as LHC and SIS100 need to be specially designed for their required beam properties like higher intensity, brilliance, energies, and power in the range of thousand billion Watts [23] depending on their research purposes and medical applications. To fulfill these requirements, the particle accelerator facilities run under an Extreme High Vacuum (XHV) environment with typical pressures less than  $10^{-12}$  mbar. Naturally, the main challenge reaching an XHV pressure is how to reduce the residual gas densities, like helium and hydrogen, below  $n_{\text{H}_2} = 10^4 \text{ cm}^{-3}$  equivalent to the pressure of  $P_{\text{H}_2} = 10^{-10}$  mbar at room temperature. This can be achieved by using ultra-high vacuum pumps like turbo molecular pumps, ion sputter pumps, and Non-Evaporable-Getter pumps (NEG). An XHV pressure is generally generated at cryogenic vacuum environments [24]. Cryogenic vacuum systems, such as those found in particle accelerators using superconducting beam guiding components, are typically operated at liquid helium (LHe) temperatures. In these low-temperature systems, pressures in the lower UHV range and even in the upper XHV range can be routinely generated via cryopumping. At temperatures between  $T = 5 \text{ K}$  to  $20 \text{ K}$  the gas particles condensate on the interior surface of the accelerator tubes. The pressure can be reduced to less than  $10^{-12}$  mbar. If the pressure in the system increases, the collisions between the residual gas and the beam particles increase too. These collisions cause the processes like particle stimulation, beam deflection, and discharges, which typically lead to beam emittance.

Thus for saving the XHV state by intercepting vacuum disturbance factors, a precise and reliable measurement of the vacuum in the entire system is essential. But so far it is not obvious which one is better: the vacuum or its measurement [25]. A device for a reliable measurement of the pressures less than  $10^{-12}$  mbar, without disturbing the cryogenic vacuum environment is the missing link in the XHV chain. What we know is that “the generation or measurement of pressures of about 1/100 of a femtobar or less, is particularly attractive, because it pushes science to completely new and undiscovered areas” ([25]).

---

<sup>1</sup> To simplify comparisons with the literature, for pressure the unit millibar (mbar) instead of SI unit Pascal (Pa) is used.  
1 mbar = 100 Pa

## 1.2 Gas pressure measurement and ionization gauges: a brief review

Measuring gas pressure in an enclosed gaseous system is defined by force per area,  $\frac{dF}{dA}$ , exerted on the chamber walls. In ultra-high (UHV) and extreme high vacuum (XHV) regimes, the vacuum cannot be measured using the basic definition of pressure. Thus U-tubes, diaphragm gauges, or even Pirani gauges cannot be used due to the very low density of just a few particles per cubic centimeter. In these cases, the physical quantity of gas pressure or gas density must be transformed into another physical quantity which signals are more convenient to measure [26]. As shown in Figure 1.1, UHV can be measured indirectly via ionization gauges using free electrons, photons (laser), or ions that bombard and ionize the residual gas molecules. Thus the negative electron current  $I_-$ , for instance, will generate a positive ion current  $I_+$  which

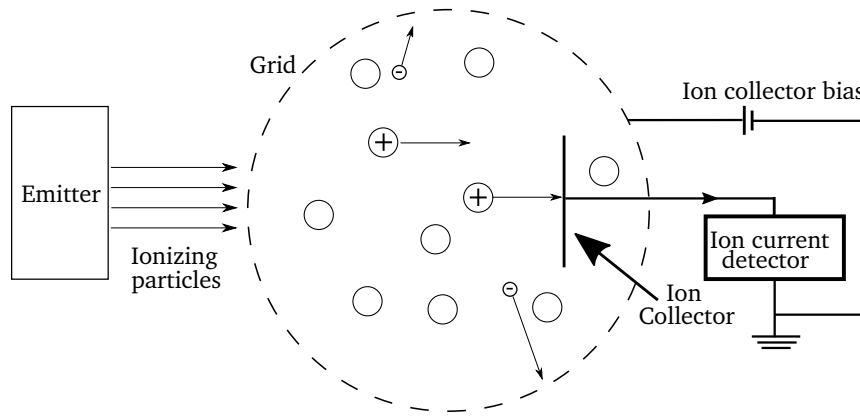


**Figure 1.1:** Basic of ionization gauges. An emitter generates ionizing particles like e.g. electrons. The electrons with current  $I_-$  accelerate towards the grid with positive potential. The transmitted electrons through the grid ionize the residual gas in the gauge volume and the ion current can be measured via the ion collector electrode in an ion current detector.

is proportional to the gas density  $n$  in the gauge volume. The  $I_+$  current will be measured at a collector electrode. At known gas temperatures  $T$  in an enclosed system in equilibrium, the pressure  $P$  can be calculated using the ideal gas relation

$$P = nk_B T \quad (1.1)$$

where  $k_B$  is the Boltzmann constant. These gauges commonly use electrons for the bombardment of gas molecules, because it is economically feasible. Since the invention of ionization gauges between 1909 and 1916 by Baeyer and Buckley [27], some basic ideas are the same in today's gauges. As shown in Figure 1.2, the gauges generally consist of three electrodes: a cathode, as the source of electrons, an anode for extracting and/or accelerating the electrons, and a collector of positive gas ions. To collect the positive ions and not the electrons, the electrical potential of the ion collector must always be negative compared to the cathode. The electron source of an ion gauge whose lowest limit for pressure measurement lies in the ultra-high vacuum range must necessarily deliver a net emission current of at least  $200\mu A$ . This requirement is the result of the fact that at ultra-low pressures the output current of the gauge (i.e. ion current) reaches extremely low values in pA range or even lower. This current, which is directly proportional to the pressure, must still be measurable using a conventional electrometer and picoammeter. A second

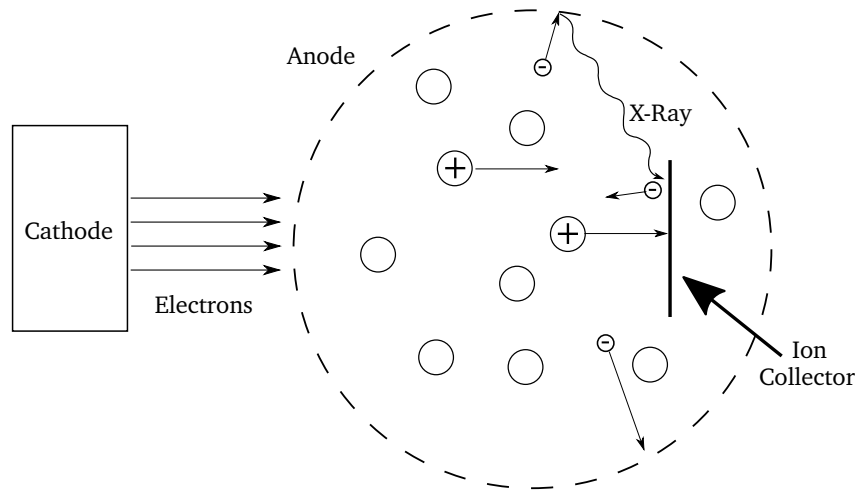


**Figure 1.2:** The electrons generated by the cathode accelerate and partially transmit through the grid, and oscillate inside the grid. The process continues until the electrons collide with a gas molecule and ionize it. Other electrons which hit the grid cause x-ray emission from the grid. The incident x-ray on the surface of the ion collector can free up electrons.

important aspect to be considered is the kinetic energy of electrons leaving the cathode. The ionization probability of gas molecules is energy-dependent. For most gases, the ionization probability governed by electron impact reaches its maximum at kinetic energies of about 100 eV to 250 eV. Thus the voltage to be applied to the extractor grid should be higher or equal to 100 V to keep the energy of the electrons high enough along their path and not exceed 250 V. In the early gauges, the lowest pressure measurement was limited to  $10^{-8}$  mbar. After a period of blockade in measuring vacuum pressures below  $10^{-8}$  mbar during the 1940s, it was suggested that the lower pressure ranges of the triode gauges are not limited by vacuum pumps. But this limit is caused by x-ray effects in ion collectors. The x-ray can be generated by e.g. collisions between electrons and the anode grid. The incident x-ray on the ion collector electrode, makes the electrons eject from the surface (see Figure 1.2 ). This gives an inaccurate ion current  $I_+$  measurement. There are different design ideas for the development of ionization gauges to enable ultra-low vacuum measurements. In the design of these ionization gauges we have to deal with four main challenges to increase the sensitivity of the gauges and cover wider upper and lower gas pressure measurement ranges:

- how to generate the electrons
- how to shape the path of the electrons toward the gas molecules
- how to shape the path of the ionized gas toward the ion collector
- how to design and place the ion collector

In general two types of ionization gauges are the most used commercial gauges which will be introduced as follows:

### Type 1:

In 1950, R.T. Bayard and Daniel Alpert introduced a new design of the vacuum gauge with reduced x-ray limit [28], which made it possible to measure vacuum pressures less than  $10^{-8}$  mbar, for the first time [29]. As shown in Figure 1.3a, the Bayard-Alpert gauge consists the same elements as the conventional ionization gauges. But they use a fine wire with a small surface as the ion collector instead of a wide

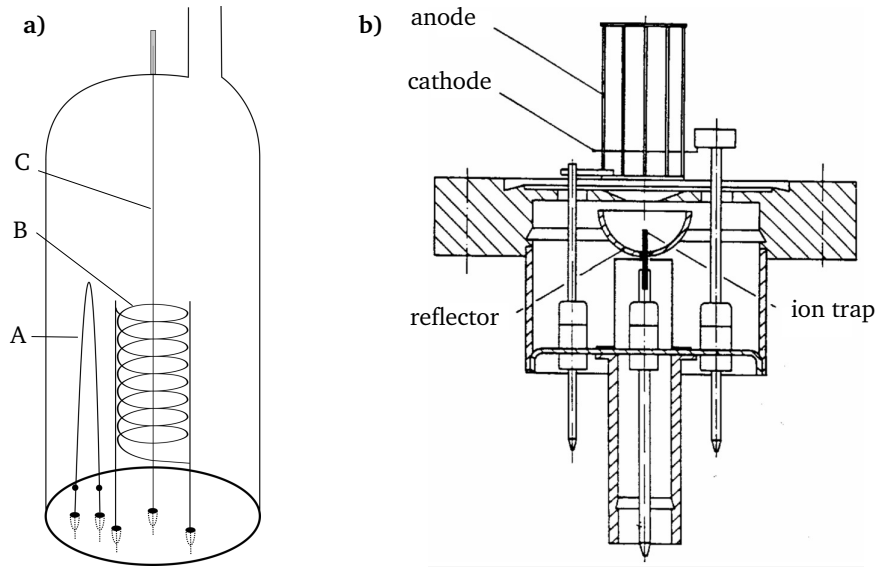


**Figure 1.3:** a) Bayard-Alpert ionization gauge. This gauge has a triode structure with a hot filament (A) as the electron source, anode grid (B) and ion collector (C). The ion collector is made of a thin wire to reduce the surface and consequently the x-ray effect. b) An extractor gauge manufactured by Leybold company [30]

surface electrode. Bayard-Alpert gauges use a hot filament as the electron source, and the generated electrons are accelerated toward an anode grid. The transmitted electrons through the anode grid traverse the space inside the grid and collide with the gas molecules and ionize them. The positive ions are trapped in the enclosed space with the positive grid until they reach the collector in the middle. The measured current  $I_+$  in this gauge is highly and linearly dependent on the pressure, which is one of the advantages of the Bayard-Alpert design. With such gauges, a pressure range of  $10^{-4}$  to  $10^{-9}$  mbar can be measured. Measuring pressures down to  $10^{-11}$  mbar was even done by doing some changes in the design of the Bayard-Alpert gauge, such as maximizing the volume enclosed by the anode grid, reducing the diameter of the collector wire, and using an end cap to minimize the x-ray.

For measuring pressures less than  $10^{-11}$  mbar, different approaches such as measuring the x-ray current and subtracting from the ion collector current or changing the geometry were performed. This led to the development of a gauge at the beginning of the 1970s known as the extractor gauge. An extractor gauge is shown schematically in Figure 1.3b. In an extractor gauge, the collector is much smaller and is removed from the space inside the grid. A reflector around the collector reflects the ions to the tip of the collector for higher sensitivity. In this way, a pressure measurement of about  $10^{-12}$  mbar has resulted.

## Type 2:

So far several varieties of the second type of ionization gauges like Penning, magnetron, and inverted magnetron have been developed. All these gauges use crossed electric and magnetic fields to trap the electrons while the magnetic field increases the path of the electron from cathode to anode. The electron plasma generated in the gauge is responsible for gas ionization. These gauges need a voltage from 2 kV to 6 kV and magnetic fields in the range of 0.1 T to 0.2 T. The electrons in these gauges are generated generally by discharge between the cathode and anode. Electron discharge is generally not stable. At pressures less than  $10^{-4}$  mbar the discharge is a pure electron plasma. In an inverted magnetron gauge,



---

the anode is a cylinder in the middle of the gauge. The electrons rotate around the anode and achieve enough energy to ionize the gas molecules. The generated ions are gathered by an auxiliary cathode where its current is proportional to the gas density and pressure. With these gauges typically pressure ranges from  $10^{-2}$  to  $10^{-9}$  mbar can be measured. The current-pressure proportionality of such gauges is not linear like Bayard-Alpert gauges. Therefore, in some cases, a table is used to read the pressure. A detailed historical review of these gauges can be found at [30].

---

### 1.3 Motivation: Improving the specifications of electron emitters

---

Two types of gauge designs have been introduced above. As mentioned, a major difference between these two types is how the electrons are generated:

1. The first type, also known as “Hot Cathode Ion Gauge”, is the most commonly used gauge type. In this type, the electron-emitting cathode generates the electrons by a hot filament or thermionic cathode. These cathodes emit electrons at  $T=800$  K for oxide-coated cathodes to  $T=2500$  K for tungsten cathodes. In hot cathodes the emission current can be generated with relatively simple electronics and the current can be controlled and kept constant by controlling the heat power of the filament. This emission current ranges from a few  $\mu\text{A}$  to a few mA. But these gauges have some known disadvantages:

- They disturb the thermodynamic equilibrium of the environment
- Their power consumption is high
- Hot cathodes irradiate light in their surrounding area
- The outgassing of the cathodes material and other components in the gauge is not negligible
- Cathodes material evaporates in the system
- Such hot filaments are not proper to use in corrosive environments
- They have a short lifetime and are destructed easily by air shocks or heavy vibrations

The majority of commercial gauges with hot cathodes have the Bayard-Alpert design.

2. The second type is “Cold Cathode Ion Gauge”, whose electrons are generated by electrical discharge. This type of gauge, as mentioned above, is also known as a crossed field gauge.

In a cryogenic vacuum environment, the physical adsorption of the gas particles on the surface has a low atomic binding energy in the range of 10 to 100 meV compared to the chemical adsorption binding energies of about 10 eV. This means that the system should be in thermal equilibrium and any temperature rise can free the adsorbed particles from the surface. The beam deflects by collision with the freed particles, which makes more particles free from the surface. Thus this process is a self-amplifying process that causes an avalanche-like increase in the pressure [31]. Besides thermal induced desorption, also leakage in the system and outgassing due to contamination can lead to a local pressure increase. Such disturbances in the system should be monitored and detected as fast as possible by a real-time pressure measurement at different locations along the system to prevent the diffusion of gas particles all over the system after some hours or days. It saves a huge amount of time and energy to repair, re-evacuate, and cool down the chambers and tubes in just one station instead of in a large part or even the entire length of the system.

---

Despite the disadvantages of the hot cathodes mentioned above, the non-heating operation of the field emission cathodes is one of the major reasons why the cold cathode gauges are proper for measuring XHV. However, the cold cathode gauges have some technical shortages, which face their usage in a cryogenic vacuum system with problems:

- Their electron extraction voltages are in the range of kV that still inject a high amount of energy into the system
- Outgassing of electron emitters locally changes the pressure of the system
- Achieved current to perform a measurement is not sufficient
- Their fabrication process is complex, time-consuming, and expensive
- Electrical behavior of the electron extractors in long-term applications should be investigated.

Thus, today there is no vacuum gauge available, which can be used unconditionally for measurements in a cryogenic environment. Developing a technology to fabricate a proper electron emitter, as a cold cathode, for use in an extractor vacuum gauge is the subject of this thesis. This technology tries to eliminate or minimize the problems of field emitter based gauges and improve the electrical behavior and magnitude of emission current.

---

## 1.4 Dissertation outline

---

In Chapter 2, the state-of-the-art of field emitter gauges will be reviewed and the technological problems in the fabrication of such gauges will be discussed. Then, a concept based on metallic nano-objects to eliminate these problems will be introduced. In Chapter 3, the fabrication of metallic nanowires and their integration in micro systems will be discussed. In an accelerator facility, the vacuum should be measured at different stations along the path to detect any leakage in a short time. For an accelerator area more than 1 km up to 400 measuring gauges are conceivable. To achieve a higher current more than three cathodes can be mounted in each gauge. Fabricating 1200 cathodes plus reserves need a proper scaled up fabrication process. In chapter 4, it is shown how this novel integration technique is upscaled for large areas of about  $(300 \times 300) \text{ mm}^2$ . In Chapter 5, the modification of nanowires into conical geometry will be introduced. This modification step is necessary to overcome some problems of nanowires based emitters. In Chapter 6, the field emission characteristics of the cathodes fabricated with this technology will be explored and discussed. In Chapter 7, a novel bonding technology, as an application of the metallic nanowires, will be introduced. In this chapter, the fabrication process of the electron field emitter will be introduced and the simplification of the fabrication process with the new bonding technology will be discussed. In Chapter 8 the new nanowires based heat-free bonding technique will be investigated. This technique can be applied to different types of substrates like glass, silicon, all types of metals, polymers, ceramics, FR4, etc... This technique can be applied to contact pads with an edge length of  $3 \mu\text{m}$  to  $300\,000 \mu\text{m}$ . This technology is a promising method to improve the packaging in the semiconductor industry. The very low electrical and thermal resistance of the connections and their high mechanical strength also makes them suitable for high current and heavy-duty contacts like bus bars in electro-mobility applications.

## 2 Field emitter-based cathodes in ionization vacuum gauges

In thermionic emission of electrons, the electrode is heated up to the temperature  $T$  and thermal energy is transferred to the electrons with electrical charge  $e$ . The electrons on the surface with sufficient kinetic energy overcome the vacuum electrochemical potential barrier  $\phi_w$  and eject into the vacuum. As schematically illustrated in Figure 2.1, the electron energy must be higher than  $e\phi_w + \epsilon_f$ , where  $e\phi_w$  and  $\epsilon_f$  are the work function and the fermi energy respectively. This means that the electrons near the Fermi

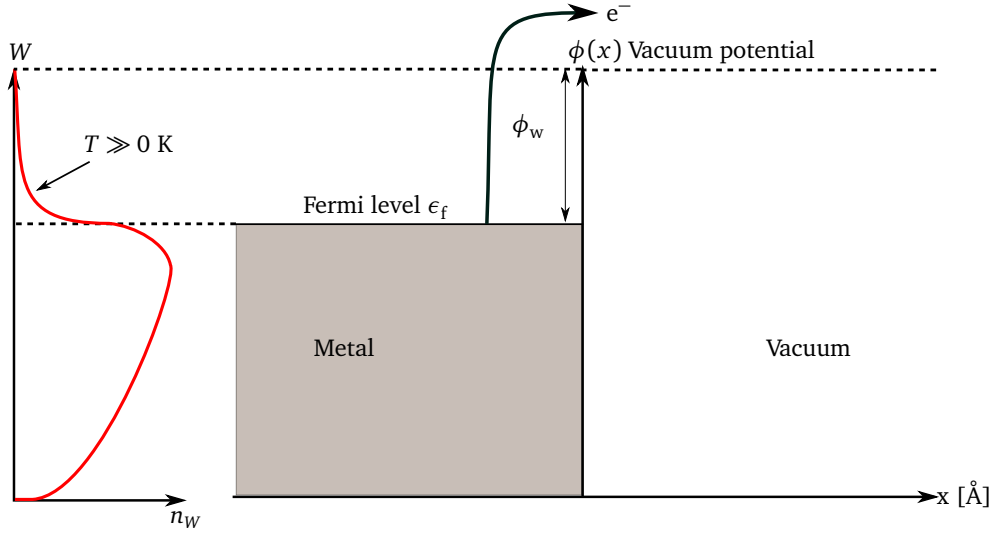


**Figure 2.1:** Potential-energy diagram of the electrons at a metallic surface. At temperatures  $T \gg 0$  K the Fermi-Dirac distribution function is non-zero above the Fermi level  $\epsilon_f$ . The electrons can occupy the available states above the Fermi level till the electrons with energies higher than the work function can overcome the vacuum potential barrier and escape.  $\phi(x)$  is the electrostatic potential in vacuum and  $n_W$  is the number of electrons per unit energy per unit volume.

level  $\epsilon_f$  must reach an energy level higher than the material work function  $e\phi_w = \frac{1}{2}m_e v^2 = \frac{p^2}{2m_e}$ , where  $m_e$  is the electron mass,  $v$  the electron velocity, and  $p$  the momentum of the electron in  $x$  direction. This occurs at the momentum of

$$p = (2m_e e\phi_w)^{\frac{1}{2}}. \quad (2.1)$$

The thermionic emission current density  $J_{th}$  equals to [32]

$$J_{th} = AT^2 e^{-e\phi_w/k_B T}, \quad (2.2)$$

where  $k_B$  is the Boltzmann constant and  $A$  is the so-called Richardson constant.  $A$  can be estimated by

$$A = \frac{4\pi m_e k_B^2 e}{h^3} = 1.20173 \left[ \frac{A}{m^2 K^2} \right], \quad (2.3)$$

where  $h$  is the reduced Planck constant. The work functions of most high-melting metals are about 4 eV to 5 eV. Thus, for sufficient electron emission, temperatures higher than 1500 K are needed. There are just a few devices that can be heated up to such high temperatures. The disadvantages of the thermionic process for generating free electrons, used in vacuum gauges to measure UHV and XHV ranges in the

cryogenic regime, are mentioned in Chapter 1. Free electrons can also be generated using alternative physical mechanisms with no heat. These alternative physical mechanisms are photoemission, secondary electron emission, and field emission.

The generation process of free electrons by photoemission is shown in Figure 2.2. The photon energy  $h\nu$ , needed to let the electrons eject, is the amount of work function  $e\phi_w$  plus the kinetic energy of free electron  $W_{\text{Kin}}$ . This means the kinetic energy of the emitted electrons depends on the photon frequency. This frequency ranges from ultraviolet to X-ray.

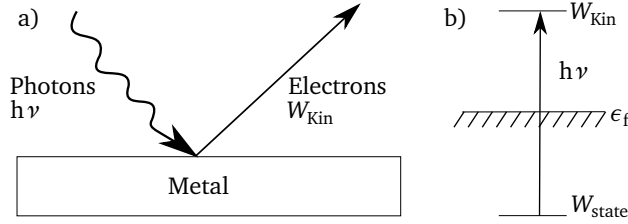


**Figure 2.2:** a) Direct photoemission effect. Incident photons let the electrons escape from a given metallic surface. b) Simplified potential model for the photoemission.  $h$  is the Planck constant,  $\epsilon_f$  the Fermi level, and  $\nu$  the frequency.

The Fowler's law predicts a quadratic dependence of photoemission current  $i$  to the photon energy [33]

$$i \propto (h\nu - e\phi_w)^2. \quad (2.4)$$

Also, the number of emitted electrons from the surface depends on the light intensity. Thus UV or X-ray sources with high intensities are needed. However, the electron emission current is not still sufficient. Furthermore, the metallic photocathode is strongly sensitive to the adsorption effects. The next candidate, the secondary electron emitter, is commonly used in photomultipliers and also image intensifier tubes. These emitters need a primary electron or ion source to bombard the surface of the material to generate free electrons. They are also sensitive to gas adsorptions, which means that the field emission is the only considerable heat-free alternative mechanism for the thermionic process to generate free electrons. In this chapter, this mechanism and its theory and the state-of-the-art research will be focused on. Finally, a concept for a field emission cathode will be introduced.

## 2.1 Basic theory of field emission

The field emission is defined as the emission of electrons from the surface of a condensed phase into another phase, usually vacuum, by applying a high static or quasi-static electric field  $E \geq 10^9 \frac{\text{V}}{\text{m}}$ . The focus of this thesis is the emission from metallic surfaces into the vacuum. This phenomenon is discovered and studied independently since the 1880s. It is essentially a quantum mechanical problem and cannot be explained by classical physics. As shown in Figure 2.3, the applied electrical field deforms the vacuum potential and the potential barrier height is changed to  $\phi(x) = \phi_f + \phi_w - Ex$ . This is the fundamental difference between the field emission process, the thermionic emission, and the photoemission. For a vacuum potential height of  $\phi(a) = \phi_f + \phi_w - Ea$  the barrier thickness  $a$  at the Fermi level is

$$a = \frac{\phi_w}{E}. \quad (2.5)$$

This equation shows that the thickness of the barrier is proportional to the work function of the material. But this thickness can be reduced by applying high electrical fields on the surface. Thus the electrons with a kinetic energy  $W_{\text{kin}}$  near the Fermi energy are able to tunnel the barrier with a specific thickness equal to or less than  $a$ . Therefore, for the electron emission, a minimum electrical field known as on-set field  $E_{\text{on}}$  is needed.

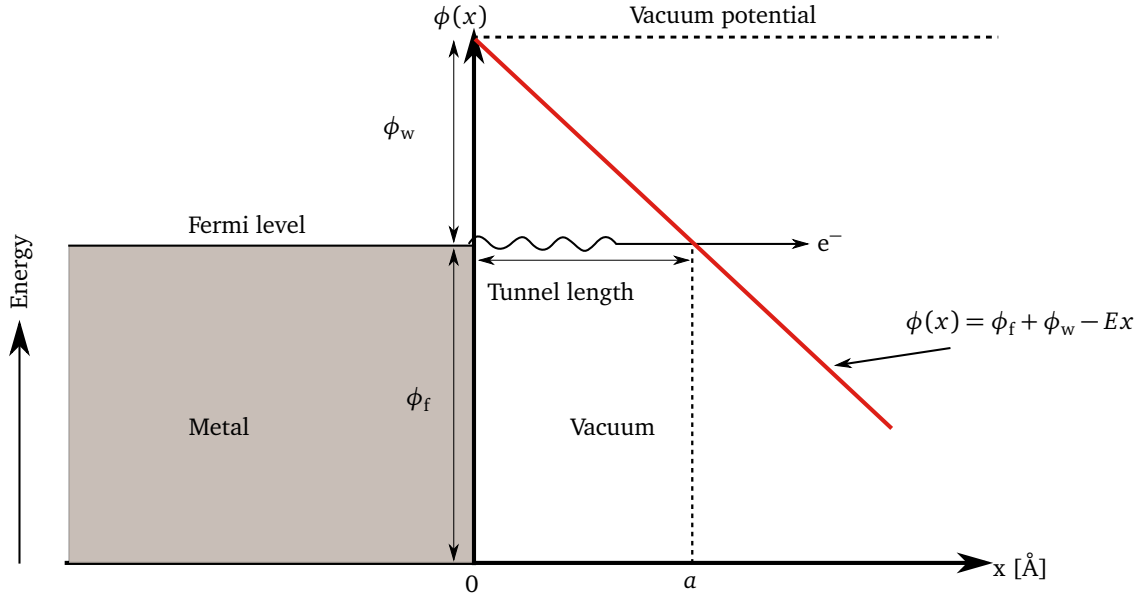


**Figure 2.3:** Schematic diagram of tunnel effect. Applying an electrical field  $E$  on the surface of the metal will deform the vacuum potential-barrier. The electrons can tunnel through this narrow wall.

Considering the uncertainty relation  $\Delta p \cdot \Delta x \cong \frac{\hbar}{2}$  with  $\hbar = \frac{h}{2\pi}$  and  $h$  being Planck's constant, for electrons near the Fermi level, with the momentum  $p$  given in the equation (2.1), the uncertainty in position equals

$$\Delta x \cong \frac{\hbar}{2(2m_e e \phi_w)^{\frac{1}{2}}}. \quad (2.6)$$

Using (2.5) near the Fermi level gives

$$\frac{\phi_w}{E} \cong \frac{\hbar}{(8m_e e \phi_w)^{\frac{1}{2}}}. \quad (2.7)$$

The minimum electrical field is required for the unexcited electrons to be able to tunnel the deformed potential barrier and emit into the vacuum is

$$E_{\text{on}} \cong \left( \frac{8m_e}{\hbar} \right)^{\frac{1}{2}} \frac{(e\phi_w)^{\frac{3}{2}}}{e}. \quad (2.8)$$

This equation shows that the metals with lower work functions need lower minimum electrical fields for the field emission.

The quantum mechanical description of the tunnel effect begins with the Schrödinger equation for the case in which the energy of the electron  $W_{\text{kin}}$  at  $x = 0$  is less than the potential height  $\phi(a)$  with the potential barrier thickness  $a$

$$\frac{\hbar^2}{2m_e} \partial_x^2 \psi(x) + (W_{\text{kin}} - \phi(x))\psi(x) = 0, \quad (2.9)$$

where  $\psi(x)$  is the probability distribution of the electron wave at the point  $x$ . As shown in Figure 2.4, the transmission probability  $S(W, \phi)$  is defined as the probability that an electron transmits the potential barrier from the left side to the right side and does not turn back. The transmission probability for a

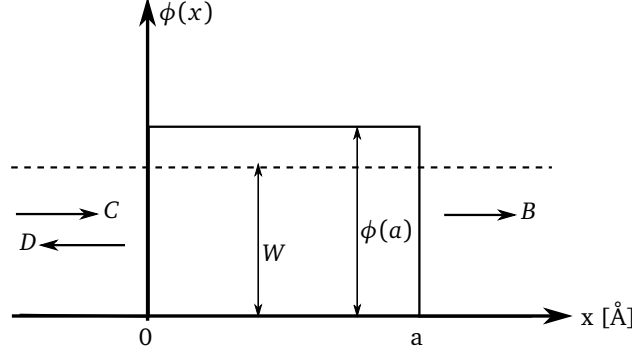


**Figure 2.4:** Electron tunneling through a rectangular potential barrier.  $C$ ,  $D$ , and  $B$  are respectively the amplitudes of the incident, reflected, and transmitted electron waves. The transmission probability is defined as  $S(W, \phi) \cong [\psi(a)/\psi(0)]^2 = B/C$ .

rectangular barrier reads as [34]

$$S_{\text{rect}}(W, \phi) \cong f(W, \phi) \exp \left( -2a \sqrt{\frac{2m_e}{\hbar^2} (\phi(a) - W)} \right), \quad (2.10)$$

where  $f(W, \phi) = \frac{16W\phi}{(W+\phi)^2}$  is an insensitive function of  $W$  and  $\phi$ . The variable  $f$  can be approximated by a constant value. In a triangular potential barrier like the barrier shown in Figure 2.3 this transmission factor can be expressed as an integral of the potential along the electron path,

$$S_{\text{tri}}(W, \phi) \cong f(W, \phi) \exp \left( -2 \left( \frac{2m_e}{\hbar^2} \right)^{\frac{1}{2}} \int_0^a \sqrt{(\phi(x) - W)} dx \right). \quad (2.11)$$

The right hand side of the (2.11) represents a non-exact but nearby triangular shape with a base length of  $(e\phi_f + e\phi_w - W_{\text{Kin}})/Ee$  and a height of  $\sqrt{e\phi_f + e\phi_w - W_{\text{Kin}}}$ . The area under the triangle can be written as

$$A \cong \frac{1}{2} \frac{(e\phi_f + e\phi_w - W_{\text{Kin}})^{\frac{3}{2}}}{Ee}. \quad (2.12)$$

Substituting (2.12) in (2.11) gives

$$S_{\text{tri}}(W, \phi) \cong f(W, \phi) \exp \left( - \left( \frac{2m_e}{\hbar^2} \right)^{\frac{1}{2}} \frac{(e\phi_f + e\phi_w - W_{\text{Kin}})^{\frac{3}{2}}}{Ee} \right). \quad (2.13)$$

This transmission factor is very similar to the  $S$  for an abrupt potential step at the metal surface theoretically calculated by Fowler and Nordheim [35]

$$S_{\text{FN}} = \frac{4 \left[ W_{\text{Kin}} (e\phi_f + e\phi_w - W_{\text{Kin}})^{\frac{1}{2}} \right]}{e\phi_f + e\phi_w} \exp \left( - \frac{4}{3} \left( \frac{2m_e}{\hbar^2} \right)^{\frac{1}{2}} \frac{(e\phi_f + e\phi_w - W_{\text{Kin}})^{\frac{3}{2}}}{Ee} \right). \quad (2.14)$$

Limiting (2.14) just to the electrons near the Fermi level with  $W_{\text{Kin}} \cong e\phi_f$  the equation is simplified as

$$S_{\text{FN}} = \frac{4(\phi_f \phi_w)^{\frac{1}{2}}}{\phi_f + \phi_w} \exp \left( -6.8 \times 10^7 \frac{(\phi_w)^{\frac{3}{2}}}{E} \right). \quad (2.15)$$

As shown in Figure 2.5, for a more accurate calculation of the tunneling conditions, considering the potential decay is necessary. The classical image potential term  $\phi_{\text{im}} = -e^2/16\pi\epsilon_0 x$  near the metal surface, for  $\phi_{\text{im}}$  in volts and  $x$  in angstrom, can be used.  $\epsilon_0$  is the vacuum permittivity. By applying the electrostatic field  $E$ , the potential at the metal surface can be expressed as

$$\phi(x) = (\phi_f + \phi_w) - \frac{e^2}{16\pi\epsilon_0 x} - eEx. \quad (2.16)$$

The maximum value of  $\phi(x)$  is the effective work function potential  $\phi_{\text{eff}}$ . This value and its location  $x_{\text{max}}$  can be calculated by differentiating (2.16) and setting it equal to zero. This gives

$$x_{\text{max}} = \left( \frac{e}{16\pi\epsilon_0 E} \right)^{\frac{1}{2}}, \quad (2.17)$$

and with  $\phi(x) = \phi_f + \phi_{\text{eff}}$  the effective work function potential can be calculated as

$$\phi_{\text{eff}} = \phi_w - \left( \frac{e^3 E}{4\pi\epsilon_0} \right)^{\frac{1}{2}}, \quad (2.18)$$

and the Schottky barrier can be written as

$$\Delta\phi = \phi_w - \phi_{\text{eff}} = \left( \frac{e^3 E}{4\pi\epsilon_0} \right)^{\frac{1}{2}} = 3.8E^{\frac{1}{2}}. \quad (2.19)$$

It is important to mention that at the surface of a planar and clean metal the electron cloud in the Fermi sea

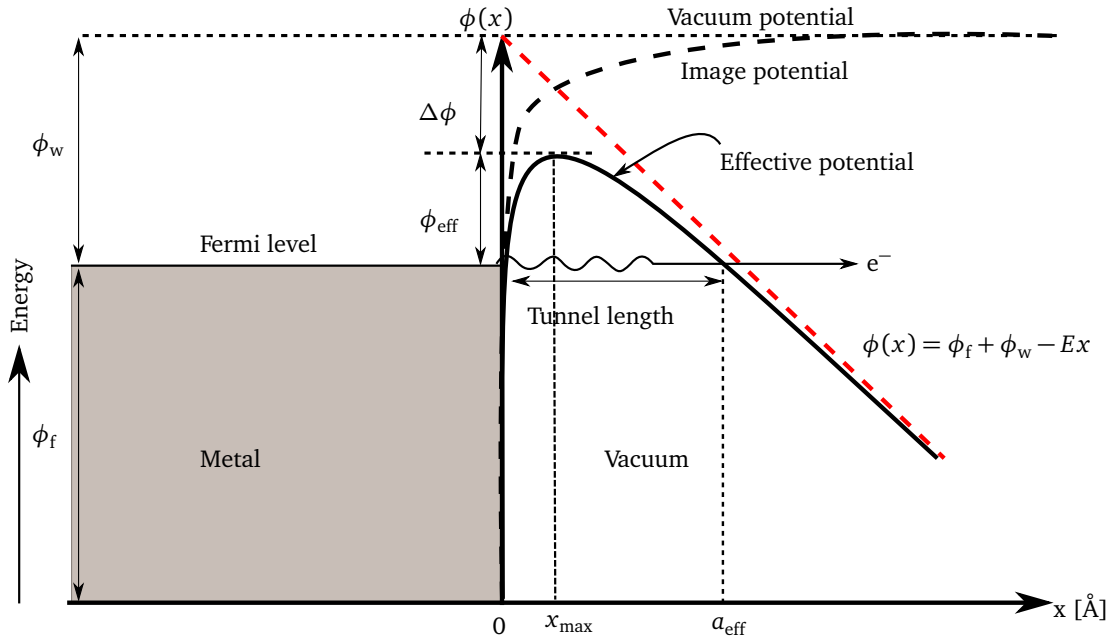


**Figure 2.5:** Tunnel effect with image potential included on the surface of the metal will deform the vacuum potential barrier, which the electrons can tunnel through this narrow wall.

will not terminate abruptly at the surface and the electron wave function has a gradual decay. This gives rise to a double layer on the surface. As all electrostatic contributions of the double layer to  $\phi(x)$  vanish quickly in large distances, this can be ignored in field emission phenomena for finite crystals [32]. But for very rough surfaces or surfaces that become rough by absorption, the double layer electrostatic contribution should be considered too. After applying the electrostatic field  $E$ , the emission current density  $J$  can

be calculated by multiplying the transmission factor  $S$  by the differential rate of arriving electrons with energies between  $0 \leq W_{\text{kin}} \leq \epsilon_f$  and integrating as,

$$J_{\text{FN}} = e \int_0^\infty N(W)S(W, E)dW, \quad (2.20)$$

where  $N$  is the number of incident electrons per second with velocities along the emission direction and energies between  $W$  and  $W + dW$ , on  $100 \text{ mm}^2$  of the surface [36]. For the triangle case with assumed image potential, the calculation of transmission factor  $S$  is not trivial as the case calculated in (2.15). It can be calculated analytically with the Wentzel, Kramers, Brillouin (WKB) approximation and using (2.16). The WKB approximation leads to an image correction factor for the calculated area under the potential curve. The classic Fowler Nordheim (FN) current density formula at  $T = 0 \text{ K}$  is [36]

$$J_{\text{FN}} = \frac{e^3 E^2}{8\pi h t^2(y) \phi_w} \exp\left(-6.8 \times 10^7 \frac{(\phi_w)^{\frac{3}{2}}}{E} \nu(y)\right), \quad (2.21)$$

where  $\nu(y) = (1-y)^{\frac{1}{2}}$  and  $t(y) = \nu(y) - (2y/3)(\frac{d\nu(y)}{dy})$  are the image potential multiplicative correction factors known as Nordheim function with  $y = 3.8 \times 10^{-4} E^{\frac{1}{2}} / \phi_w$ . The values for Nordheim functions are tabulated in the literature, see e.g. [37]. Neglecting the image charge and using the transmission factor (2.15) will reduce the FN equation to

$$J_{\text{FN}} = 6.2 \times 10^6 \frac{(\phi_f \phi_w)^{\frac{1}{2}}}{\phi_f + \phi_w} \cdot E^2 \exp\left(-6.8 \times 10^7 \frac{(\phi_w)^{\frac{3}{2}}}{E}\right) [\text{A/cm}^2]. \quad (2.22)$$

For the electrical fields  $E$  about  $3 \times 10^9$  to  $6 \times 10^9 \frac{\text{V}}{\text{m}}$ , the current would be about  $10^2$  to  $10^3 \frac{\text{A}}{\text{cm}^2}$  [32].

## 2.2 State-of-the-art field emitter-based cathodes

Regarding (2.21), two variables determine the emission current: one is the material work function of the emitting object and the other is the applied electrical field. The work function is restricted by nature and just a few techniques like optimizing the crystal structure [38] or coating the surface with a donor layer [39] can reduce it. For the electrons field emission, a large electrical field  $E$  in the range of  $10^9 \frac{\text{V}}{\text{m}}$  is needed. The usual way to obtain this electrical field is to use a very sharp and long structure. The reason for using this special structure will be explained in the next section. Besides these two criteria, there are some other aspects like adsorption of external molecules, oxide layers, changes in the emitter geometry, and material outgassing in UHV which must be considered during the design process. So far, various combinations of techniques and materials have been investigated to reach a proper field emitter-based cathode (FEC). As discussed in Chapter 1, a proper field emitter means a field emitter that yields enough emission current to perform a vacuum measurement at a low extraction voltage of less than 1 kV. Such emitters must emit a stable current for a long time and have a cost-efficient and not complex fabrication technique for commercial applications. In this section, some usual FE designs and materials and their specifications will be summarized:

1) Single tip: The simplest idea for a FE to be used in the form of FEC is a sharply etched tip. The fabrication process is nearly the same as the fabrication process of the atomic force microscope cantilevers and needles. The sharp 3D tips can be made by growing the tips with the atomic beam epitaxy. This technique reaches a sharp punctual single metallic tip. The emitting electrons from a single tip are not



flexible in the emission angle, due to the perpendicular electrical field at the tip. As mentioned in Chapter 1, for a maximum gas ionization probability the energy of the electrons should be in the scale of 100 eV. The emitted electrons from a single tip have energy in the range of keV. The high energetic electrons give a very small ionization cross-section. Furthermore, in a while, the sharp tips will be rounded by an ionic bombardment of the tip or by gas-particle adsorption at higher pressures. Also, the emission current for tip diameters below 10 nm [40] is in the range of some  $\mu\text{A}$  or lower which is not an appreciable current for using as an FEC for measuring XHV.

2) Field-emitter array (FEA): The FEAs consist of thousands to millions of small tips per square centimeter in the form of a matrix seating next to each other on the substrate. The most common FEAs are made of silicon or Molybdenum with a top-down or bottom-up process on a silicon substrate. The first developed FEA was fabricated from Mo and introduced by Spindt in 1968 [41][42]. Spindt reported an emission current density of about  $10 \frac{\text{A}}{\text{cm}^2}$  with an applied voltage of just 300 V. Compared to the metallic single tips with few  $\mu\text{A}$  current at some kV voltage, the Spindt FEA was a great success. The invention of this new FE type at the Stanford Research Institute was a revolution in vacuum microelectronics. That is the reason that this type of FEC is also known as Spindt-cathode. As shown in Figure 2.6a, the tips are made of molybdenum and have a conical shape. They are about  $1.5 \mu\text{m}$  long and have a tip radius of 50 nm. Tips density is typically between  $10^5$  to  $10^9 \frac{1}{\text{cm}^2}$ . The fabrication process is shown in Figure 2.6b:

- (a) The process begins on a 0.75 mm thick silicon wafer with oxidizing the wafer to  $1.5 \mu\text{m}$   $\text{SiO}_2$ -thickness. Then a layer of Mo with about  $0.4 \mu\text{m}$  is deposited on the oxidized surface by a PVD process. In a lithography step with e-beam, the spots are defined on the surface and the silicon oxide is etched selectively. This results in the structure shown in step (a) of Figure 2.6b.
- (b) Under an angle  $\alpha$  a thin sacrificial layer of aluminum is deposited, which can define the opening size. The deposition angle will determine the conical geometry of the metallic tip in the cavity in the next step.
- (c) A metallic layer, like Mo or W will be deposited.
- (d) The sacrificial aluminum layer is etched and the deposited metal layer is released by lift-off.

The fabrication process of the Spindt array includes more than seven steps and needs a silicon fabrication facility. The cones are mounted on the wafer, the extraction gate is integrated, and the distance cannot be varied anymore. Nevertheless, the Spindt FECs are widely and successfully used in different prototypes like flat panel displays and microwave amplifiers. They have also been used in ionization gauges, mostly as a substitution for hot filaments. Also, other types of FEAs are fabricated and investigated, such as ungated, double-gated, or multi-layer tips covered with e.g. diamond-like carbon (DLC). It has been shown that the FEAs could be a good alternative for hot cathodes. Due to the technical problems and fabrication complexity of the FEAs they have not still found their way from a lab development stage to mass production. Furthermore, the emission performance of the FEAs is extremely related to their environment. At higher pressures, the gas adsorption will round off the tips of the FEAs and also change the work function. So the FEAs should be backed or substituted. Apart from that, the researchers have observed outgassing of FEAs [43]. The FEAs are outgassing due to the materials like silicon dioxide as an insulator in their structure, or fluorine and chlorine used in their fabrication process. Mainly  $\text{H}_2$ , CO, O,  $\text{CO}_2$  and F have been detected [43]. Also, the low tolerance of these FEAs against high temperatures makes the baking with temperatures over  $200^\circ\text{C}$ , for the reduction of outgassing, impossible. Another problem is the diffi-

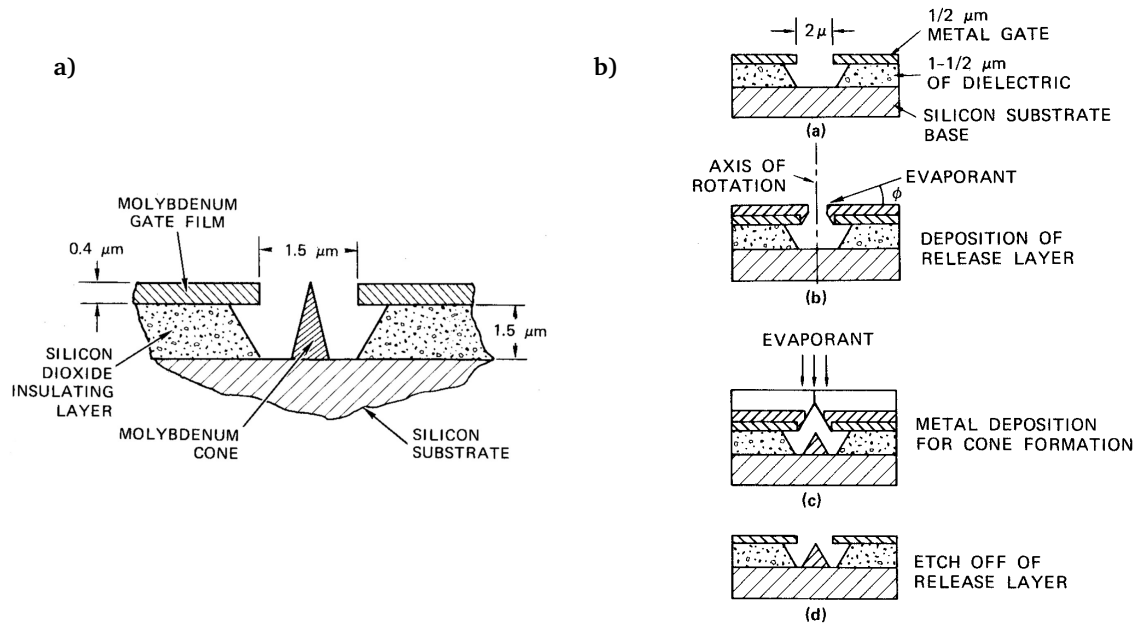


**Figure 2.6:** a) The cross-section of a single tip. b) The fabrication process of Spindt array [42]

culty to pump out the unwanted gas gathered in the cavities of the Spindt FEAs. Despite the appreciable properties of such FEAs in terms of the amount of current, current stability, power consumption, and low turn-on voltage, they are not still applicable for measurement in the XHV regime at LHe temperatures.

3) Silicon structures: The widespread available silicon micro-fabrication technology gave the silicon-based structures and devices a rise to be used in a FE structure. In an n-type or p-type silicon-based emitter the Fermi level will be shifted in the bandgap towards the conduction band or valance band. But never the number of the free electrons in the conducting band will reach zero in equilibrium and non-absolute-zero temperature. Thus, always free electrons for tunneling under an electric field of high strength are available. Devices like p-n junction diodes can operate as a FE in a reverse direction. The electrons in the exhaustion zone with higher energies can tunnel into the vacuum. But the number of electrons is not enough to reach a high current [43]. By reactive ion etching (RIE) of silicon, FEAs with very sharp conical geometry can be developed. Also, it is possible to grow silicon nanowires with Vapor-Liquid-Solid (VLS) process [44]. In [45] emission currents of  $0.1 \mu\text{A}$  for p-type and  $0.6 \mu\text{A}$  for n-type for an array of  $3 \times 10^5 \frac{1}{\text{cm}^2}$  Si tips are reported.

4) Carbon Nano Tubes (CNT): For the first time, Baker [46] could show that graphite fibers as a new electron source have better stability compared to many metals in different environments. In 1991 CNTs were invented and introduced. The CNTs can be fabricated by numerous methods like discharge between two carbon electrodes or thermal and plasma chemical vapor deposition (CVD). CNTs have good temperature resistance and can be heated up to 2000 K [47], which is an advantage for UHV applications. They have a diameter between 0.5 to 50 nm and a length between 1 to 100 μm. This geometry lets them have a lower emission threshold compared to e.g. Mo tips. Thus CNT-based cathodes are one of the most thoroughly studied field emitter cathodes in ionization gauges, which are characterized by a low turn-on field and outstanding field emission properties in terms of current density and short-term stability. It has been shown that the CNTs are more sensitive to small pressure fluctuations in LHe temperatures than hot cathodes and

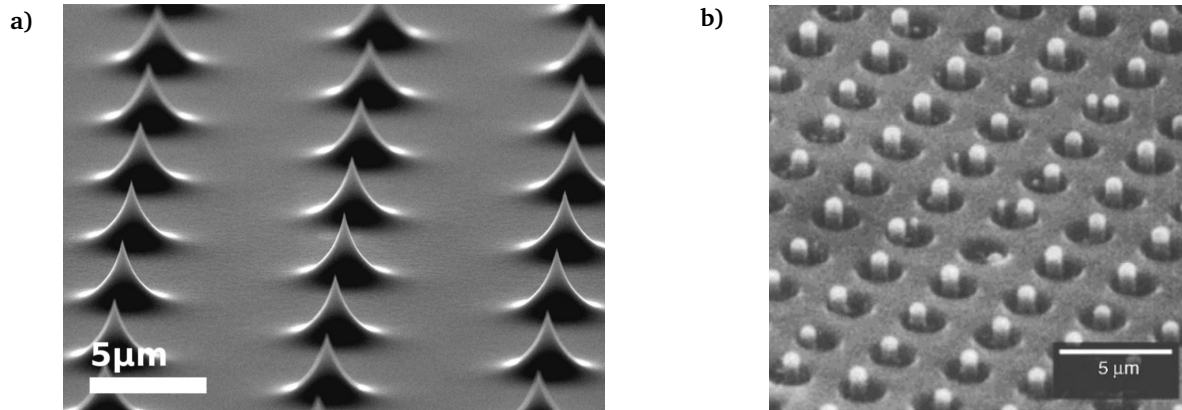


**Figure 2.7:** a) SEM Image of a p-Si FEA fabricated by RIE anisotropic dry etching of silicon and wet chemical etching of SiO<sub>2</sub> [45]. b) Array of integrated gate Si nanowires as an emitter array. The Si wires are grown with VLS process [44].

provide meaningful pressure readings regarding fluctuations in temperature [24]. In most cases, however, CNT films do not emit uniformly across their emitting surface area (i.e., they possess emission hot spots) because the film homogeneity and the growth behavior are difficult to control during the preparation [48]. Furthermore, the poor electric contact between the substrate and the CNT layer can be problematic because it restrains the electron transport and reduces the field emission yield. As a consequence, when the extraction voltage becomes too high, excessive amounts of ohmic power is dissipated in the resistive substrate so that the contact area can even melt [49]. Also, the rapidly progressing emission degradation of the CNT cathodes, when operated at higher pressures, indicates that they cannot be used unreservedly as an alternative cathode in ion gauges at cryo temperatures. Furthermore, the high fabrication cost, besides the problematic integration of the CNTs in complex systems is a disadvantage of them.

### 2.3 Metallic nanowire arrays as field emitter

A promising alternative to CNT cathodes are the metallic nanowire arrays. Owing to their specific mechanical, electrical, and chemical properties, they offer the opportunity to develop highly effective field emission sources with field emission properties similar to CNT cathodes but with fewer drawbacks. In contrast to CNT cathodes, metallic nanowire array preparation can be well-controlled in terms of areal density, wire diameter, wire length, and tip radius. Additionally, the electrical contact problems between the substrate and the emission layer are less significant. Moreover, the metallic nanowires do not have the “hairy” surface structure of the CNT cathodes, where huge amounts of gases can be absorbed and accumulated for a long time. Recently, the field emission properties of gold nanowires have been investigated intensively by Dangwal et al. [50] who showed that the ratio of emitting wires to deposited wires in a gold nanowire cathode is substantially higher than that in the typical CNT cathodes. To design a metallic nanowire-based FEC some criteria must be considered. One is the so-called field enhancement factor  $\beta$ . As shown in Figure 2.8a the macroscopic parallel electric field lines from infinity enter the metallic nanowire surface perpendicularly. The enhanced local field  $E_L$  at the rounded tip of a wire can be written as

$$E_L = \beta E. \quad (2.23)$$

As shown in Figure 2.8b, the enhancement factor  $\beta$  can be calculated theoretically by modeling the wire as a floating sphere in space with the radius  $\rho$  and an apex distance of  $h$  from the emitter surface with the charge  $-Q$ . Considering the image charge  $+Q$  gives the  $\beta$  factor as [51], [52]

$$\beta = E_L/E = 2.5 + h/\rho. \quad (2.24)$$

This means the longer the whisker's length is, the larger the enhancement factor will be. Also,  $\beta$  has a proportional dependence on the wire tip sharpness. For a cylindrical wire with a length of  $20\mu\text{m}$  and a diameter between 400 to 100 nm a  $\beta$  factor between 100 to 400 is expected. However, in real situations for an array of wires,  $\beta$  lies between 10 to 40. Many researchers have experimentally shown that the enhancement factor depends on the gap between the anode electrode and the emitting tips of the wires [53], [54], [55]. Craig Miller [56] has theoretically calculated the gap effect on the enhancement factor for

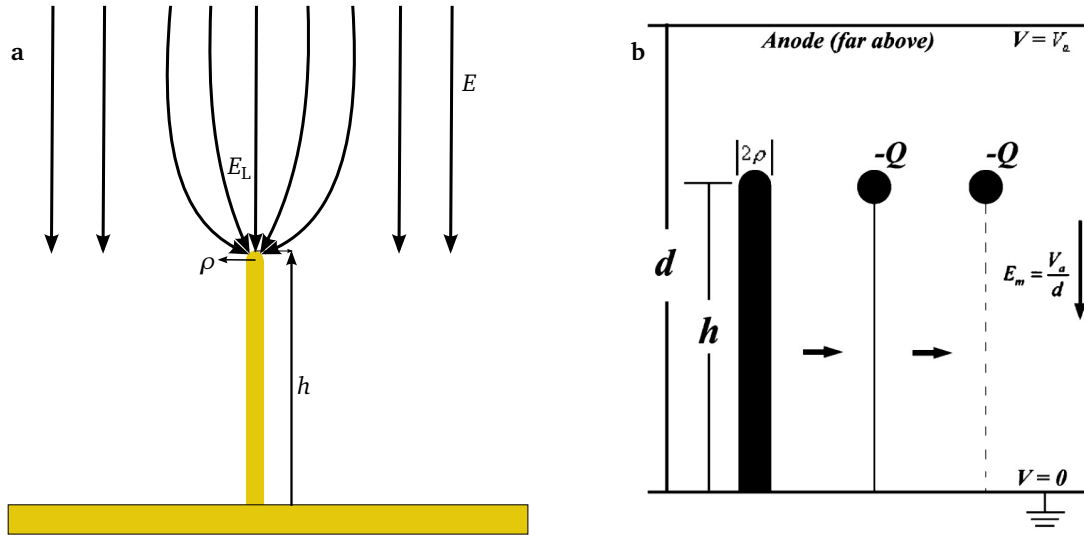


**Figure 2.8:** a) Alone standing metallic nanowire with a tip radius of  $\rho$  and an apex length of  $h$  b) Modeling the wire with a floating sphere with charge  $Q$  [52]

a model shown in Figure 2.9a as

$$\beta = \left(2.5 + \frac{h}{\rho}\right) \frac{d-h}{d} + \exp\left[-\left(\frac{d-h}{h}\right)\left(2.5 + \frac{h}{\rho}\right)^{0.5}\right]. \quad (2.25)$$

By decreasing the gap between the grid and the tips of the wires, the enhancement factor decreases. Other than that in very short gaps, electrical breakdowns predominate. By increasing the gap a higher voltage  $V_{\text{ext}}$  is needed to reach the turn-on field. So an optimum gap should be considered in the design. Furthermore, another important parameter that influences the FE characteristic is the interspace  $a$  between the wires. As shown in Figure 2.10a, for wires with low interspacing, the electrostatic field is shielded by the neighbors. The enhancement factor is maximum, for a single wire and reduces by the field-shielding effect in an array of wires [57]. The theoretically calculated function  $\bar{W}$  for a matrix of wires is shown as a diagram in Figure 2.10b. The enhancement factor for an array with an interspace of  $a$  can

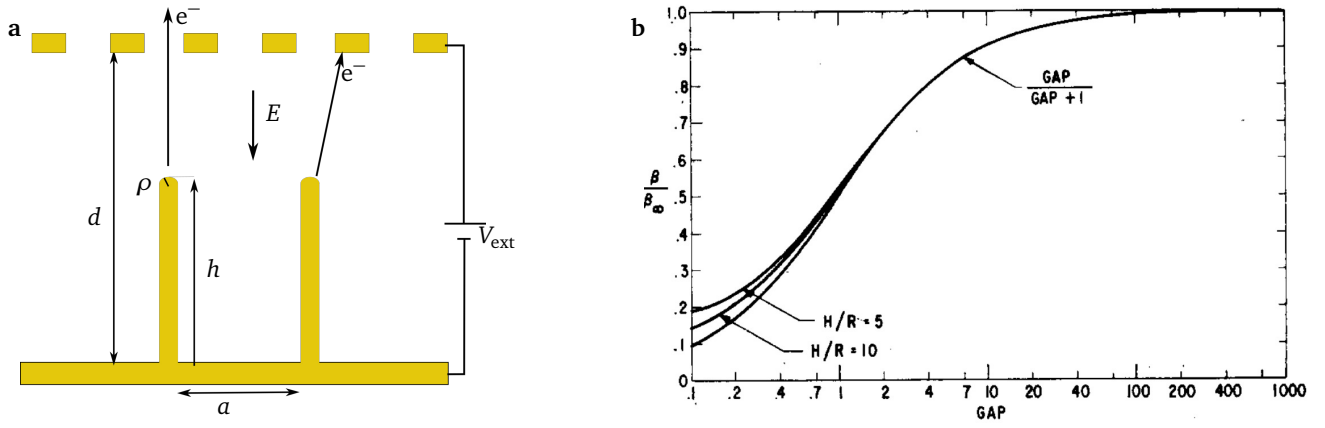


**Figure 2.9:** a) Extraction anode at the distance  $d - h$  over the wire array tips. The  $\beta$  depends on this gap b) Analytical plot of  $\beta/\beta_\infty$ , which  $\beta_\infty$  is the enhancement factor for a very large gap length. In this diagram, the given  $H$  is the height of wires and  $R$  is their tip radius.[56].

be written as [52]

$$\beta = \frac{h}{\rho} + 2.5 - \bar{W}, \quad (2.26)$$

where  $\bar{W} = \frac{h}{a}K$  and  $K$  is a factor depending on the number of wires and their position. From Figure 2.10b and (2.26), it can be seen that for interspaces less than the length of the wires the value  $\bar{W}$  increases rapidly which means  $\beta$  decreases. While  $\bar{W}$  hardly changes for interspace  $a$  more than twice the length of the wires  $2h$ . The optimum number of wires to reach a maximum emission current is a wire density with  $h < a < 2h$ . In addition to the criteria mentioned above, the homogeneity in the length of the wires over the entire surface is an important parameter for a homogeneous emission current. As shown in Figure 2.11a, in an array with a deviation in the length of the wires, the longer wires have a stronger electric field on their tip and they will turn-on sooner. It leads to a current inhomogeneity over the emitting surface. For wires with different tip sharpness as shown in Figure 2.8b, the thinner wires emit sooner. Random positioning of the wires would be a negligible problem and the current inhomogeneity due to this can be neglected.

Thus in the design of metallic nanowires-based FEC the following points must be considered:

- Wires material for a minimum work function and less outgassing
- Wires length
- Tips radius
- Stability and lifetime of wires
- Wires density and the pitches
- Wires homogeneity in terms of height and thickness and coverage over the surface
- Wires integration in 3D systems
- Integration of anode electrode
- Gap size
- Geometry of the anode electrode
- Fabrication costs.

Throughout this thesis, a process for the synthesis of metallic nanowires is investigated and a process for integration of these wires in 3D complex microsystems is developed. This process for surfaces with edge lengths of 3 to 300 000  $\mu\text{m}$  is rescaled. These concepts will be introduced in the next chapter.

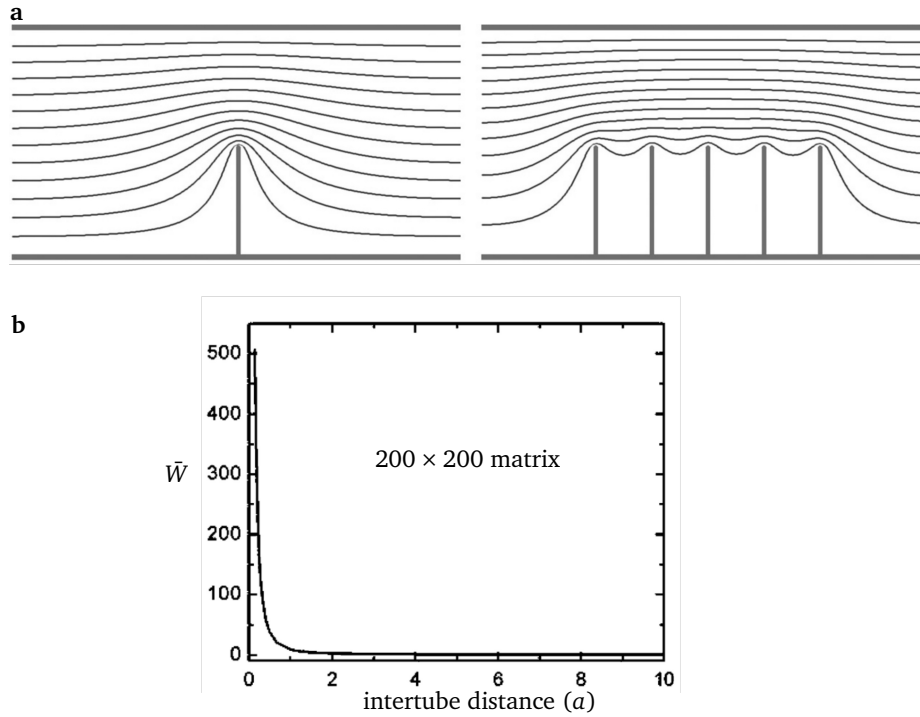


**Figure 2.10:** a) Analytical calculated equipotential lines of an electrostatic field for a single wire and an array of wires [57] b) Curve of the function  $\bar{W}$  versus intertube distance of CNTs calculated by [52]

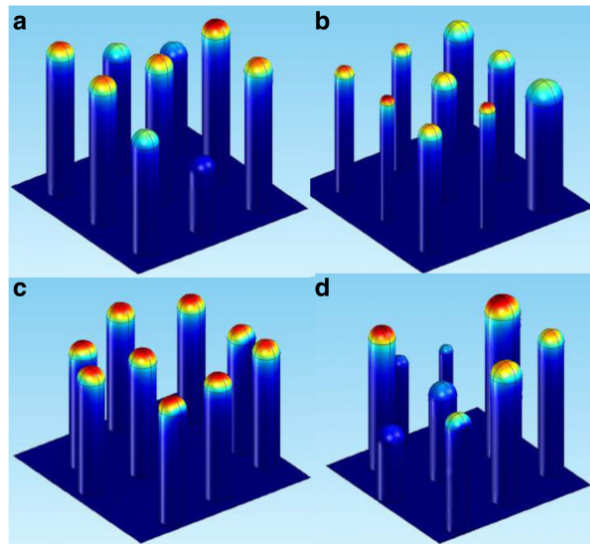


**Figure 2.11:** A  $3 \times 3$  array simulation with different geometries. The red regions indicate strong electric fields: a) different wire heights b) different wire thickness c) randomized wires position d) a combination of all parameters [58].



---

### 3 In-situ synthesis of metallic nanowires and nanocones

---

After reviewing the state-of-the-art fabrication methods of the metallic nano and microwires, in this chapter, the ion-track-etch process will be introduced. Then the process for integration of nanowires on different substrates at room temperatures up to 70 °C will be discussed. It will be shown, that with this process the wires can be integrated into 3D microsystems with no need for a manual process for placing the wires on the substrate. Finally, scaling the process from 300  $\mu\text{m}$  edge length to 8-inch wafers will be shown. Some parts of this chapter are published in [6].

---

#### 3.1 A short review of nanowires fabrication processes

---

Under the term nanowire, a nano object with a diameter much smaller than its length can be defined. The typical diameter of the nanowires lies between some nanometers to 100 nm with a length of about 100 nm to tens of microns. The wires with a diameter of more than 100 nm are mostly categorized as microwires. In this thesis, the metallic wires with a diameter from 30 nm to some microns are being discussed. For simplification, all types of wires in this thesis are quoted as nanowires. Different methods are available for the fabrication of conductive metallic or semiconductor nanowires. In the following part the most common methods will be introduced:

##### Lithographic Fabrication Process

In semiconductor industries, a very time consuming lithographic method is available to fabricate 2D nanowires as conductive tracks on chips. As the visible light wavelength is much larger than the dimensions of the nanowires, in this method, light sources with short wavelengths like UV-light (e.g. 193 nm line of ArF laser) are used. For nanowires with a thickness less than 100 nm, electron-beam (e-beam) lithography can be used. The process with e-beam exposure is shown in Figure 3.1.

##### DNA-Based Nanowires

There are some other non-lithographic methods to fabricate 2D or 3D metallic nanowires. In one of the latest methods, as shown in Figure 3.2, electric conductive nanowires are made of DNAs. In this process, the DNAs are covalent-bonded to a substrate through a so-called click reaction. These DNAs can be metalized by e.g. silver particles. The silver layer can be coated with a gold layer in a solution. The thickness of the gold layer can be well controlled with this process and the gold thickness defines the wire thickness[60].

##### VLS Process

In contrast to the lithographic and etching (top-down) methodology, a commonly used bottom-up method for a spontaneous synthesis of nanowires is the Vapor-Liquid-Solid (VLS) method. The VLS method consists of two major steps. In step one a liquid or molten droplet on a defect-free solid substrate at temperatures between 300 °C to 1100 °C is formed. In the next step, a chemical reaction between the droplet and a

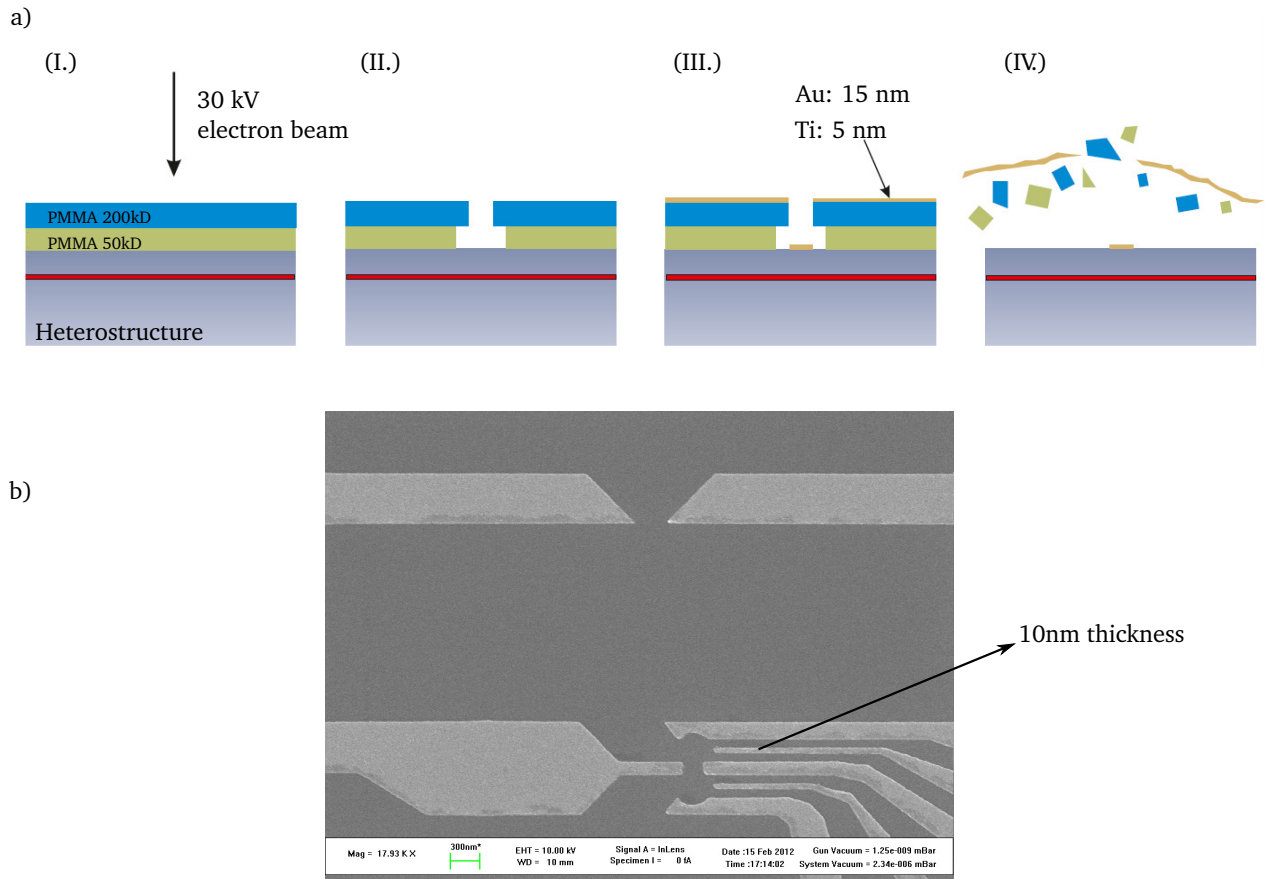


**Figure 3.1:** The fabrication process of gate structures with electron beam lithography: a) (I.) 2-layer PMMA system exposed with an electron beam with the designed structure. (II.) After the development process, an undercut appears due to the different molecular mass of the resist layers. (III.) Deposition of 5 nm Ti and 15 nm Au metallic films on the sample. (IV.) The lift-off process removes the metal excess. b) Gate structure of a double quantum dot sample imaged by SE2 detector with 10 kV acceleration voltage. The structure is used for exploring the properties of one electron transistors in a 2DEG in a GaAs-AlGaAs heterostructure [59].

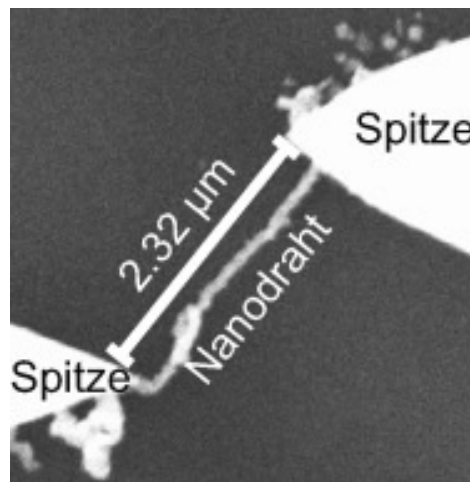


**Figure 3.2:** A Gold nanowire fabricated by stretching and bonding a DNA and coating this with a gold layer[60]



gaseous reactant takes place. The gaseous reactant contains the wires' substance. In this process, the metal droplet acts as a catalyst and produces a metallic alloy by reacting with the gas because the droplet surface has a higher sticking coefficient than the substrate [44]. The droplet becomes supersaturated and as shown in Figure 3.3, the nanowire grows outwards as the alloy liquid stays on the top of the nanowire.

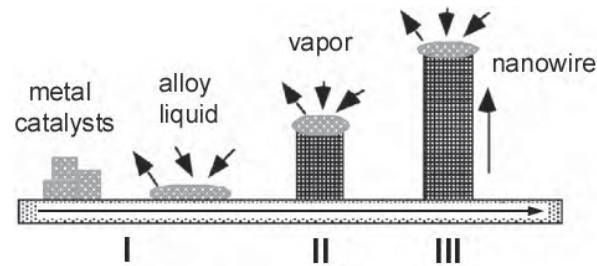


**Figure 3.3:** VLS bottom-up growth of a monocrystal nanowire: (I) Growing a metal catalyst on the surface and melting it into a liquid droplet at high temperatures; (II) The alloy saturates with a reactant gas, causing nucleation; (III) Growing the nanowire outwards [61]

### Electrochemical deposition of nanowires

Electrochemical deposition in combination with a template is also one of the non-lithographic methods widely used to grow nanowires. That is why the wires grown with this technique are also known as *template-grown wires*. For the synthesis of metallic nanowires and integration in a field emitter pressure gauge, this method is more suitable than other methods. As will be shown later in this chapter, with this method wires from different metals at low temperatures, even at room temperature, can be fabricated. This process does not need complex equipment and time consuming and expensive fabrication process. The focus of this thesis is on template-grown wires and the development of a method for the integration of wires into microsystems.

## 3.2 State-of-the-art methods for the assembly and manipulation of the nanowires

The next challenge is how to implement the advantages of the wires such as their huge surface to volume ratio and their electrical, mechanical, thermal, and chemical specifications in real commercial applications. For this purpose, the main task is to assemble the wires in microsystems. But just assembling the wires in a system will not solve the problem completely. For many applications, some requirements must be fulfilled which will be discussed in the following section.

### 3.2.1 Requirements for the integration of the nanowires

For an industrial process, the following requirements should be covered in the integration process of the nanowires:

---

### **Efficient assembly of the nanowires**

Efficiency in a manufacturable nanoscale process means high speed and low-cost production. Millions of wires should be assembled in a few steps. It is preferred that the new technology integrates the wires concurrently with the fabrication process.

### **Flexibility in the assembly of nanowires in functional devices**

This process should be flexible enough to implement not just on wafers, but even on materials with larger dimensions, different geometries, and also curved or engraved surfaces.

### **Wires of different metals on samples from a variety of materials**

The process should be compatible with systems made of different materials such as metals, semiconductors, glass, polymers, ceramics, etc. Also, the synthesis of wires from different metals must be possible.

### **Electrical conductance of the wire-arrays**

After the integration process is done, the physical characteristics of the wires like their electrical, thermal, and chemical properties must be preserved and a later electrical connection between the arrays should be possible.

### **Compatibility with other production processes**

It is preferred that the new technology can be combined with other standard processes without needing to perform any extra change in the product fabrication steps or needing a large investment in new production facilities.

### **The template material**

For template-grown wires, a flexible variation of the parameters such as thickness, pore diameter, and wire density should be possible. Furthermore, the membrane must be removable using industrial standard processes without affecting the wire structure. It would be advantageous if the membranes are available in the market as a common commercial product. Polymer membranes, especially polycarbonate, fulfill all the requirements.

---

## **3.2.2 Strategies for the assembly and manipulation of the nanowires**

---

There are three major strategies to assemble and manipulate the wires. One of these strategies is to use nanoscale devices like probes of atomic force microscopes [62] or micro grippers in SEM [63] to manipulate and position the nanowires. Such placement methods are slow, expensive, and not suitable for enabling commercial mass production nanoscale processes. Two other strategies are known as *self-assembly* and *patterned or controlled growth* of nanowires.

---

### **3.2.2.1 Self-assembly of the nanowires**

---

In this strategy, the chemically patterned nanowires are tumbled in a liquid medium, which let the wires interact with each other or with the surface of a system to form a stable structure for a special function.

---

For tumbling the wires a variety of forces can be used. These forces can also be used to control the orientation and binding of nanowires. This strategy is inspired by biological self-assembly in nature like using capillary forces [64].

### **Molecular linkers**

The molecular linker can be used to link the nanowires or nanoparticles together and arrange a complex structure of the nanowires. In the first step, the linkers must be attached to the nanowires in a solution. Then the molecular linkers form a chemical bond with each other. Even biological molecules like proteins, DNAs, or viruses can be used to link the nanowires in complex structures.

### **Electrical field-assisted assembly of nanowires**

One of the first processes used to place the nanowires in a suspension was the dielectrophoretic manipulation of gold nanowires [65]. In this process, a non-uniform electrical field is applied to the floating wires. The induced electrical dipole on the wires will force them to arrange along the field lines. The wires travel now towards the stronger electrical field. This process was used to integrate the gold wires between two electrodes (see Figure 3.4). After the wires sit on the electrodes, the solution evaporates and the wires get fixed by adhesion forces. But the adhesion forces are not enough for many applications. Also, the wires integrated with this method are not placed perpendicular to the surface.

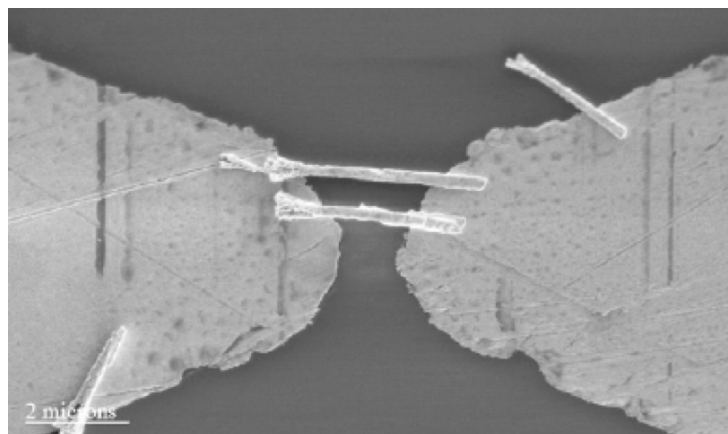


**Figure 3.4:** SEM image of two electrodes connected with gold nanowires by dielectrophoresis [65]

### **Magnetic field-assisted assembly**

The magnetic force is another interaction that can be used to manipulate nanowires made of ferromagnetic materials like nickel, iron, cobalt, or their alloys. In this method, the magnetized wires are arranged along with the magnetic fields and orient themselves so that the energy is minimized. In this process, the nanowires also interact with each other and make a network of wires (see Figure 3.5). The wires can also interact with a magnetic surface and make a bundle of wires mounted on the substrate.

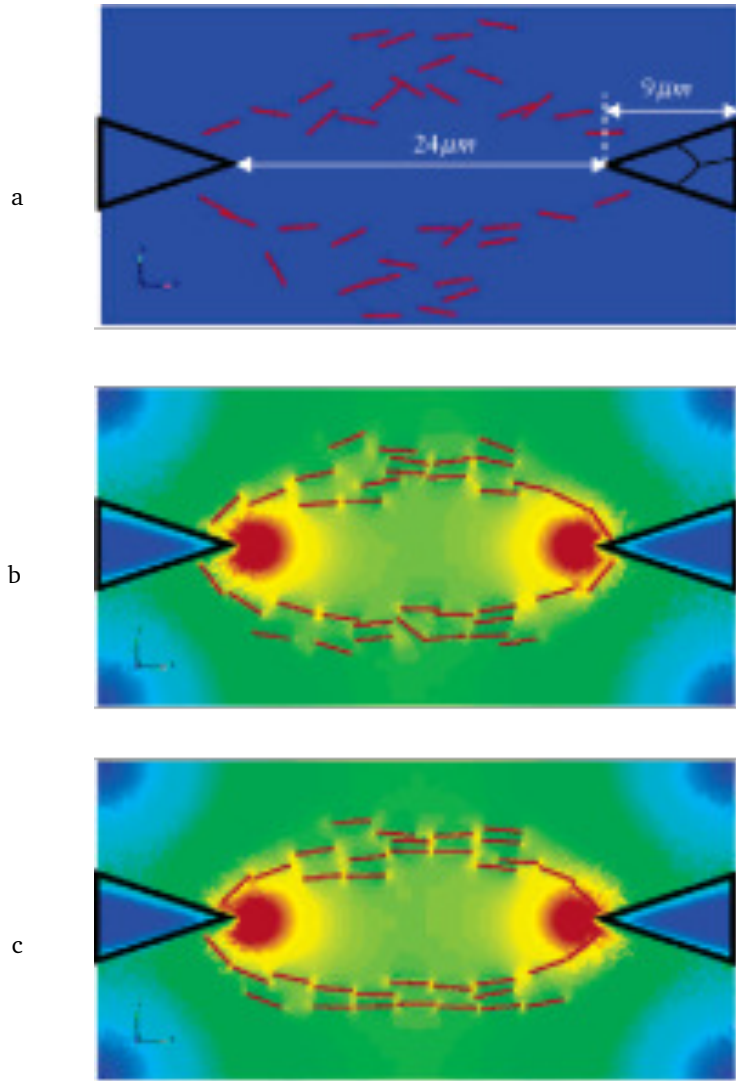


**Figure 3.5:** Sequential images of lining up magnetic wires between two triangular electrodes at an AC field of 5 MHz and field strength of  $0.5 \frac{\text{V}}{\mu\text{m}}$ . (a)  $t=0$  s; (b)  $t=0.5$  s; (c)  $t=1.0$  s [66]

### Optical trap

The suspended nanowires in a fluid are placed on the stage of a microscope. For manipulating the wires, an optical tweezer utilizes a focused laser beam, which applies force on the nanowires to trap and move them. The advantage of this approach is the ability to manipulate wires in closed chambers with a considerable spatial accuracy of less than 1 nm. This process is illustrated in Figure 3.6.

### Langmuir-Blodgett technique

This approach uses the compression of nanowires, which are capped with a surfactant on a liquid surface. The wires capped with the surfactants will float on the air-fluid interface. Using movable barriers will push and compress the nanowires on a solid substrate and cover its surface with a layer of nanowires. This process is shown in Figure 3.7

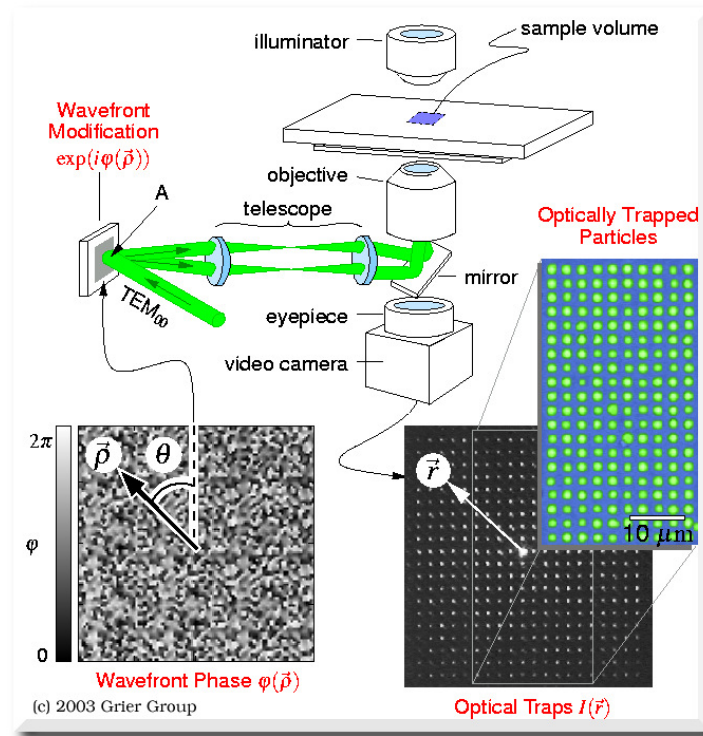


**Figure 3.6:** Large number of optical tweezers created with computer-controlled holograms. Projecting a collimated laser beam through the input pupil of a strongly converging lens such as a microscope objective creates a single optical tweezer [67]

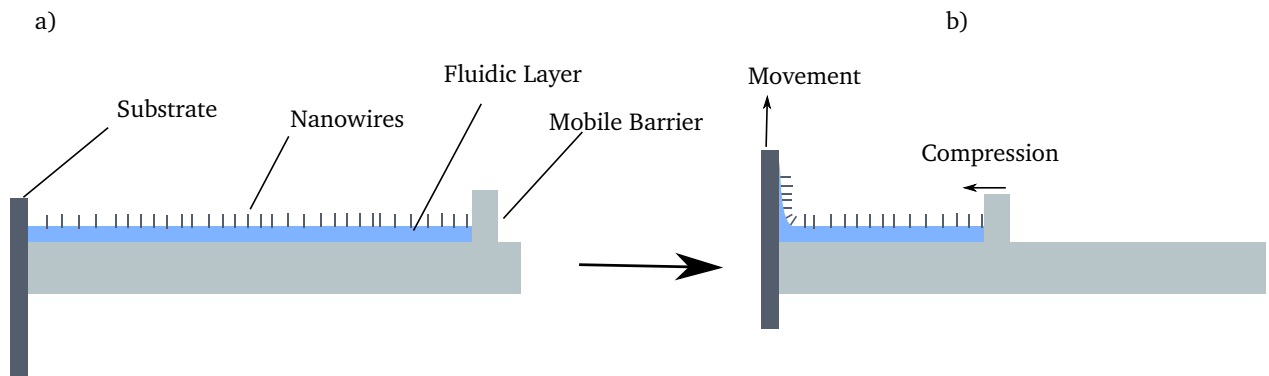


**Figure 3.7:** a) The nanowires coated with surfactants float on the surface of the liquid. A movable barrier compresses the fluid and pushes the wires towards the substrate. b) By moving the substrate a large surface area can be covered with nanowires. The wires are attached perpendicular to the surface. With this method, it is possible to cover the substrate on both sides. Furthermore, The wires can be integrated horizontally on the substrate by flipping and placing the substrate horizontally on the fluid surface.

### 3.2.2.2 Patterned growth of the nanowires

So far several processes are used to grow nanowires using a template. By patterning the template directly on the substrate, the nanowires may grow at a specific area and in a specific direction. The most interest-

---

ing integration direction in this thesis is the vertical integration of the wires on the surface. There are four main approaches for applying this process:

### **Fixing a filled membrane**

This process consists of the following steps: using a porous membrane, filling the pores of this membrane, fixing it on a substrate, and removing the membrane.

In this approach for integrating the template-grown nanowires on a substrate, the filled membrane is fixed on a substrate, and then the membrane is removed. It needs a technique to connect the metallic seed layer mechanically as well as electrically onto the substrate. In this integration process, temperatures above the melting point of the nanowires, or glass transition temperature of the membrane are not allowed. Furthermore, the strength of the mechanical connection must be able to tolerate the arisen forces by removing the template membrane. As the patterns on the membrane should be made before the wires are synthesized, placing the wire arrays on a predefined pad on the substrate is a challenge. Investigations on solving this problem in [68], [7] showed that this method is less successful.

### **Integrating a wire array**

The process consists of the following steps: using a porous membrane, filling the pores of this membrane, removing the membrane, and fixing the wires on a substrate.

In this approach, a solution is thickening the seed layer before removing the membrane. After removing the template membrane, wires on the metallic foil must still be positioned and integrated into the system. Vice versa to the previous approach, the wires are not protected in the membrane anymore. Thus the wires can be damaged during the integration process. Also, some methods like laminating the foil cannot be used. A common method is to stick the foil on the substrate with a paste. By doing this, in addition to the surface roughness of the seed layer, a wave in the stuck layer on the substrate appears. Furthermore, increasing the electrical conductivity of the interconnection between the metallic foil and the system, which is deducted by using e.g. a conductive paste, will be a challenge. These will restrict the commercial application of this method.

### **Spin coating the membrane**

The process consists of the following steps: spin coating the polymer layer, which is going to be used as a template, and then irradiating the polymer to form the pores on it.

As shown in Figure 3.8, another method to integrate the wires into a system, perpendicular to the substrate, is to spin-coat a fluid PC polymer on the substrate [69], [70]. Then the dried PC is irradiated in an accelerator and the ion-tracks are etched. Then a metal deposition takes place inside the pores, directly on the metallic layer by an electrodeposition process. At the end of the process, the PC layer is removed in a proper solution. The nanowires integrated with this method show a good electrical conductance to the substrate. But this process has low flexibility because the complete system has to be mounted in the accelerator. Thus the number of wafers to be irradiated is restricted. This process is slow and not commercial.

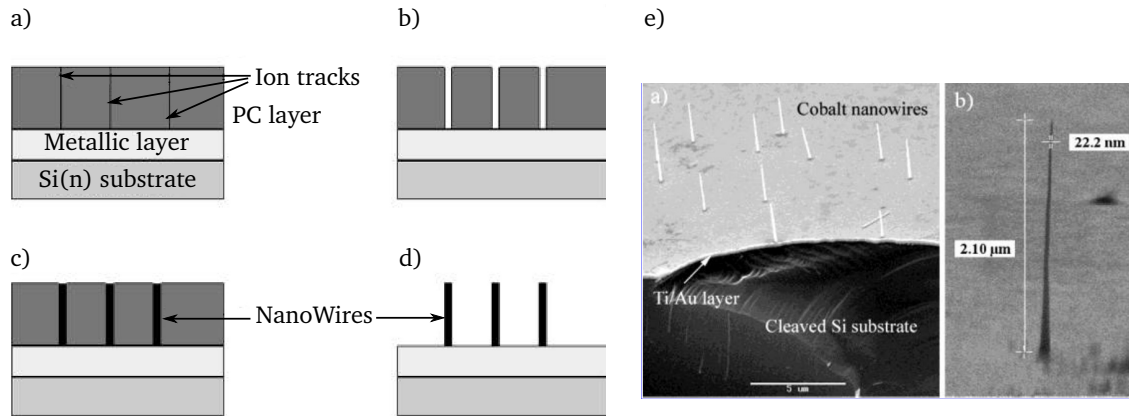


**Figure 3.8:** a) Spin-coating of PC and heavy ion irradiation; b) Chemical etching on ion-tracks; c) Electrodeposition process; d) Dissolution of PC layer e) SEM image of cobalt nanowires produced with this method [69]

### In-situ integration of the nanowires

The process consists of the following steps: using a porous membrane, fixing it on a substrate, filling the pores, and removing the membrane.

In this approach, the porous template membrane is fixed on the substrate. Depending on the method used for fixing the membrane and also the sequence of the fabrication steps, some different techniques have been developed. One technique is to use a commercial membrane and fix it on the substrate, using a photoresist as an adhesive material [71]. As shown in Figure 3.9, the commercial membrane is set on a metalized substrate. By pouring a fluid photoresist on the membrane, the fluid penetrates the pores by

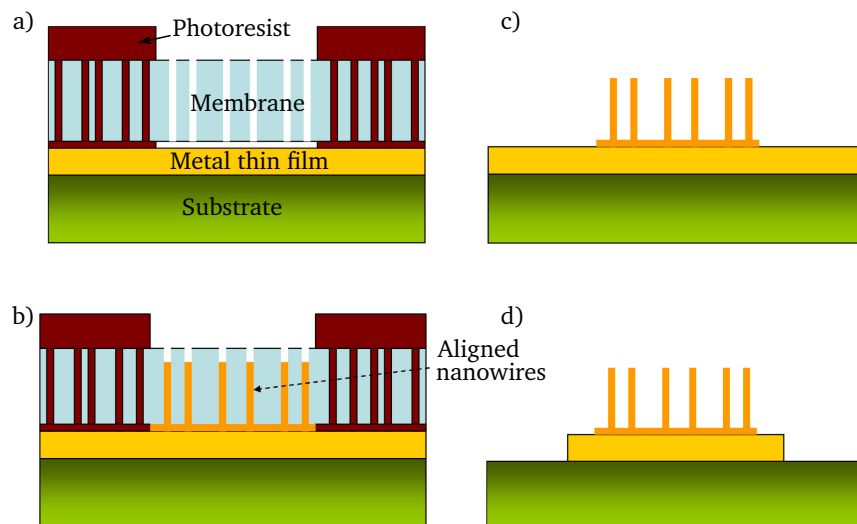


**Figure 3.9:** a) The membrane is fixed on a metalized substrate by a layer of photoresist. The middle area is freed in a lithographical step; b) growth of the nanowires by electrodeposition; c) removing the template membrane; d) defining the electrodes by an extra lithography step [71]

capillary action. Then the wafer is rotated on a spin-coater. After a baking step, the membrane is fixed. The desired areas are freed in a lithography step. The wires grow in an electrodeposition step in the freed areas. Then, the membrane and the photoresist are removed in a proper solution. The electrodes and pads



are defined in extra lithography and etch steps. With this process, an In-situ integration of the nanowires with a minimum diameter of 200 nm has been performed. Thinner nanowires can not be integrated easily with this process. Furthermore, the length of the nanowires in this process is about  $10\mu\text{m}$ . With this technique, just high density wire arrays can be fabricated. This is not appropriate for field emission applications. However, this method is the initial idea for the integration of the wires presented in the next section. Another idea that will also be discussed in the next section is the sponge press process, shown in Figure 3.10.

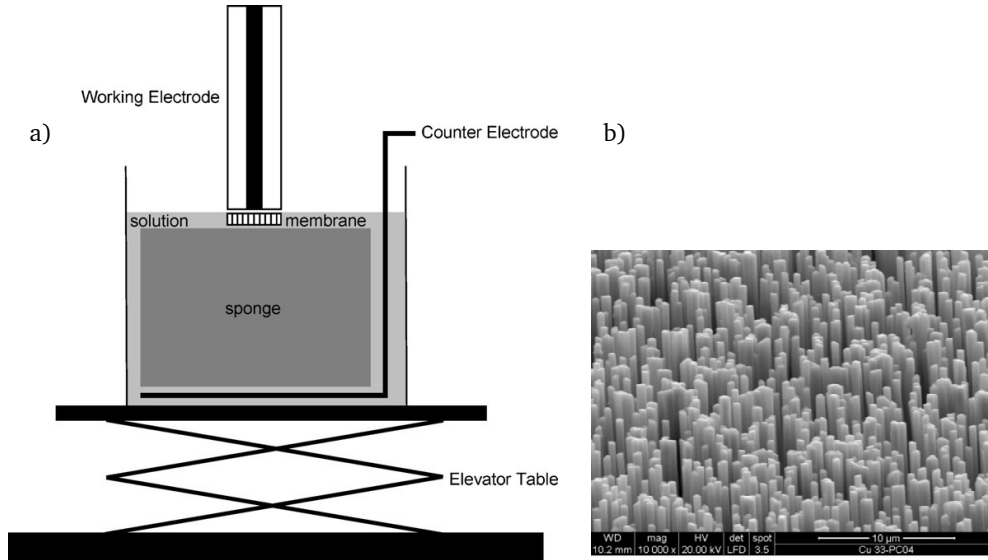


**Figure 3.10:** Sponge press process for in-situ integration of template-grown nanowires on a substrate. a) The substrate is lying upside down on a membrane. The membrane is lying on a sponge. The sponge is pressed with an elevator, while the anode is in the bath under the sponge. b) SEM image of the nanowires synthesized with this device [72].

In all four approaches, the nanowires are integrated concurrently with the synthesis of the nanowires. These processes result in a high electrical conductance between the nanowire arrays and the substrate. However, the conductivity is not the same in all four approaches. Using a standard lithography process in the in-situ integration approach to form a pattern on or underneath the membrane, gives enormous flexibility to define the pads with different sizes and geometries from some micrometer to tens of centimeters. In the next section, it is tried to reproduce and investigate the in-situ approach to obtain a commercial process for implementation on the industrial standard large surfaces like 4-inch wafers and higher.

### 3.3 Template grown nanowires

This technique was introduced by Possin et al.[73] in 1970 for the first time, in which they have grown a single wire of 40 nm diameter and  $15\mu\text{m}$  length. They have used a mica substrate, and a pore is made in this substrate by etching a damage track in it. This porous mica is used as the template to grow the metallic wire by electrochemical deposition in the etched pore. The template process is further developed and investigated by other groups [74][75][76].

Generally, the fabrication process of the template-grown nanowires contains the following major steps:



- Fabricating the porous template,
- Metal deposition inside the pores,
- Removing the template,
- Integrating the nanowires into a system.

The most used templates in a template-grown process are porous alumina and ion-track etched membranes [77].

---

### 3.3.1 Porous anodic aluminum oxide template membrane

---

Aluminum anodic oxide (AAO) has been already used for a wide range of nanowires from different materials, mainly including metals, metal oxides, conductive polymers, semiconductors, and multi-segmented nanowires [44]. In alumina templates, the pores are produced by anodic oxidation of aluminum in acidic solutions. The oxygen ions in the alumina crystal lattice form a nearly hexagonal close-packed (HCP) structure. Thus the pores are arranged in a hexagonal shape. Their density varies between  $10^9$  pores/cm<sup>2</sup> and  $10^{12}$  pores/cm<sup>2</sup>. This technique is less flexible in modifying the pores' geometries. Often a NaOH solution is used to remove these templates. The NaOH can corrode non-noble metals. Thus, this process is not proper for growing nanowires of non-noble metals.

---

### 3.3.2 Ion-track etch template membrane

---

Another type of template is the ion-track etched template. As shown in Figure 3.11a, and 3.11b these template membranes are fabricated by irradiating a polymer foil (e.g., polycarbonate (PC), polyimide (PI) or polyethylene (PE)) with swift heavy ions possessing MeV-GeV kinetic energy. The ions will pass through the polymer and break the polymer chain by losing their energy along their path in the form of thermal energy. The ion-tracks can be etched selectively by a proper solution. This frees up the pores. Depending upon the etching time and solution concentration, the diameter of the pores varies from some nanometer to some micrometer. The ion-track process is much more flexible than the alumina membrane in terms of the number of pores per unit area (pore density) and pore shape. The density of pores can be controlled between  $10^4$  pores/cm<sup>2</sup> to  $10^{10}$  pores/cm<sup>2</sup> by changing the irradiation parameters. The template thickness ranges from  $8\ \mu\text{m}$  to  $100\ \mu\text{m}$ , and this thickness determines the maximum length of the wires. By asymmetric etching of ion tracks, the shape of the wires can be tailored. Fabricating wires with conical shapes will be discussed in Chapter 5. The only drawback of this process is the need for large ion accelerators for irradiating the polymers. The commercial products on the market (e.g., it4ip, Whatman, Sterlitech, Oxyphen, etc.), which thicknesses are mostly less than  $25\ \mu\text{m}$ , can be used. Such thicknesses are sufficient for many applications.

---

### 3.3.3 Ion-track etch process for the synthesis of nanowires

---

After fabricating the porous template membrane, the next step is the synthesis of the wires by metal deposition inside the pores. In a basic technique, a thin layer of metal about 200 nm is sputtered on one side of the template. This is shown in Figure 3.11c. This layer can be used as a seed layer to fill up the pores through the electroplating process (see Figure 3.11d). In this step, the crystal structure of the metallic wires

can be controlled by adjusting the growth temperature, concentrations of the electrolyte, and electrolyzing parameters [78]. As shown in Figure 3.11e, if the electroplating does not stop before the whole length

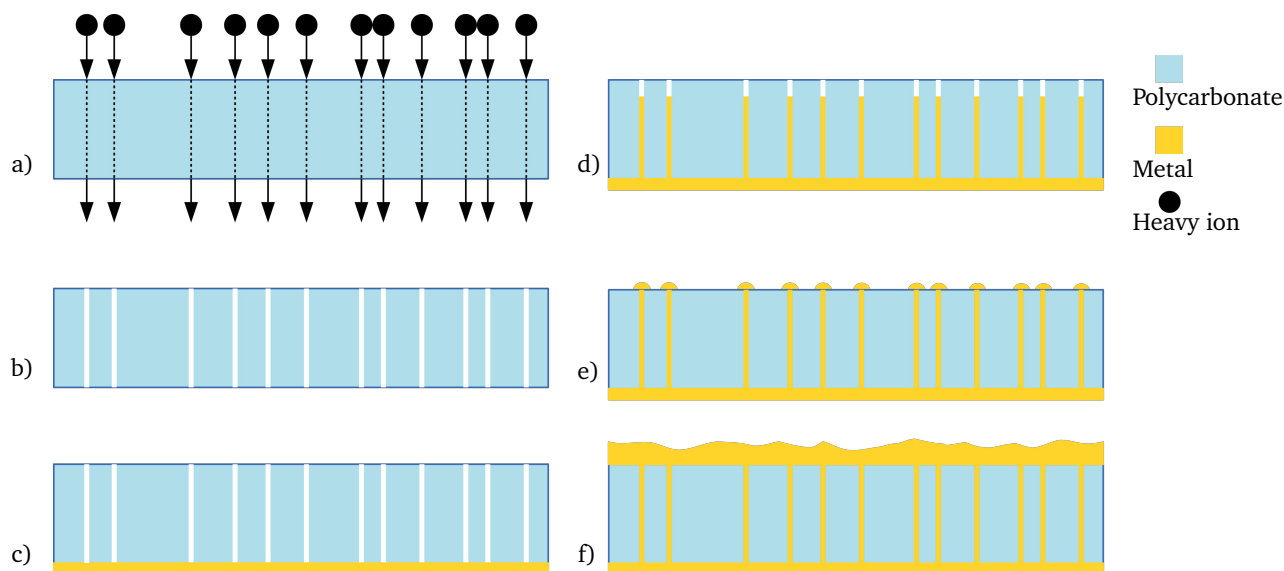


**Figure 3.11:** a) Irradiating a polymer membrane with high energetic heavy ions in an accelerator; b) opening pores in the membrane by etching the ion tracks; c) sputtering the backside of the polymer membrane; d) filling up the pores by an electroplating process; e) partially overgrown wires in a mushroom form; f) completely overgrown. The wires are sandwiched between two plates [79].

of pores are filled. A mushroom-shaped overgrowth will raise on the top. By continuing the process, this will be transformed into a layer over the membrane's top surface. The membrane back sputtering technique has some drawbacks. Looking closer to the template membrane in Figure 3.12 gives a better understanding of this process. By sputtering the porous membrane, metal atoms will cover the internal walls of the pores, but it will not close them completely and/or does not produce a smooth flat surface. It leads to the creation of a hollow space in the base of wires that makes the wires thermomechanically unstable.

### 3.3.4 Removing the ion-track etch membrane

To reach bare nanowires, the membrane has to be removed. For removing the polymer templates like PC, which is the mainly used polymer in this thesis, two processes are common. The easiest one is using appropriate organic compounds like Dichloromethane ( $\text{CH}_2\text{Cl}_2$ ), N-Methyl-2-pyrrolidone (NMP), or Cyclopentanone. With this method, the membrane can be removed, without leaving any trace on the sample. One drawback of this method is that in arrays with high-aspect-ratio wires, the adhesion between the wires is high, which causes the surface of the neighbor wires to stick to each other. This effect is larger in high-density arrays. This effect is shown in Figure 3.13. Another technique to remove the polymers is the so-called plasma ashing. This is a standard process in the semiconductor and microelectronics industries for removing photoresists from an etched wafer substrate and cleaning the wafer. In this work, the plasma stripping tool STP 2020 of the company R3T Muegge is used. In this technique, a reactive species of

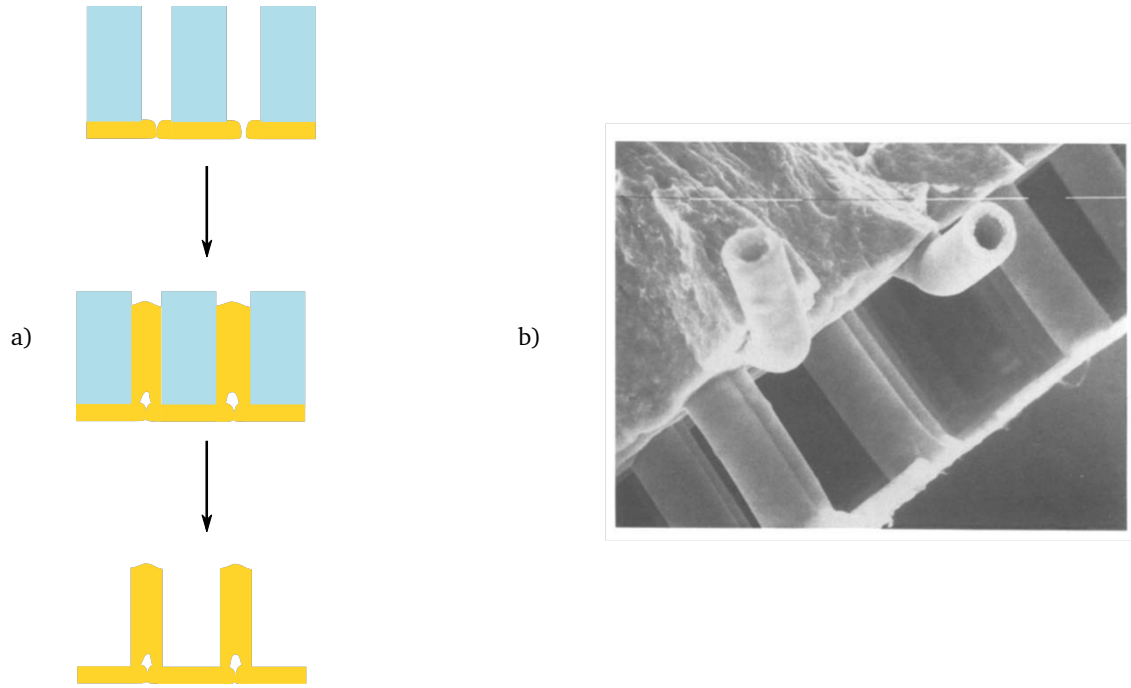


**Figure 3.12:** a) Sputtering the seed layer at the back side of the porous membrane leads to a bubble formation in the nanowire. b) A SEM image of a hollow nanowire produced with back sputtering process [74]

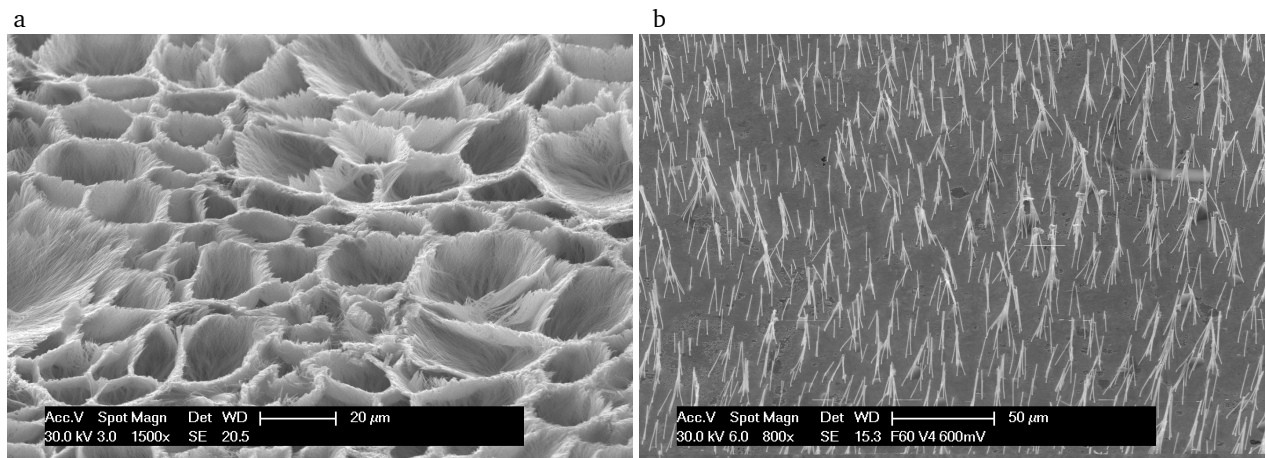


**Figure 3.13:** By removing the membrane, using a wet chemical process, the dense wires or wires with a high aspect ratio will stick to each other. a) SEM images of copper nanowires with 30 nm diameter, 25  $\mu\text{m}$  height and wire density greater than  $10^9 \text{ cm}^{-2}$ ; b) copper nanowires with 400 nm diameter, 25  $\mu\text{m}$  height and density of  $1.6 \times 10^6 \text{ cm}^{-2}$

oxygen( $\text{O}_2$ ), fluorine ( $\text{CF}_4$ ), and nitrogen ( $\text{N}_2$ ) are used.  $\text{CF}_4$  is used to increase the etch rate. But with a high amount of  $\text{CF}_4$ , some etch traces of polymer-fluorine will remain, which can not be removed anymore. Depending on the geometry of the 3D microsystems or the wire array, one of these techniques is used throughout this thesis. The processes of removing the membrane and their prescriptions are summarized in Table 3.1.

**Table 3.1:** Prescription and parameters for removing the polycarbonate membrane through a wet chemical or physical process

Process	Prescription and parameters
Wet chemical stripping	<p>Stripping in a chemical bath</p> <ol style="list-style-type: none"> <li>1. Immersing the sample in a proper organic compound like Dichlormethane for 30 min</li> <li>2. Immersing the sample in Aceton (<math>C_3H_6O</math>) to remove the adhesive layer.</li> <li>3. Rinsing the sample with Isopropanol</li> <li>4. Drying the sample with <math>N_2</math></li> <li>5. Rinsing with DI-Water should be avoided in order to prohibit the oxidization of the wires by remains of water on the surface</li> </ol>
Physical stripping	<p>Stripping by oxygen plasma ashing in Muegge R3T STP 2020</p> <ol style="list-style-type: none"> <li>1. 45 min ashing at <ul style="list-style-type: none"> <li>Power: 800 W to 1000 W</li> <li>Gas combination and concentration: <math>O_2</math>: 1000 sccm; <math>N_2</math>: 50 sccm; <math>CF_4</math>: 50 sccm</li> <li>Gas pressure: 0.6 mbar</li> <li>Temperature: 25 °C</li> </ul> </li> <li>2. Rinsing with 1000 sccm <math>O_2</math> at 25 °C with 800 W for 600 s</li> <li>3. Rinsing with isopropanol and drying with <math>N_2</math></li> </ol>

### 3.4 In-situ synthesis and integration of metallic nanowires fabricated by ion-track etch process

The ion-track etch process for the synthesis of metallic nanowires is already described in the previous section. The missing link in the microsystems fabrication chain is the integration of nano-objects into 2D or 3D complex microsystems. This field is known as Micro-Nano-Integration (MNI). In the same vein, the biggest challenge to benefit from the advantages of nanowires, in a real commercial application, is how to flexibly and commercially integrate them into a system. The requirements and approaches for the integration of the template-grown nanowires are mentioned in section 3.2. From all four approaches, the in-situ integration of nanowires can fulfill almost all requirements for an industrial application. However, this approach is not still mature enough, and it needs to be explored to find out an optimum process. The main steps of this process, are demonstrated in Figure 3.14. The challenges in the in-situ integration process are

- Patterning the arrays.
- Fixing the template on the substrate.
- Scaling the process up to standard industrial sizes.
- Homogeneity in the growth of wires all over the surface.
- Homogeneity with respect to the height of the wires by reducing the standard deviation in the length of the wires.

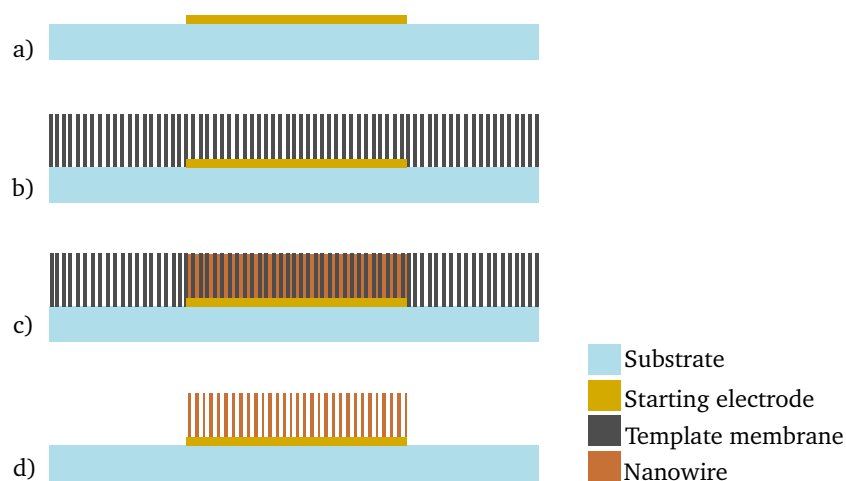


**Figure 3.14:** The basic process of in-situ integration of the nanowires; a) Structuring the substrate and patterning the electrodes of the arrays. b) Integrating the template membrane. c) Fabricating the nanowires by filling the template pores through an electrochemical deposition process. d) Removing the template.

### 3.4.1 Patterning the arrays

The fabrication process of an electron field emitter begins by using a glass wafer. A 25 nm layer of chromium is deposited on the top surface of the glass wafer. This layer is adhesive and can be substituted with other adhesive materials like titanium-tungsten alloys. The next layer is a 100 nm gold layer as a seed layer for the electrochemical deposition of nanowires. Gold is non-reactive with oxygen. Thus the gilded glasses can be stored for a longer time compared to wafers covered with copper. Due to the higher cost of gold than copper, an electroless nickel immersion gold finish on a copper layer is common in the electronics industry. In this work, mainly the gold seed layer is used. There are three possibilities for patterning the electrodes of the arrays:

#### Lift-off process

In this process, a bare glass wafer is covered with a layer of positive or negative photoresist. the desired pattern is structured in a lithography step, on the photoresist. Then with a PVD process, the metallic layers are deposited on the surface. In the lift-off process, a layer deposition technique, like evaporation is preferred. In the evaporation deposition, the metallic atoms move in a single direction without covering the internal walls of the photoresist. The stripping process can be done in acetone. To speed up the process, the acetone can be heated up to 50 °C. Although a lift-off process with a positive resist does not need a post bake and is less time consuming than a negative resist, the negative resist has the advantage that the structured electrodes have sharp edges (see Figure 3.15). Also, the negative mask can be used for other processes like an etching process. Due to the high costs of gold deposition and more time needed for lift-off by broad area structures, the lift-off process was just used in a few samples to pattern the electrodes.

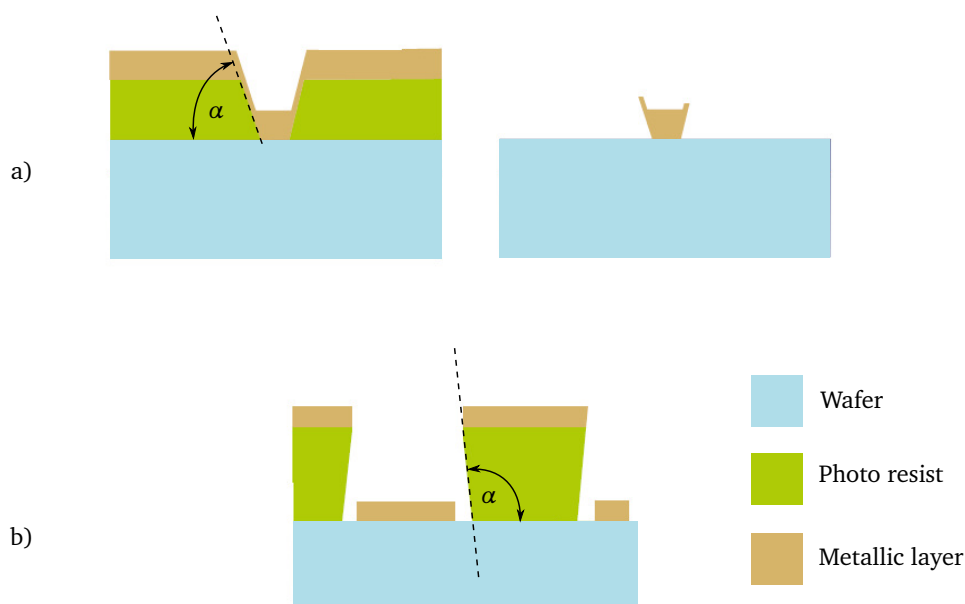


**Figure 3.15:** a) A positive photoresist will show an overcut after the development. It leaves some sidewalls on the electrodes, which can cause a short circuit between neighbor electrodes. b) Negative photoresist with an undercut that lets sharp edges on the electrodes.

### Etching the chromium-nickel joint layers

One other possibility for patterning the array electrodes is, to perform the thin film deposition at the first step. The process is done on a 4-inch borosilicate glass wafer (Borofloat, Schott AG) with  $700\mu\text{m}$  thickness. In this process a 25 nm layer of chromium and 150 nm nickel are vapor-deposited on the wafer. After that, the desired electrode template is fabricated on the surface with a photoresist and through a lithography step. In the next step, nickel and chromium layers are etched in a proper etchant and the photoresist is removed in a cleaning step. At last, the remained nickel layer is gilded in a gold immersion deposition process. This will produce an atomic layer of gold on the nickel surface. There is a lack of understanding of the electroless gold deposition mechanism from a solution. Several researchers concluded that the gold plating from a solution is a cementation reaction with the initial surface metal. Some other conclusions consider electroless plating as an autocatalytic process involving the oxidation of a reducing agent on a catalytically active surface. In our case, the nickel surface is a reductant [80]. This process is shown in Figure 3.16 and the description of the process is introduced in Table 3.2. This is a cost-efficient process. The fabricated layers have an acceptable adhesion to the surface. This high adhesion lets them be soldered or bonded to make a connection. The gilded surface will not oxidize during the nano wiring process as well.

### Etching chromium-gold joint layers

One other possibility for patterning the array electrodes is to deposit a 100 nm to 200 nm gold layer directly on the 25 nm chromium layer and to skip the nickel film. In this process, a gold boat for the thermal evaporator is needed. Nevertheless, by vapor-deposition of more than 10 wafers at once, the costs

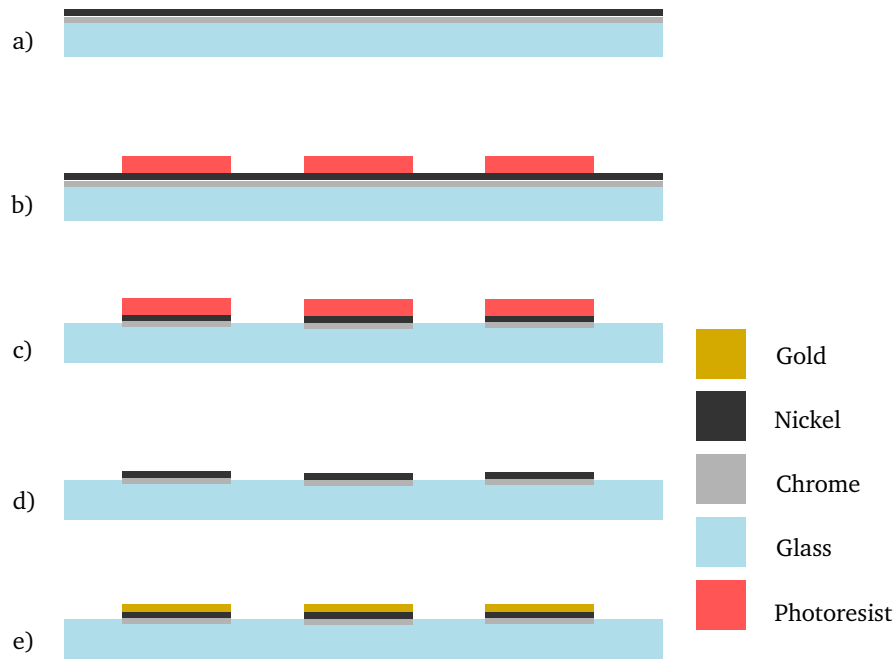


**Figure 3.16:** Patterning the array electrodes on a glass wafer; a) vapor deposition of chromium-nickel thin films on the glass wafer; b) transforming the electrodes pattern by a positive photoresist; c) etching the chromium-nickel layers; d) removing the photoresist; e) covering the electrodes with a gold film.

are comparable with the immersion gold process. The structuring steps in the process are the same as the chromium-nickel etch process. But the etchant for gold is an iodine-potassium iodide solution in DI-Water. The prescription can be found in Appendix B.1. The advantage of this process is that it takes less time to prepare the electrodes compared to the immersion gold process. In Figure 3.17, a processed wafer with this method is shown. This electrode is designed as a test electrode for growing the nanowires for a field emission application.

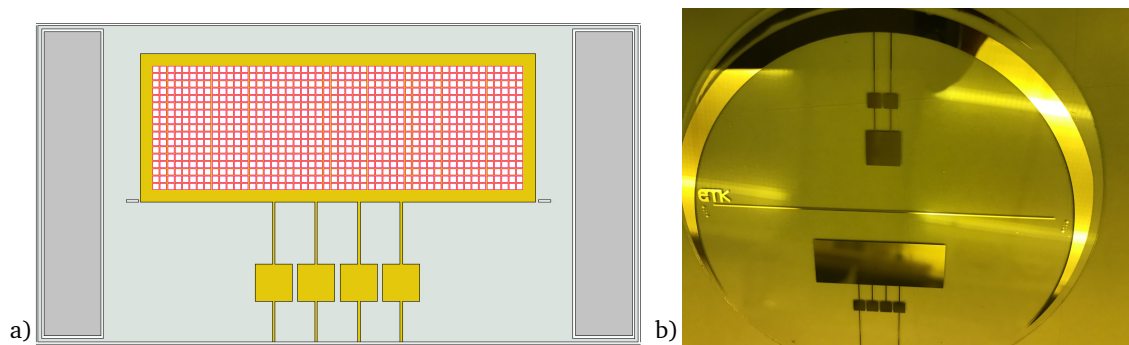


**Figure 3.17:** A preliminary design of the field emitter electrode for testing the integration of the nanowires. a) The designed two-layer mask for preparing the electrode and structuring the photoresist for fixing the PC membrane on the electrode. b) Two different sizes of gold electrodes prepared on a glass wafer with a chromium-gold etch process.



**Table 3.2:** Prescription and parameters for structuring the desired electrode pattern on the wafer by etching chromium-nickel layers

Process	Prescription and parameters
Vapor deposition of metal film	<ul style="list-style-type: none"> <li>25 nm chromium, 150 nm nickel on a 4 inch borosilicate wafer with 0.7 mm thickness</li> </ul>
Photolithography	Using positive photoresist ma-P 1215 (Appendix B.1) <ul style="list-style-type: none"> <li>Spin-Coating: ca. 4 mL of photoresist; 30 s at 1500 rpm</li> <li>Soft bake at 100 °C for 2 min</li> <li>Exposure:               <ul style="list-style-type: none"> <li>ghi-Line filter</li> <li>Dose: <math>55 \frac{\text{mJ}}{\text{cm}^2}</math></li> </ul> </li> <li>Developing: 2 min in ma-D 331 (micro resist technology GmbH)</li> </ul>
Etching the metal layers	<ul style="list-style-type: none"> <li>Etching the nickel layer: <math>\text{H}_3\text{PO}_4 : \text{HNO}_3 : \text{CH}_3\text{COOH} : \text{H}_2\text{O}</math> 3:3:1:1. In this process, every 15s the substrate must meet the air oxygen to oxidize the nickel surface. Alternatively, <math>\text{H}_2\text{O}_2</math> can be added to the etchant for nickel oxidation; Etch rate: <math>60 \text{ nm min}^{-1}</math></li> <li>Etching the chromium layer: The commercial chromium etchant “Chrome etch n° 1” of microchemicals company consists of ceric ammonium nitrate: perchloric acid: water = 10.9% : 4.25% : 84.85% with an etching rate of about <math>60 \frac{\text{nm}}{\text{min}}</math> at room temperature.</li> </ul>
Removing the photoresist	<ul style="list-style-type: none"> <li>Stripping with acetone; If needed using ultrasonic bath; Rinsing with Isopropanol; Rinsing with DI-Water; Drying with nitrogen gas</li> <li>Cleaning for 1min in argon RIE with 1000 W power</li> </ul>
Gild the electrodes	<ul style="list-style-type: none"> <li>Activating the surface: in a HCL 10% for about 30 s at room temperature</li> <li>Rinsing with DI-Water</li> <li>Gilding: immersing in a bath of MacDermid Enthone’s Affinity ENIG 2.0 which is a potassium dicyanoaurate compound.</li> </ul>

### 3.4.2 Fixing the template membrane on the substrate

After patterning the metallic electrodes and preparing them as starting layer, the next step is to bring the template membrane to the substrate and fix it on the electrodes. The requirement in this step is good adhesion between the membrane and the surface all over the substrate in a way that the membrane does not slip on the surface. Also, it must be possible to cover the desired areas selectively with the wires. This can be done in a lithographic masking step. At last, wetting under the membrane is a challenge. An improper wetting influences the homogeneity of the wires due to ion impoverishment under the template membrane or inside the pores.

#### 3.4.2.1 Thermal lamination of the membrane

As we are using a polymer membrane, a thermal lamination process may be used to fix the template membrane on the substrate. The method shown in Figure 3.9 tries to attach and pattern the membrane by photoresist from the top of the membrane. In this thesis, primarily, the patterning process is done on a photoresist layer on the substrate. Then the patterned photoresist is used as an adhesive to fix the membrane by a thermal lamination on it. Unlike the previous process, this process can be performed on



membranes with different pore sizes and pore densities. Also, the processing time will be reduced and a bubble-free placing of the membranes with larger dimensions is possible.

### Hot-melt adhesive films

One possibility to bring an adhesive layer to the substrate is to use a hot-melt adhesive (HMA) film. As described by S. Quednau et al. in [79], this film is applied to the pre-structured substrate. By baking the substrate on a hotplate up to 150 °C, it will be melted and stuck on the surface. At this step, the adhesive film must be patterned. As shown in Figure 3.18, this can be done by applying a metallic mask, like a 1  $\mu\text{m}$  to 2  $\mu\text{m}$  layer of copper, on it and structuring the copper layer. Now, the HMA film can be etched by oxygen plasma. Then, the copper layer can be removed selectively. To reach a more homogeneous surface, the cavity should be filled in an electrochemical step before the membrane is laminated. Afterward, the PC membrane can be laminated on the structured adhesive layer in a thermal lamination device at a temperature between 135 °C to 150 °C. This process takes about 60 min. The adhesive layer in this process is about 20  $\mu\text{m}$  to 25  $\mu\text{m}$  thick. Now, the system is ready for growing the wires inside the pores of the PC membrane in an electrochemical deposition step. The deposition process will be discussed in Section 3.5. The time-consuming plasma etching and the complexity of the preparation steps make this

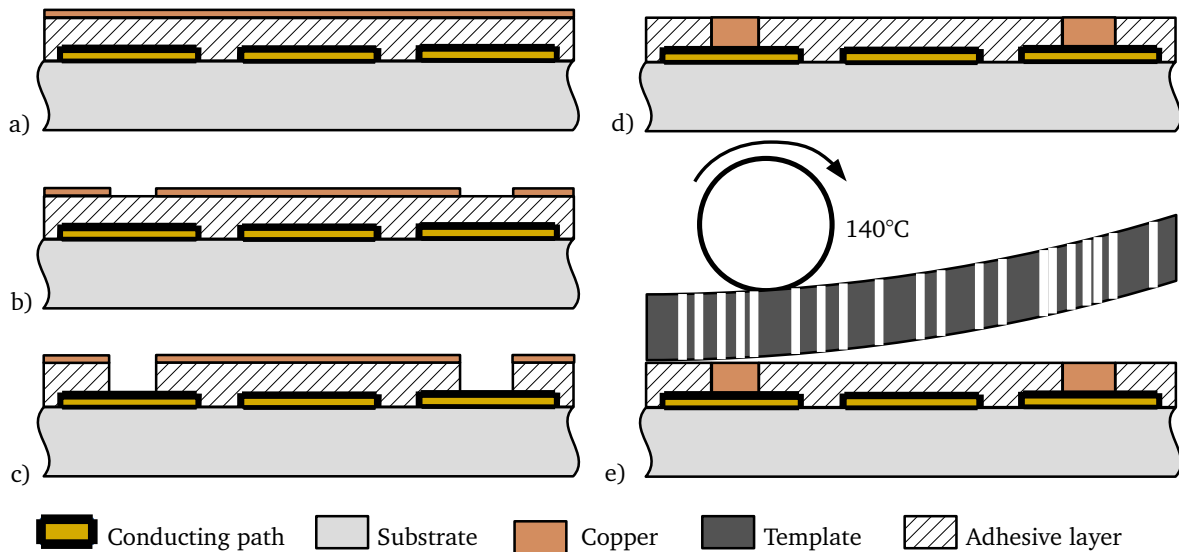


**Figure 3.18:** Process of structuring a hot melt adhesive film. a) Setting the adhesive film on the substrate and sputtering 100 nm chromium-copper system. Thickening the copper layer up to 2  $\mu\text{m}$ . b) Structuring the copper layer c) Structuring the adhesive film in an oxygen plasma ashing machine. d) Filling the cavity and removing the copper layer. e) Laminating the PC membrane with a temperature between 135 °C to 150 °C. Image from [79] and translated with permission.

process less interesting. Also, the high thickness of the adhesive layer makes it necessary to fill up the cavities in an extra electrochemical deposition step. The eventual lapping step is another disadvantage of this process. The solution would be a thinner adhesive layer like a layer of positive photoresist.

### Thermal lamination on positive photoresist

An alternative for a hot-melt adhesive film is a photoresist with a much lower thickness less than  $2\mu\text{m}$ . This prohibits some disadvantages of the previous process. For this, a positive fluid photoresist of the *Micro Resist Technology GmbH* company, ma-p1215 (see Appendix B.1) is used. The photoresist is spin-coated on the pre-structured substrate. Then in a photolithography step, the desired patterns of supporting walls are transferred to the photoresist. After the development step, the PC membrane is laminated on the photoresist supporting walls. The lamination takes place by using a heated roll laminator at a temperature of  $135^\circ\text{C}$ . This process is shown in Figure 3.19 and the process prescription is described in Table 3.3. As

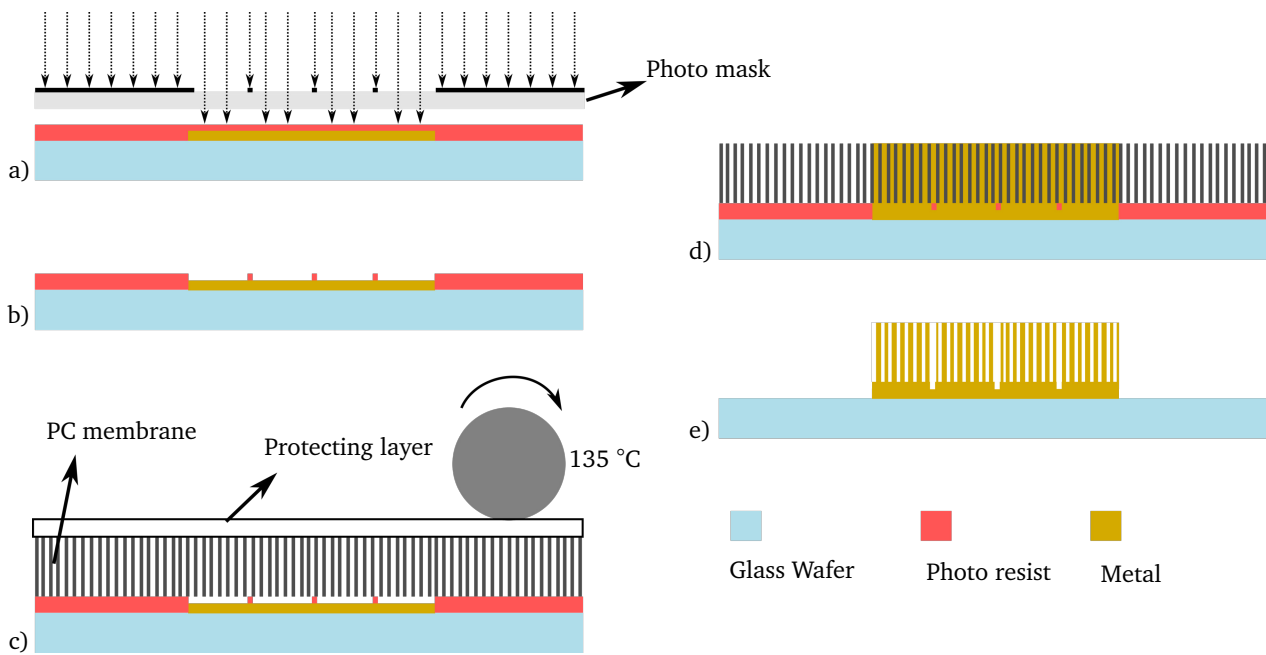


**Figure 3.19:** Lamination process of the PC membrane on a photoresist layer. a) The photoresist layer with a thickness of  $1.5\mu\text{m}$  is spin-coated on the substrate. This layer will be structured through a photolithography step. For wide electrodes, the supporting walls are needed on the electrode surface to ensure a better homogeneity in the growth of the nanowires. b) Developing the photoresist. c) Laminating the PC membrane on the photoresist adhesive layer. A protecting foil is lying between the PC membrane and the laminator roll. d) Growing the wires. e) Removing the membrane and the photoresist.

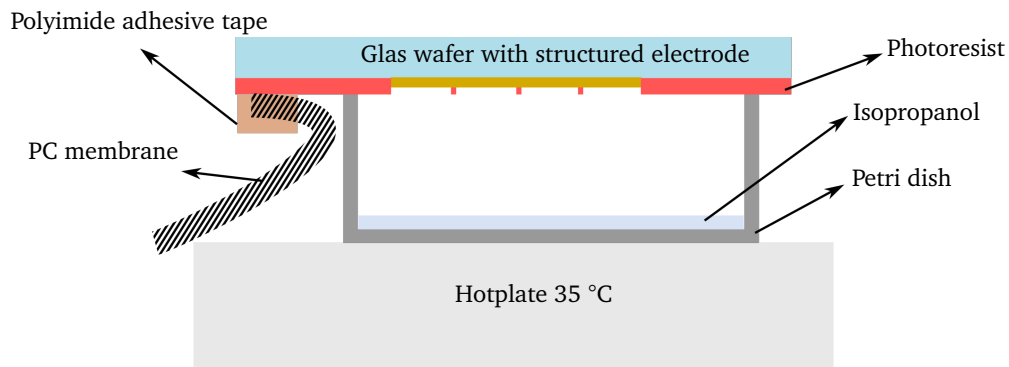
mentioned above, the thinner photoresist layer makes a much smaller cavity under the membrane, which does not need to be filled up in an extra step. The membrane can be laminated almost parallel to the surface, which means better planarity in the under-growing surface. But this method still has a problem. The thermal expansion coefficient of the PC membrane is higher than that of the glass substrate. It means that after the system has cooled down, there is still surface tension on the membrane. This surface tension separates the photoresist easily from the substrate. There are two possible solutions. One is to thicken the adhesive photoresist layer, the other one is to reduce the lamination temperature. A photoresist layer of  $15\mu\text{m}$  is not desired. Therefore, in the next paragraph lowering the lamination temperature is followed.

**Table 3.3:** Prescription and parameters for thermal laminating the PC membrane on a photoresist adhesive layer

Process	Prescription and parameters
Coating with an adhesion promoter	At this step a layer of Ti-Prime (B.2) is spin-coated on the wafer: <ul style="list-style-type: none"><li>• Spin coating the Ti-Prime, <math>t = 30</math> min , <math>U = 3000</math> rpm</li><li>• Activating the adhesion promoter, <math>t = 1</math> min at <math>\theta = 120^\circ\text{C}</math> on a hotplate</li></ul>
Photolithography	Using positive photoresist ma-P1215 (Appendix B.1. The photoresist will function as an adhesion layer for PC membrane) <ul style="list-style-type: none"><li>• Spin coating: ca. 4 mL photoresist; 30 s at 1500 rpm</li><li>• Soft bake at <math>100^\circ\text{C}</math> for 2 min on a hotplate</li><li>• Exposure: ghi-Line filter Dose: <math>55 \frac{\text{mJ}}{\text{cm}^2}</math></li><li>• Developing: 2 min in ma-D 331 (Micro Resist Technology GmbH)</li><li>• Rinsing with deionized water and drying with nitrogen</li></ul>
Laminating the PC membrane	<ul style="list-style-type: none"><li>• Bringing the polymer template membrane on the substrate (The flat surface looks down)</li><li>• Pre-fixing the template with a piece of Kapton tape</li><li>• Laminating the wafer while a laser printing film is used as a protecting layer on the membrane</li></ul> <p>Roller speed on level 1 (lowest level)</p> <p>Roller Temperature <math>\theta = 135^\circ\text{C}</math></p>

### Low temperature lamination of PC membrane

To reduce the surface tension on the PC membrane a low-temperature lamination process is developed. This prohibits the separation of the photoresist layer from the glass substrate. As shown in Figure 3.20, the PC template membrane is fixed with a piece of polyimide adhesive tape (e.g. Kapton tape) at the edge of the substrate. A small amount of isopropanol, which slightly covers the bottom of a Petri dish is heated on a hotplate at  $35^\circ\text{C}$ . The Petri dish is covered during this step. The cover is removed and the substrate is put upside down on the Petri dish for 20 s to 22 s. After that, the wafer is removed and the PC template membrane is placed on the photoresist, and it is laminated at room temperature. This process works because the photoresist is softened by the isopropanol vapor. Thus, the lamination process must be performed immediately. As the photoresist has a thickness of about  $1.5 \mu\text{m}$ , the process is very

**Figure 3.20:** The process of softening the photoresist for laminating the membrane on the wafer.

sensitive to softening time on the petri dish. By keeping the wafer much longer on the isopropanol vapor,

the photoresist will be pressed and spread all over the surface or even some holes will be made on the photoresist area which will let wires grow on unexpected locations. To make the process much more robust, a thicker positive photoresist AZ9620 is used. The process for room temperature lamination is described in Table 3.4. Despite the advantages of the cold lamination process, performing this process

**Table 3.4:** Prescription and parameters for room temperature laminating the PC membrane on a photoresist adhesive layer.

Process	Prescription and parameters
Coating with an adhesion promoter	At this step a layer of Ti-Prime (Appendix B.2) will be spin-coated on the wafer: <ul style="list-style-type: none"> <li>Spin coating the Ti-Prime, <math>t = 30</math> s, <math>U = 3000</math> rpm</li> <li>Activating the adhesion promoter, <math>t = 1</math> min at <math>\theta = 120^\circ\text{C}</math> on a hotplate</li> </ul>
Photolithography	ma-P1215, $1.5\ \mu\text{m}$ (Appendix B.1) <ul style="list-style-type: none"> <li>Spin-Coating: ca. 4 mL photoresist; 30 s at 1500 rpm</li> <li>Soft bake at <math>100^\circ\text{C}</math> for 2 min on a hotplate</li> <li>Exposure: <ul style="list-style-type: none"> <li>ghi-Line filter</li> <li>Dose: <math>55\ \frac{\text{mJ}}{\text{cm}^2}</math></li> </ul> </li> <li>Developing: 2 min in ma-D331 (Micro Resist Technology GmbH)</li> <li>Rinsing with deionized water and drying with nitrogen</li> </ul> AZ9260, $7\ \mu\text{m}$ (Appendix B.39) <ul style="list-style-type: none"> <li>Spin-Coating: ca. 4 mL photoresist; 8 s at 500 rpm then 50 s at 3500 rpm</li> <li>Soft bake at <math>100^\circ\text{C}</math> for 8 min on a hotplate</li> <li>Rehydration for ca. 30 min</li> <li>Exposure: <ul style="list-style-type: none"> <li>ghi-Line filter</li> <li>Dose: <math>680\ \frac{\text{mJ}}{\text{cm}^2}</math></li> </ul> </li> <li>Developing: 2 min in 3 : 1 AZ400K : Deionized water</li> <li>Rinsing with deionized water and drying with nitrogen</li> </ul>
Softening the adhesive photoresist layer	<ul style="list-style-type: none"> <li>Heating up Isopropanol at <math>35^\circ\text{C}</math> in a covered petri dish for making solvent vapor</li> <li>Fixing the PC template membrane on the wafer with adhesive tape</li> <li>Putting the wafer upside down on the petri dish for 20 s to 22 s, gently pressing the membrane on the wafer with the finger.</li> </ul>
Laminating the PC membrane	<ul style="list-style-type: none"> <li>laminating the wafer while a laser printing film is used as a protecting layer on the membrane <ul style="list-style-type: none"> <li>Roller speed on level 1 (lowest level)</li> <li>Roller at room temperature</li> </ul> </li> </ul>

is harder than the hot process and the failure probability is high. In the next section, some problems with this process will be shown.

### 3.5 Electrochemical deposition of nanowires

In this section, the electrochemical deposition process of nanowires will be explained. After laminating the porous PC membrane on the desired electrode (see Figure 3.19c), the pores can be filled in an electrochemical deposition step .

By contacting a solid electron conductor, known as the electrode, with an ionic conductor, known as the

electrolyte, a half-cell is set up. By connecting two half-cells, an electrochemical cell is performed, in which different electrical charges, including electrons and ions, can be transferred through different interfaces. An electrochemical cell is a fundamental apparatus in electrochemistry. The electrolyte is a solid ionic salt (MX) solution in a dissolvent, like water. The dissolving reaction can be written as



The used electrolytes for growing the nanowires in this thesis from different metals (e.g., copper, gold, and nickel), are non-toxic aqueous solutions. In the electrochemical cell, the produced electrons at one half-cell electrode interface need to be neutralized. It will be done by the migration of the cations (the positive metallic ions) in the electrolyte toward this electrode. This electrode is known as the cathode or the working electrode. The reaction at the working electrode is an electrochemical reduction. The metal will deposit on the working electrode during this reaction. The reduction reaction is given as



Simultaneously, another reduction happens at the anodic half-cell, and the released electron will migrate through the external circuit to the cathodic half-cell. It means, that always a redox couple cooperates for a deposition process. The driving mechanism for such reactions is a so-called Galvani potential difference  $\Delta\phi = \phi_{\text{M}} - \phi_{\text{Electrolyte}}$  in the half-cell at the interface of the electrode-electrolyte. Due to the Galvani potential in equilibrium, the metallic electrode-electrolyte interface attracts oppositely charged ions. It shapes a so-called double layer region, in which the ions diffuse in this region from the bulk electrolyte toward the electrode surface. Measuring the electrode potential  $\phi_{\text{M}}$  at the electrode-electrolyte interface can not be done experimentally. Therefore this potential is always measured by using a reference standard hydrogen electrode (SHE) with a defined potential of  $\phi_{\text{H}} = 0$  in an extra cell

$$\Delta\phi_{\text{M}} = \phi_{\text{M}} - \phi_{\text{H}}. \quad (3.3)$$

In Table 3.5, the potentials of some electrodes relative to the SHE are listed. In an electrochemical cell the cell potential is the potential difference between two electrodes  $V_{\text{cell}} = \Delta\phi_{\text{M1}} - \Delta\phi_{\text{M2}}$ . Now for elec-

**Table 3.5:** Electrode standard potential of used metals in this thesis at  $\theta = 25^\circ\text{C}$  [81]

Electrode material	Electrochemical reaction	$E_{\text{M}}$ [V]
Cu	$\text{Cu}^{2+} + 2e^- \rightleftharpoons \text{Cu}$	0.3402
Au	$\text{Au}^+ + e^- \rightleftharpoons \text{Au}$	1.42
Ni	$\text{Ni}^{2+} + 2e^- \rightleftharpoons \text{Ni}$	-0.23

trochemical deposition of metal on the working electrode, i.e. the wafer substrate, an external potential  $\Delta\phi_{\text{ext}}$  must be applied to the electrodes. The potential difference from equilibrium  $\eta = |\Delta\phi_{\text{M1}} - \Delta\phi_{\text{ext}}|$  is known as the overpotential. The overpotential causes an electron flow from the external circuit to the working electrode. So, the available cations will migrate toward the working electrode. The higher concentration of the ions means a higher diffusion of the metal ions through the double layer and a higher deposition rate. Generally, regulating the mass transport of ions and electrons can control the rate of electrochemical reactions. Thus measuring the electrical current flow expresses the number of such reactions

in the cell. Such an electroplating cell is schematically shown in Figure 3.21a. In this apparatus, by connecting a current supply a constant DC current  $I_M$  flows. The problem with this apparatus is the changing resistance in the system because of changes in the ion concentration, temperature fluctuation, changes in the geometry of the electrodes, or small changes in the electrode distance. In the worst case, the power supply voltage will jump over the hydrogen overpotential and a hydrogen layer will cover the surface of the working electrode. By growing the nanowires in small pores, these hydrogen gas bubbles will stop the deposition process. To prevent this problem, a three-electrode apparatus, as shown in Figure 3.21b, is

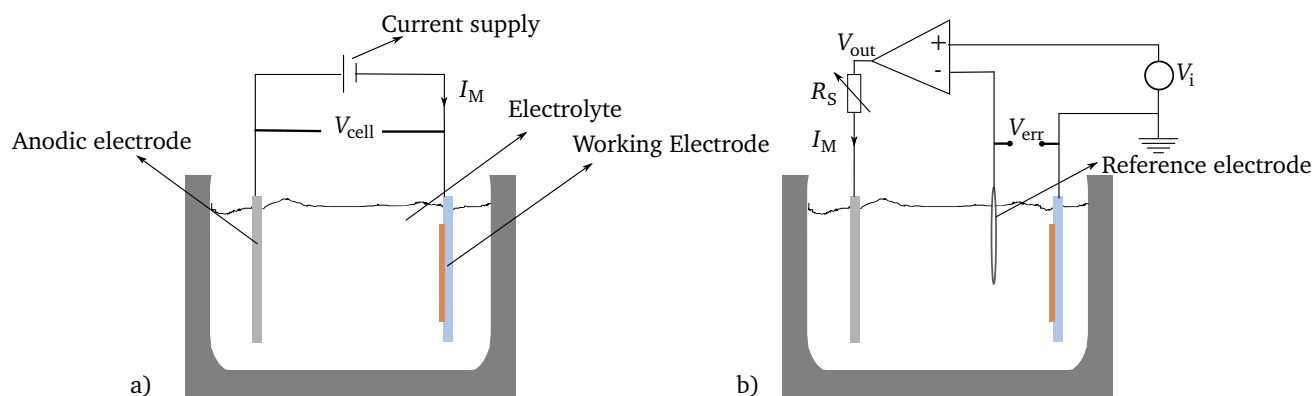


**Figure 3.21:** a) A simple electrolyzing cell. b) Electrolyzing cell with a reference electrode connected through a potentiostat.

used. In this case, a reference electrode is used. Instead of cell potential, always the working electrode potential relative to the reference electrode is measured. The reference electrode has a near-zero current. In Table 3.6, different types of such electrodes are listed. Now the potential difference between the work-

**Table 3.6:** Reference electrodes and their reactions and potentials in relation to SHE at 25°C [82].

Electrode, Solution	Half-cell reaction	$\Delta\phi_{REF}$ R. SHE [V]
Hg/Hg <sub>2</sub> Cl <sub>2</sub> , KCl (0.1M)	$Hg_2Cl_2(s) + 2e^- \rightleftharpoons 2Hg_{(iq)} + 2Cl^-$	0.3337
Hg/Hg <sub>2</sub> Cl <sub>2</sub> , KCl (1M)	$Hg_2Cl_2(s) + 2e^- \rightleftharpoons 2Hg_{(iq)} + 2Cl^-$	0.2801
Ag/AgCl, KCl (0.1M)	$AgCl(s) + e^- \rightleftharpoons Ag_{(s)} + Cl^-$	0.2881
Ag/AgCl, KCl (1M)	$AgCl(s) + e^- \rightleftharpoons Ag_{(s)} + Cl^-$	0.2368
Ag/AgCl, KCl (Saturated)	$AgCl(s) + e^- \rightleftharpoons Ag_{(s)} + Cl^-$	0.1976

ing electrode and the reference electrode is applied to a control amplifier. The amplifier is responsible for keeping the voltage between the reference electrode and the working electrode as much as possible near the applied voltage by the power supply. It means that e.g. for copper deposition from a copper sulfate solution on a copper working electrode with a silver/silver chloride electrode the overpotential can be defined as

$$\eta = \Delta\phi_{WE} - \Delta\phi_{REF} = 0.3402V - 0.1976V = 0.1426V. \quad (3.4)$$

To begin the deposition an input voltage

$$V_i \cong V_{\text{err}} < \eta \quad (3.5)$$

is needed. The deposition of metal begins and it can be controlled by changing the voltage or current at the potentiostat. By measuring the current flow over the resistor  $R_s$  and integrating it over time, the amount of charge transfer  $Q$  can be calculated. This charge value represents the mass  $m$  of deposited metal. It can be calculated by using Faraday's laws of electrolysis

$$m = \frac{M}{zF} \int_0^T i(t) dt \quad (3.6)$$

where  $M$  is the molar mass of the substance in  $\frac{\text{kg}}{\text{mol}}$ ,  $F = 96\,485 \frac{\text{C}}{\text{mol}}$  is the Faraday constant and  $z$  is the valency number of ions of the substance which represents the electrons transferred per ion.

### 3.5.1 Electrochemical deposition device for the synthesis of nanowires

After fixing the template membrane on the substrate by using the procedure described in Section 3.4.2, the sample is ready for the synthesis of nanowires. For this purpose, an electroplating bath is developed by Quednau et al., which is shown in Figure 3.22. This device is designed for a 4-inch-wafer. But the bath

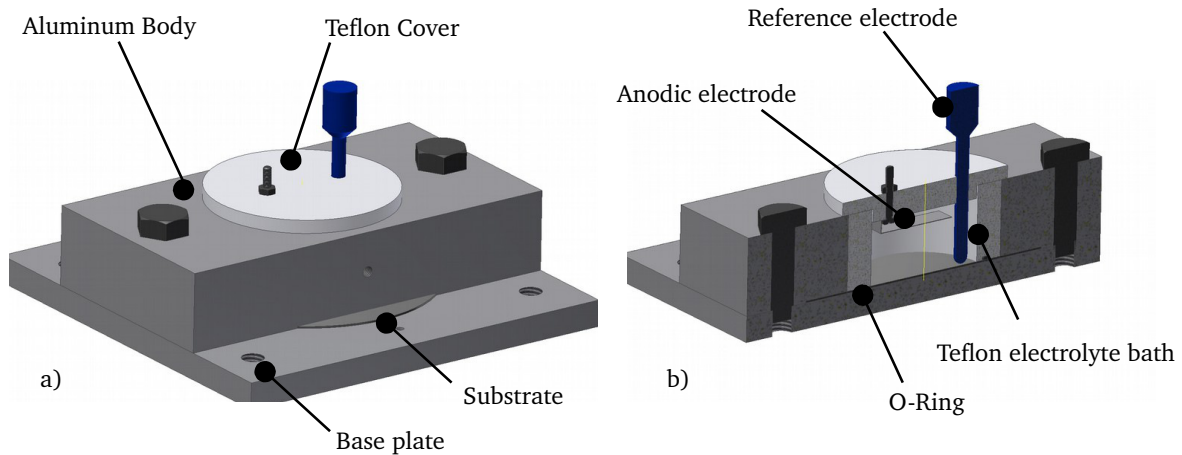


**Figure 3.22:** The electrolysis cell. a) The metallic body and the base plate are for a better thermal distribution all over the bath. A Teflon cover will prohibit vaporization and rapid changes in the concentration of the electrolyte. b) The cell consists of an anodic electrode on the top with a connection over the Teflon cover. A Teflon bath pressed inside the metallic body and an opening for RE. Image from [79] and translated with permission.

in the middle has a diameter of about 3 cm. The wafer will be put on the base plate and should be fixed with a piece of adhesive tape. As shown in Figure 3.17b, the designed electrode on the wafer is connected to a ring shaped metallic structure at the outer edge of the wafer. This can be used to connect the working electrode to the potentiostat. The bath is placed on the wafer. Through an O-ring under the bath, the whole system is sealed. The metallic body is fixed on the base plate by two screws. In some cases like gold or nickel deposition, a higher temperature than the room temperature is needed. The metallic body of the bath ensures a better heat distribution in the whole bath volume. For this purpose, aluminum with a

high thermal conductivity is a good choice. But the disadvantage of aluminum is its corrosion because of some additives in electrolytes. An alternative material is using stainless steel. Although steel is heavier, more expensive, and has a thermal conductivity less than aluminum, its advantage is a higher resistance against many chemicals. In this device, no electrolyte circulation is intended, because the deposition takes place in the small pores of the membrane. Circulation in the bath has no impact on the ion concentration inside the pores' interior volume. The general circuit configuration for the deposition device is shown in Figure 3.23. In this configuration, an Ag/AgCl reference electrode (Meinsberg SE 11) is used. This

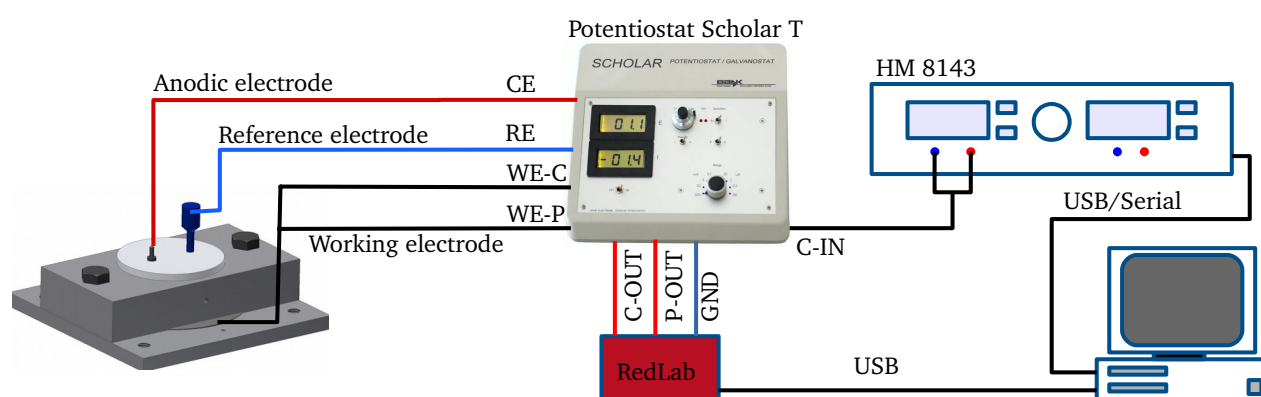


**Figure 3.23:** The circuit connection to the electrolysis bath for controlling and monitoring the deposition process. Image from [79] and translated with permission

electrode as well as anodic and working electrodes are connected to a potentiostat (Bank IC Scholar T B.4). This potentiostat can function in two potentiostatic and galvanostatic modes. This makes it possible to carry out the deposition both with a controlled constant voltage and with a controlled constant current. Although the potentiostat has an internal DC power supply, for a pulse or pulse reverse deposition, an external power supply (Rohde & Schwarz HM8143) with a computer controlled pulse generator is used. The measured analog current and potential are transferred to a Lab-view program by an 8-bit digital data logger (Meilhaus RedLab 1208 LS). The Lab-view software controls the voltage or the pulses of the function generator. Furthermore, it saves the received data from the data logger. The output of the function generator  $U_{\text{setpoint}}$  enters the C-IN connection of the potentiostat. The potentiostat adjusts the voltage on CE in a way that the measured voltage between the RE and WE connections equals  $U_{\text{setpoint}}$ . With this configuration, a voltage resolution less than 1 mV and current resolution in the range of nA are measurable. A real image of this device is shown in Figure 3.24.

## 2-Electrode arrangement

In the absence of RE, a two-electrode deposition arrangement is possible as well. In this case, the RE and CE connectors are short joined and  $V_{\text{setpoint}}$  is the voltage between the anodic electrode and the working electrode. This is done for example for cyanide containing gold electrolyte, as it is toxic and it can contaminate the reference electrode.



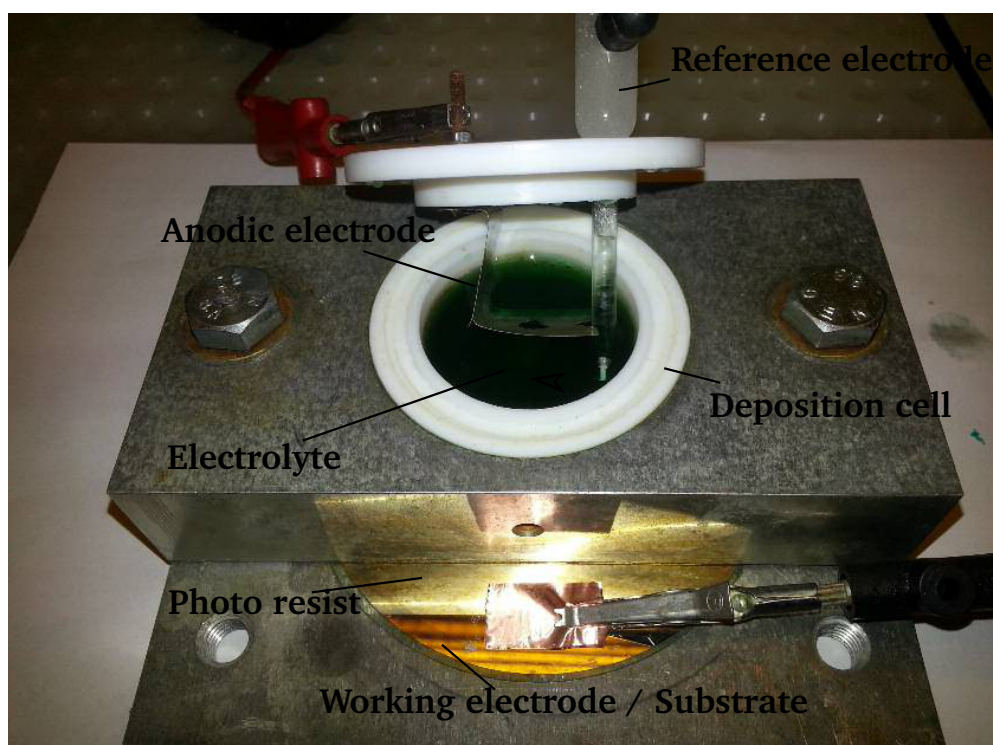


**Figure 3.24:** The real deposition cell used for growing the nanowires

### 3.5.2 Wetting the template membranes

As shown in Section 3.4.2, the template membrane is fixed on the photoresist structure on the wafer. To enable the initiation of the electrodeposition process, the electrolyte should penetrate the pores and wet the cavity underneath. For pores with diameters larger than over 200 nm or for membranes with a pore density greater than  $10^8 \text{ cm}^{-2}$ , the structure may be immersed for some hours in deionized water. Due to the hydrophobic characteristics of the polycarbonate, in some cases, even after some hours, the fluid does not penetrate completely into the pores (see Figure 3.25a). For pores smaller than 200 nm in diameter or low pore densities of about  $10^6 \text{ cm}^{-2}$ , especially in broad area nanowire arrays larger than  $1 \text{ cm}^2$ , it is in most cases impossible to wet the membrane and the cavities. To avoid this problem, different methods have been tested:

#### Exposing to water vapor

For this process, at the first step, deionized water is heated up to  $60^\circ\text{C}$  in a petri dish. The wafer, with PC membrane laminated on it, is placed upside down on top of the petri dish. Now by cooling the backside of the wafer for approx. 5 min with e.g. some drops of acetone or blowing nitrogen gas on it, water vapor diffuses and condenses inside the pores and in the cavity. After this step, the wafer is immersed in water for at least half an hour. Then, the wafer is installed in the deposition cell. The process must begin before the wafer gets dry.

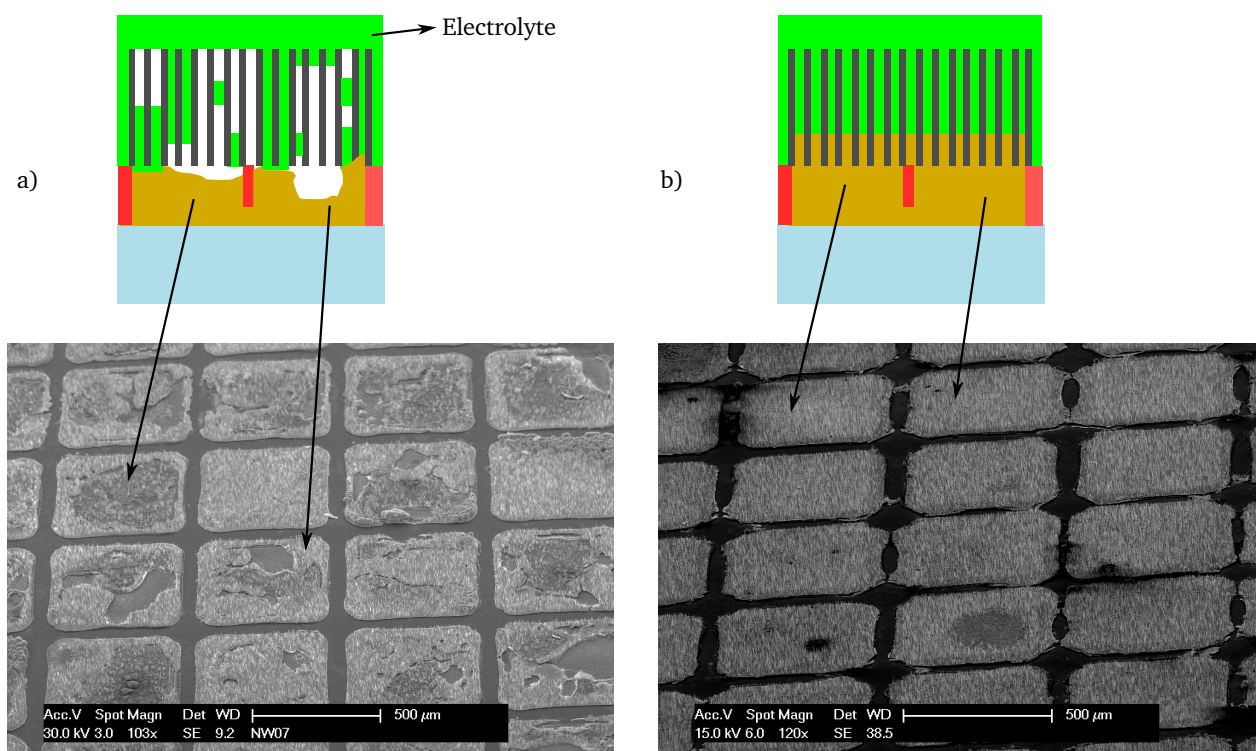


**Figure 3.25:** Wetting the PC template. a) By just immersing the wafer in the electrolyte fluid, even after some hours, the electrolyte cannot penetrate the pores. This leads to defects in the structure or inhomogeneous growth of the wires. b) Using some other techniques like water vapor, detergent solution, or plasma hydrophilization improves the wetting, and the homogeneity in the surface coverage increases.

### Wetting in a detergent solution

In this process, the wafer is immersed in a 0.006 M sodium dodecyl sulfate (SDS) solution. This is equal to  $2 \frac{g}{L}$  SDS. After about 90 min, and controlling the wetting process under a microscope, the deposition process can begin. The disadvantage of this process is the presence of an extrinsic detergent solution in the deposition process.

### Communicating vessels

To increase the number of wet pores and pad surfaces, the cavities are designed as communicating vessels. The electrolyte is injected under the foil through a channel. It is shown in Figure 3.26.

### Hydrophilization

All the processes mentioned above are still time-consuming. Because the membrane and the photoresist are hydrophobic, wetting in the electrolyte and detergent solution is necessary. To overcome this problem, the membrane and photoresist can be activated by an oxygen plasma treatment. It has been shown that after plasma treatment, the oxygen-containing functional groups on the PC surface increase. It means an improvement in the adsorption and wettability of the PC surface [83]. The activation is done in an R3T plasma machine with a power of 100 W for 5 min. After this activation step, the interior walls of the pores are still not activated. A chemical post-treatment would increase the capillary permeability

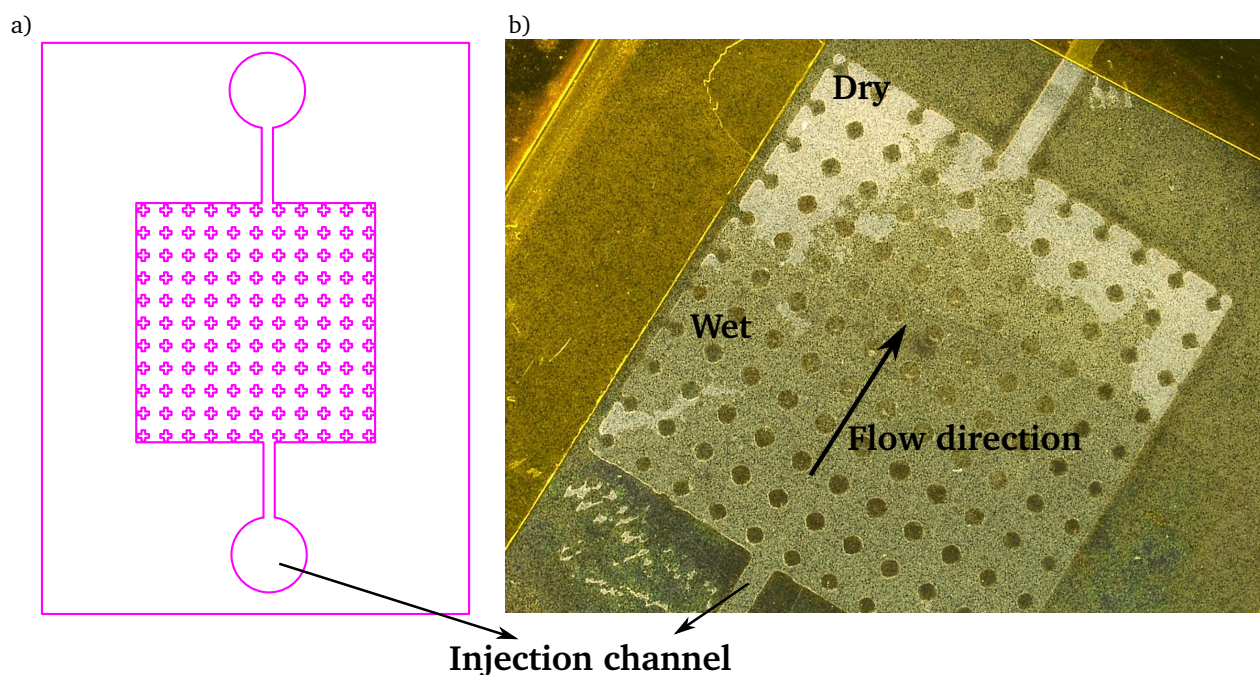


**Figure 3.26:** Communicating vessels. a) The mask with cross structures instead of supporting walls is used for laminating the membrane. An injection inlet is designed at both ends of the channels. b) The fluid is injected under the membrane. The wet area and still dry areas are marked in the image. The cross structures are deformed to semi-round shapes under laminator pressure, due to a longer softening time.

in the pores. For this, after an argon plasma treatment, the porous membrane will be immersed in a polyvinylpyrrolidone (PVP) solution. It decreases the hydrophobicity of the PC membrane [84]. By using polycarbonate track etched membranes treated with PVP (PCTE-PVP), the wetting time is reduced to a few minutes and no detergent is needed anymore. No changes in the wire's diameter and wire surface structure are detected. In this thesis, the commercial PCTE-PVP membranes from it4ip company are used.

### 3.5.3 Parameters for the synthesis of nanowires inside porous templates

The metallic deposition of gold and nickel is the general goal of this thesis. Because their work function and chemical properties, like oxidation resistance in normal air, are proper for the electron field emission application. Despite this, for some electrochemical deposition experiments, the copper electrolyte is used. The reason is that the deposition of copper is a low-temperature process, faster and more cost-efficient than other electrolytes.

#### Deposition of copper wires

Copper with an atomic number of  $Z=29$  has its d-valance states almost full, like Au ( $Z=79$ ), and Ag ( $Z=47$ ). In physics, the expression "noble metal" is sometimes confined to copper, silver, and gold<sup>1</sup>. The electric potential of noble metals against a standard hydrogen electrode (SHE) is greater than zero. During their

<sup>1</sup> The low corrosion resistance of copper against hot air, sulfuric acid, and nitric acid exclude copper from some lists of noble metals in electrochemistry.

electrochemical deposition, no hydrogen will be generated. Thus the electrochemical deposition of copper wires with a DC voltage is possible. Furthermore, a copper electrolyte with a high ion concentration is cost-efficient, compared to a gold electrolyte. The used compounds in the copper electrolyte can be found in Appendix A.3. As mentioned above, to initiate the deposition, a lower input voltage  $V_i$  than the overpotential  $\eta$  is needed. In this thesis, copper wires are deposited at room temperature and with a DC Voltage of  $V_i = 0$  mV to  $-200$  mV against an Ag/AgCl reference electrode.

### Deposition of Gold wires

To obtain a more homogeneous wire growth, the deposition voltage can be applied for many cases as pulses instead of a DC voltage. There are different possibilities to apply a pulsed voltage. As shown in Figure 3.27a, the pulse deposition process consists of a deposition time and a resting time. In this phase, the amplitude is adjusted relative to the SHE potential  $\eta$  of the working electrode (zero current potential) which interrupts the deposition in a so-called off-time. In a pulse reverse deposition shown in Figure 3.27b, the potential in off-time exceeds the SHE potential. During this time, partial dissolution of the previously deposited ions takes place. By using a non-soluble anode, the ion impoverishment inside the

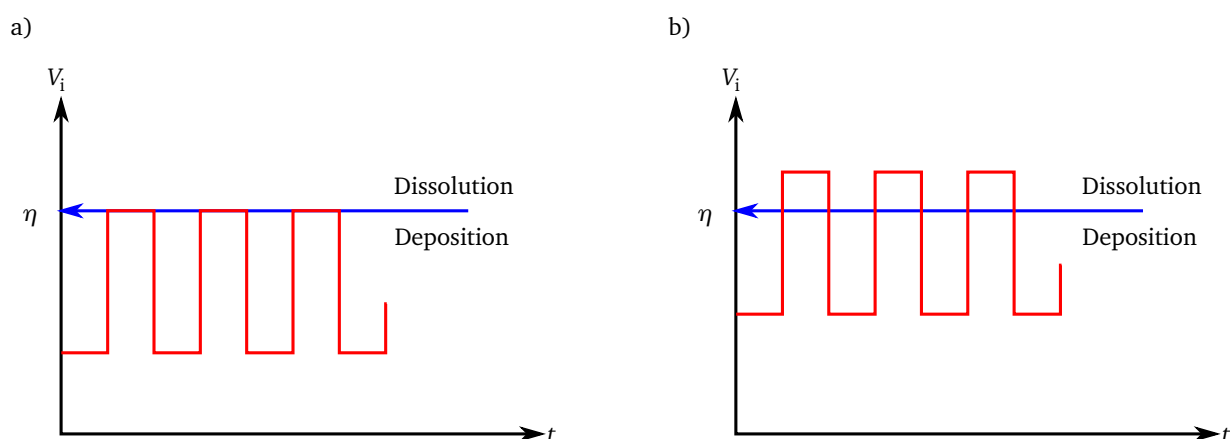


**Figure 3.27:** Schematically comparison of two types of pulse deposition; a) pulse deposition b) pulse reverse deposition

pores is a problem, which causes inhomogeneity in the growth of the wires array. The ion impoverishment increases disproportionally to the ion concentration. In a pulse deposition process, the ion concentration is compensated for during the off-time, as the ions diffuse into the diffusion layer within the pores during this time. Generally, the diffusion layer in the pulse deposition process is thinner than in the DC deposition process. By a pulse reverse deposition, the previously deposited layer of the metal and the ions, which are less tied to the surface will be partially dissolved during the off-times. It reduces the nucleation rate and the crystal texture coefficient increases. Pulse reverse deposition increases the uniformity and homogeneity of the deposits. It is also reported that the level of internal stress in the crystals deposited with a pulse reverse process is reduced. In this thesis, a sulfite-based gold electroplating bath, Gold-SF of company METAKEM (Appendix B.5), an Ag/AgCl reference electrode, and a 99.9% gold anode are used. To obtain a more homogeneous wire growth, a 20 Hz deposition pulse potential of  $-900$  mV with a zero current potential of  $-450$  mV (450 mV amplitude) at  $60^\circ\text{C}$  was applied (see Figure 3.28a). The pulse voltage



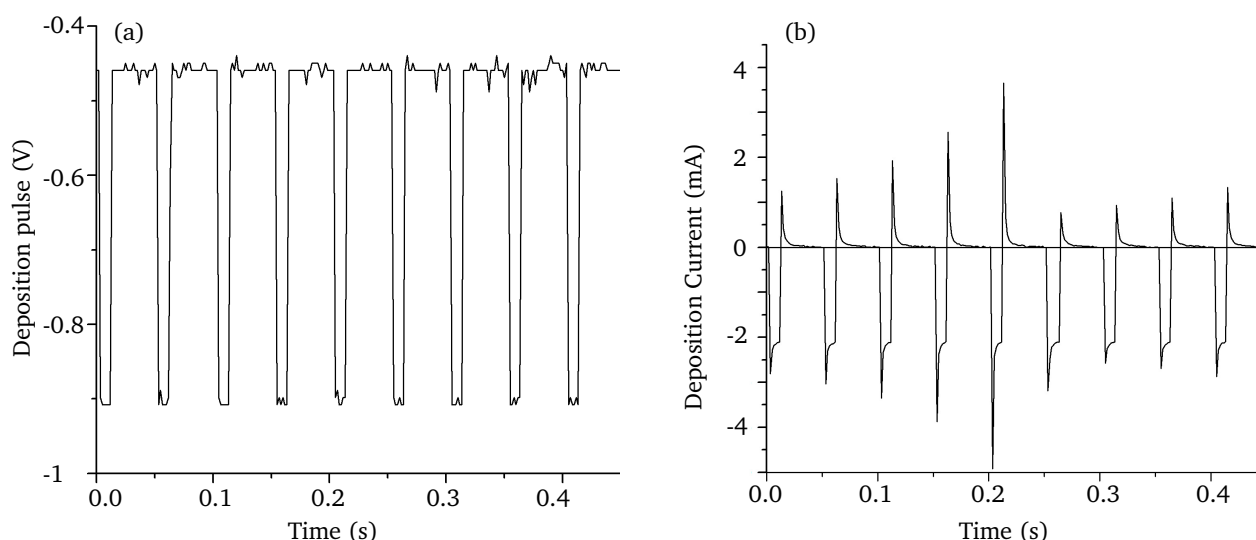


**Figure 3.28:** (a) Measured deposition pulse applied on the working electrode. A pulse voltage leads to a more homogeneous deposition compared to a direct current voltage. (b) Current pulse: The deposition takes place at negative current flow [6]

possesses a duty cycle of 20%, and the 80% resting pulse ensures that impoverishment of the metal ions near the deposition layer does not occur. As shown in Figure 3.28b, the current direction changes at the resting pulse edge. It is owing to the exponential course discharge of the capacitive charge, stored in the double layer. For base electrodes with different surface areas, the duty cycle is varied so that the discharging current reaches zero during the resting pulse. An important issue in gold nanowires is the crystal structure of the wires and its impact on field emission. The crystal structure of wires can be varied between polycrystalline and mono-crystalline changing deposition conditions [85].

### Deposition of nickel wires

Similar to the gold wires, the nickel wires are also deposited with a pulsed voltage. The prescription for the nickel bath used in this thesis is given in Appendix A.4. The used anodic electrode is a 99.9% nickel plate, which is a soluble anode. It means that the impoverishment of nickel ions in the main bath is less problematic than the one in a gold bath. But by deposition of nickel, hydrogen gas will be generated, which can clog inside the pores. To prevent this problem, pulsed voltage with proper amplitude and off-time has to be used to let the hydrogen gas molecules leave the pores. For wires with about 400 nm diameter, a deposition pulse potential of  $-900$  mV with a zero current potential of  $-400$  mV ( $-500$  mV amplitude) at  $45^\circ\text{C}$  was applied. The pulse duty cycle is about 20% and the resting pulse is about 80% for a wire density of  $2 \times 10^6 \text{ cm}^{-2}$ . The duty cycle can be increased up to 40% for wires with a larger diameter of about  $1 \mu\text{m}$  to  $2 \mu\text{m}$ . The disadvantage of pulse deposition is the longer time needed for the deposition. By increasing the duty cycle, the deposition time can be reduced. But the probability of having defects in the structure increases.

### 3.5.4 Different phases in the deposition of nanowires

Generally, the growing process of nanowires consists of different phases. As shown in Figure 3.29, the average deposition current is measured and calculated. It gives information about the various deposition states. In the beginning, in region (a), by applying a voltage, the metal ions diffuse into the membrane pores, and the current increases while the concentration of the metal ions increases. After a while in region (b), metal fills in the cavities and forms mesas under the membrane. In this region, the surface area is constant. Thus, the current is relatively constant. When the mesas reach the lower surface of the template membrane, the wires begin to grow inside the pores. In this growth phase, the total deposition surface area decreases and is associated with the current drop seen in the region (c). Finally, the current rise observed in region (d) reveals the fact that the wires are overgrown at the top side of the foil, which causes the deposition area to increase again and leads to a current increase. The current reaches a saturation level when all of the overgrowths come together as a plate and the deposition surface area remains constant. To reach a specific wire length, the process must be stopped at an appropriate time in the region (c).

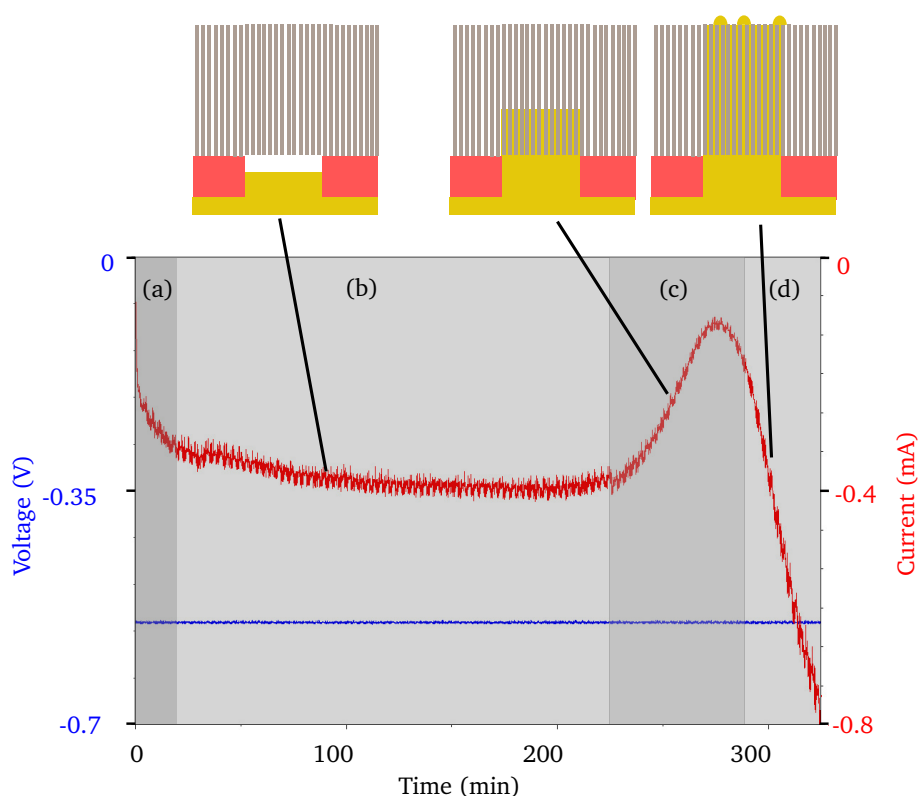


**Figure 3.29:** Measured mean value of the pulsed deposition current over time. (a) Current increases by diffusion of the ions into the pores. (b) Growth of plateaus in the cavity. (c) Nanowire growth. The current drops owing to the decreasing deposition surface area. (d) Overgrowth of the wires.

### 3.6 Results and discussion

With the developed method introduced in this chapter, it is possible to synthesize and integrate nanowires with different geometries like diameters between 15 nm to 2000 nm, heights about 10  $\mu\text{m}$  to 100  $\mu\text{m}$ , and surfaces from 300  $\mu\text{m}$  edge length up to 30 mm. An array of nickel nanowires on a gilded glass substrate is shown in Figure 3.30. This sample has dimensions of 10 mm  $\times$  30 mm consisting of a matrix of 500  $\mu\text{m}$   $\times$  500  $\mu\text{m}$  blocks.

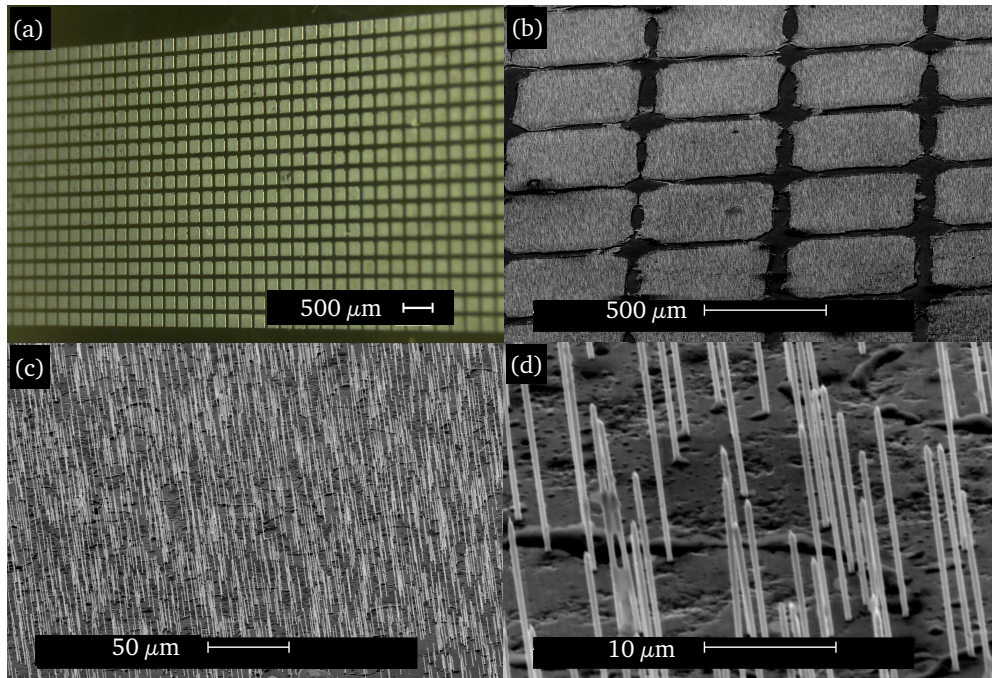


**Figure 3.30:** (a) Metallic nanowire array. The arrays consist of plateau blocks with an area of 500  $\mu\text{m}$   $\times$  500  $\mu\text{m}$ . (b) Scanning electron microscope (SEM) image of blocks fully covered with nanowires. (c) - (d) SEM images of nanowires on one block. The wires have 400 nm diameters and lengths of 25  $\mu\text{m}$ , and the arrays have a wire density of  $1.6 \times 10^6 \text{ cm}^{-2}$ .

Although the developed lamination process introduced in this chapter works properly, expanding the process to fabricate large-area arrays has caused a decrease in the fabrication yield. These wastes arise due to the defects observed in some samples. The defects are either on the entire sample surface or at least in some parts of it. Furthermore, some steps for preparing the samples can be optimized.

As a result, there are still some challenges in the whole process of nanowiring the surfaces:

- Time consuming preparation of the wafers and fixing the template membrane.
- Long waiting time for wetting the samples.
- Occurring defects in the structures. Some defects are shown in Figure 3.31.

In the case that air bubbles are being stuck under the membrane and inside the cavity, they must leave in a time-consuming wetting process. Otherwise, it will disturb the deposition process, and an empty area appears on the plateau. This effect is shown in Figure 3.31a and 3.31c. One of the defects observed is the different growth rate for the wires at the middle of the plateaus compared to those at the edges. This can be seen in Figure 3.31b. This faster growth at the edges can be explained by two phenomena: (1) field

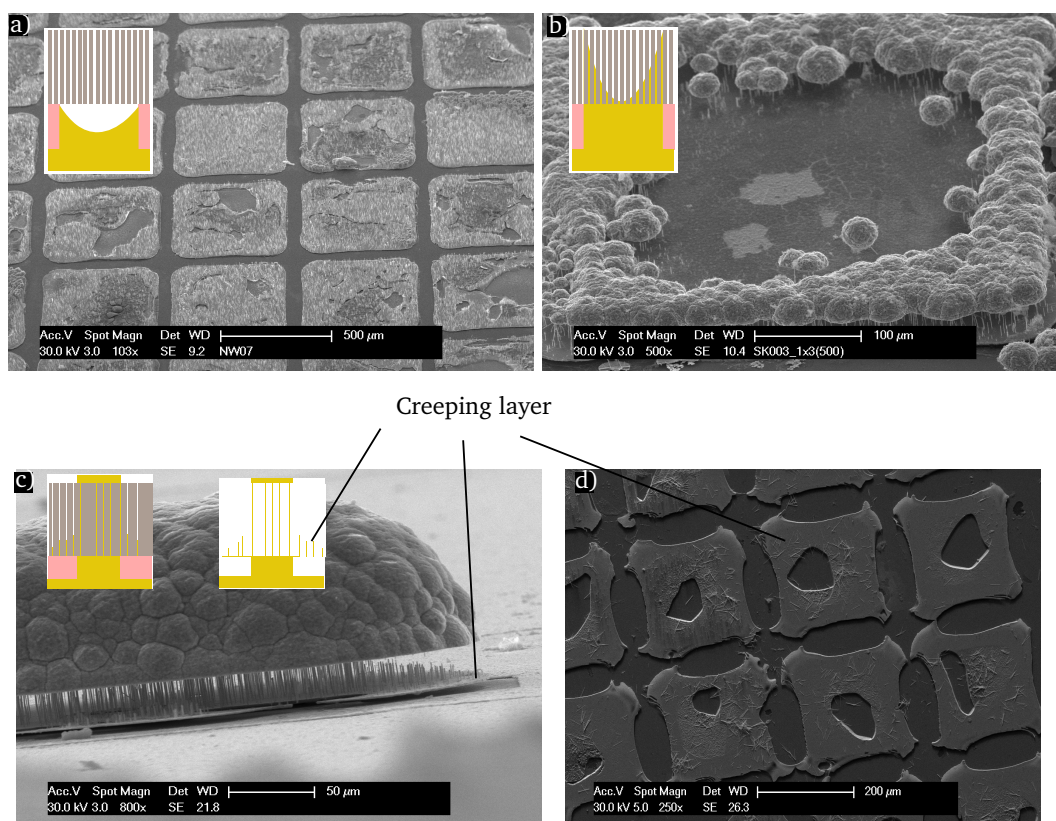


**Figure 3.31:** Defects in the structure; a) Free areas in the middle of the plateaus owing to interfacial tension. b) Faster growth of the wires at the edges of the plateaus caused by field enhancement. c), d), Creeping metallic film under the template membrane and over the supporting walls.

enhancement at the sharp edges of the plateaus that induces a higher ion current in this region, and (2) interfacial tension between the supporting walls and the electrolyte that causes an impoverishment of the ions in the middle. These effects make it impossible to stop the deposition at an appropriate time in the region (c) of the Figure 3.29 to reach the desired wires length over the entire structure. One other defect is a slight growth of metallic film over the supporting walls and under the membrane in the form of a bending beam at the edge of the structures (see Figure 3.31c). This unstable parasitic metallic beam may detach from the surface and act as a disruption in the system. In the next chapter, further development of nanowiring technology, and scaling up the surface area will be discussed.



---

## 4 Optimizing the deposition process and upscaling the nanowiring surface area

---

As mentioned previously the fabrication process for a large amount of FE cathodes and integration of an extraction grid needs to be scaled up. It is desired to use industry standard sizes larger than 4-inch wafers. In Chapter 3, a process for integration of metallic nanowires on different substrate materials, like metal, polymers, glass, silicon, and ceramics, was developed. By using this process, we cover a maximum 300 mm<sup>2</sup> surface on a 4-inch wafer. It is because of the limitations in the deposition bath. Although the process works for different materials, there are some preparation steps, like wetting the substrate, which are complicated and time-consuming processes. Therefore, there is a need for optimization. Also, the very sensitive steps of the preparation process, like laminating the membrane on photoresist supporting walls, and appearance of cavities under the membrane, can cause some defects in the sample. Therefore, it is clear that further development in the system or process would be necessary. In a new process and an optimized deposition device, the following requirements should be fulfilled:

- A faster process for wetting the surface.
- Less complex and faster process for fixing the template membrane on the substrate.
- Preventing the structural defects in the samples.
- Synthesis of nanowires on a large surface area like standard industrial wafer sizes from 4-inch to 12-inch.
- Preferably, avoiding the usage of photoresist supporting walls to increase the available area and also removing the mesa blocks.
- Reducing costs in the process by reducing the number of steps and required materials.

---

### 4.1 Fixing the membrane with a spongy material

---

Different strategies for integrating the wires onto the surfaces are discussed in Chapter 3, Section 3.2. It is shown that a spongy material can be used to fix the template membrane on a surface. But the applied technique, shown in Figure 3.10, has some drawbacks. In that technique, the anodic electrode is placed at the bottom of the bath, and the working electrode on the top. Between two electrodes, a sponge is set on the template membrane. The sponge is pressed bottom-up on the substrate by using an elevating table. Although this structure works, it is still not user-friendly. It is hard to control the electrodes' parallelism in the system during the pressing procedure, especially for large surfaces. Apart from that, the sponge may shrink under the retractive pressure with time. It leads to changes in the pressure on the sponge. One solution for preventing the sponge from shrinking is to use a solid porous material instead. It is shown in Figure 4.1. In this method, a sponge-like or porous glass plate is used to fix the template membrane on the substrate. The glass is solid and will not shrink under pressure. However, using porous glass costs more than using a conventional sponge, especially cleaning or changing the glass after a while makes it much more expensive. Also, using a glass plate is not proper for larger surfaces, as its handling is not as user-friendly and process-friendly as a sponge. On large surfaces, sliding the glass for fine adjustments will slide the membrane with the glass plate. One major problem in the system with a glass plate is the distance

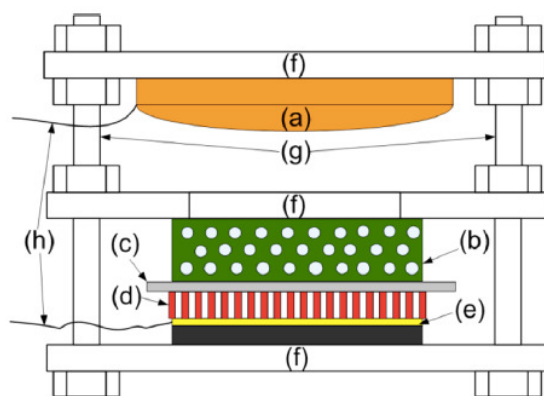


**Figure 4.1:** An sketch of metallic nanowires deposition cell; (a) copper anode, (b) porous glass plate, (c) cellulose membrane, (d) template, (e) working electrode, (f) isolation holder, (g) screw and nut, (h) copper wire. [86]

between the anodic electrode and the working electrode. This large and uncontrollable distance leads to a higher deposition bath volume, which means consuming a higher electrolyte volume. Moreover, a much higher electrical potential is needed to sustain the current flow in the electrolyte. The other disadvantage of this structure is the isolation holder used in the system. It can change the electrical field in the system or work as a shading mask in the deposition cell, which will affect the wires' growth homogeneity. To optimize the process, in this thesis a combination of both ideas is applied, in which a top-down sequence in the system and a sponge instead of a solid material are used. The mechanical design of the new system will be introduced in Section 4.2.

## 4.2 Design and structuring an optimized deposition bath

For compensating the sponge shrinking effect under the pressure, the elevating table is substituted with a spring system. The springs can sustain the pressure on the sponge in the bath during the deposition time. For designing the spring system, there are two possibilities: using a conical spring or using a compression helical spring.

- **Conical spring:** These springs can distribute the pressure all over the system. Using a spiral rod for screwing and compressing the spring, the force may not homogeneously distribute all over the system. Also, the closed structure of such springs makes it harder to design an opening for the reference electrode and it makes the operation of the device more complicated.
- **Compression helical spring:** For a homogeneous force distribution on the surface, more than three pressing points are needed. For pressing the system, a spiral rod in the middle is going to be used. Thus, it is decided to use four helical spiral springs, as shown in Figure 4.2a, to reach a sufficient force distribution.

The designed system consists of a stamp for pressing the sponge. This stamp is made of a material like PTFE, or polypropylene, that are resistant against most available chemicals in different electrolytes and solvents. The four springs are guided by 4 rods, made of stainless steel. The rods are clamped to an upper plate using an E-clip clamp washer. As shown in Figure 4.2b, a meander is graved on the bottom surface of the stamp. This meander is used to fit the gold cathode wire in it, and it is passed to the

top through a small drilled hole. The stamp is pressed into a cover plate, which has two functionalities. Firstly, it covers the bath and prohibits electrolyte evaporations; Secondly, it works as a spacer to adjust the stamp distance from the working electrode. For a less complex system, in the first version of the

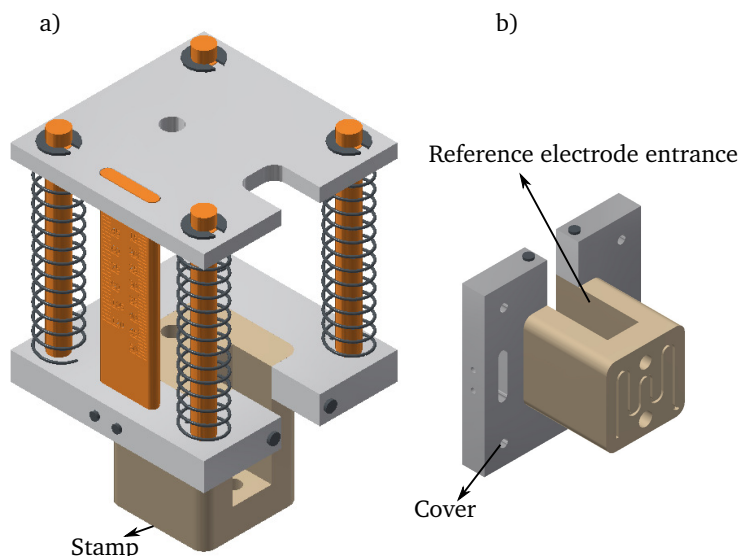


**Figure 4.2:** a) The mechanism of the spring system for fixing the membrane. b) Lower view of the stamp from CAD.

device, instead of mounting a force sensor for measuring the applied force on the working electrode, a calibrated scale is designed and installed. The force measurement with this method is not precise enough; However, this parameter does not have the highest priority in this thesis and can be neglected. Thus, using a calibrated scale makes the system less complex without impairing its functionality. The schematic of the whole device is shown in Figure 4.3. In this device, the deposition bath is made of PTFE, and it is pressed into a metallic body. This thick metallic body will keep the temperature constant all over the bath during the deposition. The wafer is fixed on a metallic plate and the integrated O-Ring under the bath will seal the bath. For fixing the metallic body to the bottom plate, four Allen screws are used. The screws are tightened with a torque screwdriver to guarantee the force distribution and sealing of the bath. The technical drawings of this device can be found in Appendix C. A real image of the bath is shown in Figure 4.4.

### 4.3 Deposition results with spring deposition bath

The new configuration for electrochemical deposition with a spring bath is shown schematically in Figure 4.5. For setting up the new spring deposition bath, the first step is to find out the optimal pressure needed for the best results. The initial tests are done with the same structure shown in Figure 3.17, in which the supporting walls are made of map-1215 and AZ9260 photoresist with a thickness of  $1.5\ \mu\text{m}$  and  $7\ \mu\text{m}$  respectively. The pressure on the structure must be optimized in a way that the photoresist is not squeezed and spread all over the surface at very high pressures and higher temperatures as well. Also, very low pressure leads to defects discussed in Section 3.6. Furthermore, lower pressures result in a larger volume

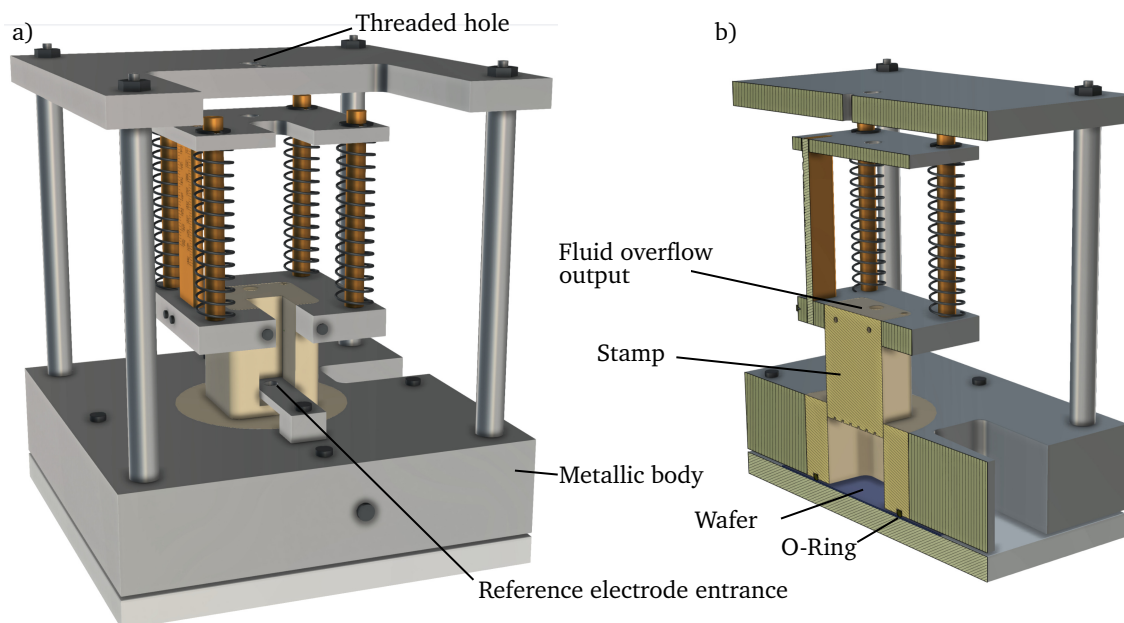


**Figure 4.3:** a) 3D CAD schematic of the optimized deposition bath with an integrated spring system. There is a threaded hole on the upper plate into which the springs are pressed with a threaded rod. b) Cross section of the system. The metallic body is connected to the lower plate using 4 screws. The notch at one side of the metallic body is used to connect the working electrode to the potentiostat.

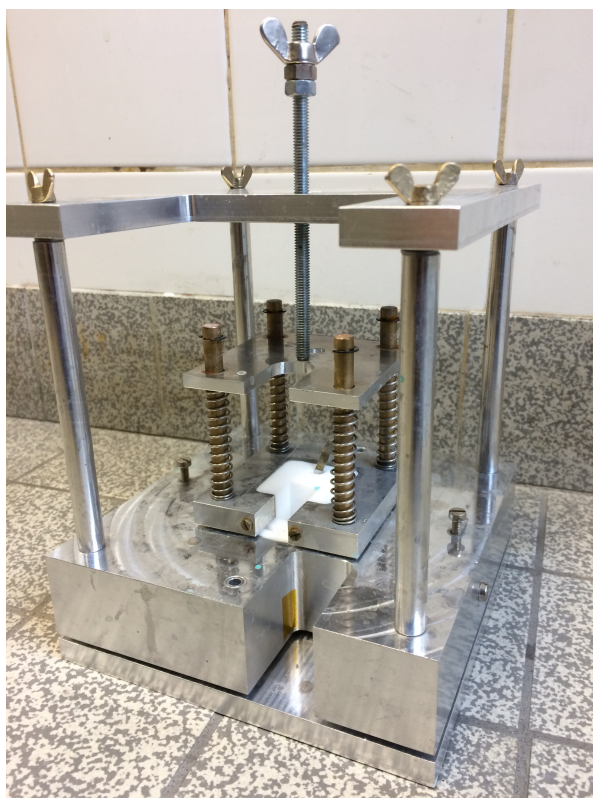


**Figure 4.4:** A real image of an optimized deposition bath with the integrated spring system.

under the stamp. It leads to a higher electrolyte consumption and also a larger distance between the anode and the working electrode. For structures fabricated with the given materials used in this thesis,

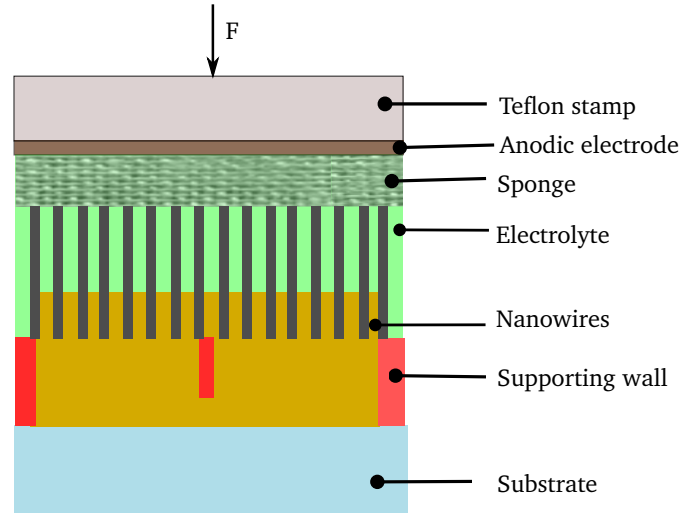


**Figure 4.5:** Electrochemical deposition configuration with the spring system. The springs exert the force  $F$  on the stamp and consequently on the sponge. The pressed sponge will fix the template membrane on the supporting walls and also let the fluid reach the pores.

a pressure of  $8 \text{ N cm}^{-2}$  showed the best results. As shown in Figure 4.6, the deposited structures have much sharper edges. Also, no creeping layer on the supporting walls can be observed. Furthermore, the

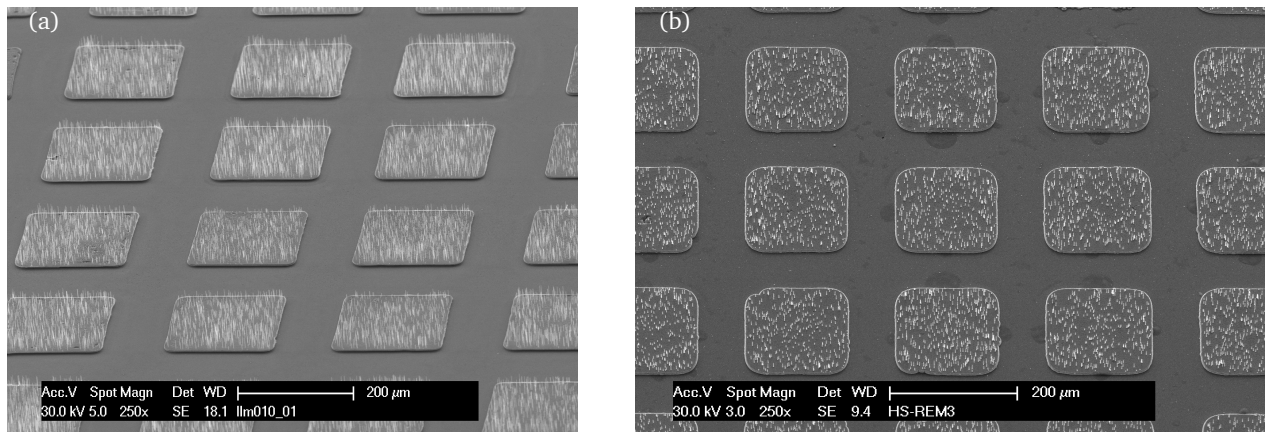


**Figure 4.6:** Arrays of nanowires fabricated by pressing the template membrane on the supporting walls. The predefined electrodes are completely covered and have sharper edges than those of the electrodes shown in Figure 3.30. No defects were observed in structures deposited with the spring device. a) Gold nanowires with 400 nm diameter and length of  $25 \mu\text{m}$ . The density is  $1.6 \times 10^6 \text{ cm}^{-2}$ . b) Copper wires with  $1 \mu\text{m}$  diameter and a density of  $1 \times 10^5 \text{ cm}^{-2}$ .

problem with wetting the structure is solved in most cases; Especially, for growing nanowires with lower densities or even smaller wire diameters. The reason is the pressed wet sponge on the membrane that boosts the capillary effect inside the pores.

At this stage, in cases in which no resist masking is needed, the substrate can be fixed in the deposition device directly. Then after wetting the surface with DI-Water or electrolyte, the membrane is placed on the substrate. It enables us to cover larger surfaces with wires. It means that the whole surface can be covered with the wires seamlessly. It also saves many steps like lamination, listed in Table 3.3. This



process should be done in a cleanroom air condition to avoid external particles as a defect under the membrane. In the next versions of the device, it is possible to upscale the system for larger areas and cover industrial standard substrates like 4-inch to 12-inch wafers or even panels. This device and the results are discussed in the next section.

#### 4.4 Upscaling the spring deposition device

For an industrial fabrication process, an adaption of the device for standard wafer sizes is needed. As mentioned in the previous chapter, with the first deposition device, synthesis of nanowires on small areas less than  $300 \text{ mm}^2$  has been enabled; and the area should be divided into an array of  $300 \mu\text{m}$  to  $500 \mu\text{m}$  pads, with supporting walls. The fabrication includes many steps, and lamination on the supporting wall is needed. But with the spring device, the predefined electrode size can vary between  $300 \mu\text{m}$  to  $30\,000 \mu\text{m}$ . It is enabled because the sponge material is responsible for fixing the membrane on the substrate instead of laminating on the supporting walls. In the next step, a 4-inch spring device has been designed and fabricated. The schematic of this device is shown in Figure 4.7a. In the design of the 4-inch device, the

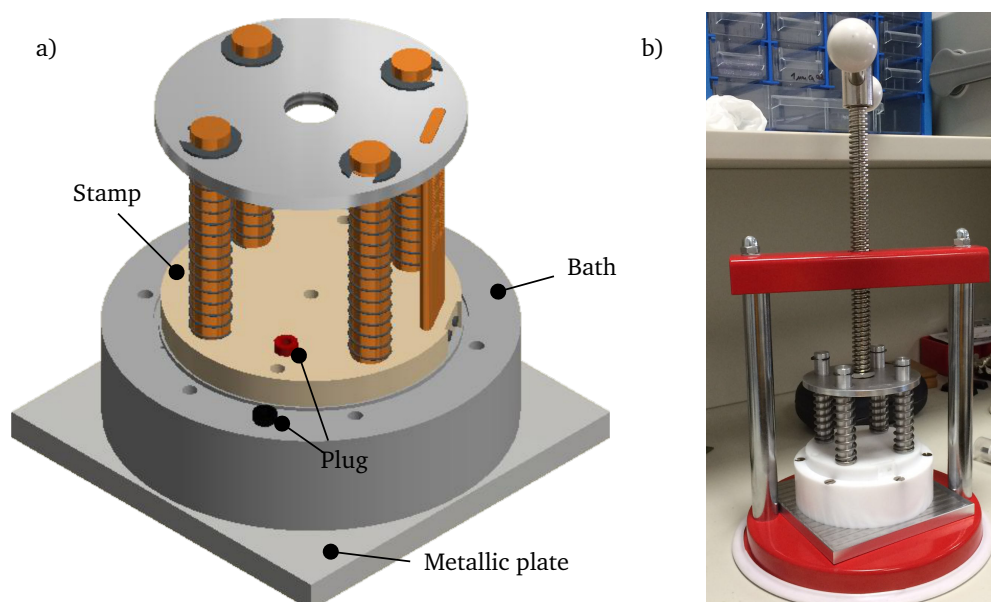


**Figure 4.7:** a) The schematic of a 4-inch deposition device. The bath is sealed by an integrated O-Ring underneath and it is fixed on the metallic plate by six screws. The anodic and working electrodes can be connected through plugs to the potentiostat. b) An image of a 4-inch deposition device with a mounted spring system in a vertical screw press.

metallic body is removed as the fluid volume in the bath is below 50 mL, which spreads like a film over the metallic plate. This plate is responsible for the heat transfer to the fluid. It means the temperature is kept constant during the deposition. Removing this part makes the device less heavy than a  $30 \text{ mm} \times 30 \text{ mm}$  device. Another change in the design is substituting the metallic chassis with a removable vertical screw press. It makes the cleaning process easier. In the 4-inch device, the notch for contacting the working electrode with the potentiostat is removed, and four spring contacts are installed under the bath. These spring contacts can be connected through a plug on the bath top side. The anodic electrode is connected to a plug on the stamp as well. The same design is used for a new device adapted to standard 8-inch

wafers. This device is schematically shown in Figure 4.8a. For better parallelism in the system and better force distribution, 12 springs are used. Similar to the 4-inch device, a vertical screw press is used to press the springs. This can be seen in Figure 4.8c. Although a round shaped bath is proper for standard wafers, it is not suitable for many devices with square form. For such samples, like PCBs, the design was updated into a 200 mm  $\times$  200 mm bath. Due to increased surface area, in this device, about 18 springs are used. A schematic of this device and a real image of it can be seen in Figures 4.8b and 4.8c.

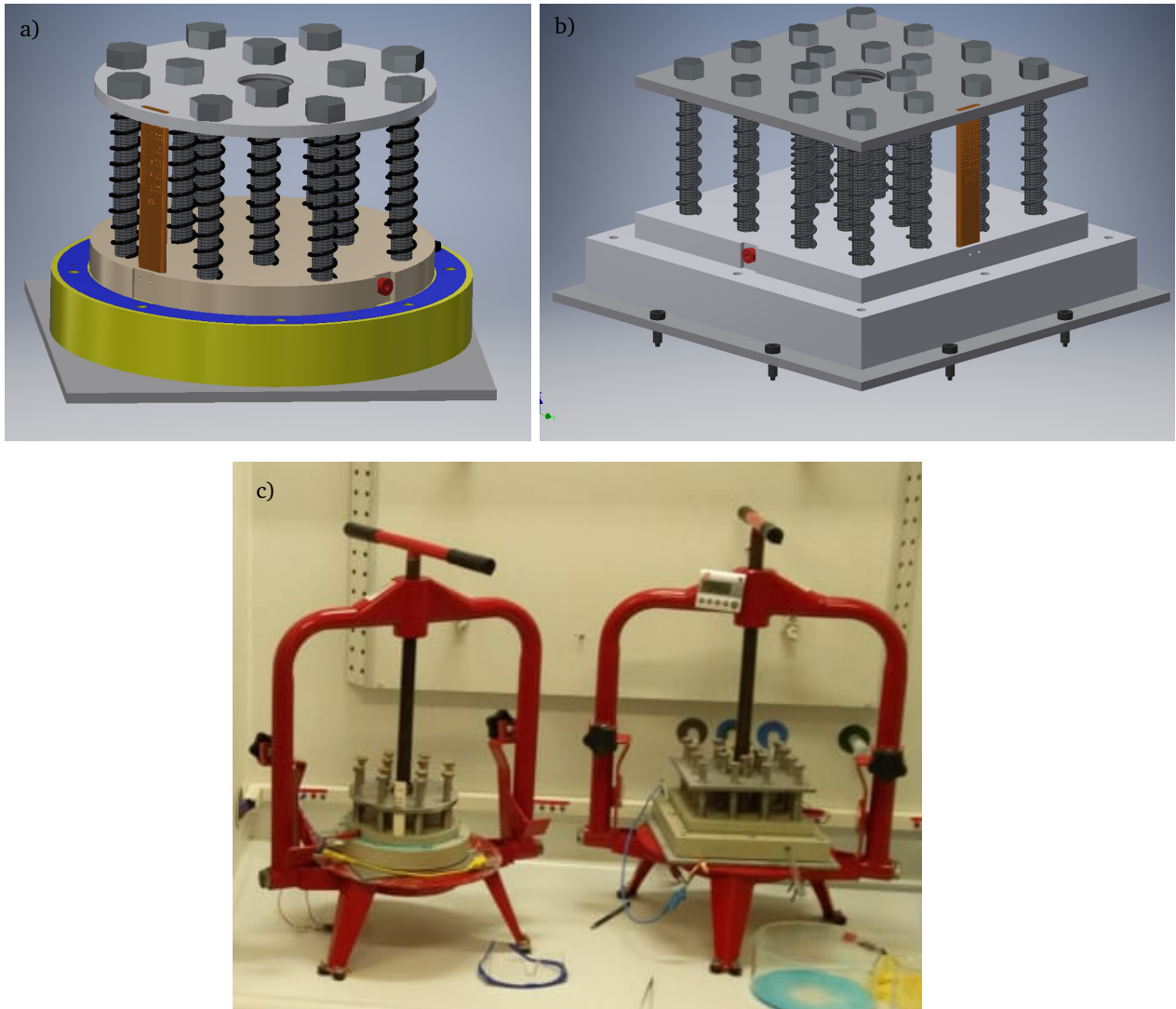


**Figure 4.8:** a) Schematic image of a deposition device for standard 8-inch wafers b) The deposition device in a square form. This device has 200 mm edge length and is suitable for different PCBs c) Both devices in the laboratory setup.

In Figure 4.9, a sample prepared with 200 mm  $\times$  200 mm device is shown. This copper plate consists of four strips of copper nanowire arrays with 200 mm  $\times$  30 mm surfaces. Compared to all devices discussed before, it is now possible to synthesize nanowires on large panels and wafers with larger dimensions. No supporting walls and no lamination is needed anymore. The wetting of the sample takes place immediately, without immersing the sample in DI-Water or an SDS solution. This device enables the deposition of nanowires with low wire density or low wire diameter with no defects on the surface. It is a progress

for the deposition of sharper structures with a proper pitch for an electron field emitter application. The deposition of such structures, like conical shaped wires, will be discussed in Chapter 5.

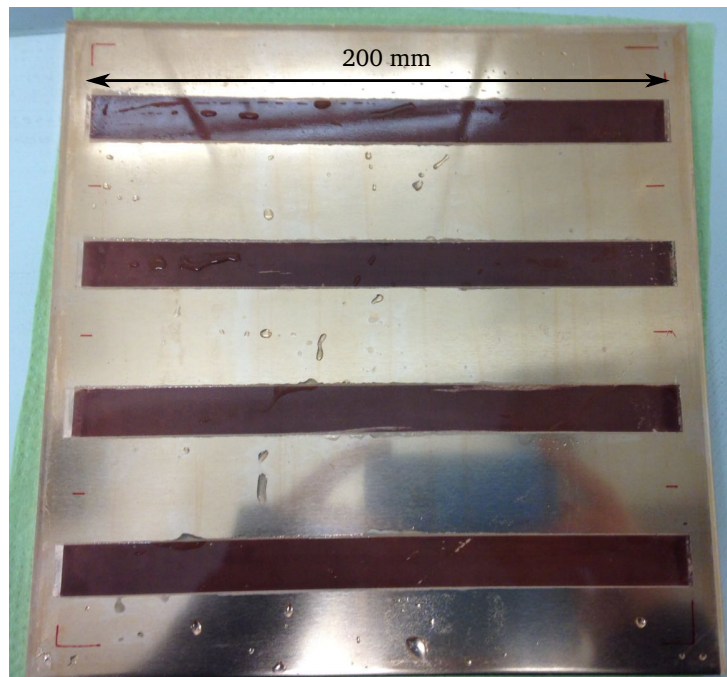


**Figure 4.9:** A copper plate covered with four strips of copper nanowire arrays each with 200 mm length and 30 mm width. No defect is obvious on the entire surface.



---

## 5 Fabrication of metallic nanocones with controllable tip diameter and apex angle

---

As discussed in Chapter 2, CNT wires have a limited stiffness, thermomechanical stability, and a hairy structure with much bending in them. Although silicon wires or sharp silicon tips can be fabricated in the shape of highly uniform arrays, the maximum achieved current in such tips is limited. Thus metal nanowires with a high aspect ratio and acceptable mechanical stability, and a better contact conductivity to the substrate are promising alternatives. After a brief discussion on better performance of nanocones as electron emitting platforms, the fabrication, integration, and tailoring the geometry of the metallic nanocones will be discussed. Some parts of this chapter are published in [8].

---

### 5.1 Electron field emission of metallic emitters

---

An interesting point about the template-grown metallic nanowires considered as emitting platforms is the flexibility in controlling their geometric parameters such as length and diameter. The reported field emission results of randomly distributed copper nanowires [87], gold-coated nickel wires [88], and gold nanowires [54] are promising. But all the measurements have shown, that just a percentage of wires contributing to the field emission, or most of these wires show an unstable Fowler-Nordheim (FN) behavior. Although in measurements on gold nanowire-arrays a homogeneous field emission is achieved [89] [90], the field emission current is still limited. This is caused by individual wires destructing during the emission. The main reasons for this destruction are the shortcomings of the fabrication methods used for producing or integrating the wires. These methods lead to an insufficient electrical conductivity in the wire-substrate interface, so a higher Joule heating can destroy the wires. The deficit in the interconnection is observed by both poly- and monocrystalline gold nanowires [91]. Using the technology developed in this thesis, wires with less inhomogeneity in terms of length, height, and coverage can be fabricated. It means a higher percentage of wires that contribute to the emission is obtained. Also, the electrical resistance of less than  $1 \frac{\mu\Omega}{\text{mm}^2}$  in the interconnection of wire-substrate can be achieved.

---

#### 5.1.1 Nottingham effect

---

For a long time, it was believed that the Joule or resistive heating of the emitting tips by emission current was the main reason for the instability of the FE current behavior and destruction of the wires. Heat can also increase by ion bombardment of the tips. This heating leads to the thermal field emission, and a higher current emission results in a further heat increase in the emitting cathode. The cathode will transit to the evaporation phase and explosive emission takes place, which causes vacuum breakdown. However, today both the theoretical and experimental calculations have shown that the “contribution to the thermal balance during FE is due to a purely quantum-mechanical energy exchange process, referred to as the Nottingham effect.”[36]. In this energy exchange mechanism, electrons with lower energy than electrons in the conduction band will tunnel from the energy levels below the Fermi level. These electrons will be replaced by electrons of the conductive band. As these electrons are more energetic, the higher energy will be released at the surface of the emitting area which is mostly at the tips of the wires, and

the temperature increases. At higher FE currents, the heat increase in association with the Nottingham effect exceeds the joule energy dissipation. Thus, the combination of the Joule heating and the Nottingham heating leads to a faster temperature increase at the tips. At temperatures beyond the so-called inversion temperature  $T^*$ , the number of electrons above the Fermi level increases. It means that most of the emitted electrons come from these energy levels. Thus, the Nottingham effect begins to cool the cathode because those electrons extract energy from the cathode. The inversion temperature  $T^*$  is expressed as [36]

$$T^* = \frac{\hbar e}{4k_B(2m_e)^{\frac{1}{2}}} \frac{E}{\sqrt{e\phi_W}t(y)} \cong 5.67 \cdot 10^{-5} \frac{E}{\sqrt{e\phi_W}t(y)} [\text{K}], \quad (5.1)$$

with  $E$  in  $\text{V cm}^{-1}$  and  $e\phi_W$  in eV. The Nordheim correction function  $t(y)$  has a value close to unity and varies weakly with the argument. The values of  $y(t)$  are tabulated in the literature, see e.g. [37]. This temperature is proportional to the local electrical field magnitude  $E$  and inversely proportional to the root of the work function  $(e\phi_W)^{\frac{1}{2}}$ . A plot of  $T^*(E)$  is shown in Figure 5.1. This result shows that the Nottingham

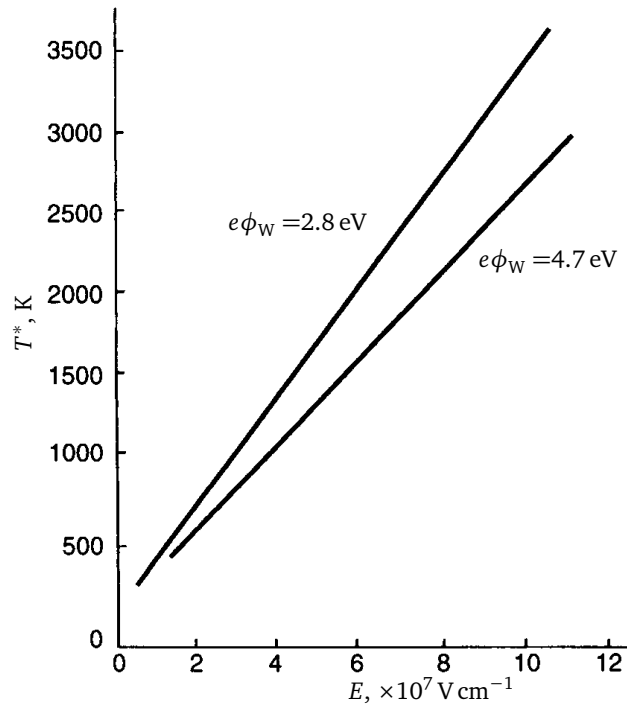


**Figure 5.1:** Variation of the inversion temperature  $T^*$  with the electric field calculated by (5.1) [36]

heating is the reason for emitter destruction for metals with a melting temperature below the inversion temperature. Furthermore, for metals with a work function in the range of  $e\phi_W = 4.5$  eV to 5.0 eV, for higher current densities an emission field of  $E > 5 \times 10^7 \text{ V cm}^{-1}$  is needed. This means refractory metals like W or Mo are proper metals for an application as high current density field emitters. Also, for metals like gold, with  $e\phi_W = 5.3$  eV and melting temperature of 1064 °C (1337 K), and nickel with  $e\phi_W = 5.0$  eV and melting temperature of 1450 °C (1728 K) the activation fields  $E$  should not exceed respectively  $5 \times 10^7 \frac{\text{V}}{\text{cm}}$  and  $6 \times 10^7 \frac{\text{V}}{\text{cm}}$ .

The thermal stability of platinum and porous gold nanowires below 100 nm diameters are studied by Rauber et al. [92] and Burr et al [93]. It is shown that Platinum wires begin to transform into a chain of

spheres after 30 minutes of annealing at a temperature around 600 °C (873 K) and porous gold wires at a temperature around 200 °C (473 K) after 1 hour of annealing. Both temperatures are much below the melting temperatures of bulk materials. This effect takes place due to surface tension and is known as Rayleigh instability. The transformation process of platinum is shown in Figure 5.2.

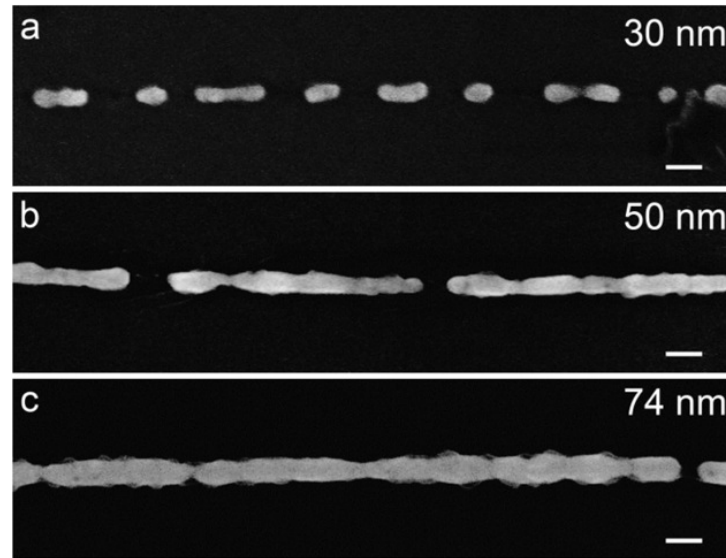


**Figure 5.2:** SEM Images of platinum nanowires after 30 min of annealing at 900 °C. The wires are obviously destructed by heating to temperatures lower than the melting temperature of the bulk material. The scale bars are 100 nm [92]

By improving the contact by modifying the geometry of the cylindrical wires into conical structures, higher mechanical stability is expected. This leads to a higher and more stable FE current [94]. Nevertheless, the metallic cones are interesting for other applications like solar cells, anti reflective coatings, or antennas. But the samples tested in the past works had similar fabrication shortcomings as the nanowires, particularly in the integration of large area nanocone arrays on a surface. In this thesis, the developed process for fabrication and integration of nanowires is also used to produce nanocones.

## 5.2 Asymmetric etching of ion-tracked polymer templates

The transition from semi-one-dimensional wires to 3D nanocones begins with preparing the template membrane by asymmetric etching of the ion-tracked polymer template. In this section, after a short review of the ion irradiation of the membranes and the etch process, the designed etch device and the process control configuration are introduced.

### 5.2.1 Heavy ion irradiation of template membrane

Irradiation of polymer membranes with swift heavy ions of MeV-GeV kinetic energy damages the polymer chain along the particle track as the energy of the projectile ion is transferred to the target electrons and nuclei [95], [96], [97]. The transfer of the energy along the travel path can be expressed as

$$\frac{dW}{dx} = \left( \frac{dW}{dx} \right)_{\text{electrons}} + \left( \frac{dW}{dx} \right)_{\text{nuclei}} . \quad (5.2)$$

The energy loss function is shown qualitatively in Figure 5.3. It can be seen that at the entering side,

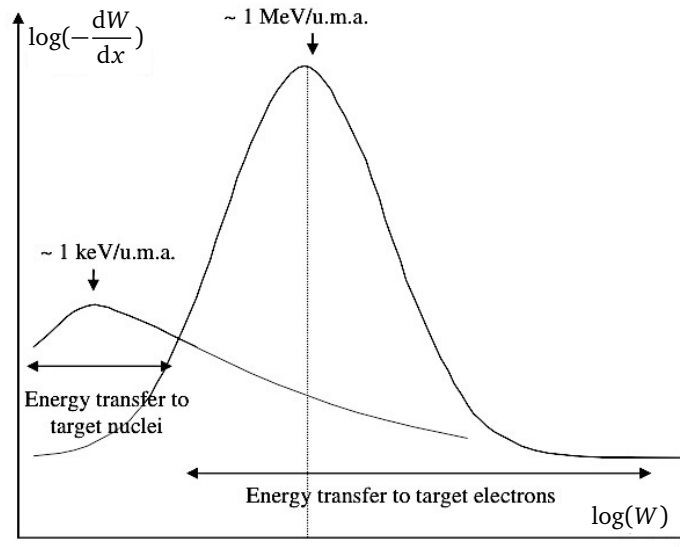


**Figure 5.3:** Qualitative schematic of the energy loss function of an irradiated ion on a polymer target as a function of its kinetic energy [97]

the energy of the high energetic ions is transferred to the electrons of the target. On the other hand, the energy of the ions with energies less than 100 keV, or the ions at the exit side, which have lost their energy by traveling through the target, are transferred to the nuclei of the polymers. The nuclear energy loss corresponds to the elastic collision between the ions and the nucleus of the polymer atoms. This kind of energy loss causes a billiard-like displacement in the atomic structure of the target and generates interstitial vacancies and defects. In contrast to the nuclear energy loss, the interaction of high energetic ions with the polymer electrons is predominant. Consequently, the electrons are excited to higher levels and an ionization process happens. The emission of energetic electrons will ionize more atoms at a radial distance from the central ion path. Some models show that the diameter of the track core is less than 10 nm, and the surrounded track halo can be defined by the maximum range of electron cascade, which ranges up to 1000 nm or higher. One important factor is the penetration range of the ion before coming to a full stop. It must be larger than the target thickness. In polycarbonate, an ion with a kinetic energy of about 11 MeV can travel over 100  $\mu\text{m}$  [77].

### 5.2.2 Cylindrical and conical channels in a template membrane

As mentioned above, irradiating the polymer will damage the polymer chain along the ion path. Consequently, by etching the polymer membrane it is observed that the etching rate along the particle tracks  $V_t$  is much higher than the bulk etching velocity  $V_b$ . Thus, by etching the ion tracks in the polymer membrane can be used to create a porous membrane to grow cylindrical or conical metallic nanostructures in the pores [74], [98], [78].  $V_t$  is not constant and correlates with the energy-loss function of the ions along the track. Subsequently, the etching rate at the entering and exit sides of the membrane is different, which is negligible in thin polymers. To reach a cylindrical pore the irradiated polymer membrane will be etched in a proper etching solution. At a specific breakthrough time,  $t = t_b$  the opening of both sides will reach the middle point, and a channel is formed. As shown in Figure 5.4, at a lower etch rate the pore shape is not exactly cylindrical. For better control of the cylinder geometry, especially in terms of diameter, the etch rate must be controlled by monitoring and adjusting the external parameters like etchant concentration.

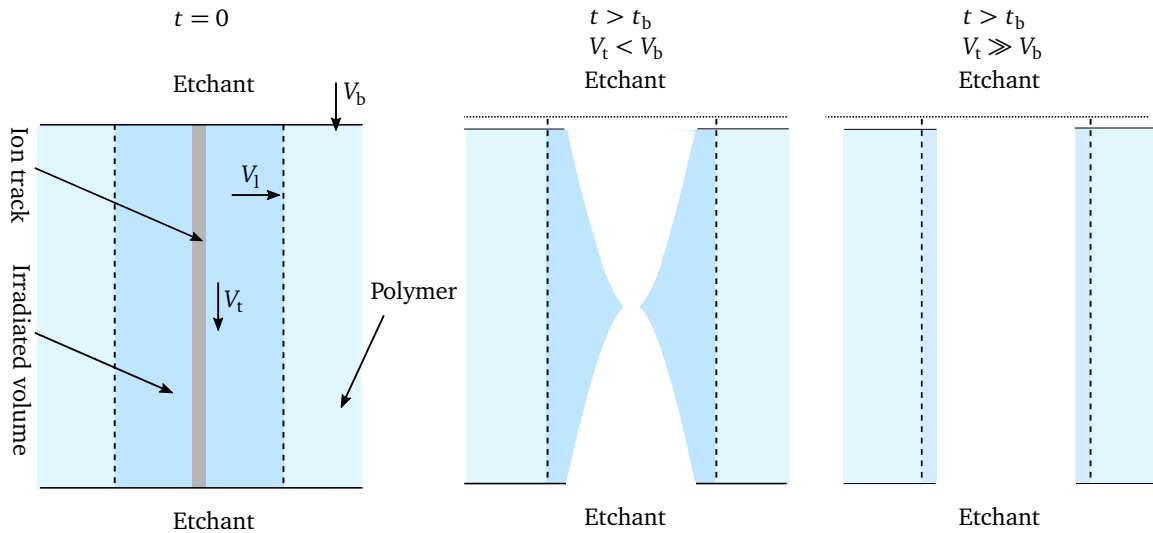


**Figure 5.4:** Schematic of etching cylindrical pores in an irradiated polymer at different times and different etch rates. To reach a cylindrical channel and have better control of the pore diameter, a proper relation between the etchant concentration and etching time must exist.

While symmetrical etching leads to cylindrical pores, to reach conical shaped pores the etch process must be performed asymmetrically at the ion entry side [97]. Such an asymmetrical etching process is schematically shown in Figure 5.5. In addition, the lateral etch rate  $V_l$  changes uniformly between  $V_t$  and  $V_b$  as a function of energy loss from the ion collision point. This is defined as a track core, and its thickness is about a few nm to some  $\mu\text{m}$  depending on the ion energy and polymer chain length. The ratios  $\frac{V_t}{V_b}$ ,  $\frac{V_l}{V_b}$  and  $\frac{V_t}{V_l}$  define the geometry of the cones. These ratios can be manipulated by several external parameters. It means the geometry of the conical pores etched in irradiated Polycarbonate (PC) membrane not only depends on the parameters like the ion energy and the ion entry side. It also depends on external parameters like the concentration of etching solution, the temperature, and external voltage applied on both sides of the membrane during the etch process [97], [99], [100] [101].

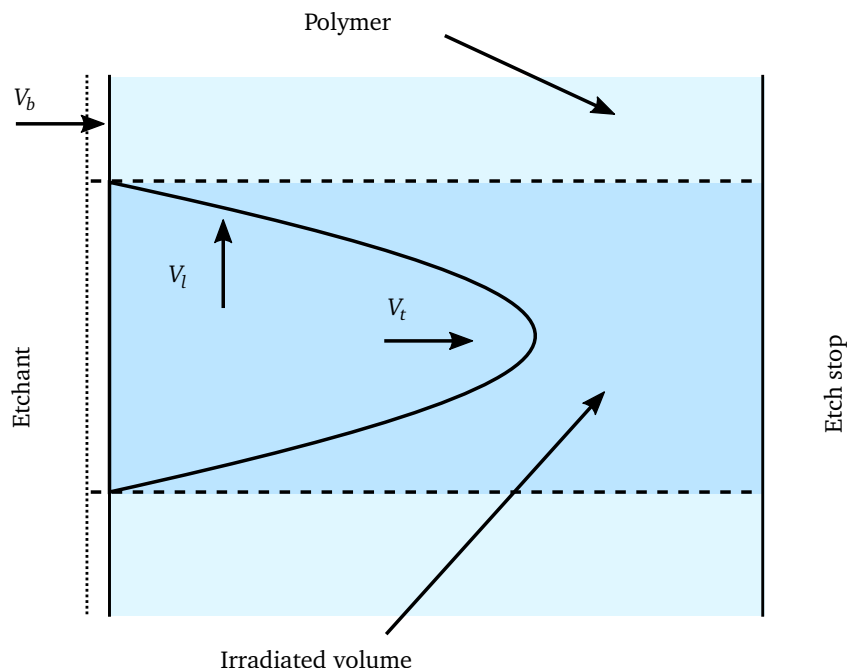


**Figure 5.5:** The polymer membrane is etching asymmetrically. On the entering side, the etching solution will etch the ion track and at the other end, the etch stop solution will slow down the etching process, as soon as the channel breaks through.  $V_b$  is the etch rate of not irradiated bulk material in etch solution.  $V_b$  is much less than the transversal and the lateral etch rates ( $V_t$  and  $V_l$ ) in the ion track area.

### 5.2.3 Experimental setup and methodology for chemical etching of the polymer membrane

In this thesis, a PC membrane with a thickness of  $24\mu\text{m}$  is used, which is commercially available from the company it4ip with a variety of ion track densities. To etch the polymer membrane an etch cell is designed, which is schematically shown in Figure 5.6. The etch-cell is constructed from PTFE. A half-cell is shown in Figure 5.6b. This cell has a round etching surface with 60 mm diameter and a depth of 3 mm, which gives about 8.5 mL volume for each half-cell. The irradiated template membrane will be sandwiched between two half-cells and fixed by four screws. The chemical resistance of the PC-membranes is given in the datasheet in Appendix B.6.

One side of the chamber is filled with 9M NaOH + Methanol (1:1) as the etchant. The other side is filled by 10% acetic acid, as an etch-stop solution [102], [103], [104]. To control  $V_t$  and  $V_l$  and thus the cone geometry, a transmembrane voltage  $U_t$  is applied. By applying the voltage with the polarity shown in Figure 5.6, the concentration of the  $\text{OH}^-$  ions on the membrane surface and their mobility in the pores can be controlled [105]. As soon as the pores open, the flowing ion-current through the pores can be measured. This current is a function of pore density, pore size, applied electrical field, temperature, and concentration of the ions in the solution. The pore size defines the resulting tip diameter of the cones. To control the tip diameter of the cones, the ion current is monitored. The circuit setup and the schematic of the apparatus are shown in Figure 5.7.

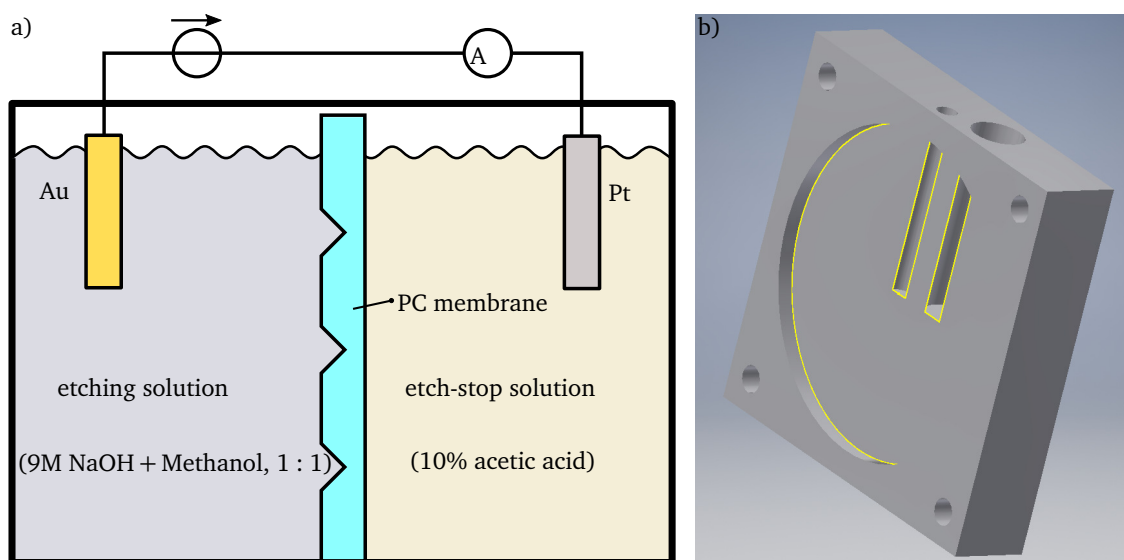


**Figure 5.6:** a) The polymer membrane etches asymmetrically. On the entering side, the etchant solution etches the ion track and at the other end, the etch stop solution will slow down the etching process, as soon as the channel opens.  $V_b$  is the etch rate of non-irradiated bulk material in the etch solution.  $V_b$  is much less than the transversal and the lateral etch rates, ( $V_t$  and  $V_l$ ), in the ion track area. b) 3D model of a half etch cell. The cell has a round shape with 60 mm diameter. There are two openings at the top: one for passing the electrode connector and one for the fluid inlet/outlet. Two half-cells are fixed with four screws and the membrane in between seals the bath.

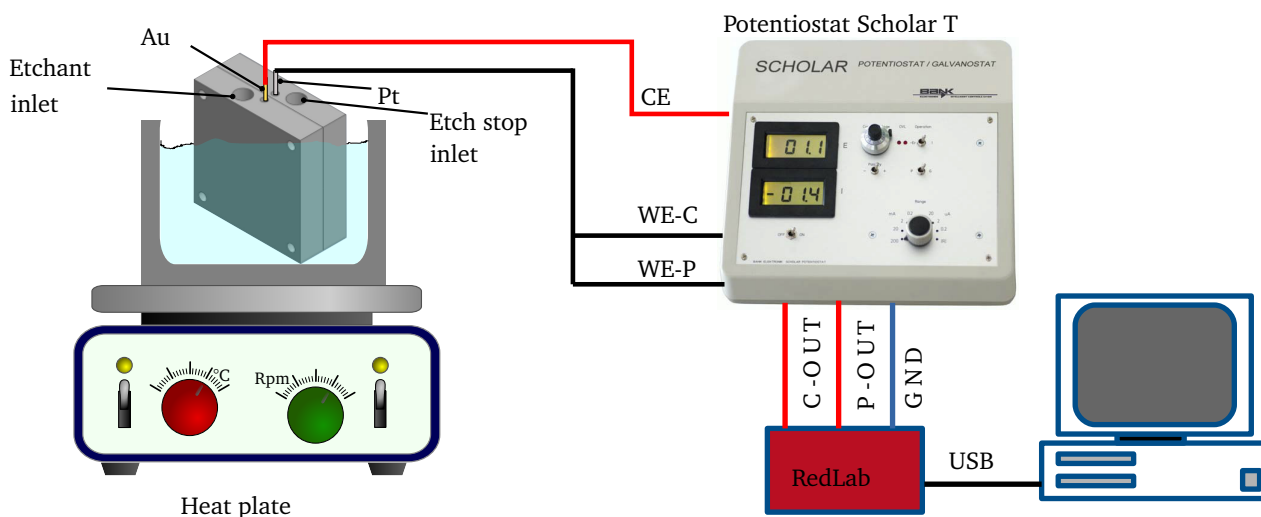


**Figure 5.7:** Membrane etching configuration. The etch cell is immersed in a heated water bath. The transmembrane voltage is applied by a potentiostat Scholar T. Current and voltage measurements are done through an 8bit Meilhaus RedLab 1208 LS digital data logger

### 5.3 Geometry control of micro cones

The etching rate of a polymer depends on the parameters such as material, etchant composition, temperature, etc. The etching rate of the ion-tracks in an irradiated polymer depends on the same parameters and

also irradiation conditions. By controlling these parameters, the base and tip sizes of the cones can be tailored. These parameters are:

- Irradiation and post-irradiation conditions,
- Sensitivity of polymer material,
- Etch temperature,
- Transmembrane voltage,
- Etchant solution,
- Etching time,
- Mechanical stress in biaxially oriented membranes,
- Hydrostatic pressure on one side of the membrane.

In this thesis, a commercial PC membrane is used. So, the two first parameters are assumed as constants. By using the same cell for etching the tracks, the mechanical stress in all cases is identical. During the investigations, a constant combination of parameters is considered as initial process parameters, which are listed in Table 5.1. Then, the investigation continues by varying each parameter from its initial value

**Table 5.1:** Defined initial membrane etch parameters

Parameter	Value
Transmembrane voltage	1 V
Etching solution	9M NaOH + Methanol; Composition not defined
Etch stop	10% acetic acid
Etch temperature	33 °C
Stop criteria	Ion current; value not defined

while keeping other parameters constant. The target values are the base diameter about  $2\mu\text{m}$  to  $3\mu\text{m}$  and a tip radius less than 400 nm. A diameter over  $3\mu\text{m}$  with a wire density of  $1.6 \times 10^6 \text{ cm}^{-2}$  is not desired, because a minimum distance between the emitting structures must be kept. For the stop criteria, two methods are tested. One is the pH measurement to detect the opening of the channels by detecting changes in the pH value. As all the channels do not open at the same time, it is not accurate to use the pH measurement for monitoring the channels' breakthrough time and the tip sizes. The second method is monitoring the transmembrane current, which is a much more accurate method. But the measured current is always dependent on the surface area and pores density. Thus, the measured values cannot generally be used for another product with a different pore density.

### Influence of etchant concentration

As mentioned above, the standard etching process for PC membranes since the seventies [99] is to use alkali compositions like NaOH aqueous solution where the hydroxide ions are responsible for the etching. For polymers like polyethylene terephthalate (PET), KOH aqueous solution is being used as the standard etchant. It means, changing the concentration of the  $\text{OH}^-$  ions will modify the etch rates  $V_b$ ,  $V_t$ , and  $V_l$ . A higher alkali concentration means a relatively low track to bulk etch ratio, and a large cone angle results



[106]. Also adding an organic solvent like methanol or ethanol can help to wet the hydrophobic damaged polymer chain tracks with the aqueous NaOH solution. It will speed up the etch process, which will help to tailor the geometry. It can be seen in Figure 5.8 that a higher concentration of ethyl alcohol/water in the etching solution can change the etch rate up to 20 times. In this case for etching PET membranes 5M KOH as the etchant and ethyl alcohol/water solution for increasing the etch rate of the hydrophobic polymer is used. In Figure 5.9, two etch current-time plots of identical PC membranes with 0% and 50% methanol

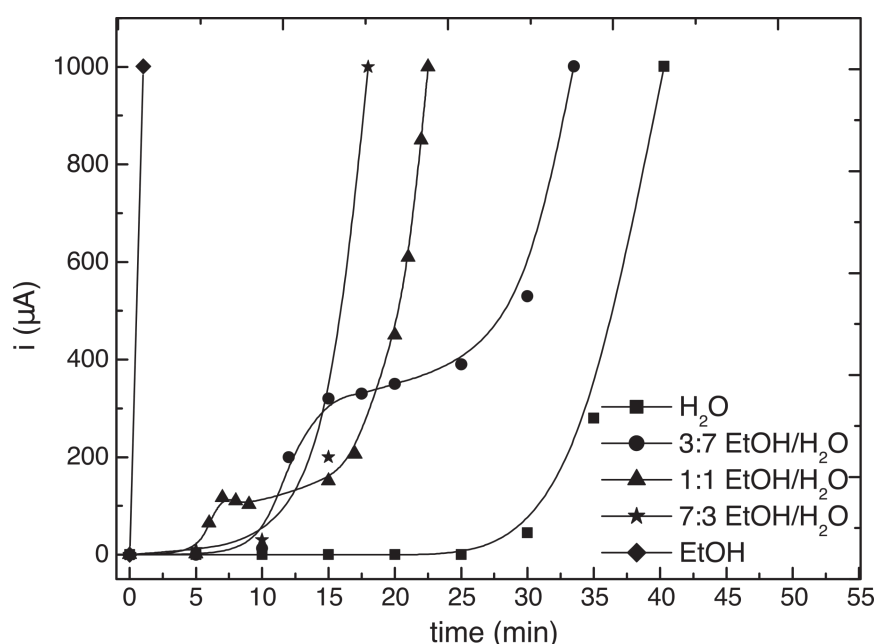


**Figure 5.8:** Comparing the measured current versus time curves by etching a PET membrane with different ethyl alcohol/water concentrations in the etching solution. 5M KOH is used as the etchant and 30V trans-membrane voltage is applied. It can be seen that a maximum ion current of 1 mA is reached faster by increasing the concentration of the alcohol in the etching solution. Pore density is  $1 \times 10^6 \text{ cm}^{-2}$  and membrane thickness is  $12 \mu\text{m}$  [101].

proportion of the etchant are shown. It is observed that adding methanol to the solution will speed up the etch process of the PC membranes like the etch process of the PET membrane. Reaching a higher ion current at a shorter time means more channels are opened faster. Simultaneously using methanol makes it possible to reach channels with the same geometry. Otherwise, as shown in Figure 5.9c the apex angles of neighbor cones are not similar. In Figure 5.10, some results of etching PC membrane with different Methyl alcohol concentrations are shown. In some samples, the cones are fabricated and in some cases, the membrane is just metalized and an SEM measurement is performed.

**Zero or low methanol proportion:** As mentioned above, by using no methanol or using just 33% Vol methanol in the etching solution, not just the etch time is longer, but also tailoring the geometry of the cones by etchant concentration is not user friendly. In almost all samples, an electrochemical deposition was not successful. The reason is the inhomogeneous breakthrough of the channels. In many channels, the tip openings are very narrow while other openings are much wider. Very narrow openings lead to insufficient ion diffusion into the conical channel with a relatively large volume. This insufficiency leads to ion depletion. Thus, not all the cones are grown, or the structures are not complete. Such a structure is

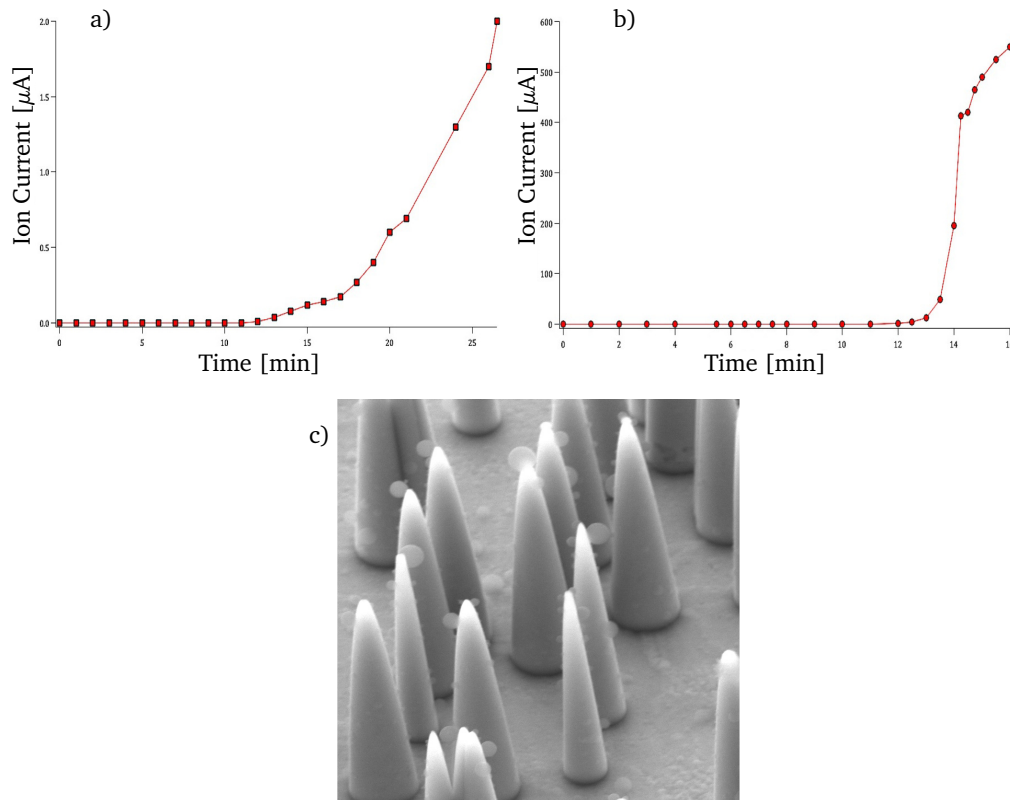


**Figure 5.9:** Measured current vs. time. a) Using etchant with 0% methanol reaches 2  $\mu\text{A}$  in 25 min. b) With etchant containing 50% methanol a 600  $\mu\text{A}$  ion current is reached within 16 min; Both samples are etched at  $\theta=40^\circ\text{C}$  by applying 1 V transmembrane voltage. The surface area is about 1.8  $\text{cm}^2$  c) Microcones with different diameters and apex angles in one sample. This happens when the membrane is not getting wet homogeneously and the channels open at different times or the polymer irradiation is not taken place homogeneously

shown in Figure 5.10a.

**50% or higher methanol proportion:** With a methanol concentration of about 80% the reached base size is smaller than the base size reached with 33% concentration. But the tip sizes with 80% concentration are larger than with 33%. Also, in a manual device, it is not easy to control the process, due to high temperature sensitivity and a higher etch rate with 80% concentration. Thus, it has decided to continue the process with 50% concentration and try to tailor the geometry by controlling the temperature and the ion current. It is worth mentioning, that with a different methanol concentration, the ion concentration changes too. So, the measured ion currents as a stop criteria are not always identical and they cannot be used as valid values for the desired concentration. With 50% methanol concentration and stopping at different currents a base diameter about 3 to 4  $\mu\text{m}$  is reached. The tips are below 400 nm and almost all tips on one sample are in the same size range. Therefore, it is possible to deposit the structures without observing any problem due to metal ion depletion.

By performing these tests, it is observed that the temperature fluctuation has a great impact on the base and tip sizes. This shows that the etch rate is extremely temperature sensitive. It means tailoring the geometry of the cones by controlling the temperature is more effective than trying to tailor the geometry by changing the etchant concentration.

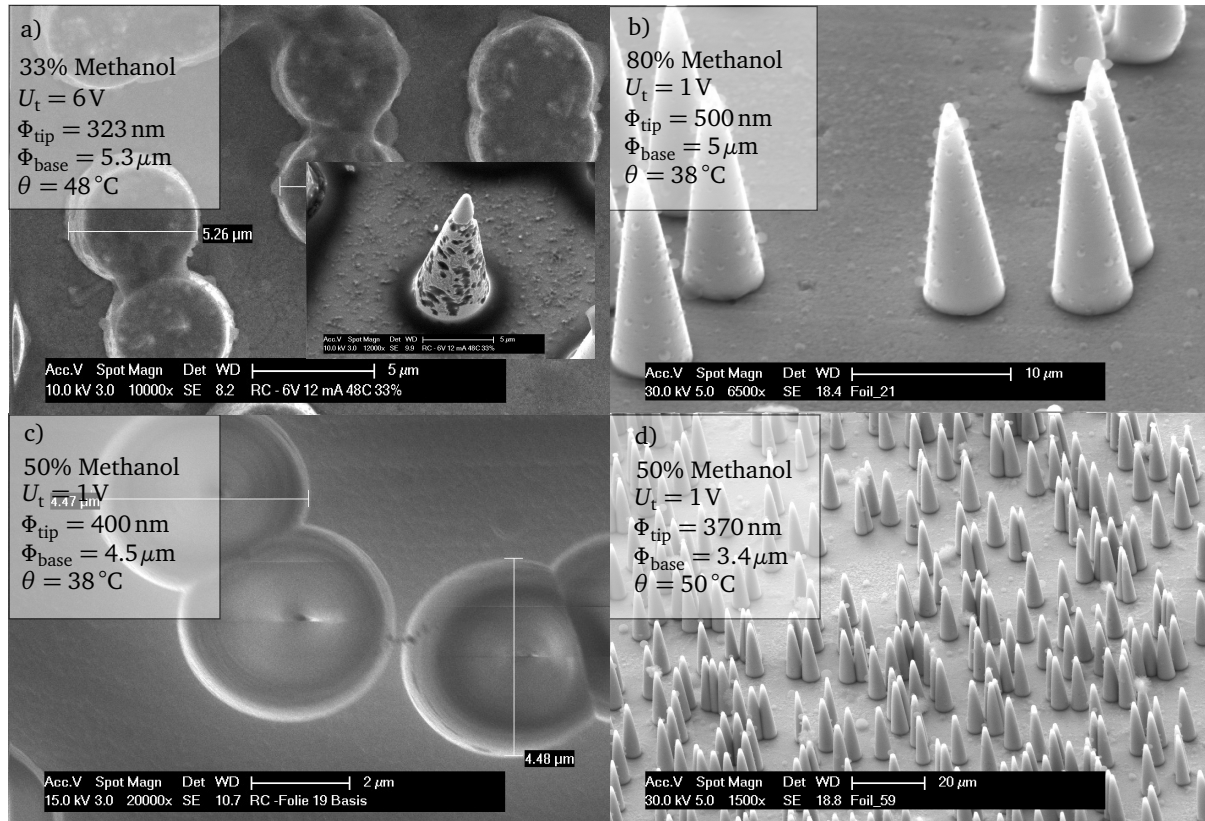


**Figure 5.10:** Results of etching a  $25\ \mu\text{m}$  thick PC membrane with  $1.6 \times 10^6\ \text{cm}^{-2}$  tracks density a) 33% methanol proportion. In this case and the case of a lower percentage volume of methanol, the etch rate in the hydrophobic PC is low and the conical channels do not open simultaneously. Not all the cones are grown completely or homogeneously. This happens because of high ion depletion in the channels. This is because of very narrow openings less than  $30\ \text{nm}$ . The measured bases are between  $5$  to  $7\ \mu\text{m}$ . b) Using  $80\ \text{Vol}$  methanol gives smaller bases in the channel breakthrough time, and the tip sizes can reach a proper size simultaneously. This enables homogeneous electrodeposition on a large surface. c) A SEM image of a PC membrane etched with  $50\ \text{Vol}$  methanol. This process has a proper etch rate for a manual device and the bases are below  $5\ \mu\text{m}$ . d) Etching at a higher temperature with  $50\ \text{Vol}$  gives a base diameter below  $3.5\ \mu\text{m}$  while the tip is about  $400\ \text{nm}$ .

### Influence of temperature on pore sizes

As the next variable, the influence of the temperature on the base sizes is explored. For this process, the concentration of the etchant is kept constant. It is expected that an increase in the etching cell temperature accelerates the etch rate [102]. To keep the temperature in the etch cell constant at the desired value, the etch cell is immersed in a water bath with a controlled temperature. The  $50\%$  etch solution and the etch stop are both heated up to the experimental temperature simultaneously in the same bath. In Figure 5.11, the measured times of reaching  $2\ \text{mA}$  ion-current as a function of bath temperature is shown. It can be seen that the breakthrough time decreases at higher temperatures, which means higher transversal etch rates  $V_t$ . At higher temperatures, the lateral etch rate  $V_l$  increases as well. But still, the reached base diameter is smaller at the moment that the channels open.

In Figure 5.12, the SEM images of two PC membranes with a track density of  $1.6 \times 10^6\ \text{cm}^{-2}$  are shown. These membranes are etched at different temperatures. For a temperature of  $35\ ^\circ\text{C}$  the resulting base

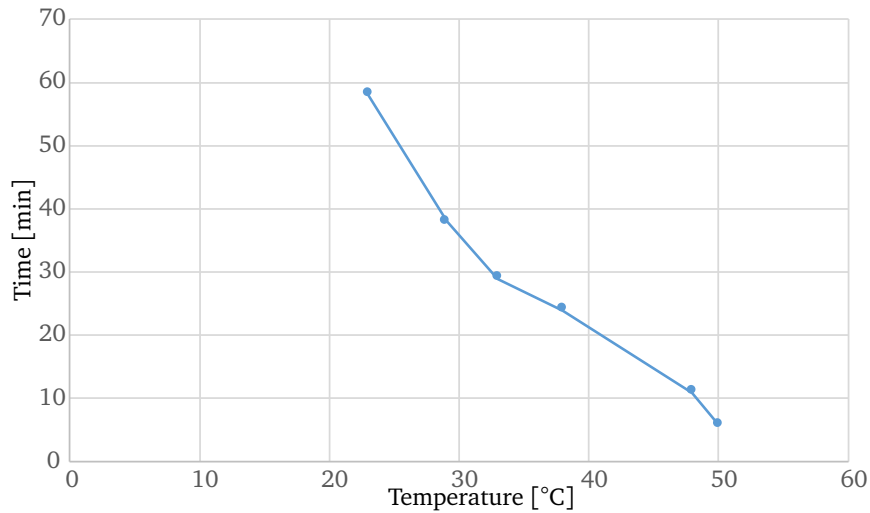


**Figure 5.11:** The measurement shows that the breakthrough time of the channel by asymmetric etching depends on the temperature.

diameter is about  $3\mu\text{m}$ , as shown in Figure 5.12a. It can be seen that at temperatures below  $30^\circ\text{C}$ , the

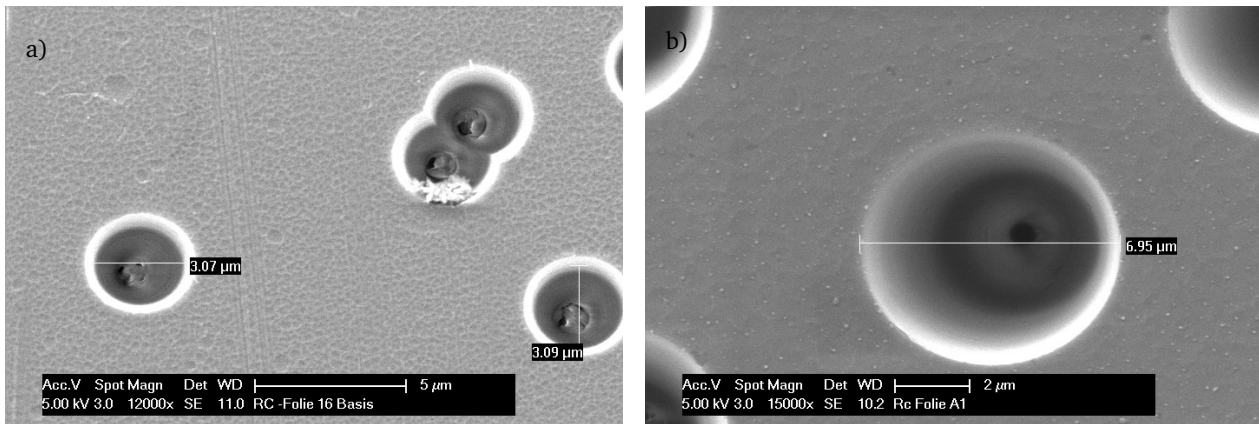


**Figure 5.12:** SEM images of two etched membranes with the standard etching parameters and different temperatures. a) Base diameter of  $3\mu\text{m}$  at  $35^\circ\text{C}$ . b) Base diameter of  $7\mu\text{m}$  at  $23^\circ\text{C}$ . [8]

etch process takes more than 40 minutes. It leads to a base diameter of about  $7\mu\text{m}$  as shown in 5.12b, for an etch process at room temperature. This allows us to vary the base diameter, and in this way, the apex angle of the cones as desired. At temperatures above  $50^\circ\text{C}$ , the etch process is very fast, and the changes in the current occur rapidly. It is hard to control the tip diameter with a manual current monitoring setup. So,  $50^\circ\text{C}$  is chosen for further process development. In an automatic device, this temperature can be increased to speed up the etch process.

### Influence of transmembrane voltage and etch stop at different maximum currents

As mentioned above, the measurements at different temperatures are stopped at a constant maximum ion current of  $2\text{mA}$ . To reach sharper tips with smaller radii, the correlation of the maximum ion-current during the template etch process, and the resulting cones' tips are explored. For this, the etch process is stopped at different maximum ion currents, while the applied transmembrane voltage of  $1.0\text{V}$  and temper-

ature of 50 °C are kept constant. Ion current curves concerning the etch time are shown in Figure 5.13. At a temperature of 50 °C, the nanopores open after about 5.5 min and a rapid increase of the ion-current

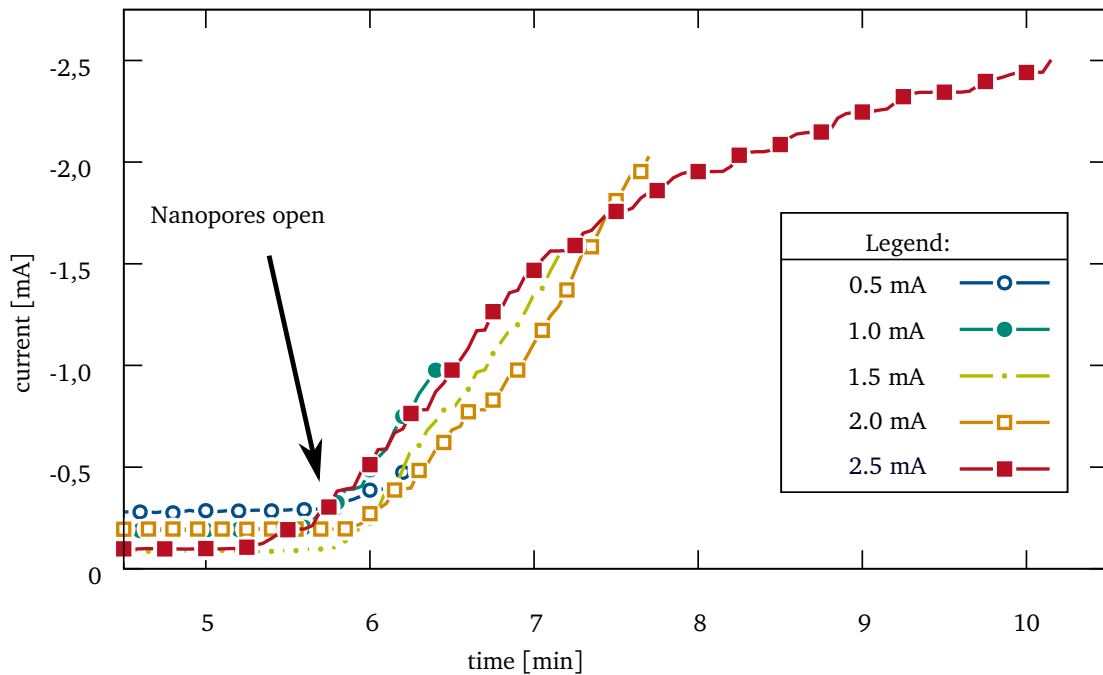


**Figure 5.13:** Measured ion current curves during the template etch process at 50 °C, by an applied voltage of 1.0 V [8].

can be observed. Slight differences in the opening times can be explained by the small fluctuation of the temperature. Above circa 2.0 mA, the slope of the current decreases, because of the decrease in the etch rate, as the etching takes place beyond the halo region [95]. The same process is repeated with a lower transmembrane voltage of 0.75 V and for the same current ranges as the previous experiment. In Figure 5.14, some resulting cones of each experiment are shown. It can be seen that for both voltages, the base diameter variations are small. But sharp tips with smaller radii can be reached by controlling the maximum ion current. The expected and planned goal of this thesis, base diameters of 2 to 3  $\mu\text{m}$  and tip radii less than 400 nm are reached. The tip radius is under control by monitoring the maximum ion current, while the temperature has low fluctuation during the process. By limiting the maximum ion current to 1.0 mA and the transmembrane voltage to 1 V, we are able to fabricate cones with an average tip diameter of about  $(115 \pm 20)$  nm. Thus, the fabrication and measurement of field emission can be performed on such cones with higher thermomechanical stability, compared to cylindrical nanowires.

## 5.4 Fabrication of micro cones

For the synthesis of the metallic cones, the in-situ process for structuring metallic vertical nanowires presented in Chapters 3 and 4 are used. The fabrication steps of nanocones are shown schematically in Figure 5.15. In this process, the conical-etched template membrane is fixed on a gilded glass wafer (Step a and Step b). Nanocones grow electrochemically on a predefined electrode (Step c). In this step, the metal ions diffuse in the pores through small openings of the tips. After finishing the deposition, the template



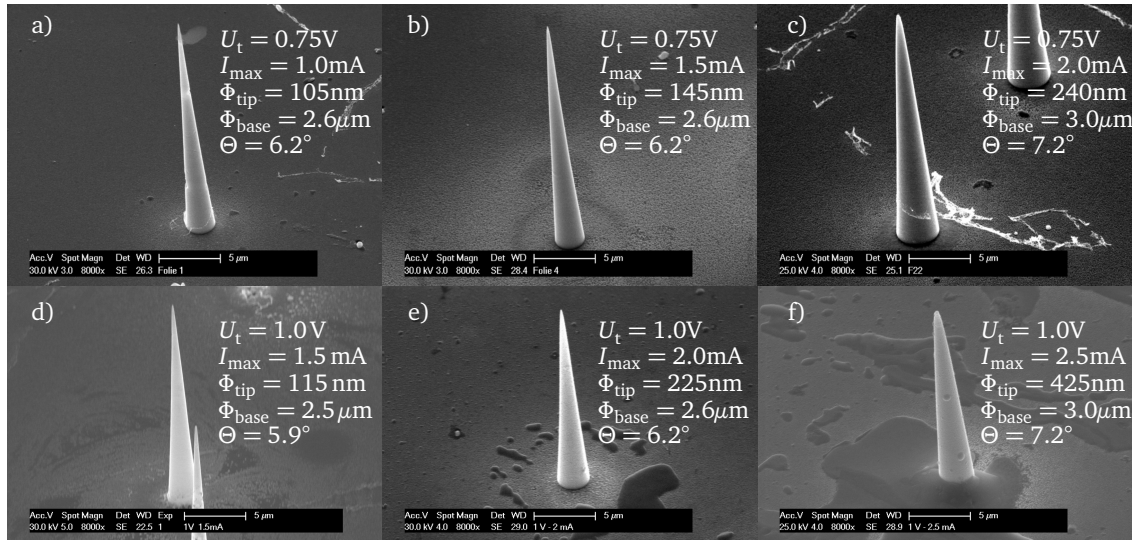


**Figure 5.14:** SEM images of different cones fabricated at different transmembrane voltages  $U_t$  and stopped at different maximum currents  $I_{max}$ . In all images, the slight change in the applied voltage did not show any big difference in the base sizes. But the tip radii change with max ion current. The tip diameter  $\Phi_{tip}$ , base diameter  $\Phi_{base}$  and apex angle  $\Theta$  of the cones are given. [8].

membrane has to be removed (Step d). This is done in a wet chemical step with e.g. dichloromethane or N-Methyl-2-pyrrolidone (NMP). Using this methodology enables the deposition of nanocones with different

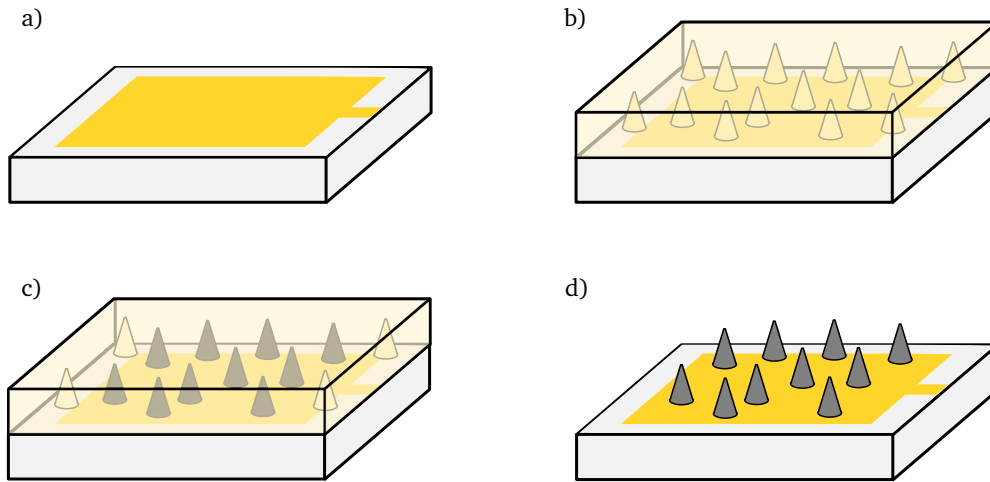


**Figure 5.15:** a) Glass-substrate with pre-defined gold electrode b) Fixed PC-template with conical pores on the electrode. c) Deposition via electro-plating through the small tips d) Removing the PC-template [8].

densities on a surface of ca.  $100 \text{ mm}^2$ . In Figure 5.16, nanocones made of gold and nickel fabricated with a density of  $2 \times 10^6 \text{ cm}^{-2}$  and different cone geometries with a  $7 \mu m$  large base and a  $3.5 \mu m$  base diameter are shown. The cones are homogeneously distributed and equally sized over a larger area. But for applications based on field-emission the electrostatic screening, which occurred due to high track density about  $2 \times 10^6 \text{ cm}^{-2}$ , is unfavorable. The appropriate pitch of the cones for an optimal emission should be the same as their height [6]. To reach this pitch size, a membrane with a track density of  $6 \times 10^4 \text{ cm}^{-2}$  for further experiments is used. Furthermore, the electric field enhancement factor of the

nanocones depends inversely on the tip radius and the apex angle of the cones. Thus, to optimize the field enhancement, a minimal tip radius and a low apex angle of cones are desired. This is discussed in Chapter 2. Etching such membranes are already achieved in Section 5.2.

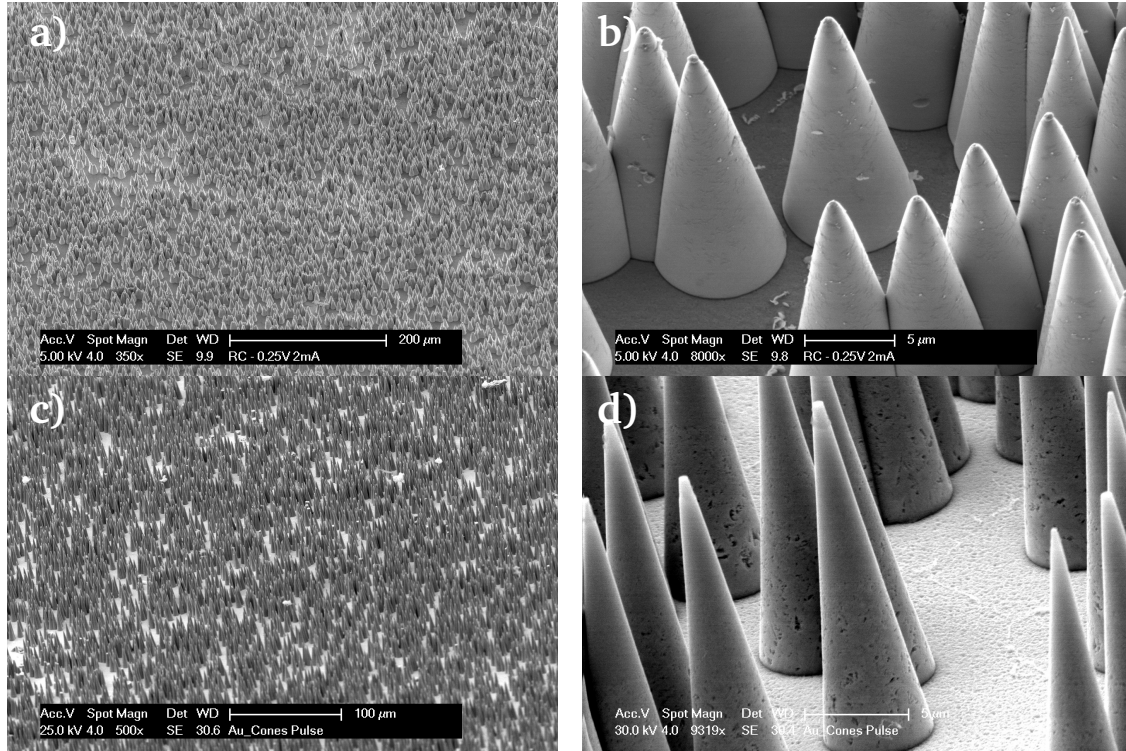


**Figure 5.16:** SEM images of deposited nanocones with different geometries on large area surfaces. The surface roughness is  $\pm 0.2 \mu\text{m}$ . Images a) and b) Nickel nanocones with 700 nm tip and  $7 \mu\text{m}$  base diameter, i.e. an apex angle of  $16.6^\circ$ . Images c) and d) Gold nanocones with 400 nm tips and  $5 \mu\text{m}$  base diameter, i.e. an apex angle of  $8.4^\circ$  [8].

For the synthesis of these cones two major challenges are faced:

- The first challenge is to prevent the depletion of the electrolyte. As mentioned previously, the depletion is a result of the low diffusion through the pores' tips. To solve this issue, the pulse reverse plating is used [107]. The principle of this method is discussed in Chapter 3 for the synthesis of cylindrical wires. The nanocones shown in Figure 5.15 are made of gold. These are obtained by using an ammonium sulphite gold (I) bath (Metakem Goldbad SF) and reverse pulse plating with  $U_{\text{on}} = -0.6 \text{ V}$ ,  $t_{\text{on}} = 10 \text{ ms}$ ,  $U_{\text{off}} = -0.05 \text{ V}$ ,  $t_{\text{off}} = 40 \text{ ms}$  at a constant temperature of  $60^\circ\text{C}$ . Identically nickel nanocones were grown by reverse pulse plating with  $U_{\text{on}} = -0.9 \text{ V}$ ,  $t_{\text{on}} = 10 \text{ ms}$ ,  $U_{\text{off}} = -0.45 \text{ V}$ ,  $t_{\text{off}} = 40 \text{ ms}$  at a constant temperature of  $65^\circ\text{C}$  using nickel sulfamate and Boric acid bath described in Appendix A.4.
- The second challenge is to remove the template with a track density in the order of  $1 \times 10^4 \text{ cm}^{-2}$ . By dissolving the PC-membrane with solvents such as dichloromethane or NMP, the membrane shrinks, and folds. It pulls off the tips of the cones. Therefore, plasma ashing is used because it is a much less stressful process and removes the membrane layer by layer. A Muegge R3T plasma system at the power of 1000W and gas ratios of O<sub>2</sub>: 1000 sccm, N<sub>2</sub>: 50 sccm, and CF<sub>4</sub>: 50 sccm at a temperature of  $21^\circ\text{C}$  is used. At higher track densities of about  $1 \times 10^6 \text{ cm}^{-2}$ , the ratio of the polymer volume

to the volume of the grown metallic structures is lower. This lower ratio forces less shear stress on the cones. Subsequently, no defect in the structures by using wet etching was observed, see Figure 5.16.

With this method, also the deposition of nanocones with a cone density of  $6 \times 10^4$  cones per  $\text{cm}^2$  over a large area is possible. In Figure 5.17, nickel nanocones deposited on an electrode with an area of  $100 \text{ mm}^2$  are shown.

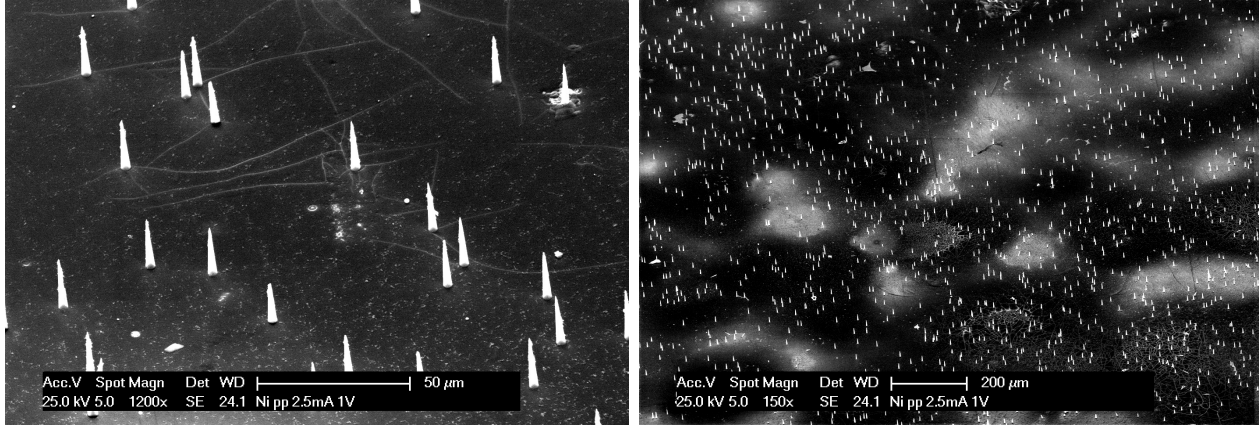


**Figure 5.17:** SEM images of nickel nanocones ( $I_{\text{max}}=2.5 \text{ mA}$ ,  $U_t=1.0 \text{ V}$ ). The nanocones are vertically aligned and homogeneously distributed over a large area. The color contrast on the surface is due to the varying thickness of the deposited nickel layer on the starting gold layer [8].

## 5.5 Conclusion and outlook

In this chapter, it is shown that by using the described methodology, the in-situ growth of nanocones with variable geometry on a large surface area is achieved. A variety of available geometries and materials with template track densities of  $2 \times 10^6 \text{ cm}^{-2}$  and  $6 \times 10^4 \text{ cm}^{-2}$  are presented. The cones can be deposited directly on any metallic surface and thus the method gives the possibility to produce pure metallic components. This reduces the outgassing and makes the method suitable for vacuum applications. From now on, the focus of further investigations will be the long term field emission tests and improvement of the emission properties in cryogenic ambient.

To improve the fabrication process of conical structures and their synthesis (e.g. to reach lower tip diameter and apex angles), detailed investigations on the impact of the plating conditions, such as applied voltage, duty ratio, and temperature, must be done. Using the process introduced in Chapter 3, in comparison to the common fabrication methods, allows the direct integration of the nanocones in a 3D microsystem. The membrane etch process is a sensitive one and the achieved results in this thesis must be adjusted in new investigation with new membranes with different polymer material, irradiation energy, or different etch device geometries, sizes, and tensile forces on the membrane. Also, temperature fluctuations should be prohibited in a semi-automatic device with automatic injection of pre-heated etchant. It means an automatic injection and evacuation of etching fluids and also a cleaning process for a more precise result is needed.



---

## 6 Field emission of micro cones and nanowires

---

In this chapter, the field emission properties of metallic microwires and micro cones, fabricated with the introduced techniques in this thesis, will be measured and discussed. Some parts of this chapter are published in [9] and [10]. The samples are prepared at the Institute of Electromechanical Design (EMK) at the Technische Universität Darmstadt. The measurements are performed at the Department of Field Emission at the University of Wuppertal, and also at the Faculty of Applied Natural Sciences and Cultural Studies at the University OTH-Regensburg. I am grateful to Prof. Dr. Günter Müller, Dr. Pavel Serbun, Prof. Rupert Schreiner and Christoph Langer.

---

### 6.1 Optimizing the nanowire structures and preparing the samples

---

Due to the Nottingham effect (see Section 5.1.1) and thermomechanical instability of the nanowires, the field emission measurement of the nanocones is focused on in this thesis. However, the metallic nanowires are advantageous, compared to the nanocones, in terms of their fabrication steps and controlling their emitting apex diameters. To combine the advantageous thermomechanical stability of the cones and the desired constant apex diameters of the wires all over the sample an experiment is designed. In this experiment, an already cylindrically etched membrane is etched again asymmetrically at one side of it for a short time. It gives a semi-conical shape at one end of the wires, and the cylindrical geometry at the apex is not changed. Thus, less metal will be deposited during the electrochemical deposition process, and the depletion problem does not occur. An array of such semi-conical wires are shown in Figure 6.1. The membrane etch process is done in the same etch device introduced in Chapter 5. For performing the

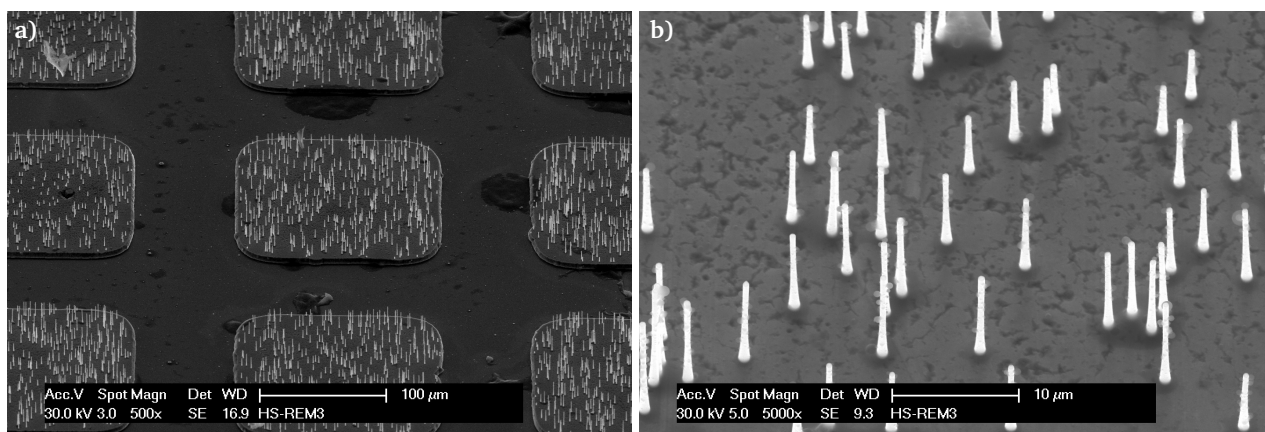


**Figure 6.1:** Copper nanowires with conical base. a) An array of semi-conical wires. Such wires can be deposited by less ion depletion compared to the conical structures with a larger volume of metal deposition. b) The conical bases of the sample are  $1\mu\text{m}$  while the apexes are  $400\text{ nm}$ .

initial field emission measurements of the nanocones, the first samples are prepared with a high density template membrane. The etch process for these samples is done with the standard 50% etchant solution and a 10% acetic acid as etch-stop at  $50^\circ\text{C}$  without applying any transmembrane voltage and for two minutes with no current measurements.

### 6.1.1 Fabricated samples

Based on this process, the following samples are prepared:

#### Sample No.1

The SEM images of this sample are shown in Figure 6.2. This sample consists of gold nanocones with a

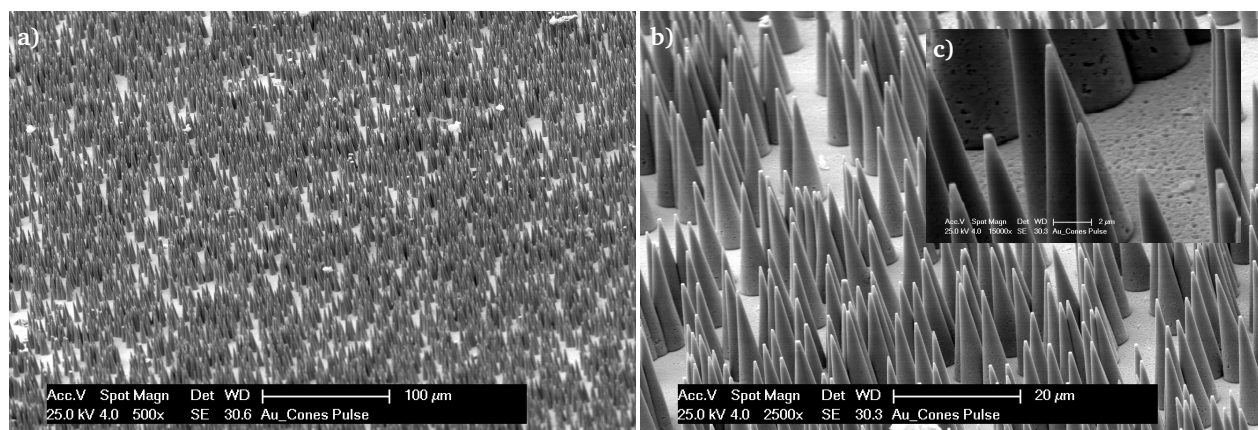


**Figure 6.2:** Sample No.1. Gold cones. a) The sample with a large area completely covered with nano cones without no defects. b) The cones have  $25\mu\text{m}$  height,  $5\mu\text{m}$  base diameter and  $300\text{ nm}$  apex diameter. The cone density is  $1.6 \times 10^6\text{ cm}^{-2}$ . c) The tips of some cones are flattened. This happens when the deposition process is stopped short before an overgrowth appears.

height of  $25\mu\text{m}$ , a base diameter of about  $5\mu\text{m}$  and an apex radius of  $150\text{ nm}$ , which are fabricated with the pulse reverse deposition process. A challenge in the electrochemical deposition of conical samples is to reach the sharpest apex by stopping the deposition process at the right time. By stopping the deposition process, while the cones are not grown completely, the apexes will be flat, and it does not give a sharp or rounded shape. Nanocones of sample No.1 with flat apexes can be seen in Figure 6.2c. In this sample, the process is stopped shortly before the cones are completely grown. By continuing the deposition process, a mushroom shaped overgrowth would appear on the apexes. Although removing these overgrowths on the apexes is possible, it is not a practical and desired solution. Furthermore, a slight length deviation of less than  $1\mu\text{m}$  can be observed. It means by continuing the deposition, some cones will overgrow while some cones are not completely grown.

#### Sample No.2

This sample consists of gold semi-conical wires (see Figure 6.3). The advantage of this sample is the constant apex diameter all over the sample. The diameters of the bases are  $1\mu\text{m}$  and the apexes have a diameter of about  $400\text{ nm}$  while the height is  $25\mu\text{m}$ .

#### Sample No.3

This sample is shown in Figure 6.4. This sample is a conical gold sample with an apex diameter of  $400\text{ nm}$

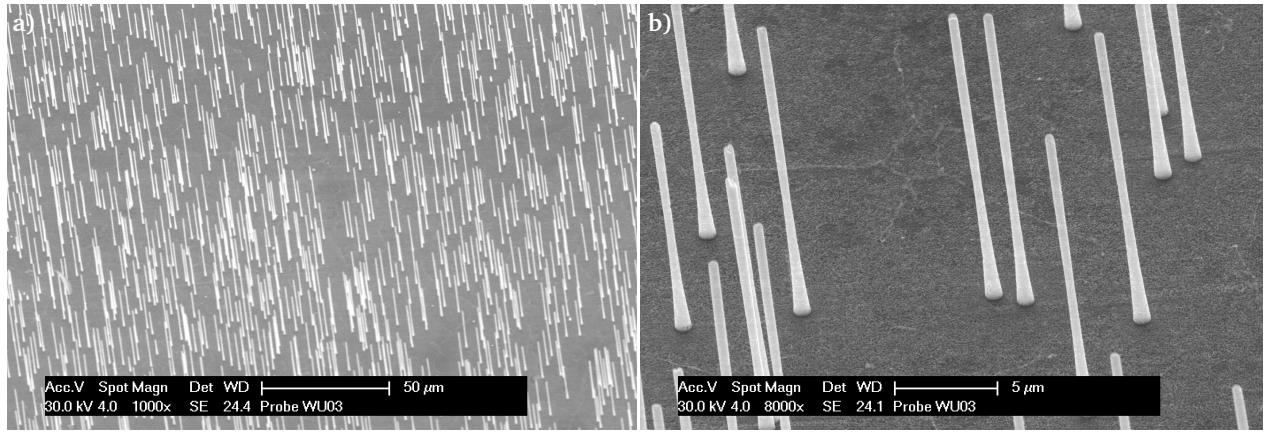


**Figure 6.3:** Sample No.2. Gold semi-cone wires with  $25\mu\text{m}$  height,  $1\mu\text{m}$  base diameter and  $400\text{ nm}$  apex diameter. The wires density is  $1.6 \times 10^6\text{ cm}^{-2}$

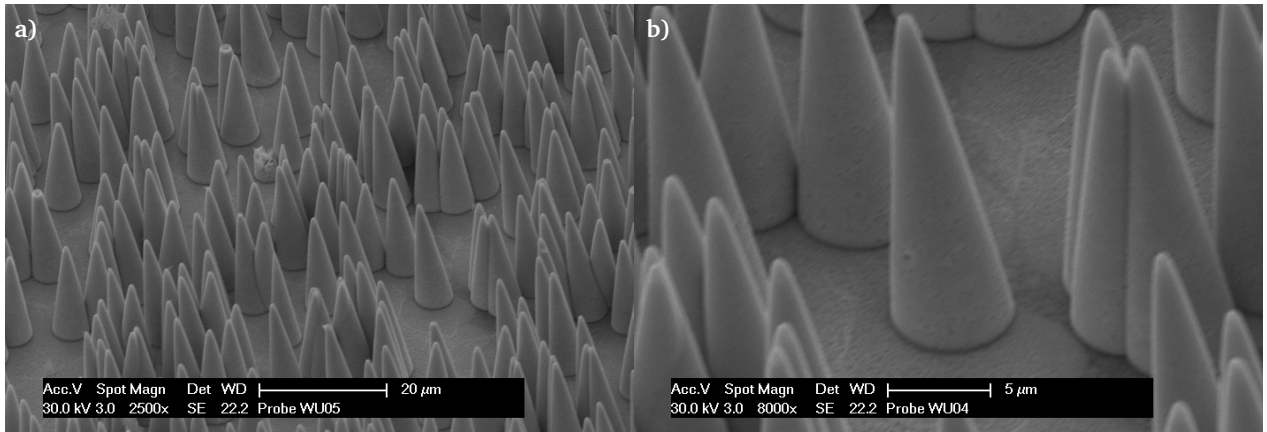


**Figure 6.4:** Sample No.3. Gold cones with  $25\mu\text{m}$  height,  $6\mu\text{m}$  base diameter and  $400\text{ nm}$  apex diameter. The cones density is  $1.6 \times 10^6\text{ cm}^{-2}$

and a base diameter of  $6\mu\text{m}$ . This structure has mostly rounded apexes and in some areas, the apexes are slightly overgrown. Most of the overgrown mushrooms are removed before stripping the sample.

#### Sample No.4

The last sample selected for the measurement is shown in Figure 6.5. This sample is a defect sample. The deficiency in this sample can be explained by the depletion of the ions in the channels. A similar defect appears in samples with lower cone density due to the impact of mechanical tensions from the PC membrane during the stripping step. This impact is usually higher in a porous polycrystalline material. An example of such samples is shown in Figure 6.6. Sample No.4 has a base diameter of  $6\mu\text{m}$ , but the cones are broken and the apexes are not available. The polycrystalline gold gives many sharp tips on the surface of the structures. Such tips can emit electrons, which makes this sample interesting for field emission measurement.



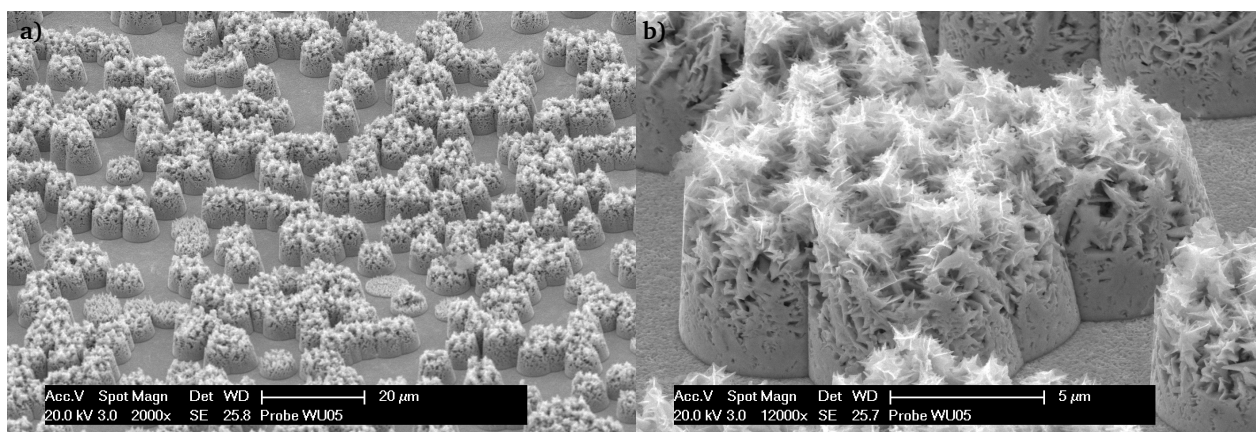


**Figure 6.5:** Sample No.4. uncompleted gold cones with  $6\mu\text{m}$  base diameter. The polycrystalline structure of the gold has given a surface covered with many sharp apices. The density of cones is  $1.6 \times 10^6 \text{ cm}^{-2}$

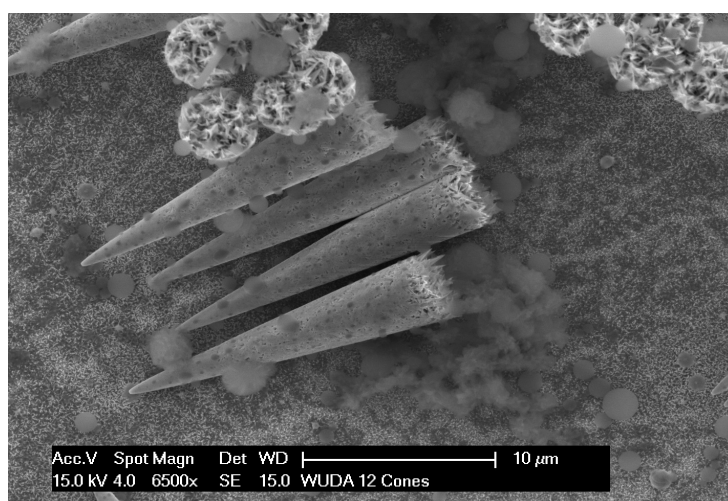


**Figure 6.6:** Broken apices of gold conical structures. This happens during removing the template membrane by mechanical stress from the polymer on the fragile structure with a porous polycrystalline structure.

### 6.1.2 Profilometry of samples

The topographies of the selected cathodes are measured using an optical scanning device, MicroProf®, of Fries Research & Technology GmbH company. The resulted measurements are shown in Figure 6.7. This device can perform 2D and 3D topographical measurements using the principle of chromatic aberration. In this technique, the incident white light reflects from the surface. The spectral distribution of the reflected light depends on the height of the structures on the surface. The spectral distribution can be measured by a lens with different refractive indexes. The device has a lateral resolution of  $2\mu\text{m}$  and a vertical resolution of  $2\text{ nm}$ . Compared to the samples presented in [94] and [108] with a surface roughness of  $3\mu\text{m}$  to  $5\mu\text{m}$  on  $(5 \times 5) \text{ mm}^2$  surface, the measurements on all samples prepared show a homogeneous surface roughness of  $\pm 0.8\mu\text{m}$  all over the samples.

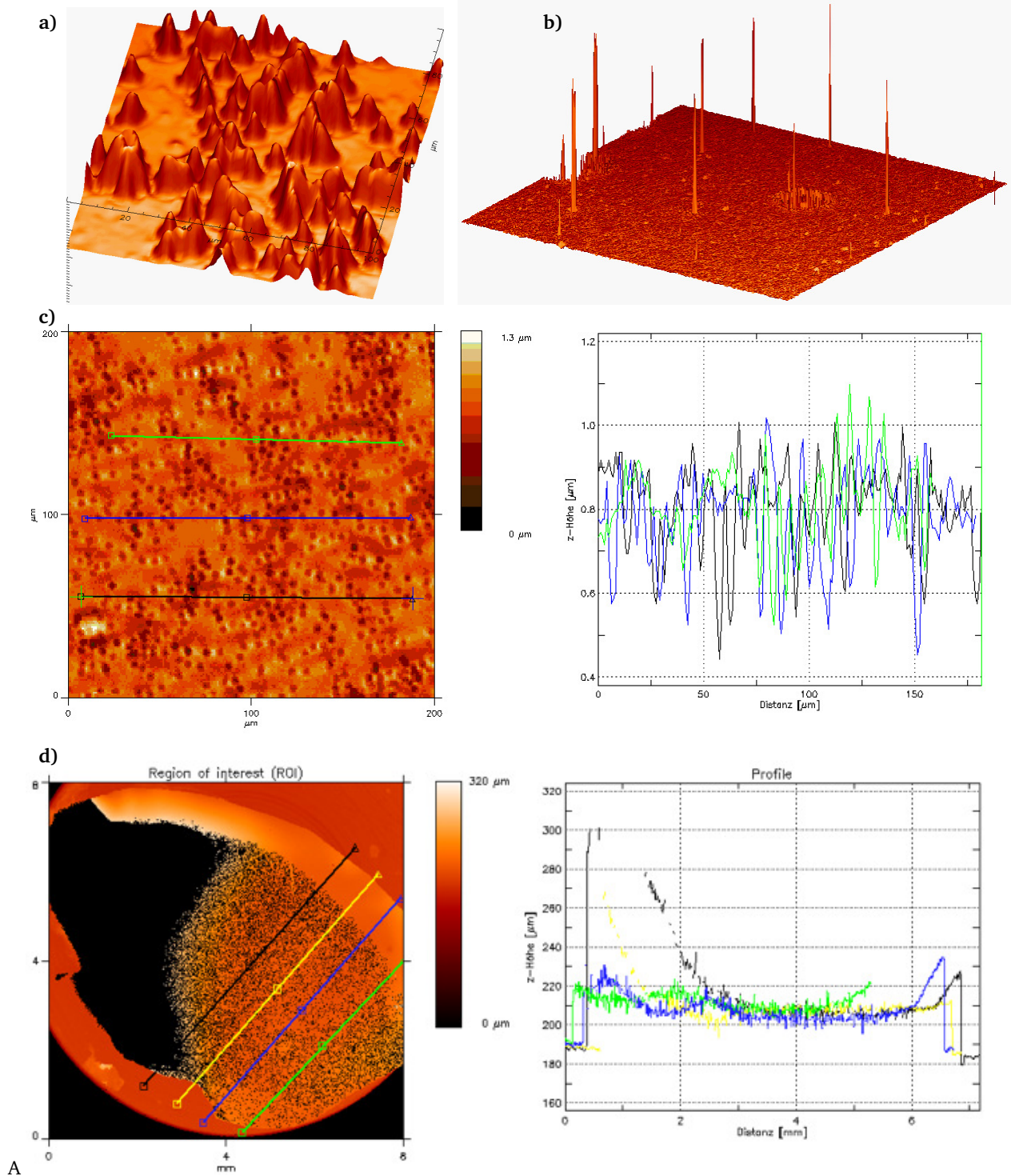


**Figure 6.7:** a) The measured topography of sample No.1. b) Topography of sample No.2. c) The surface roughness measurement of sample No.2 at the region of interest. All over the surface, the maximum roughness is about  $\pm 0.8 \mu\text{m}$ . This value is valid over the entire sample with a surface of  $(10 \times 10) \text{ mm}^2$ . d) Measurement on the stuck samples of other groups with an edge length of 6 mm. In addition to the roughness, the sample shows a waviness of about  $\pm 90 \mu\text{m}$  in the region of interest. The waves appear by placing and sticking processes on the substrate [108].

## 6.2 FE properties of high density cones

For measuring the FE properties of the samples, the emission current  $I$  by a known gap between anode and cathode is measured as a function of applied voltage  $V$ , or applied electrical field  $E$ . This measurement is done by sweeping the voltage up and down. The measurements on samples No.1 to No.4 are done in two different measurement devices, which are explained in the next section.

Sample No.1: The FE measurement of this sample is performed in a *Field Emission Scanning Microscope* (FESM). This device is a unique microscope for measuring the FE properties of emitters. It is shown schematically in Figure 6.8. The sample is installed on a stage below a tungsten anode in a vacuum

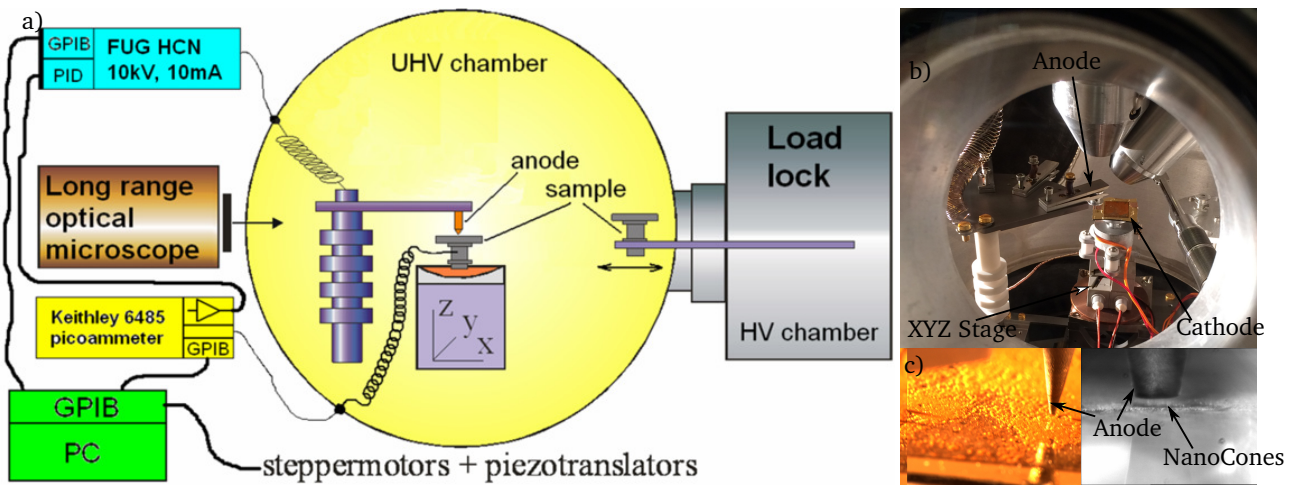


**Figure 6.8:** a) Schematic image of the FESM device [109]. b) Sample No.1 is mounted in FESM on an XYZ piezo translator stage. c) Anode with a controlled distance over the sample. Anode is a tungsten tip with  $360\mu\text{m}$  apex diameter.

chamber with a pressure of  $10^{-9}$  mbar. The power supply HCN 100M of the company FUG Elektronik GmbH, controlled with a PID controller, provides a DC voltage up to 10 kV and a maximum current of 25 mA. The FE current between 20 fA to 20 mA is measured with a Keithley 6458 multimeter. The constant gap  $\Delta z$  between the anode and the cones is controlled with a long-distance microscope (Questar QM 100,  $1\mu\text{m}$  resolution), and the actual electric field for a voltage map is calculated as the ratio of applied voltage  $V$  to  $\Delta z$ , while the stage during the FE measurement moves. In this device, there are two possibilities to perform a measurement. One is to scan the emitting surface while the gap is kept constant. It gives a current emission map over the surface without considering the impact of the screening effect. The other possibility is to scan over the surface while the gap is changed to keep an emission current of 1 nA constant. This measurement gives a map of the on-set field  $E_{\text{on}}$  for all emitting objects without considering the impact of the screening effect. The measured  $I$ - $E$  curves of sample No.1 at one area are shown in Figure 6.9. The plot of  $\ln(I/E^2)$  versus  $I/E$  is known as Fowler-Nordheim Plot (FN-Plot). Considering the relation given by (2.22), in the case of a pure FE current flow the FN-Plot is linear and its slope defines the enhancement factor  $\beta$ . Any nonlinear behavior of the FN-Plot can be explained by current leakage or destruction of the tips. The measurement of sample No.1 confirms the linear dependence of the  $\ln(I/E^2)$  to the  $I/E$  during the descending voltage. This measurement is repeated at four different regions of the



sample. During the initial voltage increase at each area, many current fluctuations are observed. These fluctuations are due to the outgassing from adsorbates or partial melting of the apexes of the cones. The stepwise activation and deactivation of nanocones cause hysteresis in the ascending and descending current measurements. It stabilizes the current flow in the succeeding voltage sweeps. The anode in this measurement has a distance of  $60\mu\text{m}$ . The current step at  $80\mu\text{A}$  can also be explained by the stepwise changes in the number of dominant emitters. A current up to  $250\mu\text{A}$  is achieved for the gold cones. The cathode yields an on-set field of  $E_{\text{on}}=27\frac{\text{V}}{\mu\text{m}}$  and the enhancement factor  $\beta=137$ . Measurements at other areas of the same sample show a maximum  $\beta$  of 200 and a minimum  $E_{\text{on}}=22\frac{\text{V}}{\mu\text{m}}$ . The achieved low  $\beta$  value can be explained by the high density and the flat apexes of the cones (see Figure 6.2). For this sample, a stable maximum current of  $100\mu\text{A}$  for 300 s is measured. The other samples (No.2 to No.4)

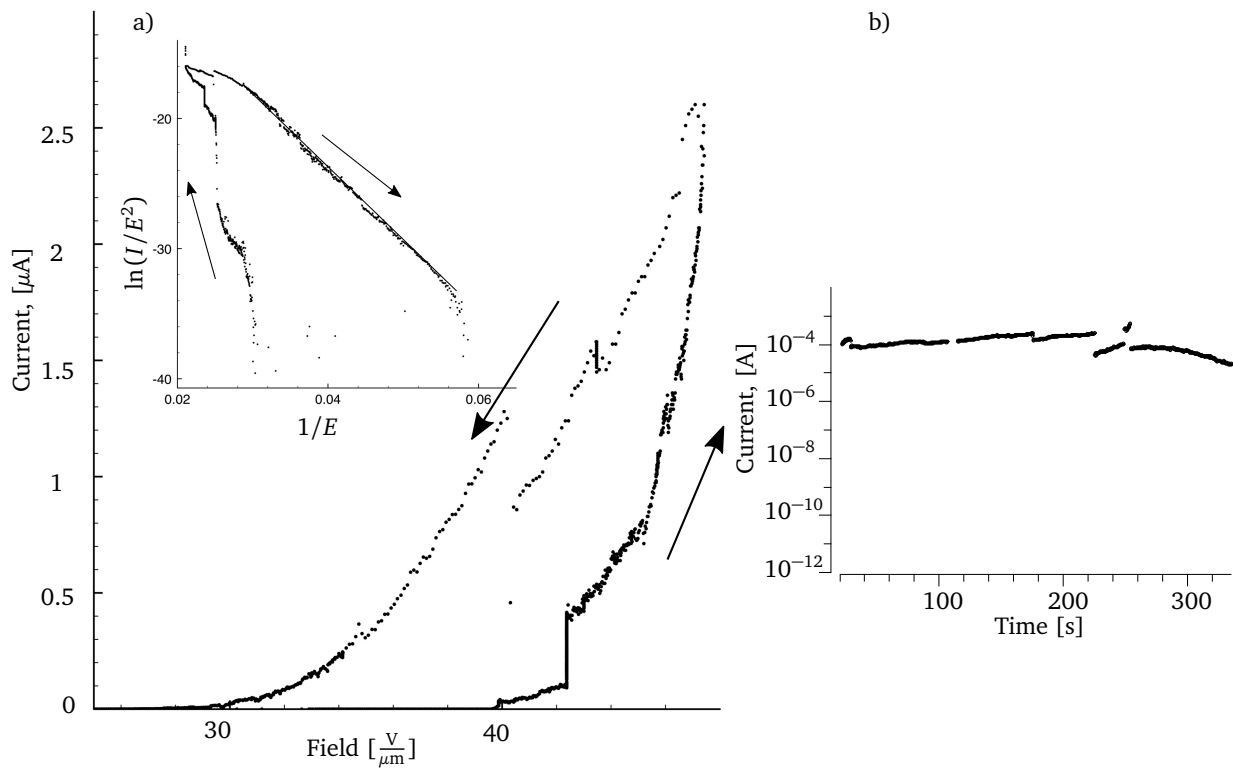


**Figure 6.9:** a) Local measured  $I$ - $E$  curves and FN plot for an emitting area. b) A stable current of  $100\mu\text{A}$  for ca. 5 minutes is measured.

are measured in an *integral measurement system with a luminescent screen (IMLS)*. This technique is convenient for measurement over the entire cathode surface. The schematic image of the device is shown in Figure 6.10. The cathode is installed in a vacuum chamber, on a stage with a z-stepper motor to adjust the distance to a gate anode. The gate anode grid is mounted on the top, while its parallelism can be adjusted through a tiltable holder. A ZnS-based phosphor luminescent screen is mounted over the gate-anode, which provides optical information about the FE current distribution over the cathode. In this device the measurement with a triode (with gate anode) as well as with a diode configuration (without gate anode) is possible. The resolution of the luminescent screen is limited to the phosphor grain size on its surface. The ZnS-based phosphors have a minimum screen response threshold of about  $10^{-7}\text{A cm}^{-2}$  at 500 eV. As a result, it would be possible that the measured emission cannot be optically detected on

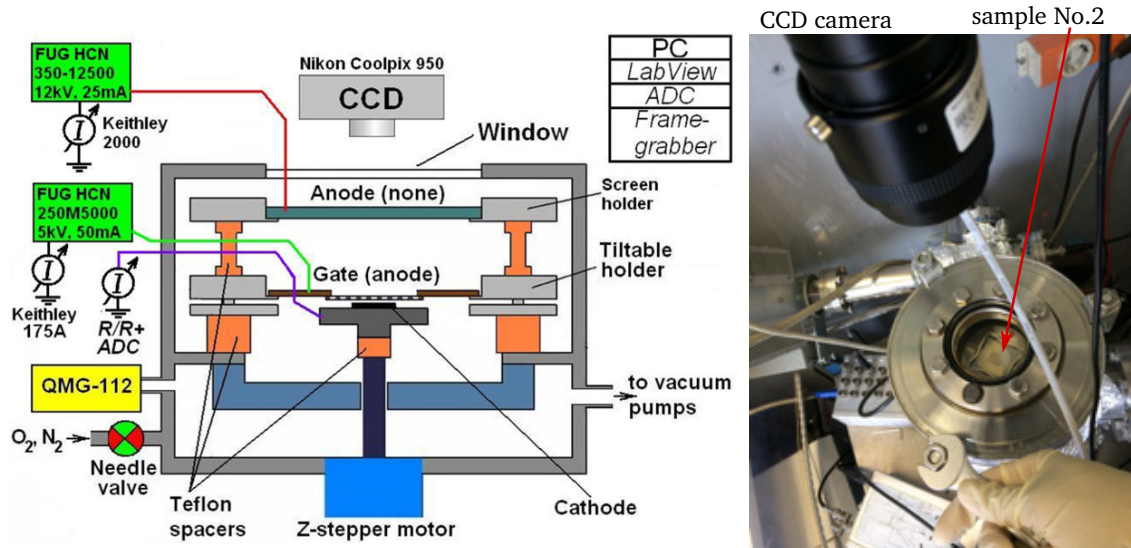


**Figure 6.10:** The schematic of the IMLS device and circuit setup for the current and voltage control and measurement. The emitting cathode is mounted in the chamber under a luminescence window and the emission will be captured by a CCD camera on the top.

the screen at lower power. At higher electron energies, this device results in a proper optical overview of the FE current distribution over the emitting surface. An electrical resistor in the range of  $200\ \Omega$  to  $1\ \text{M}\Omega$  is plugged into the circuit for protecting the cathode against discharges. This resistor is also used for reading the FE current. The measurement in this device takes place at  $10^{-7}$  mbar. The device has also the ability to prove the reaction and lifetime of the cathode in presence of different atmospheres and pressures. On samples No.2 to No.4, a measurement in diode configuration is performed. These measurements are shown in Figure 6.11.

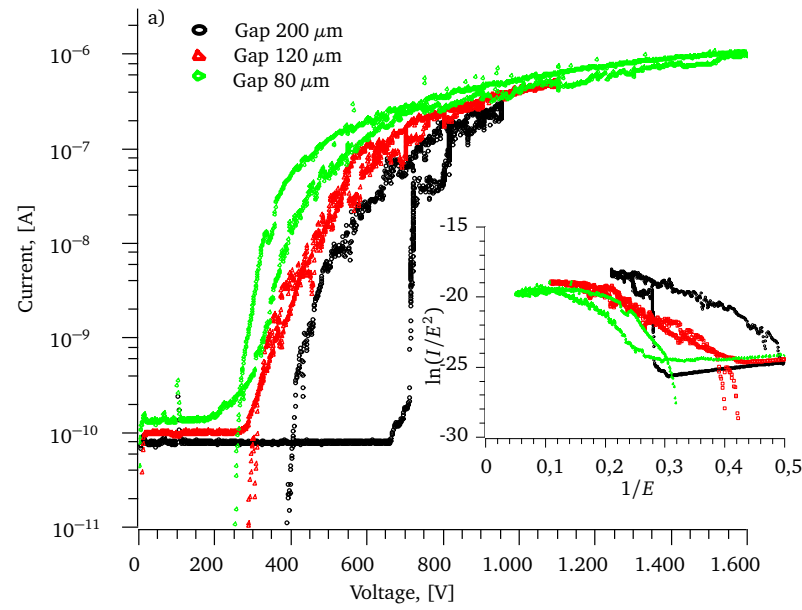
**Sample No.2:** On this sample, three voltage sweeps at three different gaps of  $200\ \mu\text{m}$ ,  $120\ \mu\text{m}$  and  $80\ \mu\text{m}$  are performed. As it is shown in Figure 6.11a, by the first voltage sweep for a  $200\ \mu\text{m}$  gap, a larger hysteresis and also fluctuation in the rising current are observed. It is due to the outgassing of the adsorbates and partial apex destruction. The hysteresis disappears in succeeding voltage sweeps and the FE current is more stable. The measured values are listed in Table 6.1. At this gap, a maximum current of  $0.3\ \mu\text{A}$  is

**Table 6.1:** Measured values of sample No.2

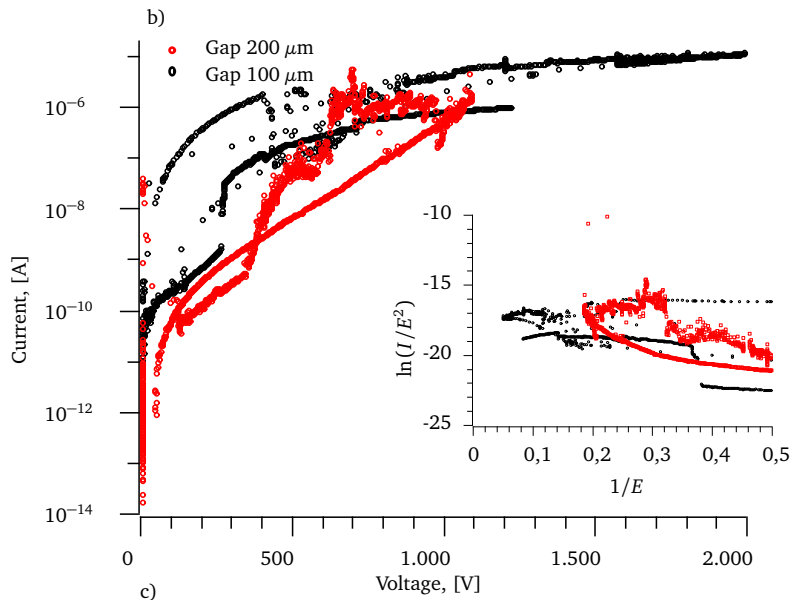
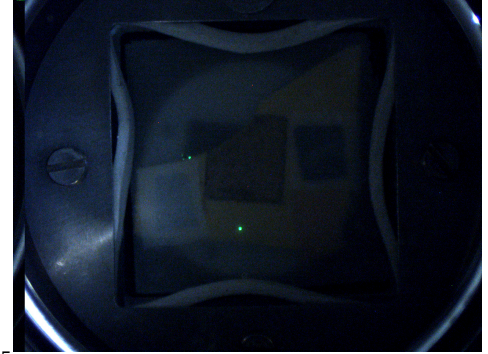
Gap size [ $\mu\text{m}$ ]	On-set field [ $\frac{\text{V}}{\mu\text{m}}$ ]	$\beta$	Emission current [ $\mu\text{A}$ ]
200	2.2	21	0.3
120	4	38	0.6
80	4.9	55	1

measured. Defining the on-set field as the electric field to emit a current of  $1\ \text{nA}$ , the on-set field  $E_{\text{on}}$  of about  $2.2\ \frac{\text{V}}{\mu\text{m}}$  is measured. The achieved enhancement factor  $\beta$  from the FN plot is about 21. At a gap of

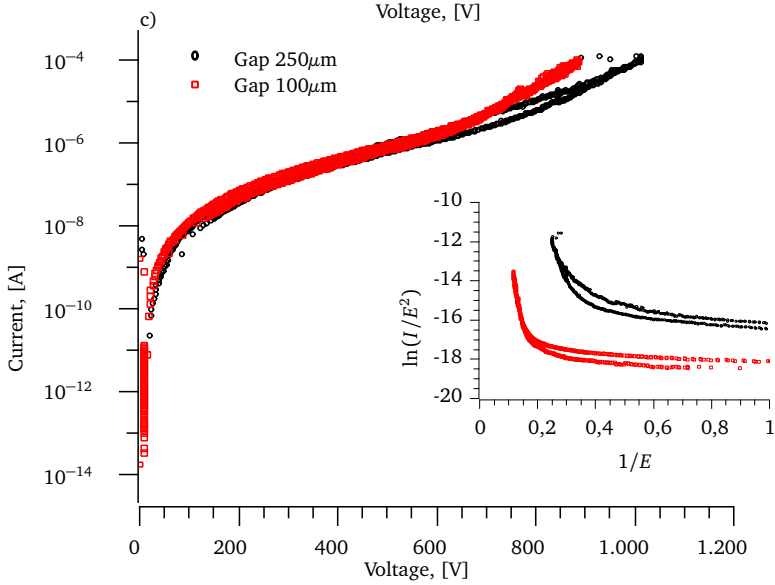
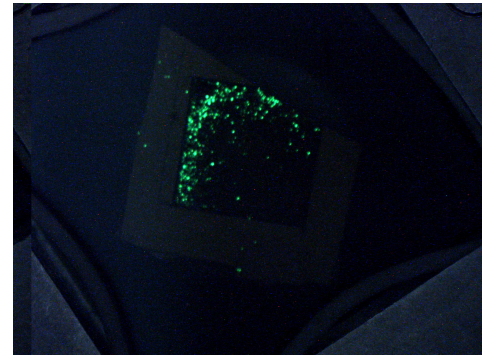




Sample No.2



Sample No.3



Sample No.4

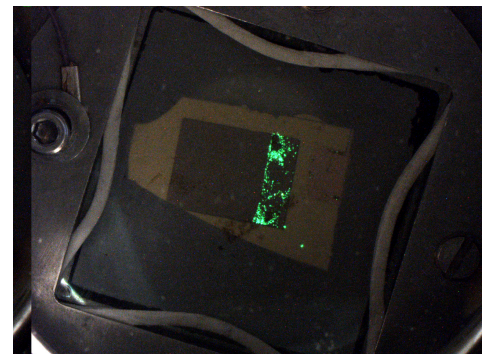


**Figure 6.11:**  $I - V$  curves and corresponding FN-Plots of nanocone arrays, integrally measured in DC mode at different gaps. The hysteresis in the curves is attributed to partial apex destruction.

120  $\mu\text{m}$ , the maximum current of 0.6  $\mu\text{A}$  and an  $E_{\text{on}} = 4 \frac{\text{V}}{\mu\text{m}}$  are measured. The read  $\beta$  value from the FN plot is about 38. At the gap of 80  $\mu\text{m}$ , the maximum current of 1  $\mu\text{A}$  and a  $E_{\text{on}}$  of 4.9  $\frac{\text{V}}{\mu\text{m}}$  is measured. The  $\beta$  value of about 55 is achieved from the FN plot. A nearly linear dependence between the enhancement factor  $\beta$  and the gap size  $d$  is observed. This agrees with the relation (2.25), that by decreasing the gate gap, a linear increase in the  $\beta$  value is expected. Nevertheless, the on-set field is increased by reducing the gap distance. Although, the needed voltage to reach the on-set field is decreased by decreasing the gap. The reason for the increased on-set field is the high density of the wires and the screening effect, at higher electrical fields.

At the lower gap of 80  $\mu\text{m}$ , the FN plot is not linear as expected. This non-FN behavior happens at high voltages and in a FE current saturation region. It can be explained by the limitations of the FE current caused by the supplying emission electrons. At higher voltages, an emission from other areas, out of the region of the wires, can be observed. It is shown in the live image of the sample during the measurement in Figure 6.11b. An SEM image of this sample after the measurement is shown in Figure 6.14a. No falling or even bending wire is observed in this sample.

Sample No.3: It can be seen in Figure 6.11b, that the measured emission current shows a hysteresis by the first voltage sweep, at a gap of 200  $\mu\text{m}$ , which can be attributed to the degradation and destruction of the microcones. By the second voltage sweep at a gap of 100  $\mu\text{m}$ , the hysteresis is still available. However, at voltages over 500 V, it slightly disappeared. The reason for the hysteresis is the outgassing of destructed apexes by the first sweep. Also, an emission from areas outside of the region of the cones is observed (see Figure 6.11b). The measured values are given in Table 6.2. At the 200  $\mu\text{m}$  gap, the on-set field is 1.8  $\frac{\text{V}}{\mu\text{m}}$  and the maximum current of 1.6  $\mu\text{A}$  at 4.7  $\frac{\text{V}}{\mu\text{m}}$  (Voltage = 1000 V) is measured. The  $\beta$  value is 18. For the gap of 100  $\mu\text{m}$  the on-set field  $E_{\text{on}} = 2.3 \frac{\text{V}}{\mu\text{m}}$ , and the measured FE current at the field of 20  $\frac{\text{V}}{\mu\text{m}}$  is about of 12  $\mu\text{A}$ . The measured current at the field of 4.7  $\frac{\text{V}}{\mu\text{m}}$  is 0.18  $\mu\text{A}$  (Voltage = 500 V). Due to the high density of the cones and screening effect not all emitting cones are already turned on at this gap and electrical field. An SEM imaging after the FE measurements shows that the cones are exploded or molten and also

**Table 6.2:** Measured values of sample 3

Gap size [ $\mu\text{m}$ ]	On-set field [ $\frac{\text{V}}{\mu\text{m}}$ ]	$\beta$	Emission current [ $\mu\text{A}$ ]
200	1.8	18	1.6
100	2.3	26	12

some cones are bent, see in Figure 6.12. This can be explained by rapid voltage changes, the high density of the cones, and produced heat by FE current. This explains the observed current fluctuations and the hysteresis in the  $I - V$  curve by the initial voltage increase. Generally, the conical structures have larger base contacts than the cylindrical wires. Therefore they show better thermomechanical stability. But the apexes of the cones can get even overheated. A theoretical 3D analysis and simulation of the emitter apex self-heating, as a result of the Nottingham effect and Joule effect, are shown in Figure 6.13.

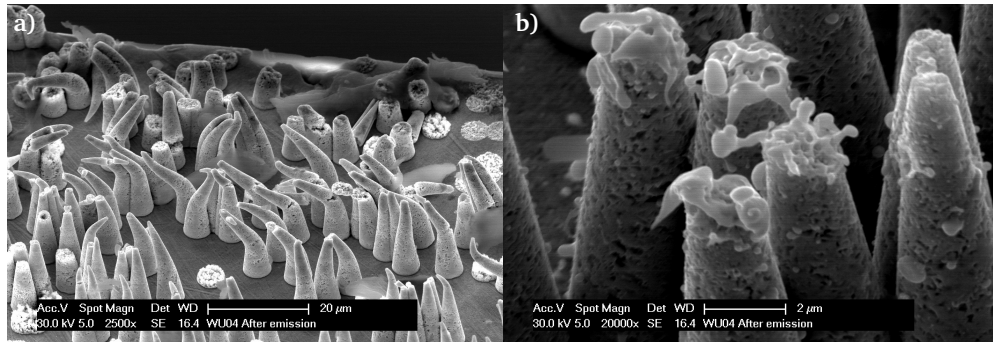


**Figure 6.12:** SEM images of sample No.3 after FE measurements. a) Bent cones with broken apices in some regions. b) Exploded and melted apices.

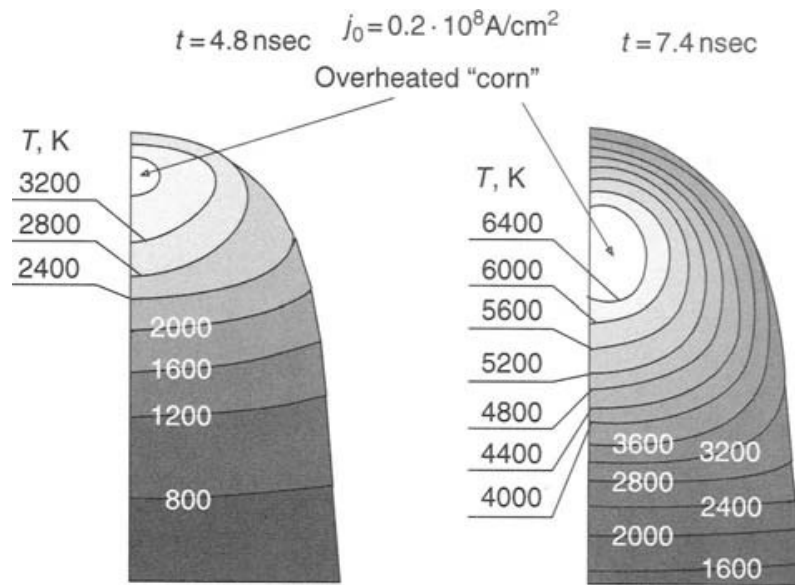


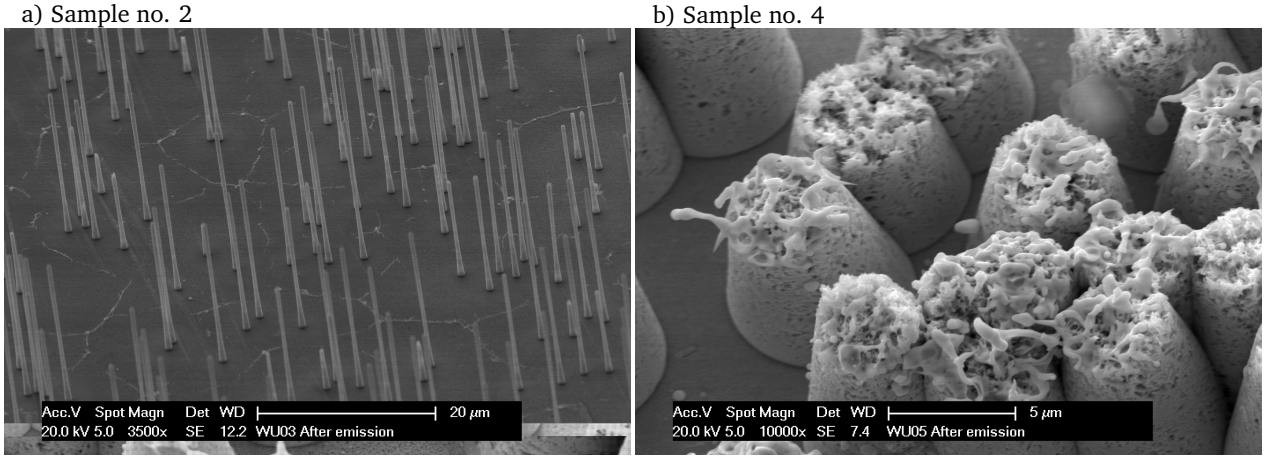
**Figure 6.13:** Theoretically calculated temperature profile in the core of an emitter apex [36]. Although the temperature gradient from the core to the surface of the cones is lower than the melting temperature of the metal, it leads to thermoelastic stresses, up to  $2 \times 10^9$  Pa, which can explosively destroy the apices before it even reaches to the melting point. It explains the bent cones as a result of mechanical stress and the explosive melting of the tips.

Sample No.4: This sample is measured integrally like samples No.2 and No.3. The measured  $I - V$  curves are shown in Figure 6.11c. By mounting and connecting the sample in the measurement device was broken, and just the right side of the sample was connected correctly. It can be seen in the live image of the sample in Figure 6.11c, that just the connected side is emitting. The measurement is done at two gaps of  $250 \mu\text{m}$  and  $100 \mu\text{m}$ . The results are listed in Table 6.3. The  $E_{\text{on}}$  at the  $100 \mu\text{m}$  gap is  $0.33 \frac{\text{V}}{\mu\text{m}}$  and the maximum measured current is  $86 \mu\text{A}$  at a field of  $8.7 \frac{\text{V}}{\mu\text{m}}$  (Voltage 870 V). The achieved  $\beta$  value from FN-Plot is 70. At a gap of  $250 \mu\text{m}$ , the on-set field  $E_{\text{on}} = 0.2 \frac{\text{V}}{\mu\text{m}}$ , and the maximum current of  $47 \mu\text{A}$  at  $4.0 \frac{\text{V}}{\mu\text{m}}$  (Voltage 1000 V) are measured. The  $\beta$  value is 25. As it can be seen in FN-plot, a rapid change in the  $\beta$  value is obvious. It can be explained by the dominant FE behavior of the sharper or higher apices at lower voltages. By increasing the voltage more apices begin to emit and the  $\beta$  value increases from a certain

**Table 6.3:** Measured values of sample 4

Gap size [ $\mu\text{m}$ ]	On-set field [ $\frac{\text{V}}{\mu\text{m}}$ ]	$\beta$	Emission current [ $\mu\text{A}$ ]
250	0.2	25	47
100	0.33	70	86

field strength. The SEM imaging of the sample, shown in Figure 6.14b, shows an explosive melting of the sharp small apexes, like sample No.3.

**Figure 6.14:** SEM images of sample No.2 and sample No.4 after field emission measurement

Comparing the measured FE currents shows that the highest maximum current and the lowest  $E_{\text{on}}$  are achieved for sample No.4, with small sharp dense apexes of the gold crystal structure. But the applied maximum field in this measurement has destroyed the apexes. It means, that the real stable current is lower than the measured one in this measurement. The measured current from the semi-conical wires of sample No.2 shows the lowest emission. After applying an electrical field of  $20 \frac{\text{V}}{\mu\text{m}}$ , and emission of  $1 \mu\text{A}$ , no wire is melted, bent, or detached. As discussed in Section 2.3, to reach the maximum FE current, an optimized field emitter structure is needed.

For such an optimization, different aspects must be considered. For example, the geometry of the emitting objects, their inter-spacing, and the position of the extractor grid play important roles in reducing the on-set field and increasing the FE current. Furthermore, the web size of the grid defines the transmission percentage of the electrons. Other parameters like the material of the emitting objects, applied voltage, vacuum pressure, homogeneity in the emitter heights, etc. are determinant factors in the design of a field emitter device. The integral measurements on all of the samples in this section showed that a density of  $1.6 \times 10^6 \text{ cm}^{-2}$  gives an enhancement factor less than 70. Simulations show that in the case of randomly distributed emitters, like structured emitters in this thesis, an optimum next neighbor distance will be achieved, with a cone density in the range of  $1 \times 10^4 \text{ cm}^{-2}$  to  $2 \times 10^4 \text{ cm}^{-2}$  [110], where the heights of the cones are  $24 \mu\text{m}$  and the apex radius is about 25 nm. In the following section, the measurements on three samples with lower cone densities are shown.



### 6.3 Measurements on low density cones array

Some parts of this section are published by Bieker et al. in the Journal of Vacuum Science & Technology B [10]. A key aspect in the application of the nanocones in an ionization vacuum gauge is a long time stable FE current in the order of  $100\mu\text{A}$ . To achieve high emission current yields, at this step, the emitter density has been varied and the field emission properties of the gold nanocones with lower density than the samples in the previous section, are investigated. For this experimental set, three glass chips with circular metallic electrodes, with a diameter of 2.5 mm are structured. The electrodes are prepared using the described procedure in Table 3.2. In the next step, the gold nanocones are synthesized with the described process in Chapter 5. The steps are schematically shown in Figure 5.15 and the SEM images of the prepared samples are shown in Figure 6.15. Details about the geometries and properties of the prepared samples are listed in Table 6.4. It has to be mentioned that the emitter densities are assumed to be nominal pore densities of the template membranes. However, during the electrodeposition, local depletion of the electrolyte causes a non-homogeneous growth, so that not all the cones are completely filled and therefore, the given pore density has to be taken as a maximum value for the emitter density. Exemplary faults are indicated with white arrows in Figure 6.15b.

**Table 6.4:** Properties of the samples with gold nanocones

Sample	A	B	C
Cones density [cones/cm <sup>2</sup> ]	$6 \times 10^4$	$4 \times 10^5$	$1 \times 10^6$
Height [ $\mu\text{m}$ ]	24	24	24
Apex diameter $\Phi_{\text{tip}}$ [nm]	<500	<300	<300
Base diameter $\Phi_{\text{base}}$ [ $\mu\text{m}$ ]	3.0	3.6	3.75

#### Experimental setup for FE measurements

To investigate the field emission properties of the gold nanocones, the measurements were performed in the work group facility of Prof. Schreiner at OTH Regensburg university. The samples were mounted into a sample holder and used as cathodes. A Mica foil with  $50\mu\text{m}$  thickness was used as a spacer and a fine-meshed silicon nitride grid, metalized with aluminum, was used as an anode. All parts were fastened with an aluminum clamp and put into an electron source setup in an ultrahigh vacuum chamber with a pressure of about  $10^{-9}$  mbar. The grid, as well as the cathode, were electrically connected with tungsten needles to a high voltage source (HCP 350–12500, FuG Elektronik). A picoamperemeter (Keithley 6487) was used to measure the emission current and was protected against discharges with a serial resistor. In Figure 6.16 the setup is shown.

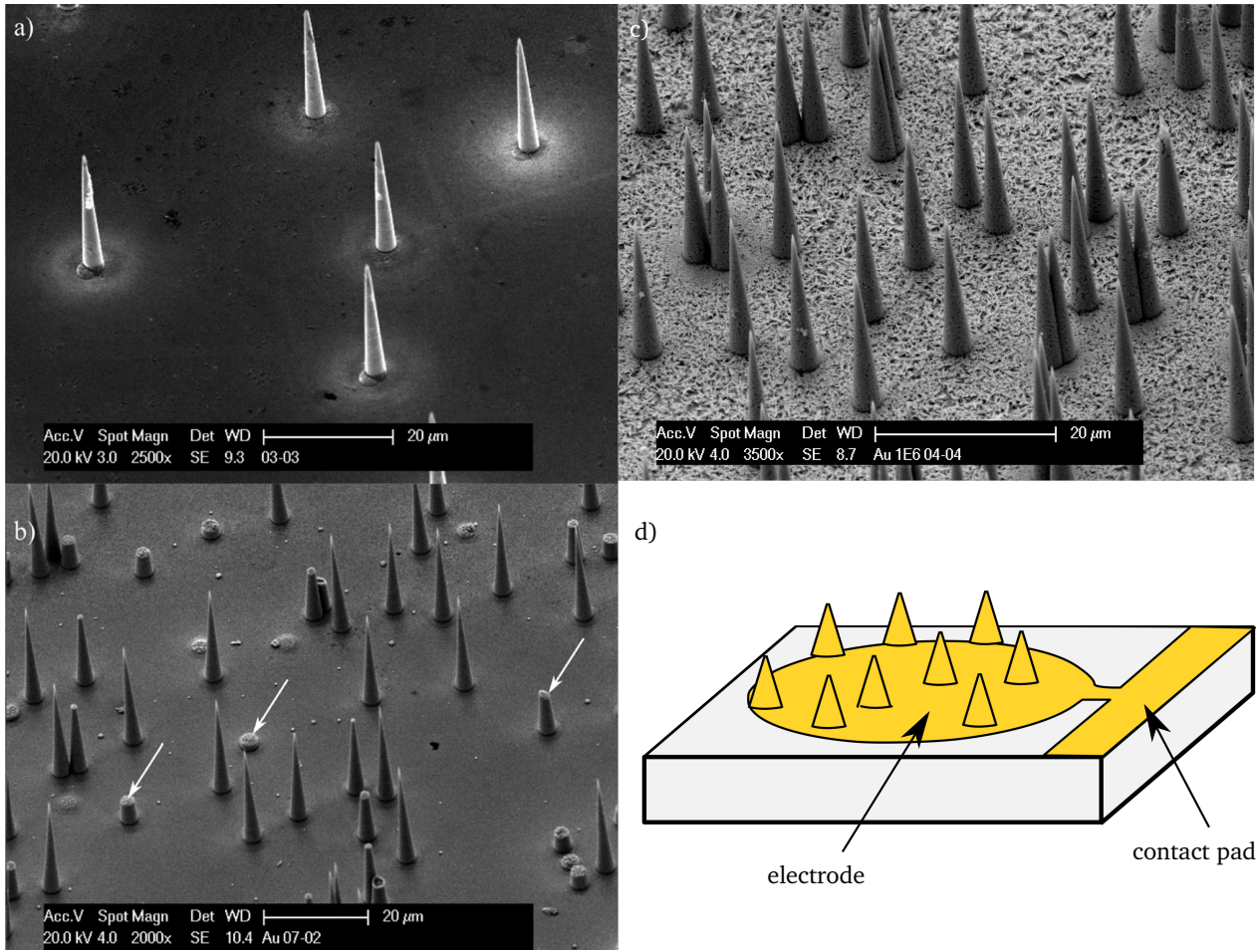


**Figure 6.15:** (a) SEM image of sample A prepared using a template with  $6 \times 10^4$  cones/cm<sup>2</sup> (b) Sample B ( $4 \times 10^5$  cones/cm<sup>2</sup>). Faults are indicated with white arrows. (c) Sample C ( $1 \times 10^6$  cones/cm<sup>2</sup>). (d) The schematic of samples with round shaped electrodes and contact pads [9], [10].

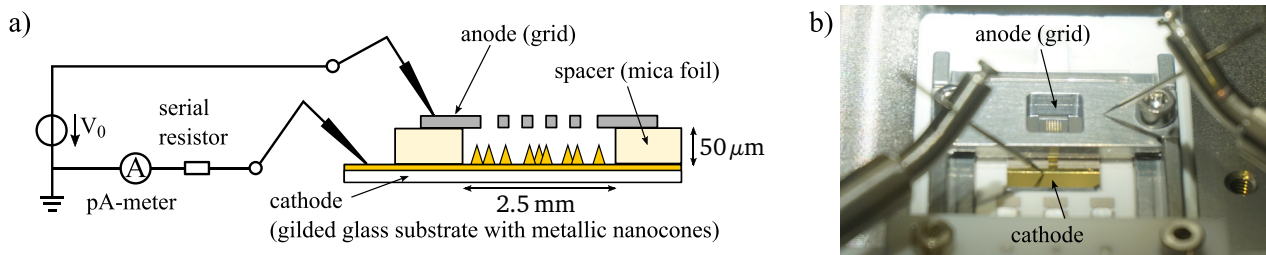


**Figure 6.16:** (a) Schematic drawing of the experimental setup used for integral field emission measurements. (b) Photo of the sample holder, including the fine-meshed metalized Si-grid as anode and the cathode with the nanocones [10].

## FE Measurement

As mentioned before the on-set field is defined as the applied electric field needed to gain a threshold emission current  $I_T$  of 1 nA. Since an integral emission current was measured, only an effective field enhancement factor  $\beta$  was determined, which fits the slope of the Fowler-Nordheim-plot using the approximation of an average current density from [57]. The electric field  $E$  is calculated from the applied voltage and the distance between the two electrodes (50 μm). The voltage  $V$  describes the voltage applied to the

anode and cathode. The voltage drop at the serial resistor is always subtracted from the initial voltage  $V_0$ . Representative  $I$ - $V$ -curves and the corresponding Fowler-Nordheim-plots of all samples are shown in 6.17. As one can see, sample A reaches the threshold current with an on-set field  $E_{\text{on}}$  of about  $6.4 \frac{\text{V}}{\mu\text{m}}$  ( $V \approx 320 \text{ V}$ ).

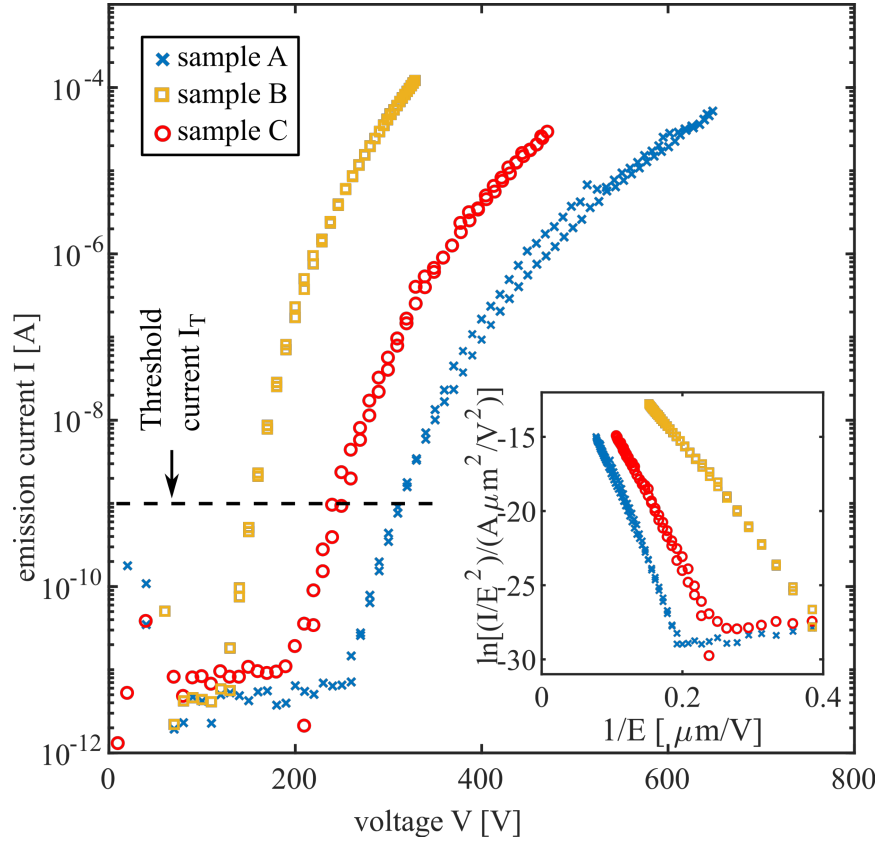


**Figure 6.17:** Integrally measured  $I$ - $V$  curves and Fowler-Nordheim-plots (inset) of sample A (blue crosses), sample B (yellow squares), and sample C (red circles) [10].

The maximum observed emission current during all measurements is  $I_{\text{max}} = 37.5 \mu\text{A}$  at an applied voltage of  $V_{\text{max}} = 623 \text{ V}$  ( $E = 12.46 \frac{\text{V}}{\mu\text{m}}$ ). Fitting the slope of the Fowler-Nordheim-plot by using a work function of  $4.8 \text{ eV}$  for gold [111] gives an effective  $\beta$  factor of about 640. In comparison, sample C shows a lower on-set field of  $E_{\text{on}} = 5.0 \frac{\text{V}}{\mu\text{m}}$  ( $V \approx 250 \text{ V}$ ). The maximum measured emission current during all measurements was  $I_{\text{max}} = 29.1 \mu\text{A}$  at an applied maximum voltage of  $V_{\text{max}} = 471 \text{ V}$  ( $E = 9.42 \frac{\text{V}}{\mu\text{m}}$ ). An effective  $\beta$  factor of about 800 can be derived from the curve. Comparing all samples, sample B shows the lowest on-set field of  $3.1 \frac{\text{V}}{\mu\text{m}}$  ( $V \approx 155 \text{ V}$ ). The maximum measured emission current during all measurements  $I_{\text{max}} = 142.2 \mu\text{A}$  occurred at an applied voltage  $V_{\text{max}}$  of  $339 \text{ V}$  ( $E = 6.78 \frac{\text{V}}{\mu\text{m}}$ ). An effective  $\beta$  factor of about 1240 has been extracted. The results of the  $I$ - $V$ -measurements of the samples are summarized in Table 6.5. For the calculation of the maximum current density  $J_{\text{max}}$ , the total area of the cathode  $A = 4.9 \text{ mm}^2$  is used. Comparing the results of the integral field emission measurements with the given geometries of the samples, one can observe that the impact of two factors influences the field emission properties strongly: On the one hand, the pitch of the field emitter structures, on the other hand, the shape or size of the emitter apices. Focusing only on the pitch and, therefore, the density of the field emitter structures, the field enhancement factor of sample A should be higher than the one of sample B, and the field en-



**Table 6.5:** Summarized results of the integral FE measurements

Sample	A	B	C
On-set fields $E_{\text{on}}$ [ $\frac{\text{V}}{\mu\text{m}}$ ]	6.4	3.1	5.0
Max. current $I_{\text{max}}$ [ $\mu\text{A}$ ]	37.5	142.2	29.1
Max. current density $J_{\text{max}}$ [ $\frac{\text{mA}}{\text{cm}^2}$ ]	0.76	2.90	0.59
Applied voltage $V_{\text{max}}$ [V]	623	339	471
Effective $\beta$ factor	$\approx 640$	$\approx 1240$	$\approx 800$

hancement factor of sample B should be higher than the one of sample C, following the theory of mutual shielding [112][113]. A high density of the emitter structures (emitter pitch and height in the same order of magnitude) leads to a reduced field enhancement. For wire-shaped field emitters, an optimum regarding high emitter density and field enhancement factor can be achieved for an emitter pitch of two times their height. However, samples B and C show better performances. The SEM images revealed that the samples B and C have sharper apexes with diameters below 300 nm and also a stronger polycrystalline structure, which leads to a stronger local field enhancement. Anyway, the highest field emission currents and lowest on-set field were reached with sample B, also having sharp apexes with diameters below 300 nm. This leads to the assumption that a mutual shielding is already given at sample C due to the high density of emitter structures. These results are published by Bieker et al. at [10]. Additionally, the long-term stability of the emission current of sample B was investigated. In Figure 6.18a, a cumulative measurement of the emission current for over 50 h is presented. Therefore, four, consecutive measurements with a duration of

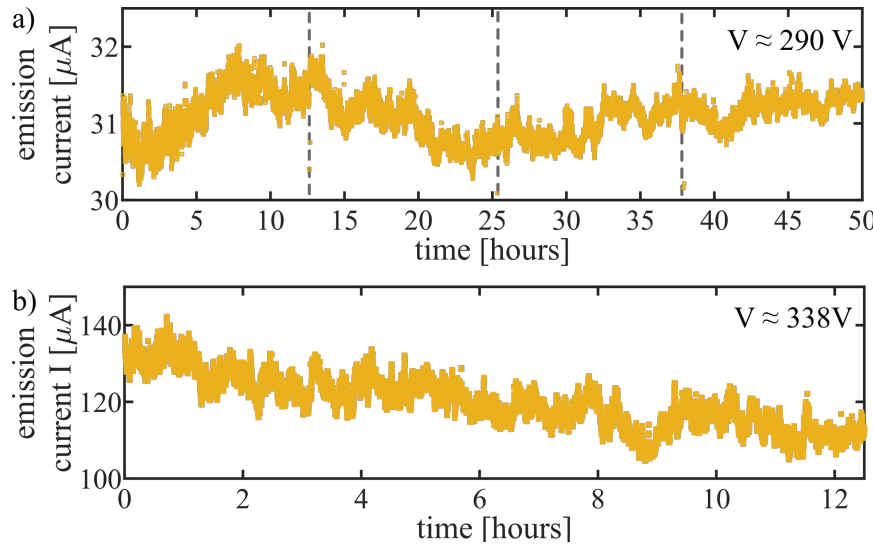


**Figure 6.18:** Cumulative measurement of the emission current stability of sample B for over 50 h, combining four, consecutive measurements with a duration of 12.5 h (indicated by the dashed lines). (b) Measurement of the emission current starting at 140  $\mu\text{A}$  for 12.5 h [10].

12.5 h are combined. The measurements were done using a serial resistor of 10 M $\Omega$  and an initial voltage

$V_0$  of 600 V, resulting in a change of the applied voltage to the cathode of about 10 V/1  $\mu$ A. The average emission current during the measurements is  $(31.0 \pm 1.3) \mu$ A at an average applied voltage  $V$  of 290 V ( $E = 5.8 \frac{\text{V}}{\mu\text{m}}$ ). As one can see, the short-time current fluctuations decrease as well as the long-time behavior of the current smoothens with progressing time. This behavior is typical for metallic field emission cathodes, which usually need a conditioning sequence at the beginning of the operation to provide a stable emission current [114]. The applied voltage  $V$  was further increased to check if any degradation of the field emitter can be observed at the currents above 100  $\mu$ A. To reduce the voltage drop across the serial resistor, a 10 k $\Omega$  resistor was used. Additional measurements of about 12.5 h were performed. In Figure 6.18b, the emission measurements using an initial voltage  $V_0$  of 340 V, resulting in an average applied voltage  $V$  of about 338 V, is shown. The decrease of the emission current shows that the emitter structures are slowly degrading at currents in this order of magnitude. The field emission measurements were finally verified by adding another tungsten needle over the grid and measuring the electron emission in a triode setup, which is shown in Figure 6.19a. Applying a voltage  $V_0$  of 340 V, the currents shown in Figure 6.19b were obtained. The transmission current is about 39% of the cathode current, which is in agreement with

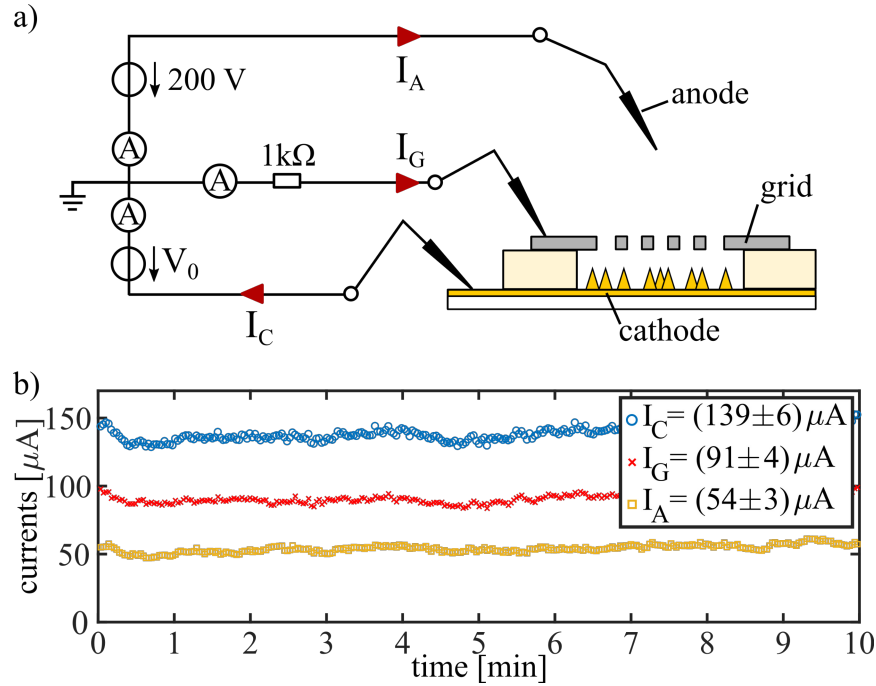


**Figure 6.19:** (a) Triode setup to measure the transmission current. (b) Current during the transmission measurements from the cathode, the anode, and the grid [10].

the optical transparency of the grid.

## 6.4 Summary and outlook

In this chapter, it is shown that the newly developed fabrication technique for integrating nanocones with different heights, base diameter, apex radius, and density on a cathode surface is a fast, reliable, and reproducible process. This process enables the fabrication of nanocones based field emitters on large surfaces. Although the field emitter cathodes revealed field enhancement factors comparable to conventional array

---

structures [115], still an optimum emitter density with the given geometries base diameters around  $3\mu\text{m}$  and apex diameters below  $300\text{ nm}$  has to be investigated thoroughly. Additionally, the obtained results, especially the dependence of the emission current on the emitter density, have to be validated and refined with higher statistical significance in future experiments. This is necessary to fabricate reproducible field emission cathodes for future commercial applications. Averagely a stable emission current of  $31\mu\text{A}$  at an applied voltage of about  $290\text{ V}$  was observed for several hours. Emission currents above  $100\mu\text{A}$  have shown the potential of the emitter structures, but the generation of stable currents in this order of magnitude is still an issue, which has to be solved. In upcoming experiments also the areal homogeneity of the emission should be investigated. This will reveal if the emission current is delivered only by a few emitters or homogeneously by the whole emitter array. This might enable further improvements of the emitter structures, to reach higher stable emission currents at lower applied voltages. Besides that, nanocones made of other elements, such as copper, nickel, or platinum, are feasible. One of the issues to be solved is the geometry optimization of the extraction grid. Furthermore, the integration of the extraction grid in the microsystem is a challenge and it will be discussed in the next chapter.

---

## 7 A new concept for the integration of extraction grid

---

The Nanowires and the nanocones are promising structures for vacuum nano-electronic applications. In previous chapters, a new method for the fabrication and integration of the nanowires and nanocones, with a focus on vacuum gauges is introduced. In Chapter 4, the scaling of the fabrication process for a standard industrial batch process is discussed. The field emission measurements on the nanocones are performed, and it is shown how the structure should be optimized to maximize the FE current and reduce the on-set field. After optimizing the design of the nanocones and the geometry of the array, the next step is to fabricate and integrate the extraction grid at a specific height over the emitter. This step is going to be a challenge because the integration of the extraction grid must be done after the synthesis of the cones. The integration process must be vacuum compatible and also a low-temperature process, to avoid damaging the cones. The general structure of a field emitter is shown in Figure 7.1. In some applications, a collimator grid is also needed to focus the generated beam-let for higher intensity or higher brightness on the anode surface. For an application like a vacuum gauge, the net current is responsible for the ionization in the gauge volume. Thus, the collimator can be neglected. For commercial mass production of such gauges,

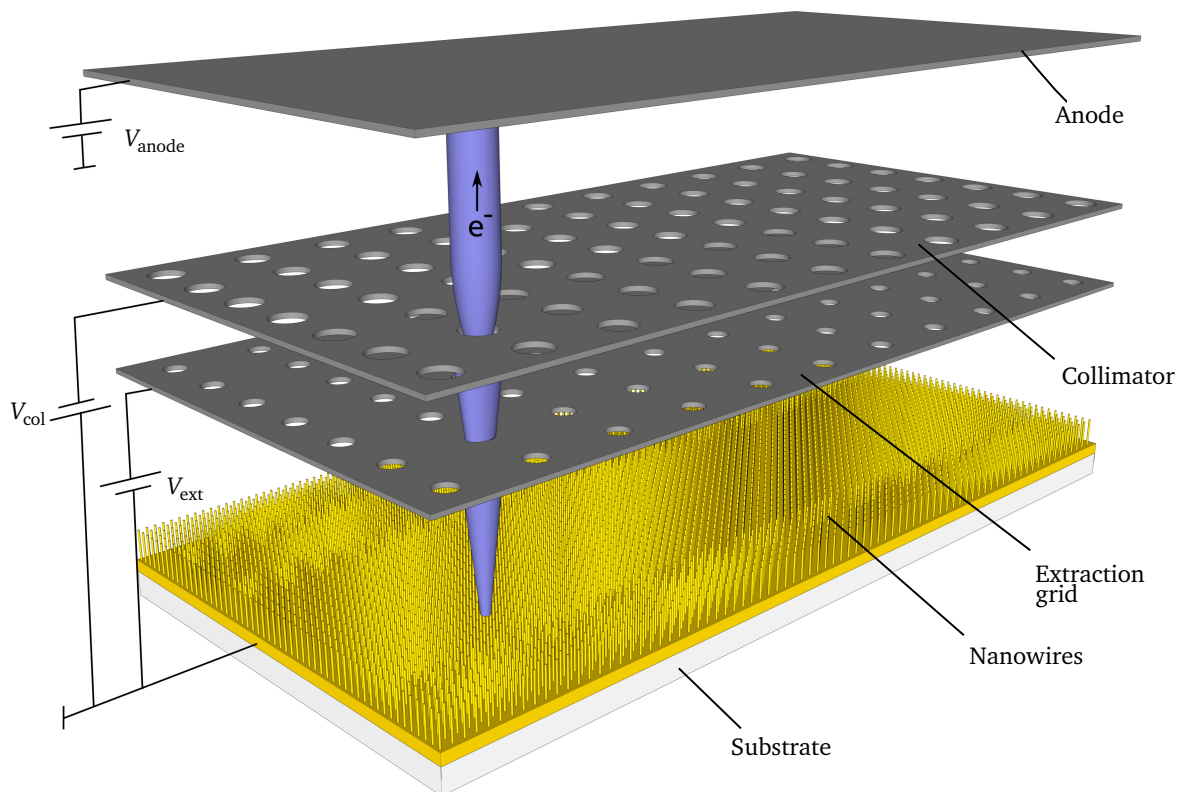


**Figure 7.1:** A general schematic of an electron field emission device. The device consists of emitting objects like nanocones, an extraction grid, and an anode in a triode setup. A collimator is needed in some applications for the beam parallelization.

the integration step should fulfill the following criteria:

- integrating the grid in the system with cryogenic UHV compatible materials and enough shear force strength,
- controlling the height of the grid over the nanocones,
- adequate parallelism of the grid,
- feasible batch processing for commercial application.

In the following section, some methods for integrating the extraction grid are shown and compared.

## 7.1 Methods for integrating the extraction grid

There are different ideas for integrating and fixing a grid on the emitting cathode in a bottom-up fabrication process. Some of these ideas are taken into account in commercial and experimental samples. For example in the field emitters of the Xintek company CNTs are synthesized on printed Ag electrodes, on glass or Molybdenum coated stainless steel substrate. The products with an integrated gate on them, are known as triode cathodes. The cathodes with no gate are known as diode cathodes, where the extraction grid must be integrated by the end-user on the available printed dielectric spacers. Such emitters are demonstrated in Figure 7.2. In one product, a tungsten gate is placed on top of a stainless steel cathode housing. In another product, the gate is placed over the substrate, on a spacer made of glass/stainless steel compound. In both cases, the gates are fixed via micro screws.

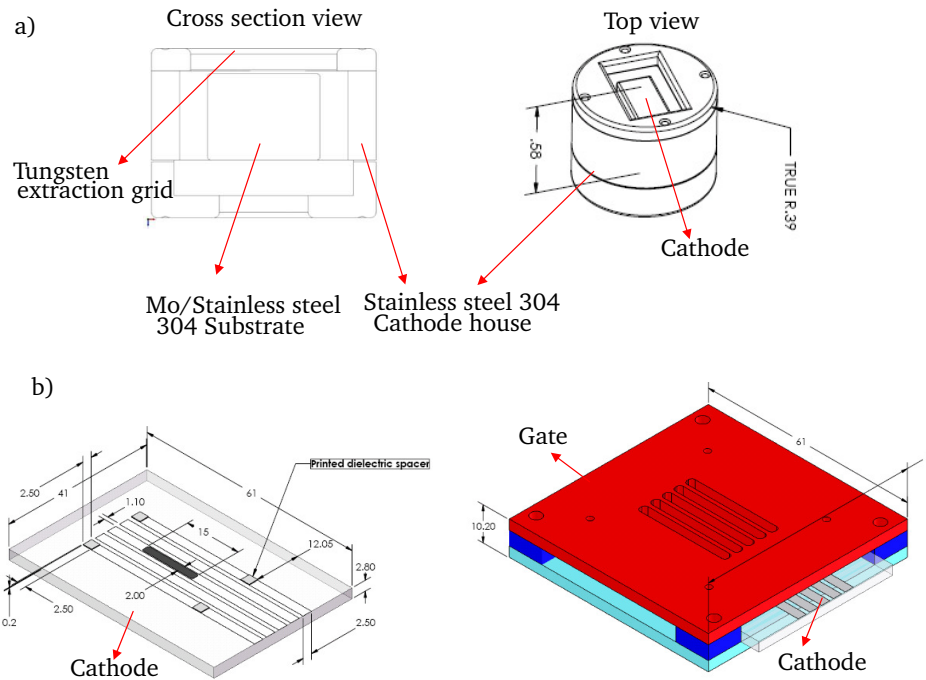


**Figure 7.2:** CNT cathodes of the Xintek company. a) Triode cathode setup with one pixel on a Mo/stainless steel substrate. The gate is made of tungsten. As shown, the gate is adjusted over the cathode in a steel case and fixed by four screws at a height of  $200\mu\text{m}$ . b) The CNTs are grown on the Ag printed silver electrodes on a glass substrate. A dielectric spacer can be grown on the structure to be used in the diode mode. Alternatively, it can be fixed on another glass substrate, and place a micro milled tungsten gate on it for a triode structure. The gate is fixed with four screws on the steel spacers [116].

For mass production of such structures, fabricating the spacers with a minimum deviation in their height is needed. Also, mounting all spacers must be done individually and manually, as no fixing paste for an XHV application should be used. However, in Xintek products, it is not known how the cathode chip is fixed on the carrier glass substrate. One other example is the structure of a gas ionization sensor, shown in Figure 7.3. The anode plate made of highly doped silicon is placed on a polypropylene spacer and is stuck by Teflon glue. This structure is made of many different materials with different thermal expansion coefficients, which make it brittle and unsuitable for cryo temperature applications. Also, some of the used materials are outgassing at UHV and XHV.

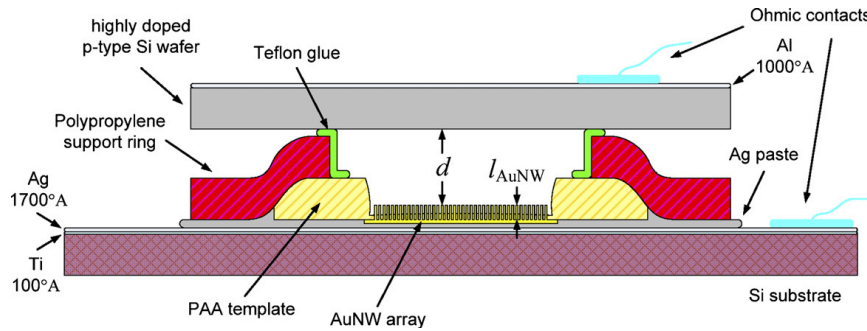


**Figure 7.3:** Structure of a gas ionization sensor [117]. The used paste and polymers are not compatible with cryogenic ambient and XHV pressures.

## 7.2 A new concept for the integration of the extraction grid

As shown in two previous examples, the first challenge is to develop a method for integrating a spacer with XHV compatible materials. The next challenge is to place and fix the extraction grid on the spacers. The integration method must result in acceptable parallelism between the cathode and the grid structure. Generally, there are four possibilities for the fabrication of such spacers:

1. Preparing a separate low carbon 304 steel housing for the cathode and fixing the anode grid on it like the example shown in Figure 7.2: For the fabrication of a separate steel housing, an extra micro-milling process is needed. This is undesired for a parallel batch process. Also, a later integration of the cathode via gluing in the housing and installing the anode on the top makes the process more complicated. Nevertheless, fixing the anode needs to be done via micro screws or clamps.
2. Using an isolator foil, like Mica, as a spacer: Using a Mica foil as a spacer is an easier method. Mica is a UHV compatible material with an acceptable outgassing rate. The disadvantage of this method is the limitation of the gap distance to the foil thickness. Also, micro screws or clamps are still needed for fixing the whole structure. By using a Mica spacer, a micromachining process for preparing the spacer is needed.
3. In-situ fabrication of the spacers on the cathode substrate: The nanowires and the nanocones are grown in an electrochemical deposition step. Therefore, the spacers can also be grown with the same fabrication process in an extra step, directly on one of the cathode electrodes.

4. In-situ fabrication of the spacers on the anode grid: The anode grids are usually prepared by an etch process. In many cases, a commercially prepared grid is used. Further working on these grids needs an extra preparation step for the electrochemical deposition.

Comparing the four possibilities shows, that growing the spacers on the cathode electrode matches better the whole fabrication process of the nanocones. With this method, the spacers can be grown for many cathodes on a wafer simultaneously. Details about this decision are discussed in Chapter 8.

## 7.2.1 Fabrication process of the spacers

The fabrication process of the spacers is schematically shown in Figure 7.4a. After performing the synthesis of nanowires or nanocones, the pattern of the spacers is prepared in a lithography step. For patterning the structures with a height between  $15\text{ }\mu\text{m}$  to  $100\text{ }\mu\text{m}$ , the AZ 40 XT Photoresist (Appendix B.7) of Microchemicals company is a proper photoresist. The photoresist layer masks the nanocones simultaneously, which protects the cones in the further fabrication steps. The spacers are grown in an electrochemical deposition step, in the same bath used for growing the nanocones. The surface of the spacers may show unevenness, which can be flattened using a lapping machine. As shown in Figure 7.4b, after removing the photoresist and cleaning the sample with acetone, the anode grid can be placed on the spacer. These

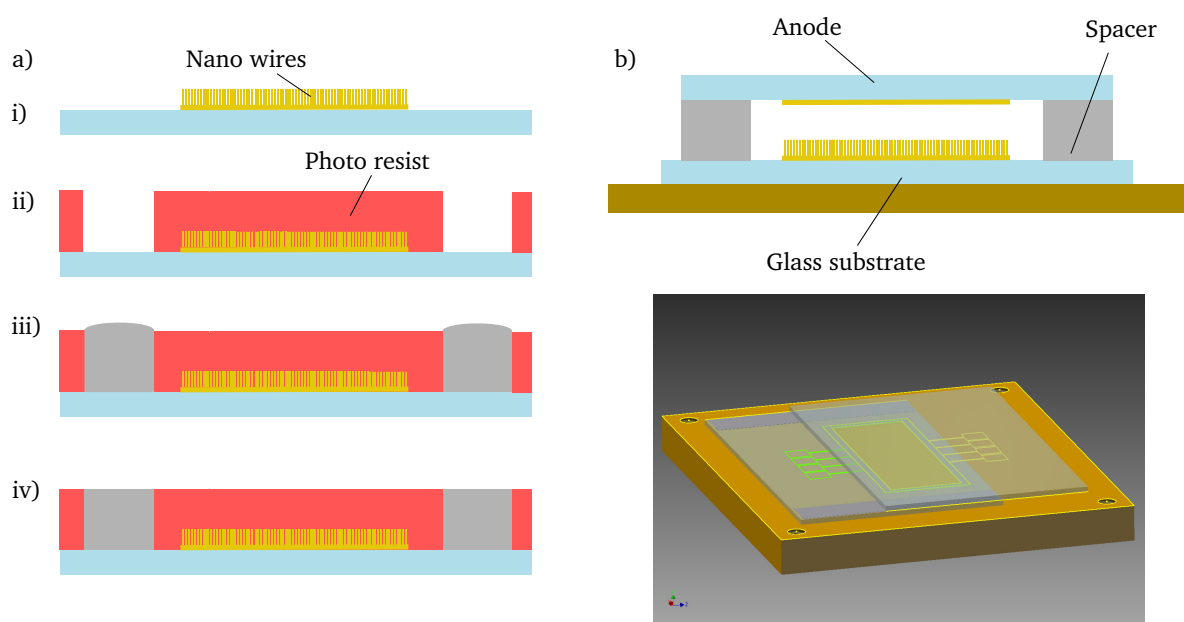


**Figure 7.4:** a) i) An array of nanowires or nanocones. ii) The template of spacers is shaped with a photoresist, in a lithography step. iii) The metallic spacers are grown in a galvanic bath. iv) The spacers are lapped to flatten the surfaces. b) The anode is placed on top of the spacers. A 3D view of the structure is illustrated.

spacers are pure metallic with a low outgassing rate. The height of the spacers can be adjusted by controlling the thickness of the photoresist. The spacers are integrated into the system and there is no extra micro-milling process needed. One disadvantage of this process is the extra lapping process. In this solution, fixing the anode electrode on the spacers is still a problem. Like samples shown in Figure 7.5,



the placed extraction grid can be fixed using micro screws or clamps. It is also possible to use a spring system to be able to substitute the cathode or anode easier. Although the shown methods in Figure 7.5

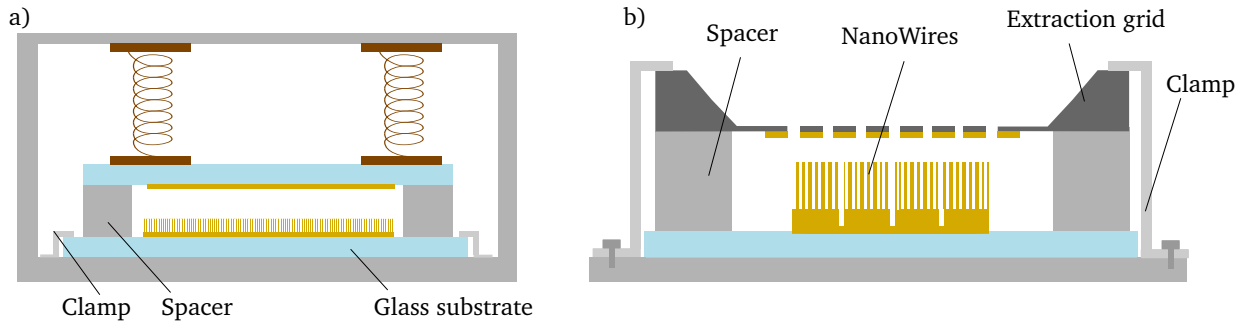


**Figure 7.5:** a) The anode is fixed on the spacers via a spring structure. The cathode is fixed in a housing with clamps b) The anode/extraction grid is fixed on the spacers by a clamp. The clamp is screwed to a sample holder.

are feasible, they are consisting of many parts like clamps, screws, housing, carrier substrate, and the spring system. The more the number of parts, the more cavities are available in the system. Gas and water molecules can retain in those cavities and this can deteriorate the vacuum. For such structures, a longer baking time is needed. Furthermore, as mentioned previously using different materials with different thermal coefficients in the joints is not desired too. The new idea in this thesis is to use a unique metallic hook-and-loop fastener for joining the anode electrode and the spacers. In the next section, the concept for a room temperature interconnection technique using metallic nanowires is introduced.

## 7.2.2 Nanowires as a hook-and-loop fastener for joining dies

The nanowires with a small diameter, in the range of 100 nm to 1000 nm, enable the migration of the atoms from the crystal lattice of one nanowire to the other one, while two wires are pressed together. This process is shown in Figure 7.6. This effect appears in the nanowires, by an appropriate pressure, and at

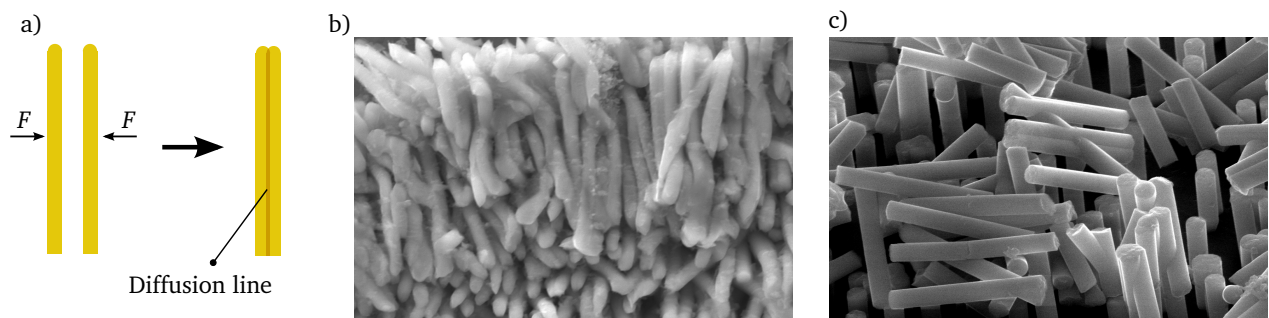


**Figure 7.6:** a) By pressing two nanowires with a minimum force, an atomic migration between the crystal structure of two wires takes place. It leads to the diffusion of the wires in each other. b) An SEM image of diffused copper wires under pressure. c) Broken nickel wires under mechanical pressure.

room temperature due to their high surface/volume ratio. The minimum pressure needed for the diffusion of the wires depends on the rigidity of the material. For example, low pressures in the range of 5 MPa to

---

10 MPa result in a higher entanglement for copper or gold wires compared to the nickel wires. As shown in Figure 7.6c, a part of nickel nanowires break by applying the same range of pressure on them, and they are not entangled like copper wires. At higher pressures, the number of diffused nickel wires becomes dominant. Similarly, by growing the nanowires on two surfaces and pressing them together, the nanowires on both joint partners will bend, entangle, and diffuse into each other. Thus, both surfaces are bonded at room temperature.

A higher density of nanowires achieves a larger surface/volume ratio. It means the diffusion rate increases enormously with the increased density of the wires. Indeed, under pressure, still, a fractal of the wires will diffuse into each other. The not diffused wires attract each other by intermolecular forces of attraction like dipole-dipole interactions and Van-der-Waals forces. The sum of Van-der-Waals forces and the diffused nanowires give the total shear strength of the joint. It is worth mentioning, that the diffusion process is a time-dependent process. After a while, the resulting strength increases with the increasing number of diffused wires.

This technique can be used for joining the extraction grid and the spacers in a field emitter structure. This process is shown schematically in Figure 7.7. To avoid the appearance of unevenness on the surface of the spacers, the spacers are grown while the template membrane is placed on the structure (see Figure 7.7ii). With this method, the spacers grow up to the lower side of the template membrane. Now the further growth of the spacers stops, and the nanowires grow subsequently on the spacers and in the pores of the template membrane (see Figure 7.7iii). Also, the nanowires are directly grown on the surface of the extraction grid. In this step, just a lithography step for masking the grid and defining the contact pads is needed. After removing the template and cleaning the samples, the chips can be bonded. In this step, the grid is flipped, adjusted, and pressed on the spacers. The nanowires will diffuse in each other and the chips are bonded at room temperature without damaging the nanocones. With this method, the number of parts in the device is minimized. There exist no paste with a high outgassing rate or multilayer systems with different thermal expansion coefficient in the interconnection area. Thus, any changes in the temperature do not affect the interconnection. As mentioned above, the diffusion of nanowires is a time-dependent process. Reaching the maximum strength value takes some hours. But the atomic motion process can be enhanced by inserting additional thermal energy. It increases the strength of the joints to its maximum value in a short time less than 3 min. In contrast to the previous methods, in this process, the lapping step is omitted. Also, the parallelism between the anode and cathode electrodes is acceptable. Generally, the difference in the height of the spacers on both sides is defined by the photoresist pattern. Depending on the length of the nanowires, any deviation up to  $10\text{ }\mu\text{m}$  in the height of the spacers can be compensated by long nanowires in between. This will guarantee high precision in the parallelism of the system.

In Figure 7.8, copper pillars with  $60\text{ }\mu\text{m}$  height and  $50\text{ }\mu\text{m}$  edge length are shown. These copper pillars are fabricated with the technique introduced in this chapter. The wires have a diameter of  $1\text{ }\mu\text{m}$  and a length of  $10\text{ }\mu\text{m}$ . The length of such wires can vary between  $10\text{ }\mu\text{m}$  to  $50\text{ }\mu\text{m}$ . The copper pillars can play the role of spacers in an electron field emitter. An example of bonding a die with copper pillars on a pad covered with nanowires is shown in Figure 7.9. In this process, a standard manual pick and placer of the company Finetech is used. The chip is flipped and connected to a vacuum chuck. After adjusting the pillars, the chip is pressed on the surface with about 400 N.

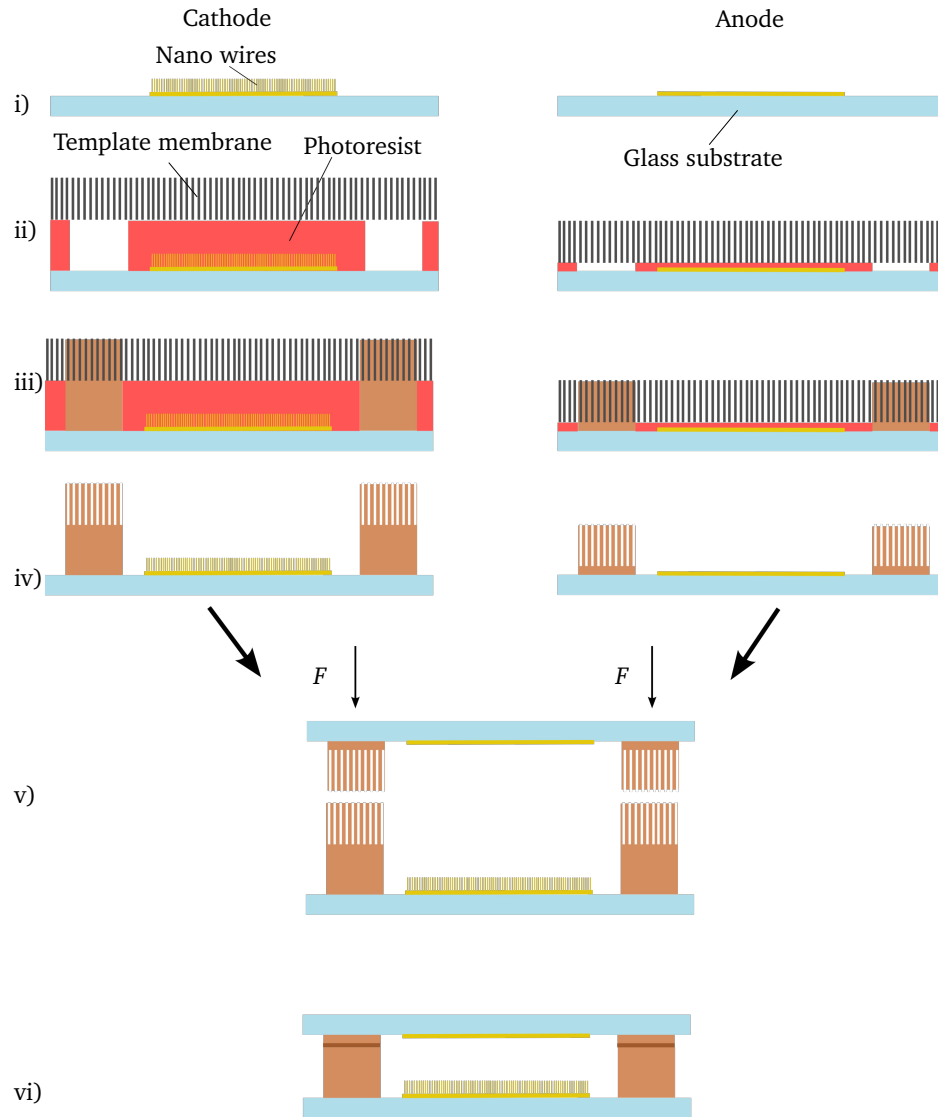


**Figure 7.7:** i) The nanowires are grown on the cathode and the anode electrodes. ii) The spacers and the contacting pads are shaped on both chips. iii) The nanowires are grown in an electrochemical deposition step on both electrodes. iv) The porous membrane and the photoresist are removed with proper chemicals. v) Two electrodes are adjusted and placed on top of each other and pressed via a pick and place machine. vi) The interconnection with a bond-line thickness of  $4\mu\text{m}$  to  $11\mu\text{m}$  is made. These interconnections are hermetically sealed connections.

To avoid any electrical current leakage between the cathode and anode through the metallic spacer, the surface of the cathode can be isolated by an initial sputtering of  $\text{SiO}_2$ .

### 7.3 Summary and outlook

The introduced idea in this chapter is a promising interconnection method, not only for the field emitter application but for mounting chips, dies, sensors, bus-bars, and even wafer-wafer bondings. Besides the mechanical connection, the connection via metallic nanowires has a high electrical and thermal conduc-

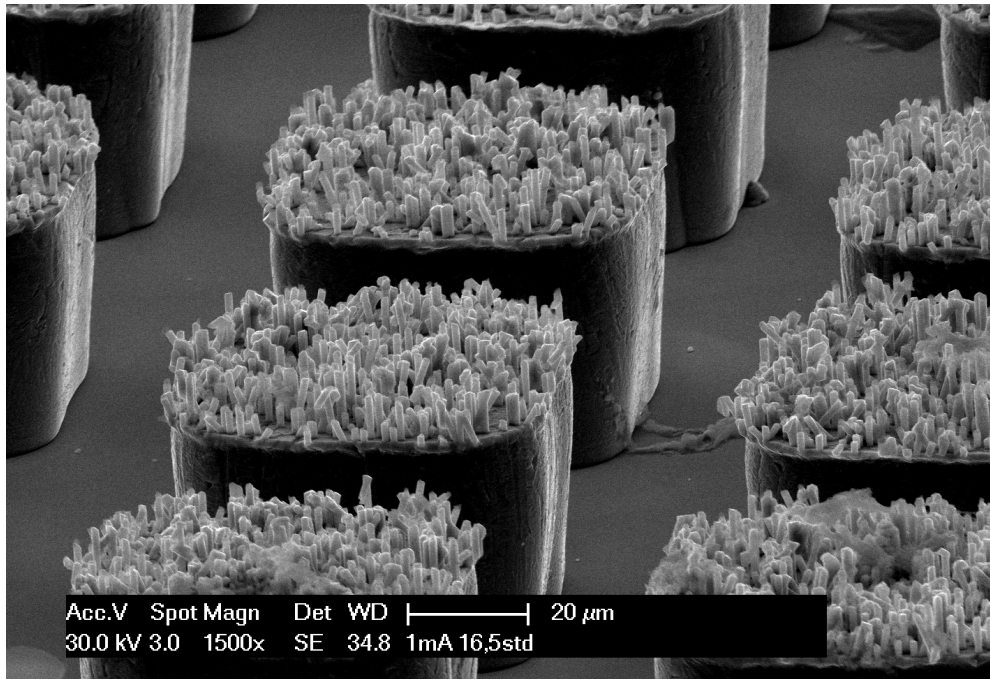


**Figure 7.8:** SEM image of copper pillars with 60 μm edge length, with nanowires grown consequently on the top.

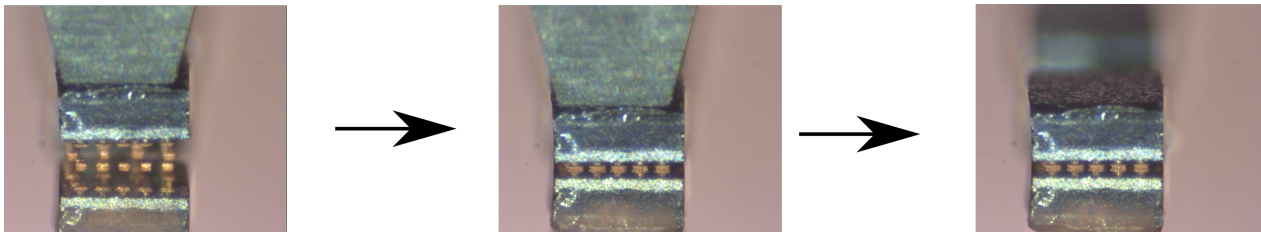


**Figure 7.9:** Bonding a diced chip with nanowired copper pillars on nanowired copper pads on a substrate. The chip is adjusted and pressed by a pick and place machine.

tance. Due to not using paste, adhesive, or alloy in the interconnection, conductance for copper nanowires can be in the range of bulk copper. The values of the shear strength, electrical and thermal conductances, and the lifetime of the connection need to be investigated. The brittleness, tightness, corrosion, and solidity against temperature shocks and vibration in such a connection must be studied as well. In Chapter 8, the shear strength of the interconnections will be discussed.

---

## 8 New room temperature bonding technology based on metallic nanowires

---

Joining two or more components has always been a major challenge in the fabrication of industrial products. For polymers and glass, gluing is a common solution. Besides screwing, punching, pressing, and deforming the materials, temperature treated processes, like welding and soldering, have also been widely used. Welding the structures is generally used for joining the same materials, while soldering or sintering is mostly used for joining two different metals to each other. In microelectronics, semiconductor, and packaging industries, many different bonding techniques for the joining and attachment of chips and dies on different substrates are used. Depending on the material properties, structures in the chips, and power consumption, one of the techniques will be chosen. These techniques are always a combination of proper adhesive or soldering substance, heat, and compression. For heat-sensitive processes, gluing or using conductive adhesive pastes like silver paste is a solution. Wire bonding combined with special gluing for electrical and mechanical bonding is a solution for devices containing gold and silicone in their structure to avoid gold diffusion in the substrate at higher temperatures.

Except gluing or using a conductive paste, and wire bonding via ultrasonic pressure, other techniques like soldering, welding, silver sintering, and reflow bonding need temperatures mostly higher than 300 °C under compression and in the presence of a reducing and inert gas. Also, in some cases, special alloys or silver nanoparticles with lower melting temperatures than the melting temperature of the pillars are needed. For stacking flip-chips on top of each other, different types of alloys are needed. These alloys must have different melting temperatures, and this is tied with high costs.

With further development in fabrication technologies, the density of electronic packages has increased too. Ball grid arrays (BGA) and land grid arrays (LGA) with a high density of connecting terminals enabled the higher miniaturization of the integrated circuits (IC). Fan-Out is one of the main solutions to fill the I/O gaps between the IC and PCB evolution. In this solution, the chip is embedded in a mold compound like epoxy, and the connecting terminals are fanned out using a redistribution layer (RDL). No PCB type layer is needed. The important competitors of this solution are fan-In solutions like wafer level chip scale packaging (WL-CSP) and flip-chip CSP (FCCSP) or flip-chip BGA (FCBGA). Anyway, all surface mounting technologies depend primarily on the high temperature treated processes like soldering, sintering, and reflow. Such processes raise the need of using new rare metals or toxic alloys. The environmental pollution caused by such metals and their recycling is a challenge. Furthermore, thermal processes have limited the technologies in terms of bumps and pitch sizes, and placement accuracy. Also, the electrical conductivity, shear strength, and the life cycle of the pads are affected by high temperature surface mounting processes. Especially fan-out packaging on panel level (FOPLP) is not adopted yet due to technical shortcomings in assembly and die placement on large panels. Furthermore, fabrication and mounting contact pads  $<10\mu\text{m}$  with pitches below  $10\mu\text{m}$  are still challenging. Using the introduced technique in Chapter 7 results in a unique bonding technique at room temperature without needing any multilayer system in the interconnection. No inert gas and under-fills are needed. With this technique, it is possible to connect any two metalized surfaces. For example, the heat-free joining of ceramic or steel with aluminum, bonding chips on flexible printed electronic polymer foils, or optical chips with pad dimensions from  $3\mu\text{m}$  to a whole 12-inch wafer and even larger panels would be possible. In such a heat-free metal joining technique,



the pillar pitches can even be reduced down to  $5\mu\text{m}$ . The shear strength and the electrical and thermal conductivity of the joint are the main properties of a connection. The shear strength of the connections based on nanowires and a method to increase the shear strength is studied in the next section.

## 8.1 Investigation on strength of nanowired connections

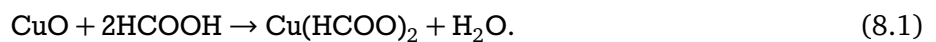
The appearance of NanoWired connections is the result of different physical effects. A single cylindrical wire with the radius  $r$  and the height of  $h$  has a lateral surface of  $2\pi rh$ . It is  $2\frac{h}{r}$  times larger than the base surface. It means for a single nanowire with 200 nm radius, the surface area for a wire length of  $25\mu\text{m}$  is 250 times larger than the base surface. This increase in the available surface area increases the net intermolecular attraction forces. Also, the number of wire diffusions increases with their density. Furthermore, the wires with a lower radius will diffuse at lower compression forces than the thicker wires. But, the thinner wires have a smaller base contact surface with the substrate. It means, that although they are entangled more, the peel force is less than those with a larger base surface. Thus, an optimal wire geometry and wire array density for the desired bonding force and the required shear strength must be detained. For most of the flip-chips, the compression pressure should not exceed 10 MPa and shear strength in the range of 15 MPa is required. For the initial investigation of the shear strength of the contacts with nanowires, an experiment is designed. In this experiment, at the first step, the influence of the bonding pressure, and the temperature on the shear strength will be investigated.

### 8.1.1 Experiment setup

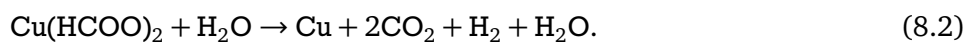
Generally, in all thermal joining techniques, the oxidation in the joint area is a reason for the weakness in the shear or tensile strength. Also, the oxidation in the interconnection has an impact on the electrical conductance of the connection. Higher energy dissipation in the contact area reduces the lifetime of the connection too. The oxidized regions in the connection will also speed up the corrosion. To avoid this problem, in industrial processes, two steps are carried out:

1. Preparing the surface by removing the oxide layer,
2. Preventing further oxidation at higher temperatures during the welding process.

The copper oxide does not dissolve in water. For removing the oxide layer on the surfaces of bond pads, one possibility is to use a so-called flux as a chemical cleaning agent. For example, a thin water solution of hydrochloric acid or sulfuric acid can be used. These solutions respectively transform the copper oxide into copper(II) chloride and copper(II) sulfate. Both compounds are easily soluble in water. The problem with such a cost-efficient wet process is removing the rest of the acid from the surface and drying the samples. Therefore in the semiconductor industry for bonding copper pillars the formic acid vapor is widely used as a standard process [118]. In presence of formic acid, the copper oxide on the surface is transformed into a copper salt. The chemical reaction is



Now by increasing the temperature in the range of  $150^\circ\text{C}$  to  $200^\circ\text{C}$  the copper salt transfers into copper as





The advantage of this process is the transformation of the copper oxide into copper instead of removing the oxidized copper. In contrast to using wet chemicals, the thin layers of copper with 100 nm thickness can be processed safely. But the disadvantage of this process is the need for higher temperatures. At higher temperatures, an inert gas is required. Thus, always a combination of nitrogen gas and formic acid vapor is used. For this purpose, a bonding chamber and a bubbler system are designed and constructed. This system is shown in Figure 8.1. The technical design of the device can be found in Appendix C.2. As shown in Figure 8.1b, the chamber is covered with a heat protection cover from Teflon. The top cover is sealed with a sealing ring, mounted in the Teflon cover. Two 200 W cartridge heaters and one W-EYK6 PT1000 temperature sensor are mounted inside the pressing plate. A gas inlet, for entering the gas mixture, and a gas outlet, as an exhaust, are added to the pressing plate. A press tool goes through the top cover to press the joint partners. For sealing the press tool, a Teflon ring is mounted on the top cover. It wears the press tool to prevent the leakage of the acid vapor. In the bubbler system shown in Figure 8.1(c-d), the

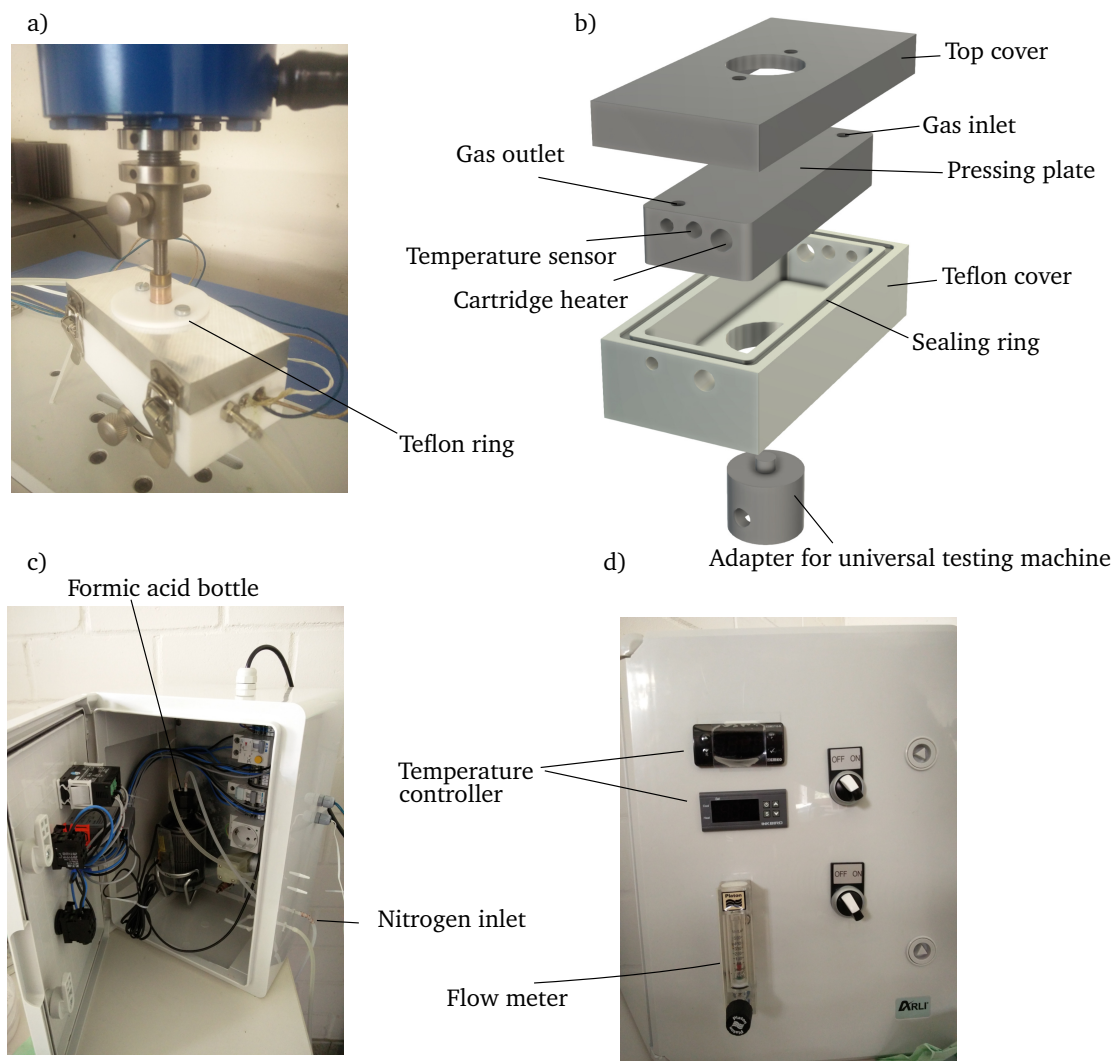


**Figure 8.1:** a) The formic acid chamber is mounted on a universal testing machine. b) The different parts of the chamber. c), d) The bubbler system. The formic acid is heated in the bottle and by flowing a controlled amount of nitrogen in the bottle and bubbling in the acid, a mixed vapor of nitrogen acid will flow out of the bottle into the chamber.

percentage of the acid in the gas mixture varies between 5% to 10% depending on the nitrogen flow rate and the acid temperature. The temperature of the acid bottle and the chamber are controlled by two PID temperature controllers. The nitrogen flow rate is controlled with a flow meter. As shown in Figure 8.2a, for measuring the shear strength of a NanoWired interconnection, oxygen free copper (OF-Cu, CW008A) strips with 0.3 mm thickness and a length  $L$  of 34 mm are prepared. The area covered with the nanowires is about 5 mm  $\times$  5 mm. As the strips are cut with a hand cutter, the exact contact area is measured individually for each sample after performing the test. One other reason for this post measurement is the inaccurate manual adjustment of the samples on the pressing plate. The strips are placed on top of each other in the process chamber (Figure 8.2b). The process chamber is mounted on a 5000 N universal testing machine of the company Hegewald & Peschke (see Figure 8.1a). After the samples are pressed and prepared, the same testing machine is used for measuring the shear strength of the samples (see Figure 8.2c). Although for a complete copper oxide transformation into copper, a chamber temperature higher

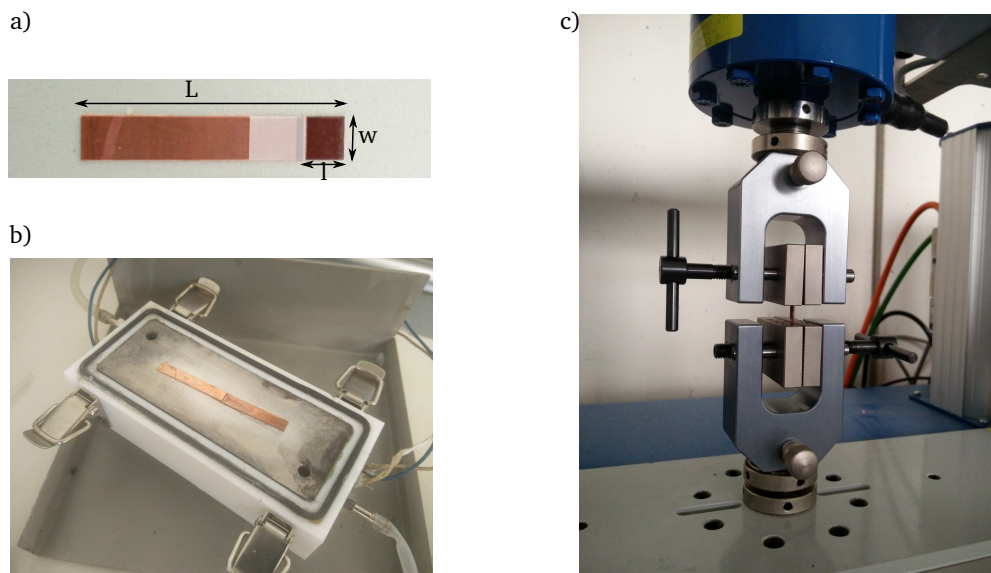


**Figure 8.2:** a) Dimensions of the samples. The length  $L$  is 34 mm and contact surface  $l \times w$  about 5  $\times$  5 mm<sup>2</sup> b) Both joint partners are placed on the pressing plate c) Measuring the shear strength of the metallic copper samples with a universal testing machine

than 150 °C is needed, for retaining the core competency of this technology and working at low temperatures, it is decided to work on temperatures below 100 °C. At such temperatures still, the transformation of copper oxide takes place, but not completely.

### 8.1.2 Results and specifications: shear strength of NanoWired connections

The initial tests, without any flux and at room temperature showed that the NanoWired interconnection does not exceed a shear strength of 10 MPa, even by a bonding pressure of 140 MPa. In the next step, optical analysis of the samples in contact with gas mixtures at different gas and chamber temperatures shows an obvious oxide reduction on the surface of the samples after 20 min at gas and chamber temperatures of 80 °C. Such a sample before and after the treatment is shown in Figure 8.3. In the first experiment, the influ-

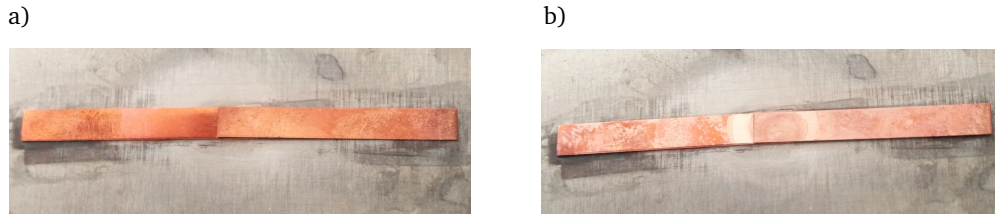


**Figure 8.3:** a) Before formic acid treatment b) after formic acid treatment and oxide reduction

ence of the bonding pressure on the shear force is explored. In Figure 8.4, the measurement results at the gas and chamber temperature of 80 °C are shown. The values in this measurement are the mean value of 5 samples for bonding forces of 250 N and 500 N to 350 N, in 500 N steps. It is equal to bonding pressures of 10 MPa to 150 MPa. At an initial pressure of 10 MPa, none of the samples were connected. The reason is the wavy surface of the samples. The low pressure can not flatten this wave and the nanowires cannot meet each other. It does not happen on rigid, flat, and polished materials like silicon or glass chips. The first rise in the values takes place at the pressure of 20 MPa. Up to 100 MPa bonding pressure, the shear force strength is in the range of 10 MPa. The reason is, that the wave-like shape of the samples is still not completely flattened. The minimum pressure needed to flatten the samples is about 100 MPa. At bonding pressures higher than 100 MPa the shear strength increases and a maximum value of 17 MPa is reached. This value is higher than 10 MPa shear strength without using any formic acid at about 140 MPa bonding pressure. In the next step, the influence of two other parameters, the gas mixture and the chamber tem-

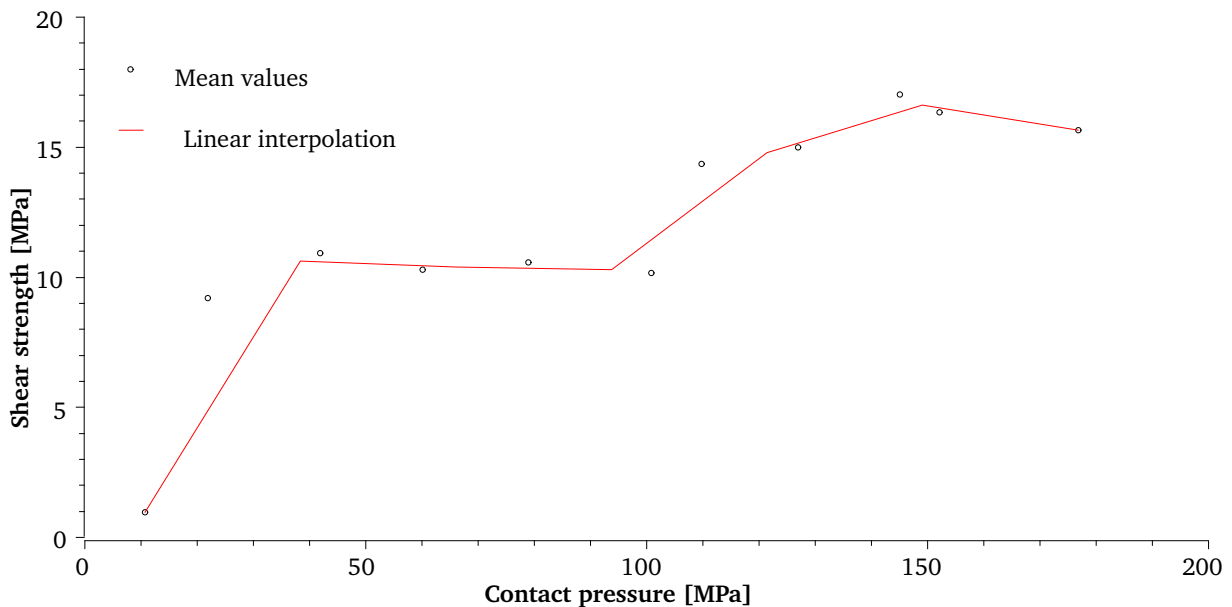


**Figure 8.4:** Shear strength measurement by varying the contact pressure

perature on the shear force strength are investigated. The results are shown in Figure 8.5. For all samples a bonding force of 3000 N, with a force increase rate of  $100 \frac{\text{N}}{\text{s}}$ , is applied. At a chamber temperature of 80 °C, a 5% increase in the shear strength by increasing the gas mixture temperature from 65 °C to 95 °C is obvious. A maximum shear strength of 18 MPa is reached at 95 °C.

By keeping the gas mixture temperature constant at 80 °C and changing the chamber temperature, it is shown that the shear strength by 3000 N bonding force has a mean value of 10 MPa. By increasing the chamber temperature, the shear strength increases as well. At higher temperatures of about 90 °C a maximum value of 20 MPa is reached. The reason for this increase is a combination of a higher oxide reduction rate in the copper nanowires and a higher diffusion rate between the wires.

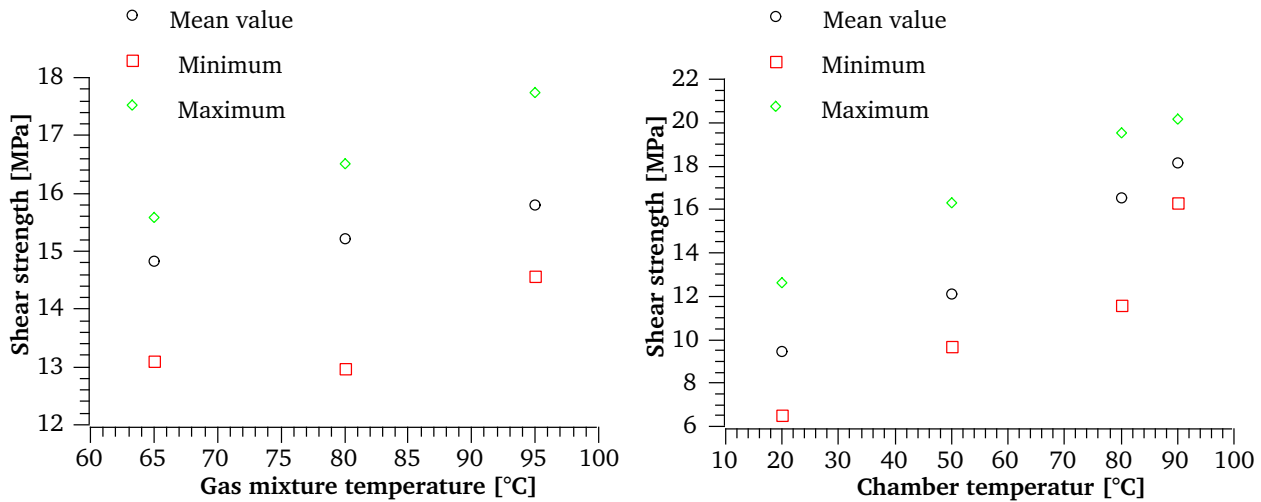


**Figure 8.5:** Shear strength measurements by changing the gas mixture and chamber temperatures

## 8.2 Progress in nanowires based bonding technique: KlettWelding, KlettSintering, KlettGlueing

Based on the developed nanowired interconnection technology, during this thesis, the company NanoWired GmbH was founded, and this type of interconnection as a new technology is commercialized. Further investigations lead to a better performance of the hook-and-loop fastener with the commercial name of KlettWelding. By performing the KlettWelding process at temperature ranges of 170 °C to 230 °C, the so-called KlettWelding+, the shear strength of the bondings increases up to 115 MPa. The shear strength in association with the bonding pressure at 230 °C is shown in Figure 8.6 It is shown that for some use cases, the sintering process also works when just one joint partner is covered with nanowires. By pressing a nanowired and a flat surface together and tempering for 10 s to 120 s a maximum shear strength of about 50 MPa is achieved. For temperature-sensitive samples, it is also possible to use an adhesive material as an underfill or for better sealing in the interior cavities and also as an extra sticking medium in the contacts. Especially the KlettGlueing can be done with just one nanowired surface and pressure of about 1 MPa, without any impact on the electrical conductance of the connection. For KlettGlueing, a drying temperature of about 70 °C to 170 °C, depending on the under-fill material is needed. Another possibility to use nanowires in the interconnection technology is to cover both sides of a copper film with nanowires, the so-called KlettWelding-Tape (KWT). The KWT can be cut or punched in the desired dimension with a standard cutting machine or even scissors. The bonding can be done by putting the KWT between the two surfaces and applying the same pressure/temperature conditions as the KlettSintering. An image of

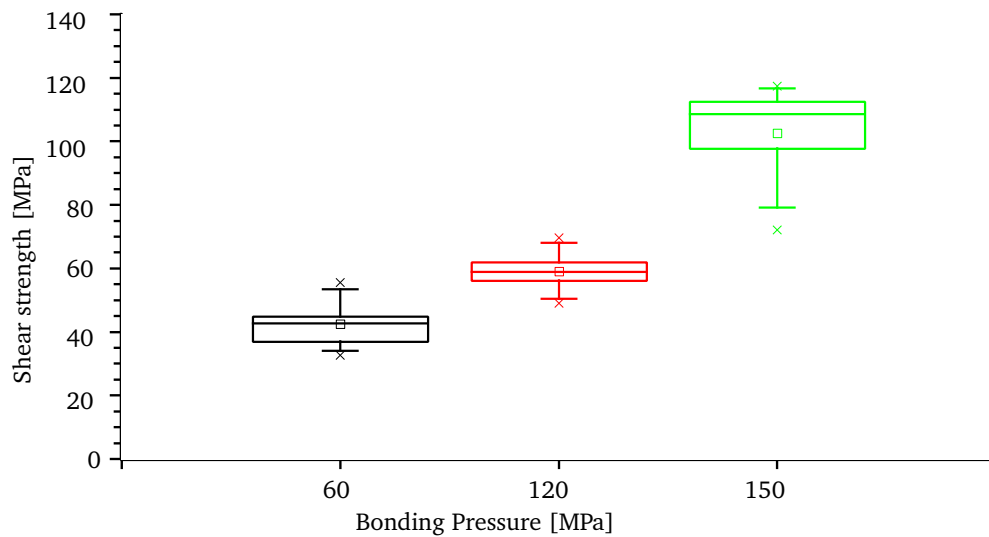


**Figure 8.6:** Shear strength of the OF-Cu bus bars. The shear strength increases by bonding pressure [11].

KlettWelding-Tape is shown in Figure 8.7 The properties of the developed technologies in the company

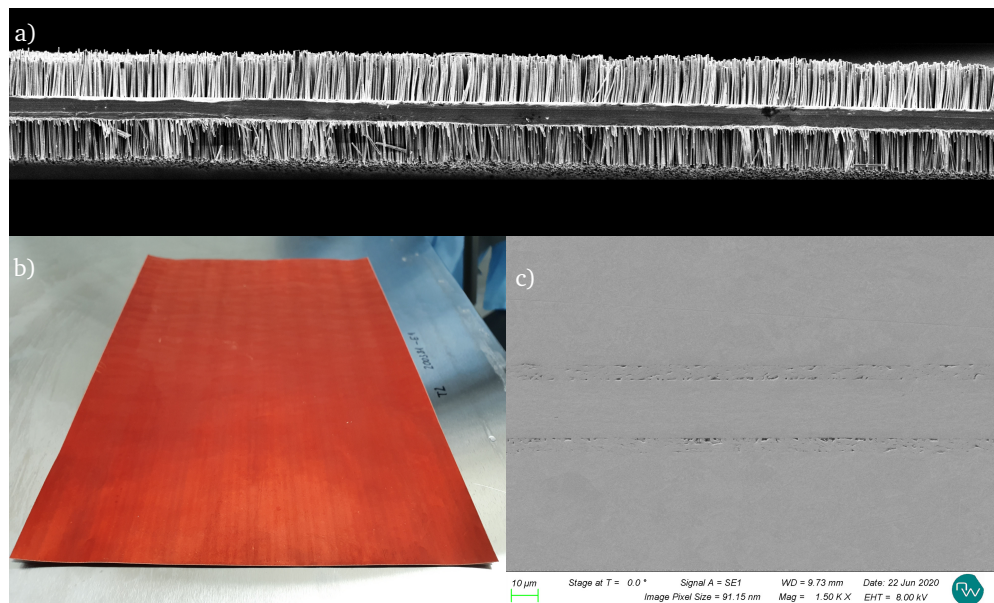


**Figure 8.7:** a) SEM cross-section image of a KlettWelding Tape. The nanowires are grown on both sides of a copper foil. b) An optical image of a DIN-A4 KlettWelding-Tape. c) The cross-section SEM image of the connection with KlettWelding-Tape at 230 °C. The bond-line thickness is about 28  $\mu\text{m}$  including the 20  $\mu\text{m}$  copper foil thickness. [11].

NanoWired GmbH are listed in Table 8.1. A 4-point electrical resistance measurement of seven KlettWelding+ samples with a HIOKI RM3545-02 DC resistance meter delivers a maximum measured resistance of 1.5  $\mu\Omega$  for a contact surface of 20 mm<sup>2</sup>.



**Table 8.1:** Properties of different methods for bonding with NanoWired surfaces [11].

Method	Bonding Pressure [MPa]	Bonding Temperature [°C]	NanoWiring	Shear strength [MPa]
KlettWelding	15 - 60	21	Both sides	15 - 18
KlettSintering	10 - 60	170 - 270	One side	37 - 50
KlettGlueing	1 - 10	140	One side	15
KlettWelding+	10 - 150	170 - 270	Both sides	40 - 115
KlettWelding-Tape	10 - 60	170 - 270	-	40 - 60

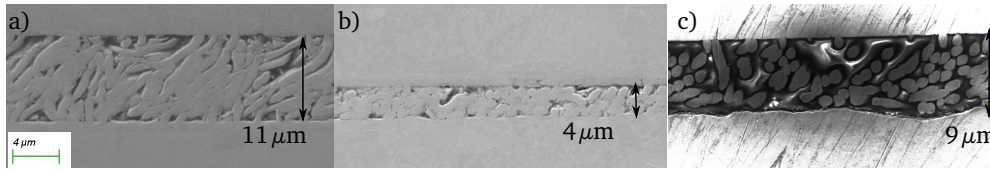


**Figure 8.8:** Cross-section images of the bond lines of different technologies. a) KlettWelding at room temperature with the bond line thickness of 11  $\mu\text{m}$ . b) KlettSintering with 4  $\mu\text{m}$  thickness. c) KlettGlueing with 9  $\mu\text{m}$  thickness [12].

### 8.3 Summary and outlook

The measurements in this chapter show that the NanoWired interconnection is a reliable alternative for conventional joining technologies in the semiconductor and microelectronics industry. The nanowired connection at low temperatures below 250 °C can reach shear strength of about 40 MPa to 115 MPa. The bonding process at room temperature, after treatment with a reducing agent, results in shear strength of about 20 MPa. For many semiconductor applications, a value between 12 MPa to 20 MPa is acceptable. Further investigations at the NanoWired GmbH company show that the annealed interconnections are hermetically sealed. In the future, an statistical investigation on more samples and also investigating the connection in different conditions like corrosive ambient and also temperature shock and thermal-humidity stress tests are necessary for certifying and industrializing this technology. This technology is advantageous for XHV and cryo applications. The contacts can tolerate temperatures up to the melting temperature of the bulk material (e.g. 1360 K for copper). The pure metallic nature of the interconnect and the hermetic seal interconnects will reduce the outgassing rate of the connections as well.



---

## 9 Conclusion and outlook

---

The studies in this thesis are dedicated to the synthesis and applications of metallic wires and cones with sub-micrometer diameters. The objective is the preparation of an on-chip electron field emitter for measuring a vacuum pressure below  $10^{-12}$  mbar in a cryogenic regime. After reviewing the state-of-the-art technologies in vacuum measurement, it is theoretically shown that vertical metallic nanowires with a high aspect ratio  $>50$  and sharp tips can improve the functionality of the field emitter based vacuum pressure gauges. The practical part of the thesis is divided into three segments:

1. The synthesis, integration, and geometry manipulation of the wires and cones.
2. Investigation on the field emission properties of nanocones.
3. Development of a novel room temperature bonding technique for anode/cathode montage and exploring its physical and mechanical properties.

During this work, the industrialization of the process is in focus. For this purpose, continuously the used chemicals and processes are substituted by standard industrial ones and the process is scaled up to standard wafers and panel sizes. As well the number of steps for the fabrication and integration of the wires and cones is reduced.

---

### 9.1 Synthesis and integration of the nanowires

---

The primarily developed technique at the Institute EMK had enabled the in-situ integration of nanowires into a microsystem. It was possible to grow nanowires with various diameters on a surface less than  $10\text{ mm} \times 10\text{ mm}$ . In this technique, the surface had to be divided into an array of blocks with  $300\text{ }\mu\text{m}$  edge length. Thus, covering the whole surface and homogeneous growth of the wires was not possible. Nevertheless, compared to the developed techniques of other groups for integrating nanowires into a system, it was a promising progress.

During this thesis, the available process is explored and further developed. The achieved nanowiring progress is shown in Figure 9.1. In the first stage, the inhomogeneous synthesis and integration of the nanowires are improved in terms of coverage and wire length. It led to a controlled growth of pads with sharp edges and a homogeneous growth of nanowires, while the number of steps is reduced and the process is less time consuming. The surface size is increased to  $30\text{ mm} \times 30\text{ mm}$  with the pads edge-lengths over  $500\text{ }\mu\text{m}$ . Still, some undesired fabrication steps, like needing an array of blocks for laminating the template-membrane on the structure or wetting the system were required.

In the second phase of the project the fabrication process was further optimized and the array of blocks was omitted. This was done in a newly developed deposition bath with an integrated spring force system, which was also developed during this thesis. With these achievements, larger surfaces can be covered with nanowires and no lamination of the template-membrane is necessary. As shown in Figure 9.1c, a DIN-A4 sheet of copper foils is homogeneously covered with nanowires. For optimizing the process and developing the new deposition devices, more than 300 wafers and copper sheets were processed and analyzed. The evaluation of the devices developed during this thesis is shown in Figure 9.2. After successful

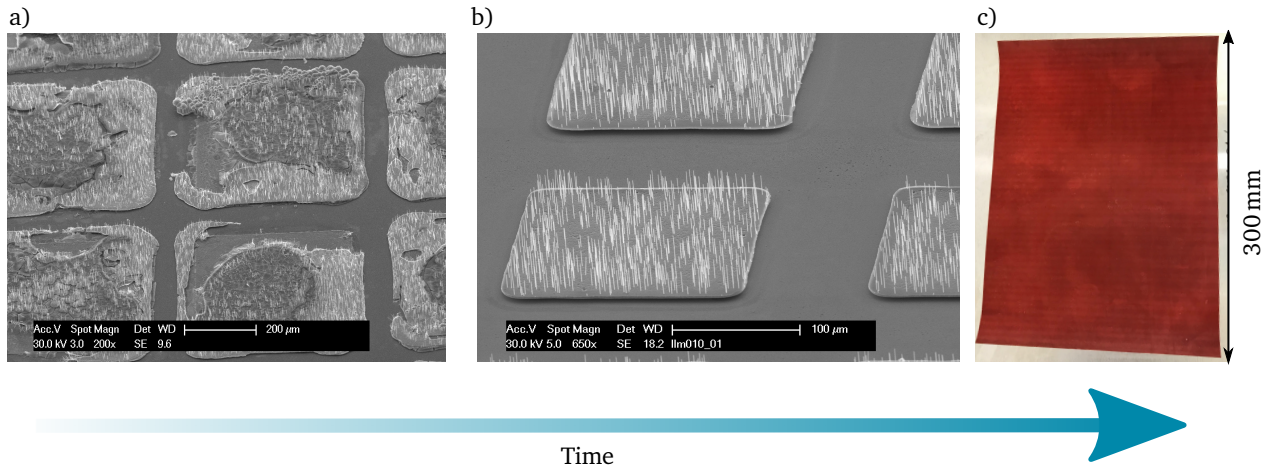


**Figure 9.1:** Time line of technology optimization during this thesis: a) Increasing total surface area to 30 mm × 30 mm as an array of 500 μm pads. b) Optimizing the process for a homogeneous growth of the wires, free of any defects across the whole surface area. c) Further optimization for scaling up the process to 300 mm × 300 mm surfaces and eliminate the need for pads. In addition, the covering of both sides of wafers, panels, and PCBs were enabled.

development and testing of the 300 mm × 300 mm device, the technology was transferred to the semiconductor, microelectronics, sensor, lighting, and automotive market through NanoWired GmbH, a company that was founded as a spin-off of the TU Darmstadt. After founding the company, a semi-automatic industrial prototype of the NanoWiring production machine with a containment system for managing the electrolyte and the electrical control unit and software was developed. Also, a fully-automated version of the machine with an integrated containment system was designed and developed.

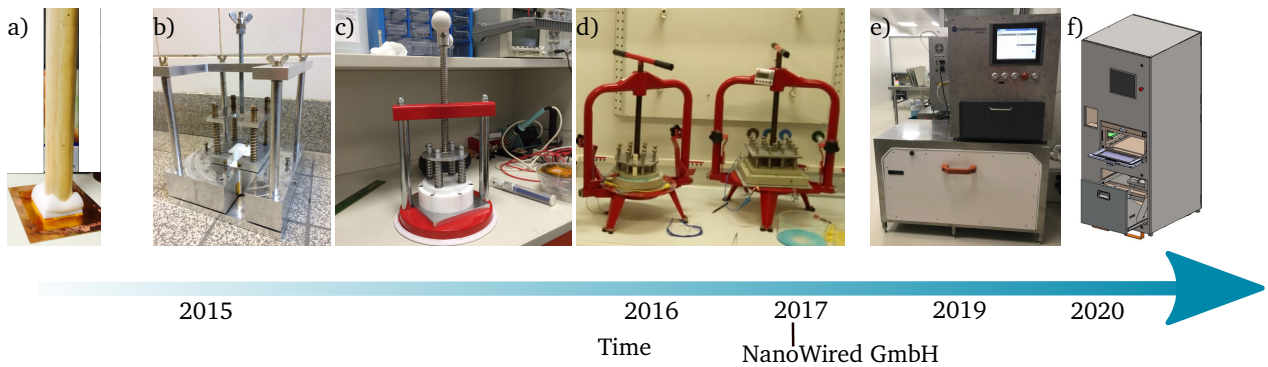


**Figure 9.2:** Evaluation of NanoWiring devices and machines: a) Idea phase before designing a pressing mechanism. b) First spring device with 30 mm × 30 mm bath. c) Scaling the device to a 4-inch wafer bath while using commercially available parts. d) Scaling up the device to 8-inch and 300 mm × 300 mm. e) Semi-automatic industrial prototype of the NanoWiring production machine with a containment system. f) Full automated production machine

Due to the better thermomechanical stability of the conical geometry at high electrical fields in an electron field emitter, during this thesis the cylindrical nanowires are tailored into conical shapes (see Figure 9.3a). For controlling the apex angle of the cones a template membrane etch device was designed and fabricated. With this device, more than 250 template samples were etched and in SEM controlled. Also,

more than 50 samples are electrochemically deposited and in SEM investigated. Two examples of the conical structures with different apex angles are shown in Figure 9.3. The new technology developed in

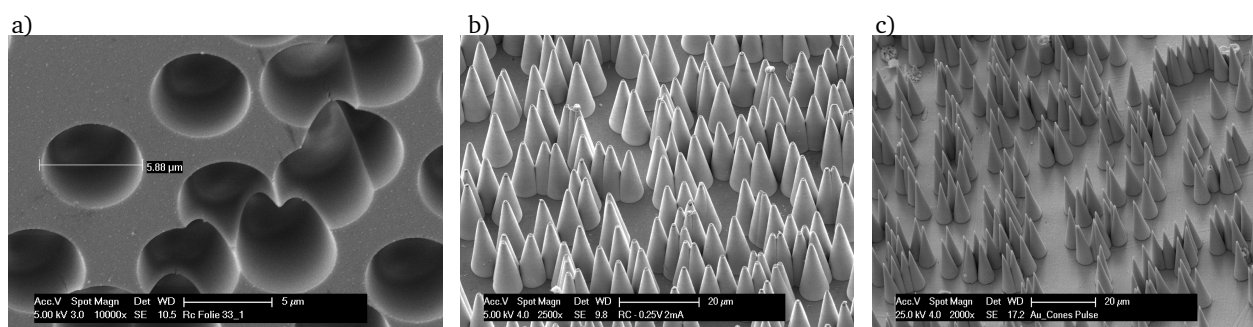


**Figure 9.3:** a) SEM image of an asymmetrically etched template membrane b) Nanocones with a base radius of  $6\mu\text{m}$ . c) Gold nanocones with a base radius of about  $4\mu\text{m}$

this thesis for integrating metallic wires and cones into different systems enables many applications like biological sensors. For example, the gold nanowires can be used as a blood cholesterol sensor [119] or as nanorod for performing biological analysis [120] or as an interface for in-vitro growth of the stem cells on gold nanowires and electrical stimulation of them to derive the reaction potential of the cells [121]. Also, the nanowires can be used as gas flow sensors [79] or chemical detectors for different types of gases [117]. Another application of the sub-micron gold wires is high performance micro-newton electronic switch. In such switches, the contact resistance is reduced by reducing the so-called A-Spots (surface of the contact points) [122]. It leads to a high electrical conductivity at lower contact forces. Two more applications of nanowires and cones are explored in this thesis. One is a better performance of the metallic nanocones as electron field emitters and the other one is a room temperature electrical and mechanical interconnect for semiconductors.

## 9.2 Field emission properties of nanocones

During this thesis, a variety of nanocones samples are fabricated. The field emission characteristics of the samples were investigated in a field emission scanning microscope and an integral measurement system with a luminescent screen in the diode and triode setup. The first measurements showed significantly that using a high dense array of nanocones in the range of  $10^6\text{ cm}^{-2}$  reduces the enhancement factor and respectively the achieved maximum field emission current. The appearing screening effect by using high density nanocones results in local destruction of overheated emitting cones. Reducing the density of the nanocones leads to some fabrication problems (see Figure 9.4). For example tension forces exerted on the cones during the wet chemical stripping process break the alone standing nanocones. This problem was solved by dry etching of the template membrane in a plasma ashing machine. The low density of the nanocones with tip diameter below 100 nanometer results in an ion-depletion during the electrochemical deposition. This problem was solved by using the spring device and applying more movements in the electrolyte fluid during the deposition process. A measurement on low density array of nanocones in the range of  $10^4\text{ cm}^{-2}$  to  $10^5\text{ cm}^{-2}$  showed a stable current emission of  $31\mu\text{A}$  for 50 h at an applied voltage of 290 V and  $100\mu\text{A}$  to  $140\mu\text{A}$  at an applied voltage of 338 V. For these samples, a maximum current

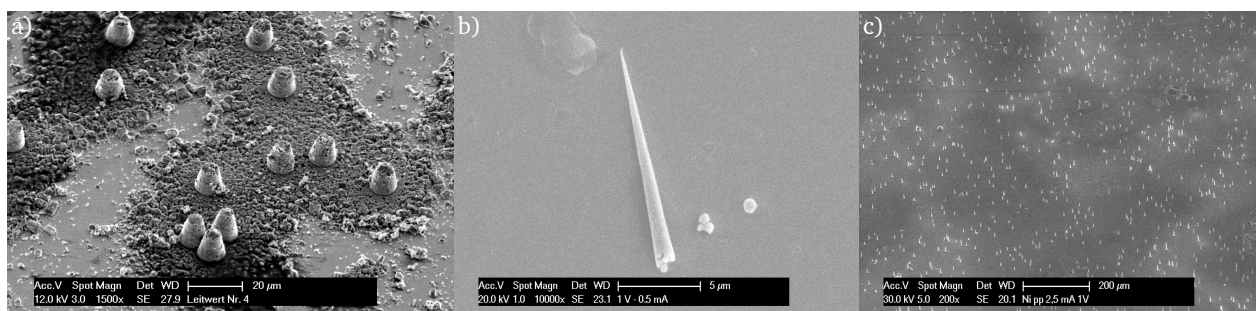


**Figure 9.4:** a) Ion-depletion by deposition of low density nanocones with small tip openings leads to incomplete growth of cones b) A broken cone by tension forces during the wet chemical stripping process. c) Successful fabrication of conical structures with low density on a large surface with a spring device. The number of broken cones is minimized.

density of  $2900 \mu\text{A cm}^{-2}$  was measured. This current is sufficient to apply this structure in a field emitter based vacuum gauge. Reducing the extraction voltage down to 100 V can be energetically a meaningful advantage for measurements in cryogenic systems. For this purpose a proper extraction grid design is required. To find the maximum current density at lower extraction voltage, the optimum grid transmission factor and the height of the grid must be simulated and calculated. One possibility for increasing the lifetime of the emitting nanocones is to cover the gold or copper nanocones with refractory metals such as W, Mo, Ta, and Re.

### 9.3 Room temperature KlettWelding bonding technology

To complete the structure of the field emitter, the extraction grid must be attached over the nanocones, at a controlled height, and with maximum parallelism. Furthermore, the used material and process must be XHV suitable and not outgassing in the vacuum environment. For this purpose, a hook-and-loop fastener based on metallic nanowires is developed. By growing the nanowires on the substrate and also on the extraction grid, both surfaces can be bonded just by pressing them on top of each other at room temperature. For a controlled height and maximum parallelism, the spacers can be grown electrochemically at one step with the nanowires. The achieved connection is free of any paste, multilayer material, and cavity in the junction. It makes them suitable for XHV and low cryogenic temperatures.

During this thesis, the electrical and mechanical properties of such connections have been investigated. This new interconnect technology, so-called KlettWelding can be used as a solution in different electronic and semiconductor, and packaging applications. With this technique, the pitch sizes and the pad sizes can be reduced below  $5 \mu\text{m}$ . Some examples of NanoWirings on contact pads and copper pillars are shown in Figure 9.5. The properties of the connection are listed in Table 9.1 The electrical resistance of such connections is comparable with pure bulk copper. The shear strength is about 24 MPa. The KlettWelding connection can be used in different ways. It can be combined with an adhesive material like glue to reduce the bonding pressure. By using glue in the connection, the NanoWiring can be performed on just one surface. The nanowires will ensure a high electrical conductance in the connection while the gluing is responsible for the mechanical strength. In a KlettWelding connection, by tempering the connection with



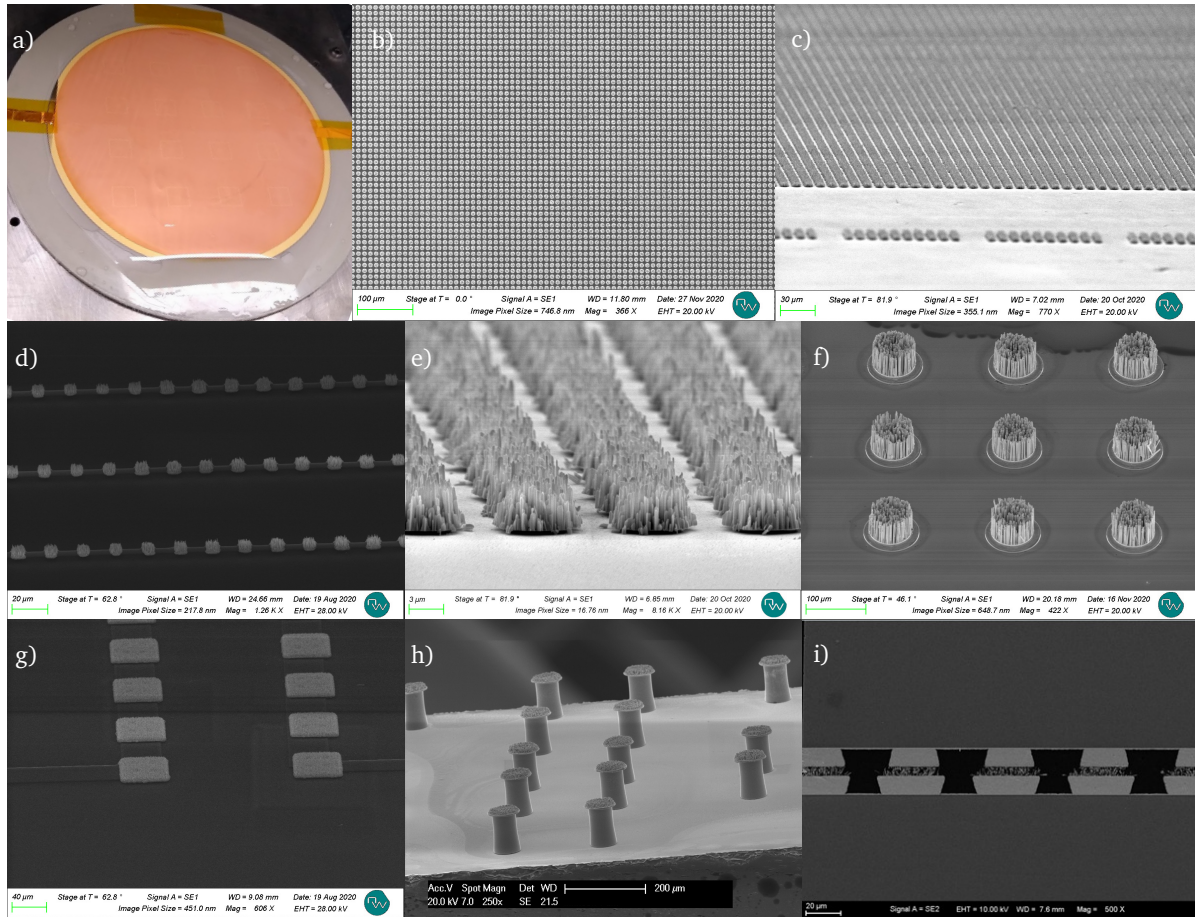


**Figure 9.5:** Different types of a NanoWiring: a) Entire wafer covered with nanowires. b), c) SEM Images of fine pitch pads on a wafer. d) Pads with  $4\mu\text{m}$  edge length and  $110\mu\text{m}$  pitches. e)  $5\mu\text{m}$  pads with  $3\mu\text{m}$  pitch f)  $50\mu\text{m}$  pads with  $100\mu\text{m}$  pitch. g)  $100\mu\text{m}$  pads as fan out solution h)  $50\mu\text{m}$  copper pillars on a die with nanowires on them i) Cross-section image of a die with  $5\mu\text{m}$  pads bonded directly on a wafer [13]

a temperature in the range of  $170^\circ\text{C}$  to  $230^\circ\text{C}$  the diffusion process is enhanced. It leads to higher shear strength in the range of  $40\text{ MPa}$  to  $70\text{ MPa}$ . It is also possible to temper the connection with NanoWiring on just one surface. As shown in Figure 9.1c, a copper foil covered with nanowires on both sides can be used between two surfaces to bond them at a temperature in the range of  $170^\circ\text{C}$  to  $230^\circ\text{C}$ . With this technology, a heavy-duty connections for high power applications like bus-bars or battery connection can be performed. As shown in Figure 9.6, a long-time aging test shows that more than 1000 temperature cycles between  $-40^\circ\text{C}$  to  $150^\circ\text{C}$  and more than 4000 h storage in a climate simulation chamber at  $85^\circ\text{C}$  and  $85\%$  humidity has no impact on the electrical and mechanical properties of the connections. Another application of such connection is wafer to wafer (W2W) and die to wafer (D2W) bonding. Using long nanowires for connecting the pads eliminates the chemical-mechanical polishing (CMP) process for planarization and smoothing the the surfaces of the wafers which is a time-consuming and costly method for W2W bonding. In this thesis, important steps for integration of nanowires and nanocones on broad surfaces and also controlling the geometry of the nano objects are taken. Miniaturizing a field emitter with developed techniques in this thesis is feasible. Also, mass production of FE cathodes and a heat-free

**Table 9.1:** Properties of nanowired contacts

NanoWiring material	gold, copper, nickel, tin, silver
Bond-line thickness	4 $\mu\text{m}$ to 12 $\mu\text{m}$
Min. Pad size	3 $\mu\text{m}$
Max. Pad size	300 000 $\mu\text{m}$ $\times$ 300 000 $\mu\text{m}$
Bonding temperature	21 $^{\circ}\text{C}$ to 230 $^{\circ}\text{C}$
Bonding pressure for flip-chips	1 MPa to 20 MPa
Bonding pressure for metallic bars	30 MPa to 70 MPa
Bonding time	60 ms
Temperature tolerance of contacts	6 K to 800 K
Contact resistance	$< 1 \mu\Omega \text{ mm}^{-2}$
NanoWiring temperature	21 $^{\circ}\text{C}$ to 65 $^{\circ}\text{C}$
Substrates	ceramic, polymer, FR4, Glas, Si, Metal

anode/cathode montage is enabled during this thesis. The new bonding technology needs to be investigated under load in terms of solidity and corrosion resistance. However, the achieved results in this thesis have shown that this new technology has the potential to substitute different bonding technologies in the semiconductor packaging industry.



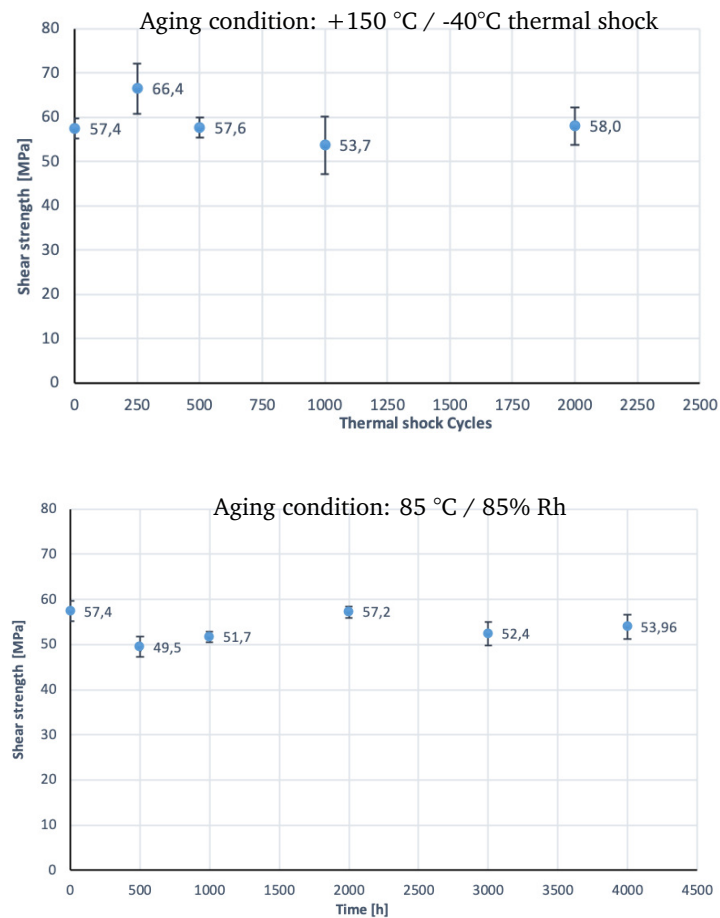


**Figure 9.6:** Measured shear strength after aging the samples. After 1000 thermal shocks and 4000 hours in the WK 111-600 climate simulation chambers of the company Weiss Technik at 85°C / 85%Rh no significant drop in the shear strength of the samples is observed. An EDX test detected no traces of oxide in the center of the KlettSintering connections. [13]

---

## Bibliography - Own Inventions and Patents

---

- [1] H. F. Schlaak, S. Quednau, O. Birlem, F. Roustaie, and F. Dassinger. “Anordnung von Halbleiterchips und Verfahren zur Herstellung davon”. Pat. DE102017104902A1. Mar. 2017.
- [2] S. Quednau, F. Roustaie, F. Dassinger, O. Birlem, and H. F. Schlaak. “Messanordnung und Verfahren zum Messen von Eigenschaften eines strömenden Mediums”. Pat. DE102017104904A1. Mar. 2017.
- [3] O. Birlem, S. Quednau, F. Roustaie, F. Dassinger, and H. F. Schlaak. “Anordnung und Verfahren zum Bereitstellen einer Vielzahl von Nanodrähten sowie Galvanikkapsel”. Pat. DE102017104905A1. Mar. 2017.
- [4] S. Quednau, F. Roustaie, F. Dassinger, O. Birlem, K. Wick, and H. F. Schlaak. “Anordnung und Verfahren zum Bereitstellen einer Vielzahl von Nanodrähten”. Pat. DE102017104906A1. Mar. 2017.
- [5] S. Quednau, O. Birlem, F. Roustaie, F. Dassinger, and H. F. Schlaak. “Anordnung miteinander verbundener Bauelemente sowie Verfahren zur Verbindung von Bauelementen”. Pat. DE102018122007A1. Mar. 2017.

---

## Own publications

---

- [6] F. Roustaie, S. Quednau, F. Dassinger, H. F. Schlaak, M. Lotz, and S. Wilfert. “In situ synthesis of metallic nanowire arrays for ionization gauge electron sources”. In: *Journal of Vacuum Science & Technology B* 34.2 (Jan. 2016), 02G103.
- [7] F. Roustaie, S. Wilfert, S. Quednau, F. Dassinger, M. Lotz, and H. F. Schlaak. “Strukturierung von Elektronen-Feldemitter auf Basis metallischer Nanodrähte”. In: *GMM-Fachbericht: Mikro-Nano-Integration*. Vol. 81. Ilmenau, 2014, pp. 118–123.
- [8] F. Roustaie, J. Bieker, R. Cicek, and H. F. Schlaak. “Novel fabrication method for integration of template grown metallic nanocones with controllable tip diameter and apex angle”. In: *Microelectronic Engineering* 180. Supplement C (Aug. 2017), pp. 81–85.
- [9] J. Bieker, F. Roustaie, H. F. Schlaak, C. Langer, and R. Schreiner. “Field emission characterization of in-situ deposited metallic nanocones”. In: *2017 30th International Vacuum Nanoelectronics Conference (IVNC)*. July 2017, pp. 120–121.
- [10] J. Bieker, F. Roustaie, H. F. Schlaak, C. Langer, R. Schreiner, M. Lotz, and S. Wilfert. “Field emission characterization of in situ deposited gold nanocones with variable cone densities”. In: *Journal of Vacuum Science & Technology B* 36 (2018), p. 02C105.
- [11] F. Roustaie, S. Quednau, F. Dassinger, and O. Birlem. “Room Temperature Interconnection Technology for Bonding Fine Pitch Bumps Using NanoWiring, KlettWelding, KlettSintering and KlettGlueing”. In: *2020 15th International Microsystems, Packaging, Assembly and Circuits Technology Conference (IMPACT)*. 2020, pp. 168–171.
- [12] F. Roustaie, S. Quednau, F. Weißenborn, and O. Birlem. “Low-Resistance Room-Temperature Interconnection Technique for Bonding Fine Pitch Bumps”. In: *Journal of Materials Engineering and Performance* 30.5 (Mar. 2021), pp. 3173–3177.
- [13] F. Roustaie, S. Quednau, F. Weissenborn, O. Birlem, D. Riehl, X. Ding, A. Kramer, and K. Hofmann. “Room Temperature KlettWelding Interconnect Technology for High Performance CMOS Logic”. In: *2021 IEEE 71st Electronic Components and Technology Conference (ECTC)*. IEEE, 1 June–4 July 2021, pp. 371–376.
- [14] K. Wick, F. Roustaie, S. Quednau, and H. F. Schlaak. “Vor-Ort-Erzeugung von Mikro- und Nanodrähten auf geraden und gekrümmten Oberflächen”. In: *MikroSystemTechnik Kongress*. Karlsruhe, Oct. 2015, pp. 177–181.
- [15] F. Roustaie, S. Quednau, F. Dassinger, H. F. Schlaak, M. Lotz, and S. Wilfert. “In-place synthesis of metallic nanowire arrays for the use in an ionization vacuum gauge”. In: *2015 28th International Vacuum Nanoelectronics Conference (IVNC)*. IEEE, 2015, pp. 176–177.
- [16] J. Bieker, F. Roustaie, C. Langer, R. Schreiner, and H. F. Schlaak. “Innovatives Verfahren zur Herstellung und Integration metallischer Nanokonzen für die Feldemission”. In: *Mikrosystemtechnik Kongress*. München, Oct. 2017, pp. 797–800.

- 
- [17] D. Strahringer, F. Roustaie, F. Weißenborn, S. Quednau, and J. Wilde. “Optimizing the NanoWiring and KlettSintering parameters for low-temperature die to DCB attach of power electronic chips”. In: *2021 16th International Microsystems, Packaging, Assembly and Circuits Technology Conference (IMPACT)*. 2021, pp. 31–34.

---

## Supervised theses

---

- [18] S. Kunz. “Untersuchung und Charakterisierung des Syntheseprozesses von Nanodrahtarrays aus Nichteisen mit unterschiedlichen Array-Geometrien”. B.S. thesis. Institute EMK, TU Darmstadt, 2015.
- [19] A. Humbert. “Entwicklung einer Galvanik-Zelle zur homogenen Abscheidung von metallischen Nanodrähten”. B.S. thesis. Institute EMK, Technische Universität Darmstadt, 2015.
- [20] R. Cicek. “Untersuchung von asymmetrischem Ätzen ionenbestrahlter Polymerfolien zur Herstellung von metallischen Nanokonen mit einstellbarem Öffnungswinkel”. B.S. thesis. Institute EMK, Technische Universität Darmstadt, 2016.
- [21] H. Soltanishirazi. “Fabrication of Nanocones Using Asymmetrical Etching of Heavy Ion Tracked Polycarbonate Foils”. B.S.thesis. the School of Engineering Science, Simon Fraser University in Vancouver/Canada, 2016.
- [22] T. Wähner. “Entwicklung einer Prozesskammer und deren Gastransport-Vorrichtung zur Untersuchung von getemperten metallischen Verbindungen”. M.S. thesis. Institute EMK, Technische Universität Darmstadt, 2017.

---

## References

---

- [23] FAIR, Facility for Antiproton and Ion Research: Beam Properties. URL: <http://www.fair-center.eu/en/public/what-is-fair/accelerators/beam-properties.html> (visited on Oct. 27, 2017).
- [24] M. Lotz, St. Wilfert, O. Kester. “Development of a field emitter based extractor gauge for the operation in cryogenic vacuum environments”. In: *2014 5th International Particle Accelerator Conference (IPAC)*. Dresden, 2014, pp. 16–20.
- [25] N. Marquardt. “Introduction to the principles of vacuum physics”. In: *CERN Accelerator School : Vacuum Technology* (1999), pp. 1–24.
- [26] S. Wilfert and C. Edelmann. “Miniaturized vacuum gauges”. In: *Journal of Vacuum Science & Technology A: Vacuum, Surfaces, and Films* 22.2 (Feb. 2004), pp. 309–320.
- [27] K. Jousten. “Pressure measurement with ionization gauges”. In: *CERN European Organization for Nuclear Research, Reports-CERN* (1999), pp. 75–88.
- [28] R. T. Bayard and D. Alpert. “Extension of the low pressure range of the ionization gauge”. In: *Review of Scientific Instruments* 21.6 (1950), pp. 571–572.
- [29] P. A. Redhead. “Extreme high vacuum”. In: *CERN European Organization for Nuclear Research, Reports-CERN* (1999), pp. 213–226.
- [30] K. Jousten. “Ultrahigh vacuum gauges”. In: *CERN Accelerator School Vacuum in accelerators* (2007), pp. 145–168.
- [31] C. Maurer. “Untersuchungen zu ionenstrahlinduzierter Desorption von kryogenen Oberflächen”. PhD thesis. Technische Universität Darmstadt, 2017.
- [32] R. Gomer. *Field emission and field ionization*. American Vacuum Society classics. New York: American Institute of Physics, 1993.
- [33] P. Lange, D. Grider, H. Neff, J. K. Sass, and R. Unwin. “Limitations of the Fowler method in photoelectric work function determination: Oxygen on magnesium single crystal surfaces”. In: *Surface Science Letters* 118.1-2 (1982), pp. L257–L262.
- [34] F. Schwabl. *Quantum Mechanics*. Springer Berlin Heidelberg, 2007, pp. 63–66.
- [35] R. H. Fowler and L. Nordheim. “Electron Emission in Intense Electric Fields”. In: *Proceedings of the Royal Society of London. Series A, Containing Papers of a Mathematical and Physical Character* 119.781 (1928), pp. 173–181.
- [36] G. Fursey. *Field emission in vacuum microelectronics*. Microdevices. New York: Kluwer Academic/Plenum Publishers, 2005.
- [37] R. H. Good et al. “Field Emission”. In: *Electron-Emission Gas Discharges I / Elektronen-Emission Gasentladungen I*. Berlin, Heidelberg: Springer Berlin Heidelberg, 1956, pp. 176–231.
- [38] K. Besocke and H. Wagner. “Adsorption of W on W (110): Work-function reduction and island formation”. In: *Physical Review B* 8.10 (1973), p. 4597.



- 
- [39] B. Bröker et al. “Gold work function reduction by 2.2 eV with an air-stable molecular donor layer”. In: *Applied physics letters* 93.24 (2008), p. 446.
- [40] T. E. Everhart. “Simplified Analysis of Point-Cathode Electron Sources”. In: *Journal of Applied Physics* 38.13 (1967), pp. 4944–4957.
- [41] C. Spindt. “A thin-film field-emission cathode”. In: *Journal of Applied Physics* 39.7 (1968), pp. 3504–3505.
- [42] C. A. Spindt, I. Brodie, L. Humphrey, and E. R. Westerberg. “Physical properties of thin-film field emission cathodes with molybdenum cones”. In: *Journal of Applied Physics* 47.12 (Dec. 1976), pp. 5248–5263.
- [43] S. Wilfert and C. Edelmann. “Field emitter-based vacuum sensors”. In: *Vacuum* 86.5 (Jan. 2012), pp. 556–571.
- [44] H. J. Fan, P. Werner, and M. Zacharias. “Semiconductor Nanowires: From Self-Organization to Patterned Growth”. In: *Small* 2.6 (2006), pp. 700–717.
- [45] F. Dams, A. Navitski, C. Prommesberger, P. Serbun, C. Langer, G. Muller, and R. Schreiner. “Homogeneous field emission cathodes with precisely adjustable geometry fabricated by silicon technology”. In: *IEEE Transactions on Electron Devices* 59.10 (2012), pp. 2832–2837.
- [46] F. Baker, A. Osborn, and J. Williams. “Field emission from carbon fibres: A new electron source”. In: *Nature* 239.5367 (1972), pp. 96–97.
- [47] B. C. Djubua and N. Chubun. “Emission properties of Spindt-type cold cathodes with different emission cone material”. In: *IEEE Transactions on Electron Devices* 38.10 (1991), pp. 2314–2316.
- [48] A. L. Prudnikava, B. G. Shulitski, V. A. Labunov, A. Navitski, V. Sakharuk, and G. Muller. “Efficient high-current field emission from arrays of CNT columns”. In: *2009 22nd International Vacuum Nanoelectronics Conference IVNC*. IEEE, 2009, pp. 257–258.
- [49] L. Nilsson, O. Groening, P. Groening, and L. Schlapbach. “Collective emission degradation behavior of carbon nanotube thin-film electron emitters”. In: *Applied Physics Letters* 79.7 (2001), pp. 1036–1038.
- [50] A. Dangwal. “Enhanced Field Emission from Metallic Surfaces and Nanowires”. PhD thesis. Wuppertal U., 2007.
- [51] R. G. Forbes, C. Edgcombe, and U. Valdre. “Some comments on models for field enhancement”. In: *Ultramicroscopy* 95 (May 2003). IFES 2001, pp. 57–65.
- [52] X. Wang, M. Wang, Z. Li, Y. Xu, and P. He. “Modeling and calculation of field emission enhancement factor for carbon nanotubes array”. In: *Ultramicroscopy* 102.3 (Feb. 2005), pp. 181–187.
- [53] D. Y. Zhong, G. Y. Zhang, S. Liu, T. Sakurai, and E. G. Wang. “Universal field-emission model for carbon nanotubes on a metal tip”. In: *Applied Physics Letters* 80.3 (Jan. 2002), pp. 506–508.
- [54] A. Dangwal, C. S. Pandey, G. Müller, S. Karim, T. W. Cornelius, and C. Trautmann. “Field emission properties of electrochemically deposited gold nanowires”. In: *Applied Physics Letters* 92.6 (Feb. 2008), p. 063115.

- [55] X. Y. Xue, L. M. Li, H. C. Yu, Y. J. Chen, Y. G. Wang, and T. H. Wang. “Extremely stable field emission from AlZnO nanowire arrays”. In: *Applied Physics Letters* 89.4 (July 2006), p. 043118.
- [56] H. C. Miller. “Change in Field Intensification Factor  $\beta$  of an Electrode Projection (Whisker) at Short Gap Lengths”. In: *Journal of Applied Physics* 38.11 (1967), pp. 4501–4504.
- [57] N. de Jonge and J.-M. Bonard. “Carbon nanotube electron sources and applications”. In: *Philosophical Transactions of the Royal Society of London A: Mathematical, Physical and Engineering Sciences* 362.1823 (Oct. 2004), pp. 2239–2266.
- [58] F. F. Dall’Agnol and D. den Engelsen. “Field emission from non-uniform carbon nanotube arrays”. In: *Nanoscale Research Letters* 8.1 (2013), p. 319.
- [59] F. Roustaie. “Heating channel optimization and thermoelectric measurement in quantum point contacts”. Diplomarbeit. Julius-Maximilians-Universität Würzburg, Oct. 2012.
- [60] J. Timper, K. Gutmiedl, C. Wirges, J. Broda, M. Noyong, J. Mayer, T. Carell, and U. Simon. “Herstellung leitfähiger Nanostrukturen durch Oberflächen- Klickreaktion und kontrollierte Metallisierung von DNA”. In: *Angewandte Chemie* 124.30 (2012), pp. 7705–7708.
- [61] Z. Gu and D. H. Gracias. “Nanowire Assembly and Integration”. In: *Nanofabrication: Fundamentals and Applications*. World Scientific, 2008, pp. 187–211.
- [62] S. Hsieh, S. Meltzer, C. R. C. Wang, A. A. G. Requicha, M. E. Thompson, and B. E. Koel. “Imaging and Manipulation of Gold Nanorods with an Atomic Force Microscope”. In: *The Journal of Physical Chemistry B* 106.2 (2002), pp. 231–234.
- [63] X. Ye, Y. Zhang, and Y. Sun. “Robotic pick-place of nanowires for electromechanical characterization”. In: *2012 IEEE International Conference on Robotics and Automation*. 2012, pp. 2755–2760.
- [64] H. O. Jacobs, A. R. Tao, A. Schwartz, D. H. Gracias, and G. M. Whitesides. “Fabrication of a Cylindrical Display by Patterned Assembly”. In: *Science* 296.5566 (2002), pp. 323–325.
- [65] J. J. Boote and S. D. Evans. “Dielectrophoretic manipulation and electrical characterization of gold nanowires”. In: *Nanotechnology* 16.9 (2005), p. 1500.
- [66] Y. Liu, J.-H. Chung, W. K. Liu, and R. S. Ruoff. “Dielectrophoretic assembly of nanowires”. In: *The journal of physical chemistry B* 110.29 (2006), pp. 14098–14106.
- [67] D. G. Grier. “A revolution in optical manipulation”. In: *Nature* 424.6950 (Aug. 2003), pp. 810–816.
- [68] S. Quednau, F. Dassinger, M. Hottes, C. Stegmann, H. F. Schlaak, and W. Ensinger. “Integration und Charakterisierung von Nanostrukturen in Mikrosysteme für sensorische Anwendungen”. In: *MikroSystemTechnik Kongress 2013*. Aachen, 2013.
- [69] L. Vila et al. “Growth and Field-Emission Properties of Vertically Aligned Cobalt Nanowire Arrays”. In: *Nano Letters* 4.3 (Mar. 2004), pp. 521–524.
- [70] M. Skupinski, M. Toulemonde, M. Lindeberg, and K. Hjort. “Ion tracks developed in polyimide resist on Si wafers as template for nanowires”. In: *Nuclear Instruments & Methods in Physics Research Section B*: 240.3 (Nov. 2005), pp. 681–689.

- 
- [71] H. Yoon, D. C. Deshpande, V. Ramachandran, and V. K. Varadan. “Aligned nanowire growth using lithography-assisted bonding of a polycarbonate template for neural probe electrodes”. In: *Nanotechnology* 19.2 (Jan. 2008), p. 025304.
- [72] A. Gambirasi, S. Cattarin, M. Musiani, L. Vázquez-Gómez, and E. Verlato. “Direct electrodeposition of metal nanowires on electrode surface”. In: *Electrochimica Acta* 56.24 (Oct. 2011), pp. 8582–8588.
- [73] G. E. Possin. “A Method for Forming Very Small Diameter Wires”. In: *Review of Scientific Instruments* 41.5 (1970), pp. 772–774.
- [74] J. Vetter and R. Spohr. “Application of ion track membranes for preparation of metallic microstructures”. In: *Nuclear Instruments and Methods in Physics Research Section B: Beam Interactions with Materials and Atoms* 79.1 (June 1993), pp. 691–694.
- [75] C. Trautmann, W. Bröchle, R. Spohr, J. Vetter, and N. Angert. “Pore geometry of etched ion tracks in polyimide”. In: *Nuclear Instruments and Methods in Physics Research Section B: Beam Interactions with Materials and Atoms* 111.1–2 (Apr. 1996), pp. 70–74.
- [76] E. Ferain and R. Legras. “Efficient production of nanoporous particle track etched membranes with controlled properties”. In: *Radiation Measurements*. Proceedings of the 20th International Conference on Nuclear Tracks in Solids 34.1–6 (June 2001), pp. 585–588.
- [77] M. E. Toimil Molaes. “Fabrication and characterisation of copper nanowires electrochemically deposited in etched ion-track membranes”. PhD thesis. Physikalisches Institut, Universität Heidelberg, 2001.
- [78] M. E. Toimil Molaes, J. Brötz, V. Buschmann, D. Dobrev, R. Neumann, R. Scholz, I. U. Schuchert, C. Trautmann, and J. Vetter. “Etched heavy ion tracks in polycarbonate as template for copper nanowires”. In: *Nuclear Instruments and Methods in Physics Research Section B: Beam Interactions with Materials and Atoms* 185.1–4 (Dec. 2001), pp. 192–197.
- [79] S. Quednau. “Galvanisch erzeugt Mikro-und Nanodrähte für die Gasflusssensorik”. PhD thesis. Institute EMK, Technische Universität Darmstadt, 2016.
- [80] V. V. Sviridov, T. V. Gaevskaya, L. I. Stepanova, and T. N. Vorobyova. “Electroless deposition and Electroplating of Metals”. In: *Chemical problems of the development of new materials and technologies* (2003).
- [81] C. Hamann, A. Hamnett, and W. Vielstich. *Electrochemistry*. Wiley, 1998.
- [82] F. Nasirpour. *Electrodeposition of nanostructured materials*. Springer, 2017.
- [83] D. Subedi, L. Zajickova, V. Bursikova, and J. Janca. “Surface modification of polycarbonate (bisphenol A) by low pressure rf plasma”. In: *Himalayan Journal of Sciences* 1.2 (2003), pp. 115–118.
- [84] L. Kessler et al. “Surface treatment of polycarbonate films aimed at biomedical application”. In: *Journal of Biomaterials Science, Polymer Edition* 14.10 (Jan. 2003), pp. 1135–1153.
- [85] J. Liu et al. “Electrochemical fabrication of single-crystalline and polycrystalline Au nanowires: the influence of deposition parameters”. In: *Nanotechnology* 17.8 (2006), pp. 1922–1926.

- [86] Y. Cui and Y. Ju. “Composite nanowires for room-temperature mechanical and electrical bonding”. In: *Advances in Nanocomposites: Modeling, Characterization and Applications*. Springer, 2016, pp. 151–175.
- [87] F. Maurer, A. Dangwal, D. Lysenkov, G. Müller, M. E. Toimil-Molaes, C. Trautmann, J. Brötz, and H. Fuess. “Field emission of copper nanowires grown in polymer ion-track membranes”. In: *Nuclear Instruments and Methods in Physics Research Section B: Beam Interactions with Materials and Atoms* 245.1 (2006). Swift Heavy Ions in Matter, pp. 337–341.
- [88] A. Dangwal, G. Müller, F. Maurer, J. Brotz, and H. Fuess. “Field emission properties of bare and gold-coated nickel nanowires grown in polymer ion-track membranes”. In: *Journal of Vacuum Science & Technology B: Microelectronics and Nanometer Structures* 25.2 (2007), pp. 586–589.
- [89] A. Navitski, G. Müller, V. Sakharuk, T. W. Cornelius, C. Trautmann, and S. Karim. “Efficient field emission from structured gold nanowire cathodes”. In: *The European Physical Journal Applied Physics* 48.3 (Oct. 2009), p. 30502.
- [90] A. Navitski. “Scanning field emission investigations of structured CNT and MNW cathodes, niobium surfaces and photocathodes”. PhD thesis. Fakultät für Mathematik und Naturwissenschaften, Universität Wuppertal, 2018.
- [91] A. Navitski, P. Serbun, G. Müller, I. Alber, M. E. Toimil-Molaes, and C. Trautmann. “Correlation between field emission current limits and morphology changes of poly-and single-crystalline gold nanowire patches”. In: *GSI Scientific Report 2010*. 2011.
- [92] M. Rauber, F. Muench, M. E. Toimil-Molaes, and W. Ensinger. “Thermal stability of electrodeposited platinum nanowires and morphological transformations at elevated temperatures”. In: *Nanotechnology* 23.47 (Nov. 2012), p. 475710.
- [93] L. Burr, I. Alber, and C. Trautmann. “Thermal Instability of Porous Gold Nanowires”. In: *GSI Scientific Report 2012* 417 (2012).
- [94] P. Serbun, F. Jordan, A. Navitski, G. Müller, I. Alber, M. Toimil-Molaes, and C. Trautmann. “Copper nanocones grown in polymer ion-track membranes as field emitters”. In: *The European Physical Journal Applied Physics* 58.1 (Mar. 2012), p. 10402.
- [95] E. H. Lee. “Ion-beam modification of polymeric materials – fundamental principles and applications”. In: *Nuclear Instruments and Methods in Physics Research Section B: Beam Interactions with Materials and Atoms* 151.1–4 (May 1999), pp. 29–41.
- [96] R. Spohr. *Ion tracks and microtechnology: principles and applications*. Ed. by K. Bethge. Reimar Spohr, 1990.
- [97] M.-C. Clochard, T. Wade, J.-E. Wegrowe, and E. Balanzat. “Influence of asymmetric etching on ion track shapes in polycarbonate”. In: *Nuclear Instruments and Methods in Physics Research Section B: Beam Interactions with Materials and Atoms* 265.1 (Dec. 2007), pp. 325–329.
- [98] D. Dobrev, J. Vetter, N. Angert, and R. Neumann. “Periodic reverse current electrodeposition of gold in an ultrasonic field using ion-track membranes as templates: growth of gold single-crystals”. In: *Electrochimica Acta* 45.19 (2000), pp. 3117–3125.

- 
- [99] P. Apel. “Track etching technique in membrane technology”. In: *Radiation Measurements*. Proceedings of the 20th International Conference on Nuclear Tracks in Solids 34.1–6 (June 2001), pp. 559–566.
- [100] C. Harrell, Z. Siwy, and C. Martin. “Conical Nanopore Membranes: Controlling the Nanopore Shape”. In: *Small* 2.2 (Feb. 2006), pp. 194–198.
- [101] P. Scopece, L. A. Baker, P. Ugo, and C. R. Martin. “Conical nanopore membranes: solvent shaping of nanopores”. In: *Nanotechnology* 17.15 (Aug. 2006), pp. 3951–3956.
- [102] S. Karim, M. E. Toimil-Molares, F. Maurer, G. Miehe, W. Ensinger, J. Liu, T. W. Cornelius, and R. Neumann. “Synthesis of gold nanowires with controlled crystallographic characteristics”. In: *Applied Physics A: Materials Science & Processing* 84.4 (2006), pp. 403–407.
- [103] D. Fink, V. Hnatowicz, and P. Y. Apel. “Transport Processes in Tracks”. In: *Transport Processes in Ion-Irradiated Polymers*. Ed. by D. Fink. Berlin, Heidelberg: Springer, 2004, pp. 93–146.
- [104] R. Spohr, C. Zet, B. Eberhard Fischer, H. Kiesewetter, P. Apel, I. Gunko, T. Ohgai, and L. Westerberger. “Controlled fabrication of ion track nanowires and channels”. In: *Nuclear Instruments and Methods in Physics Research Section B: Beam Interactions with Materials and Atoms* 268.6 (Mar. 2010), pp. 676–686.
- [105] P. Y. Apel, Y. E. Korchev, Z. Siwy, R. Spohr, and M. Yoshida. “Diode-like single-ion track membrane prepared by electro-stopping”. In: *Nuclear Instruments and Methods in Physics Research Section B: Beam Interactions with Materials and Atoms* 184.3 (Nov. 2001), pp. 337–346.
- [106] P. Y. Apel, I. V. Blonskaya, O. L. Orelovitch, B. A. Sartowska, and R. Spohr. “Asymmetric ion track nanopores for sensor technology. Reconstruction of pore profile from conductometric measurements”. In: *Nanotechnology* 23.22 (2012), p. 225503.
- [107] M. S. Chandrasekar and M. Pushpavanam. “Pulse and pulse reverse plating-Conceptual, advantages and applications”. In: *Electrochimica Acta* 53.8 (Mar. 2008), pp. 3313–3322.
- [108] F. Jordan. “Elektrochemische Herstellung von konischen Metall-Nanostrukturen und systematische Untersuchung ihrer Feldemissionseigenschaften”. MA thesis. Bergische Universität Wuppertal, Dec. 2012.
- [109] P. Serbun. “A systematic investigation of carbon, metallic and semiconductor nanostructures for field-emission cathode applications”. PhD thesis. Fakultät für Mathematik und Naturwissenschaften, Universität Wuppertal, Nov. 2013.
- [110] J. Bieker, R. G. Forbes, S. Wilfert, and H. F. Schlaak. “Simulation-Based Model of Randomly Distributed Large-Area Field Electron Emitters”. In: *IEEE Journal of the Electron Devices Society* 7 (2019), pp. 997–1006.
- [111] P. A. Anderson. “Work Function of Gold”. In: *Physical Review* 115.3 (Aug. 1959), pp. 553–554.
- [112] J.-M. Bonard, N. Weiss, H. Kind, T. Stöckli, L. Forró, K. Kern, and A. Châtelain. “Tuning the Field Emission Properties of Patterned Carbon Nanotube Films”. In: *Advanced Materials* 13.3 (Feb. 2001), pp. 184–188.

- 
- [113] L. Nilsson, O. Groening, C. Emmenegger, O. Kuettel, E. Schaller, L. Schlapbach, H. Kind, J.-M. Bonard, and K. Kern. “Scanning field emission from patterned carbon nanotube films”. In: *Applied Physics Letters* 76.15 (Apr. 2000), pp. 2071–2073.
- [114] S. Tsujino, M. Paraliiev, E. Kirk, and H.-H. Braun. “Homogeneity improvement of field emission beam from metallic nano-tip arrays by noble-gas conditioning”. In: *Applied Physics Letters* 99.7 (Aug. 2011), p. 073101.
- [115] J. L. Duan, D. Y. Lei, F. Chen, S. P. Lau, W. I. Milne, M. E. Toimil-Molares, C. Trautmann, and J. Liu. “Vertically-Aligned Single-Crystal Nanocone Arrays: Controlled Fabrication and Enhanced Field Emission”. In: *ACS Applied Materials & Interfaces* 8.1 (Jan. 2016), pp. 472–479.
- [116] X. N. Innovations. *Catalog-Xintek-CNTCathodes-v4*. URL: <https://web.archive.org/web/20170601000000/http://www.xinnanomaterials.com/images/download/Catalog-Xintek-CNTCathodes-v4.pdf> (visited on Apr. 26, 2017).
- [117] R. B. Sadeghian and M. Kahrizi. “A novel miniature gas ionization sensor based on freestanding gold nanowires”. In: *Sensors and Actuators A: Physical* 137.2 (July 2007), pp. 248–255.
- [118] N. Saeidi, T. Rogers, A. Draisey, R. Davies, D. Casey, C. Colinge, A. Demosthenous, and N. Donaldson. “The Effects of In-Situ Formic Acid Treatment on Oxide Reduction for Copper Wafer Bonding”. In: *AML Micro Engineering Ltd., Kowloon, Hong Kong* (2012).
- [119] S. Aravamudhan, A. Kumar, S. Mohapatra, and S. Bhansali. “Sensitive estimation of total cholesterol in blood using Au nanowires based micro-fluidic platform”. In: *Biosensors and Bioelectronics* 22.9-10 (Apr. 2007), pp. 2289–2294.
- [120] A. V. Kabashin, P. Evans, S. Pastkovsky, W. Hendren, G. A. Wurtz, R. Atkinson, R. Pollard, V. A. Podolskiy, and A. V. Zayats. “Plasmonic nanorod metamaterials for biosensing”. In: *Nature Materials* 8.11 (Nov. 2009), pp. 867–871.
- [121] C. Nick. “Mikrointegrierte Nanostrukturen mit hohem Aspektverhältnis als neuronale Schnittstelle”. PhD thesis. TU Darmstadt, 2015.
- [122] S. Baek and R. Fearing. “Reducing Contact Resistance Using Compliant Nickel Nanowire Arrays”. In: *IEEE Transactions on Components and Packaging Technologies* 31.4 (2008), pp. 859–868.
- [123] M. Lindeberg and K. Hjort. “A comprehensive study of ion track enabled high aspect ratio microstructures in flexible circuit boards”. In: *Microsystem Technologies* 10.8 (Nov. 2004), pp. 608–621.



---

## A Prescription

---

### A.1 Gold Etchant

---

Gold etchant with etchrate about  $1 \frac{\mu\text{m}}{\text{min}}$

---

20 g	KI	(Potasium iodine)
5 g	I <sub>2</sub>	(Iodine twice Sublimated)
200 ml	H <sub>2</sub> O	(Deionized watter)

---

### A.2 Chromium Etchant

---

Chromium etchant

---

41.15 g	(NH <sub>4</sub> ) <sub>2</sub> Ce(NO <sub>3</sub> ) <sub>6</sub>	(Ceric ammonium nitrate)
22.5 ml	HNO <sub>3</sub>	(Nitric acid)
250 ml	H <sub>2</sub> O	(Deionized watter)

---

### A.3 Copper electrolyte

---

Copper Electrolyte [123]

---

250 $\frac{\text{g}}{\text{L}}$	CuSO <sub>4</sub> · 5H <sub>2</sub> O	(Copper sulfate pentahydrate)
23.25 $\frac{\text{g}}{\text{L}}$	H <sub>2</sub> CuSO <sub>4</sub>	(Sulfuric acid)

---

### A.4 Nickel electrolyte

---

Nickel Electrolyte [123]

---

250 $\frac{\text{g}}{\text{L}}$	NiSO <sub>4</sub> · 4H <sub>2</sub> O	(Nickel(II) sulfamate tetrahydrate)
35 $\frac{\text{g}}{\text{L}}$	BH <sub>3</sub> O <sub>3</sub>	(Boric acid)

## B Datasheets

### B.1 ma-P 1215 for etching and lamination processes

ma-P 1215 photo resist is a positive resist of family ma-P 1200, proper for 1.5  $\mu\text{m}$  thickness.

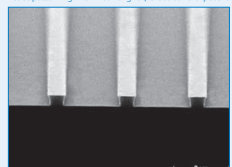
micro resist technology GmbH  
Köpenicker Straße 325  
12555 Berlin  
Germany  
Tel.: +49 (0) 30 641670 100  
Fax: +49 (0) 30 641670 200  
info@microresist.de  
www.microresist.com



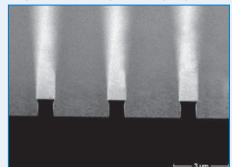
## ma-P 1200 — Positive Tone Photoresist Series

### Resists for UV Lithography

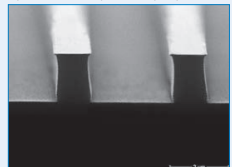
Resist patterning with mask aligner, broadband exposure



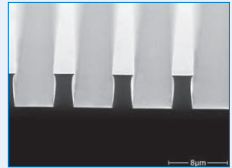
0.5  $\mu\text{m}$  ma-P 1205, 1  $\mu\text{m}$  lines, 3  $\mu\text{m}$  spaces



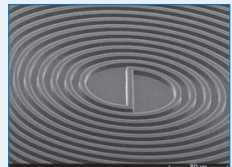
1  $\mu\text{m}$  ma-P 1210, 1  $\mu\text{m}$  lines, 3  $\mu\text{m}$  spaces



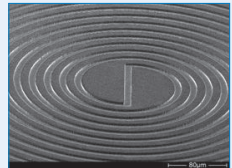
2.5  $\mu\text{m}$  ma-P 1225, 2  $\mu\text{m}$  lines, 4  $\mu\text{m}$  spaces



4  $\mu\text{m}$  ma-P 1240, 3  $\mu\text{m}$  lines, 5  $\mu\text{m}$  spaces



7.5  $\mu\text{m}$  ma-P 1275, coil, 10  $\mu\text{m}$  turns



5  $\mu\text{m}$  electroplated Ni coil, 10  $\mu\text{m}$  turns

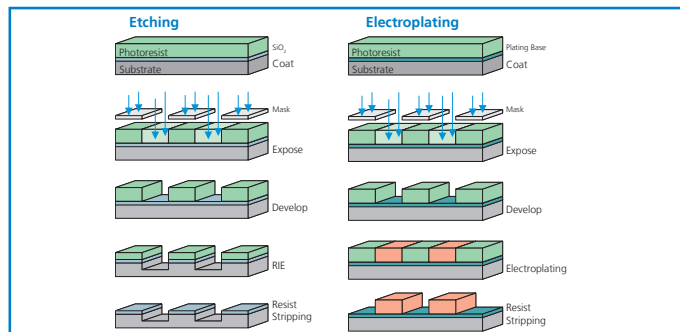
#### Unique features

- High pattern stability in wet etch processes and acid and alkaline plating baths
- Highly stable in dry etch processes e.g.  $\text{CHF}_3$ ,  $\text{CF}_4$ ,  $\text{SF}_6$
- Aqueous alkaline development
- Easy to remove
- Resists available in a variety of viscosities

#### Applications

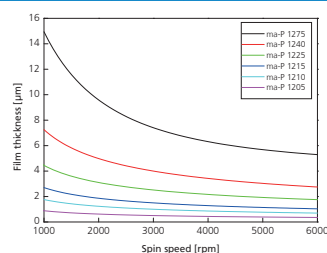
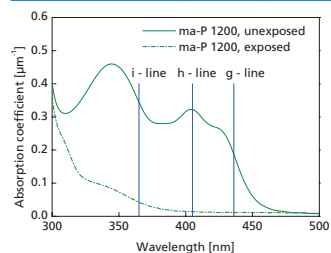
- Mask for etching e.g. Si,  $\text{SiO}_2$
- Metals
- Semiconductors
- Mask for ion implantation
- Mould for electroplating

#### Process flow



#### Technical data

Resist		ma-P 1205	ma-P 1210	ma-P 1215	ma-P 1225	ma-P 1240	ma-P 1275
Film thickness	$\mu\text{m}$	0.5	1.0	1.5	2.5	4.0	7.5
Spin coating	rpm s	3000 30					
Spectral sensitivity		broadband, g-, h-, i-line					
Dose @ 365 nm (broadband exposure)	$\text{mJ cm}^{-2}$	35	35	45	55	110	150



---

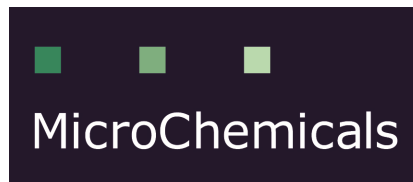
## B.2 Ti-Prime adhesion promoter

---

MicroChemicals® TI PRIME technical data sheet – revised 08/2016

### TI PRIME adhesion promoter

Technical Data Sheet  
revised 08/2002



MicroChemicals GmbH  
Nicolaus-Otto-Str. 39  
D-89079 Ulm  
Fon +49 (0) 731 977343 0  
Mobil +49 (0) 177 3332453  
Fax +49 (0) 731 977343 29  
Email [info@microchemicals.com](mailto:info@microchemicals.com)  
Internet [www.microchemicals.com](http://www.microchemicals.com)

---

#### General Information

The TI PRIME adhesion promoter improves resist adhesion on substrates like Si or glass

---

#### Processing the TI PRIME

(in chronological order)

- **Substrate preparation:** After (optional, but recommended) cleaning the substrate with acetone and subsequently isopropyle, put the substrate on the hotplate at a minimum temperature of 120 °C for 10 minutes to remove adsorbed water from the substrates surface. Alternatively, you can use a furnace at same temperature for 30 min.
- **Spin coat the TI PRIME** at approx. 2000-4000 U/min for approx. 20 seconds. After spin-coating, no residual drops or film of TI PRIME should be visible.
- **Bake** the substrate at 120°C for 2 minutes on the hotplate (when using a furnace, 130°C for 10 min is recommended)
- **Proceed** with spin-coating the resist immediately and proceed as usual.

**Note: TI Prime contains Titanium. For CMOS processes use (eg. RCA-) cleaning procedure of the substrates after lithography before you apply high-temperatures.**

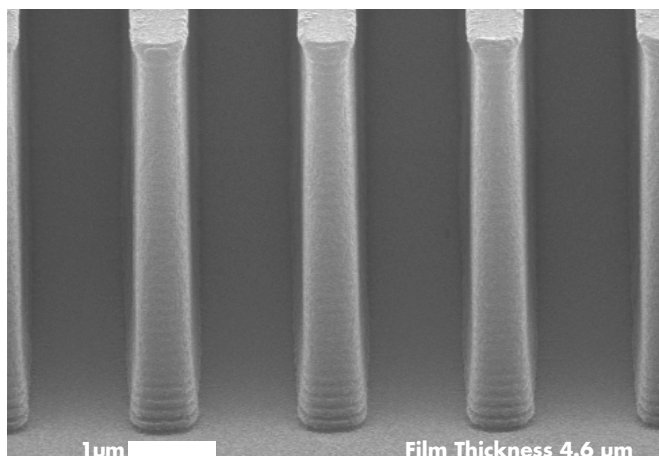


MicroChemicals GmbH Ulm – [www.microchemicals.com](http://www.microchemicals.com)

---

### B.3 AZ9260 Positive photo resist

Product Data Sheet



AZ<sup>®</sup> 9200 Photoresist

High-Resolution  
Thick Resist

AZ<sup>®</sup> 9200 thick film photoresist is designed for the more demanding higher-resolution thick resist requirements. It provides high resolution with superior aspect ratios, as well as wide focus and exposure latitude and good sidewall profiles. AZ<sup>®</sup> 9200 photoresist is available in two viscosity grades for film thicknesses of 4 to 24  $\mu\text{m}$ . Critical dimension resolutions range from  $< 1 \mu\text{m}$  lines and spaces at a film thickness of 4.6  $\mu\text{m}$ , to 3.5  $\mu\text{m}$  lines and spaces at a film thickness of 24  $\mu\text{m}$  on silicon using today's standard broadband exposure tools. Aspect ratios of 5 – 7 can be achieved.

Under the guidance of leading thin film recording head manufacturers, AZ<sup>®</sup> 9200 photoresist is optimized for both coil plating and top pole recording head applications.

AZ<sup>®</sup> 9200 photoresist can be used as a higher resolution replacement for AZ<sup>®</sup> P4000 photoresist. It can be processed on the same exposure tools using similar processing conditions; it is developed from the same chemistry and has similar curing, electrical and thermal properties.

Sensitivity to both h- and i-line makes AZ<sup>®</sup> 9200 photoresist capable for both broadband and i-line steppers.

Recommended developers are inorganic based upon potassium hydroxide. The preferred developer is AZ<sup>®</sup> 400K Developer 1:4, a buffered developer designed to maximize bath life and process stability. For integrated circuit applications, TMAH developers such as AZ<sup>®</sup> 300 MIF developer can be used.





# SCHOLAR E and SCHOLAR T

## Potentiostats / Galvanostats for Education

The potentiostats Scholar E and Scholar T are economic training instruments for practising electrochemistry. Main features are simplicity, resistance against cabling mistakes and electrode short-circuits. Nevertheless they got the features of laboratory potentiostats: precise control, fast regulation, and high reference electrode input resistance.



Scholar offers 3 operation modes: Potential measurement, potentiostatic mode and galvanostatic mode. Scholar can act both as current sink as well as current source. Thanks to its internal precision control source ranging from - 4000 mV to + 4000 mV the Scholar can be used for various applications without additional instruments. In addition, an input for external control voltages allows to connect signal generators for advanced tests like cyclovoltammetry. Monitor outputs for potential and current connect to any recorder or AD - converter.

Maximum current is 20 mA (peak current 40 mA) for model Scholar E, or 100 mA (peak 140 mA) for model T. The current resolution is 1 nA using the internal display, or 100 pA using the monitor output.

### Applications

- potential measurements (corrosion potential, redox potential)
- potentiostatic polarisation (record of stationary current-potential plots)
- galvanostatic control (electroplating, thickness measurement of platings)
- characterisation of batteries
- polarographic analysis
- cathodic protection / cathodic disbonding
- galvanic couples

### New Option

**USB-Interface MYDAQ® from National Instruments with cable set for Scholar potentiostats, including basic electrochemical software (LabView applications)**

## B.5 Gold electroplating bath

**METAKEM**  
Precious Metals+ Electrochemistry

[HOME](#) [COMPANY](#) [PRODUCTS](#) [SERVICES](#) [APPLICATIONS](#)

search...

[Home](#) > [Products](#) > [Precious Metals Electrolytes](#) > Gold - Electrolytes

### Gold - Elektrolyte



**Gold electrolytes** from **METAKEM** are used for technical and decorative applications for the depositing of pure gold layers. These electrolytes are either cyanide based or cyanide-free based on ammonium gold(I) sulphite - covering nearly the complete pH-value spectrum.

#### Gold-SF

**Gold-SF** is a sulphite-based gold electroplating bath with a neutral pH-value. Due to its extremely low chloride content this ultrapure bath shows even after long ultraviolet light exposure a high bath stability. Although generally used in the jewellery sector, uses can also be found for industrial applications such as dental electroforming etc.

Bath type:	Neutral, sulphite based
Gold content:	10-15 g per litre
Layer:	Gold 99.9%
Max. layer thickness:	max. 500 µm
pH-value:	7.5
Bath temperature:	60 °C (55-65 °C)
Current density:	1 A/dm <sup>2</sup> (0.1 - 1.5 A/dm <sup>2</sup> )
Type of application:	Jewellery, electroforming
Delivery form:	Make-up: Gold-SF (15 g Au / L)
	Replenishment: Gold-SF-R (100 g Au / L)

#### METAKEM GmbH

Achtzehnmorgenweg 3  
61250 Usingen  
Germany

Phone: +49 (0) 6081-1060-0  
Fax: +49 (0) 6081-1060-60

E-Mail: [info@metakem.de](mailto:info@metakem.de)  
Web: [www.metakem.de](http://www.metakem.de)

#### Your Contact Person:

Mrs. Ann-Katrin Haag  
[haag@metakem.de](mailto:haag@metakem.de)

Mrs. Eva Gahnz  
[gahnz@metakem.de](mailto:gahnz@metakem.de)



## B.6 Gold electroplating bath



### CHEMICAL RESISTANCE OF TRACK-ETCHED MEMBRANES

**R** = Recommended    **LR** = Limited Resistance    **T** = to be Tested    **NR** = Not Recommended

#### CHEMICAL RESISTANCE OF POLYCARBONATE, POLYESTER & POLYIMIDE MEMBRANES

		polycarbonate	polyester	polyimide
ACIDS	Acetic Acid, 5%	R	R	R
	Acetic Acid, 10%	R	R	R
	Acetic Acid, Glacial	LR	R	R
	Boric Acid	R	R	R
	Hydrochloric, 6N	R	LR	T
	Hydrochloric, Conc.	R	NR	T
	Hydrofluoric, 10%	R	R	T
	Hydrofluoric, 35%	R	R	T
	Nitric Acid, 6N	R	R	T
	Nitric Acid, Conc.	R	NR	T
	Sulphuric Acid, 6N	R	R	T
	Sulphuric Acid, Conc.	NR	NR	T

		polycarbonate	polyester	polyimide
ALCOHOLS	Amyl Alcohol	R	R	R
	Benzyl Alcohol	LR	R	R
	Butyl Alcohol	R	R	R
	Butyl Cellosolve	LR	R	R
	Ethyl Alcohol <80%	R	R	R
	Ethyl Alcohol >80%	R	R	R
	Ethylene Glycol	R	R	R
	Glycerine (Glycerol)	R	R	R
	Isobutyl Alcohol	R	R	R
	Isopropanol	R	R	R
	Methanol	R	R	R
	Propanol	R	R	R

		polycarbonate	polyester	polyimide
BASES	Ammonium Hydroxide, 6N	NR	LR	NR
	Potassium Hydroxide, 6N	NR	NR	NR
	Sodium Hydroxide, 6N	NR	LR	NR

#### it4ip s.a.

rue J. Bordet (Z.I. C - Activalis) - 7180 Senefle - Belgium  
tel : +32 (0)64 371001 — fax : +32 (0)64 371021

contact@it4ip.be  
<http://www.it4ip.be>

it4ip/info/doc/01 v1.1



## technical datasheet

# AZ<sup>®</sup> 40XT-11D Photoresist

## Chemically Amplified Thick Photoresist

### APPLICATION

Thick positive tone chemically amplified photoresist featuring aspect ratios and photospeed not possible with conventional DNQ type materials. These photoresists expose and develop very quickly for improved equipment productivity and reduced chemical usage.

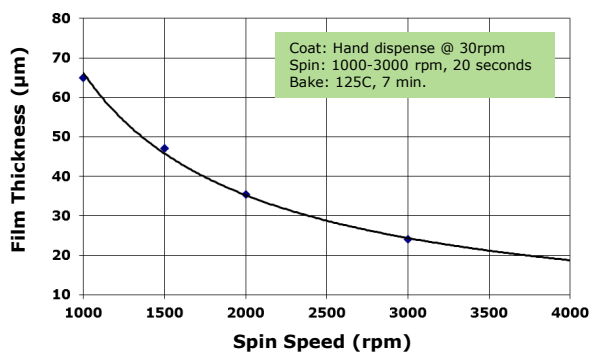
- Excellent environmental stability
- No post bake rehydration delays required
- Single coat thicknesses from 20 to >60µm
- Excellent for Through Silicon Via (TSV), plating, and RIE etch applications.

### TYPICAL PROCESS

Soft Bake: 125°C (ramped)  
 Rehydration Hold: None  
 Expose: 365nm sensitive  
 Post Expose Bake\*: 105°C/120s  
 Develop: Puddle, spray or immersion  
 Developer Type: MIF

\* PEB is required for proper imaging

### SPIN CURVE (200mm Silicon)



### OPTICAL CONSTANTS\*

Cauchy A	1.560
Cauchy B (µm <sup>2</sup> )	0.007
Cauchy C (µm <sup>4</sup> )	0.0006
n @ 633nm	1.5851
k @ 633nm	0

\* Unexposed photoresist film

### COMPANION PRODUCTS

Thinning/Edge Bead Removal

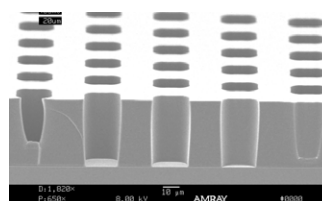
AZ<sup>®</sup> EBR Solvent or AZ<sup>®</sup> EBR 70/30

MIF Developers

AZ<sup>®</sup> 300MIF



Merck KGaA, Darmstadt, Germany

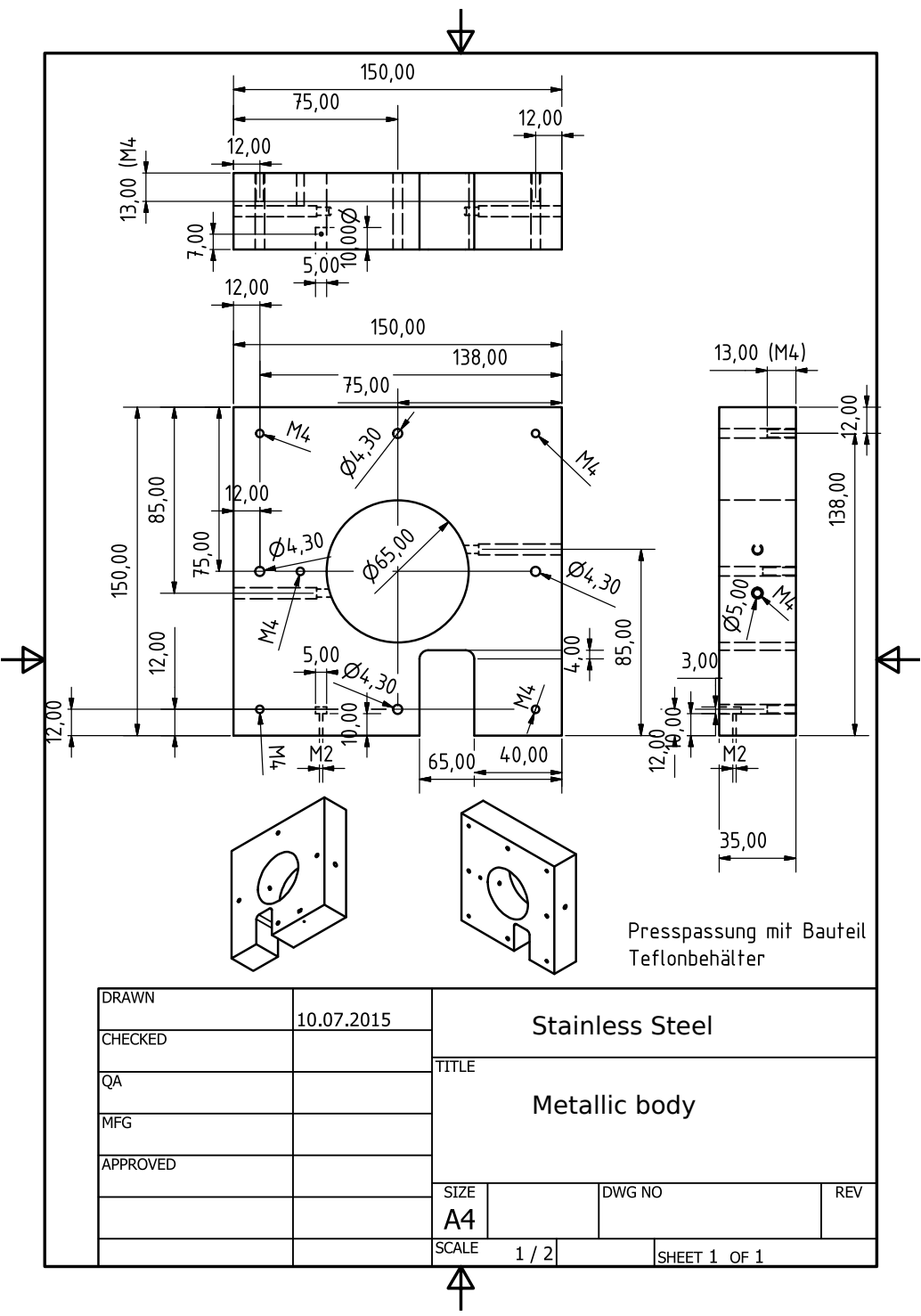


20µm holes in 40µm thick AZ 40XT  
 400mJ/cm<sup>2</sup> Exposure  
 AZ 300 MIF Develop (240s)

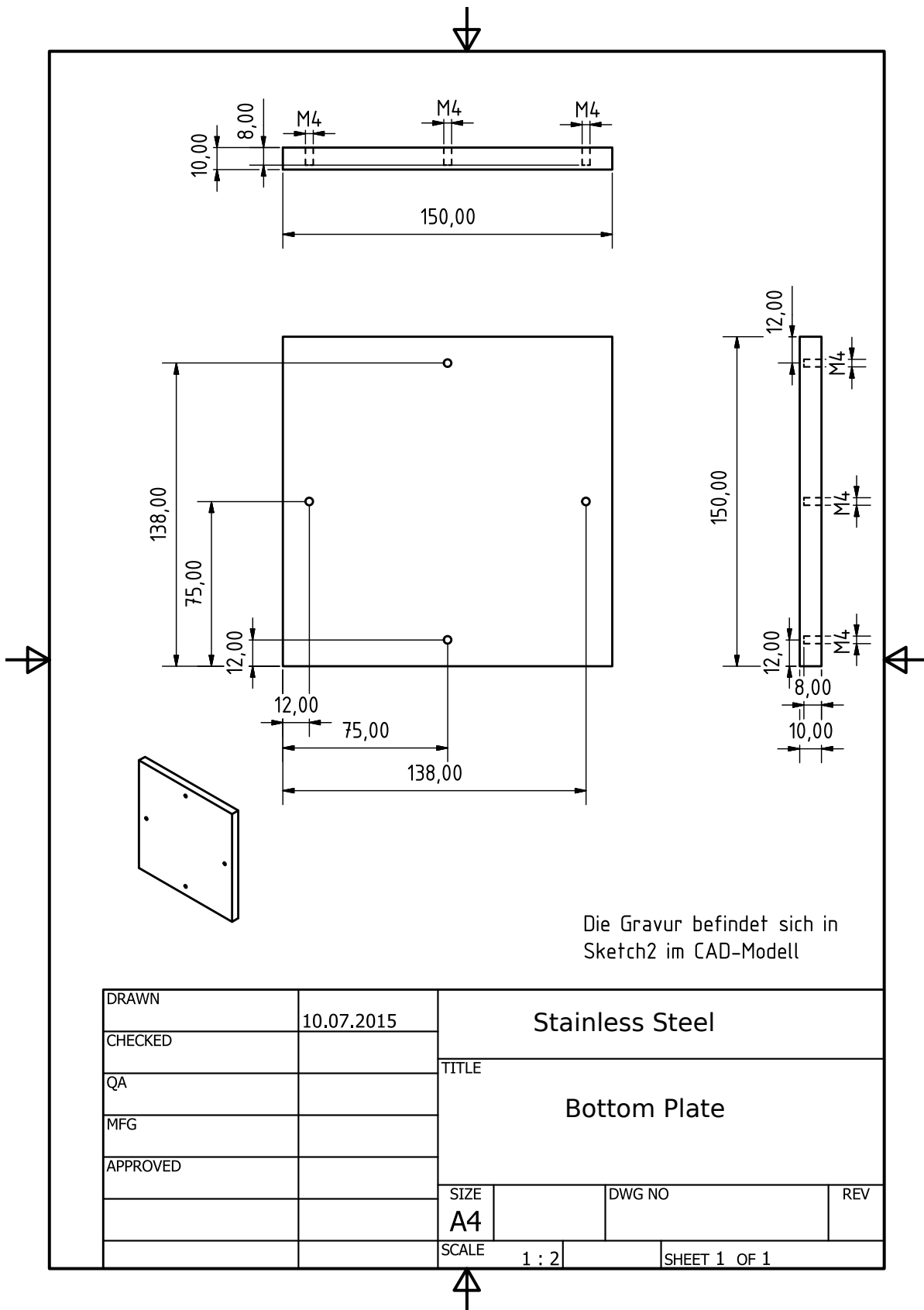
Rev. 7/2016

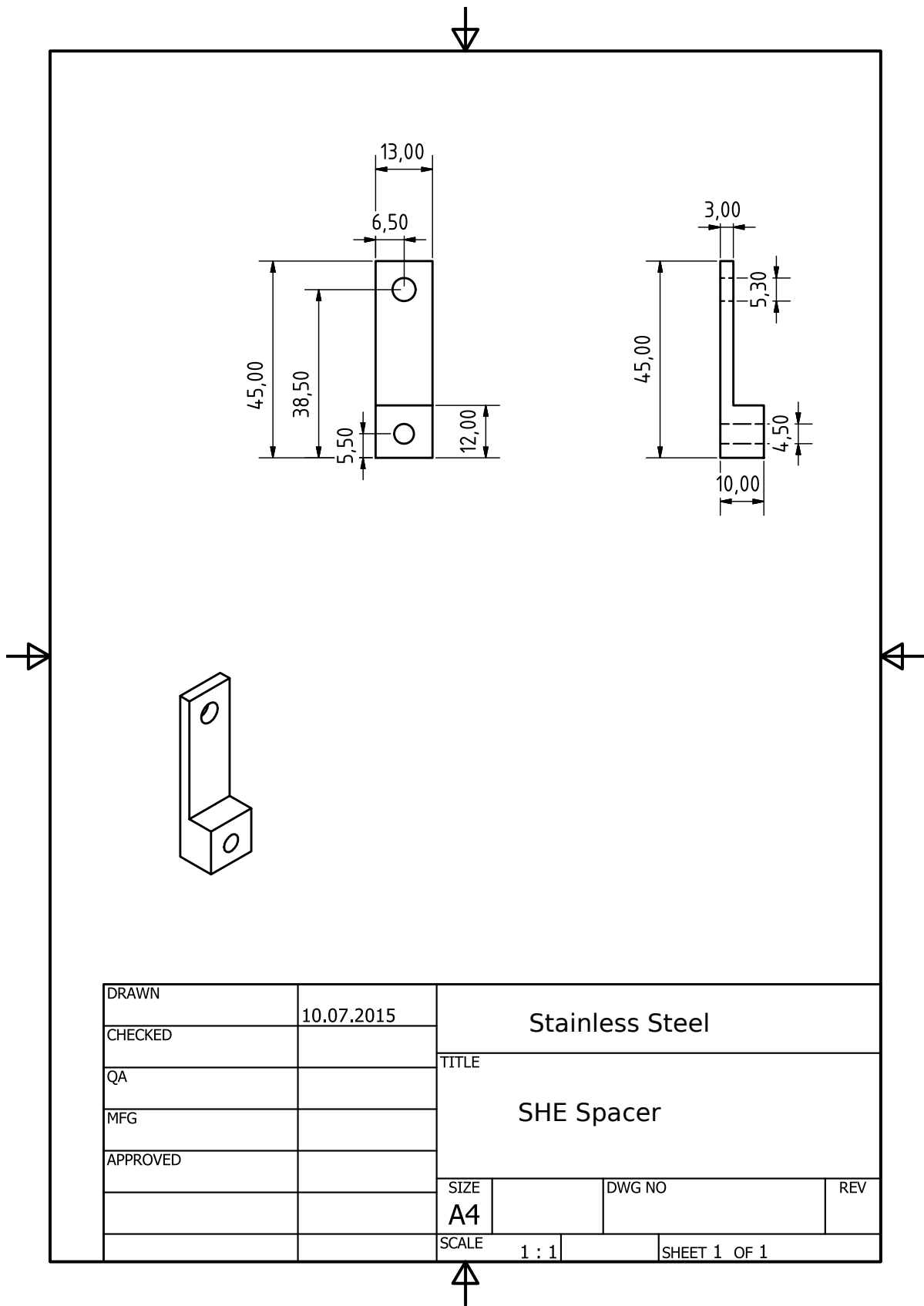
C Technical Drawings

C.1 Electro chemical deposition bath

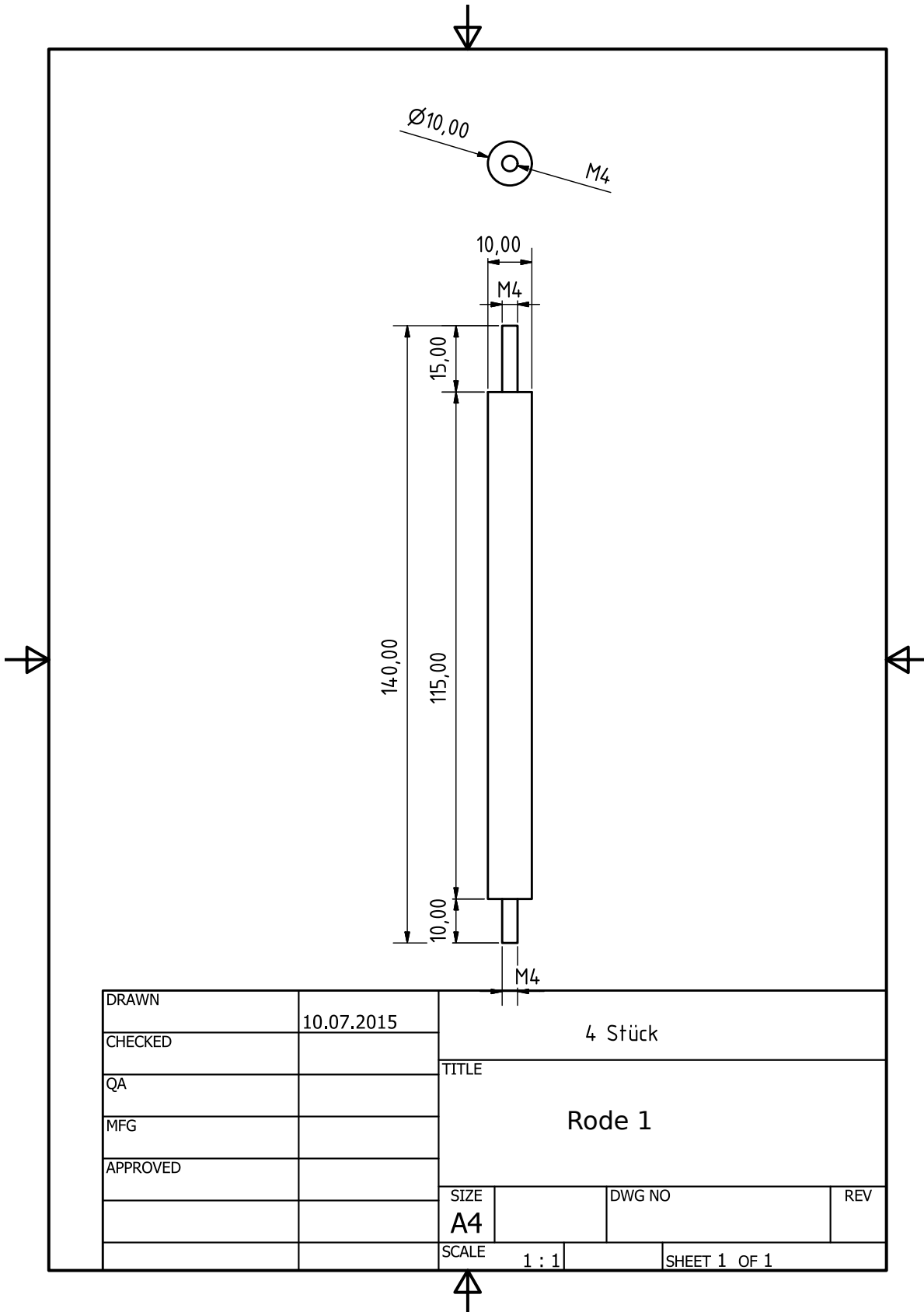


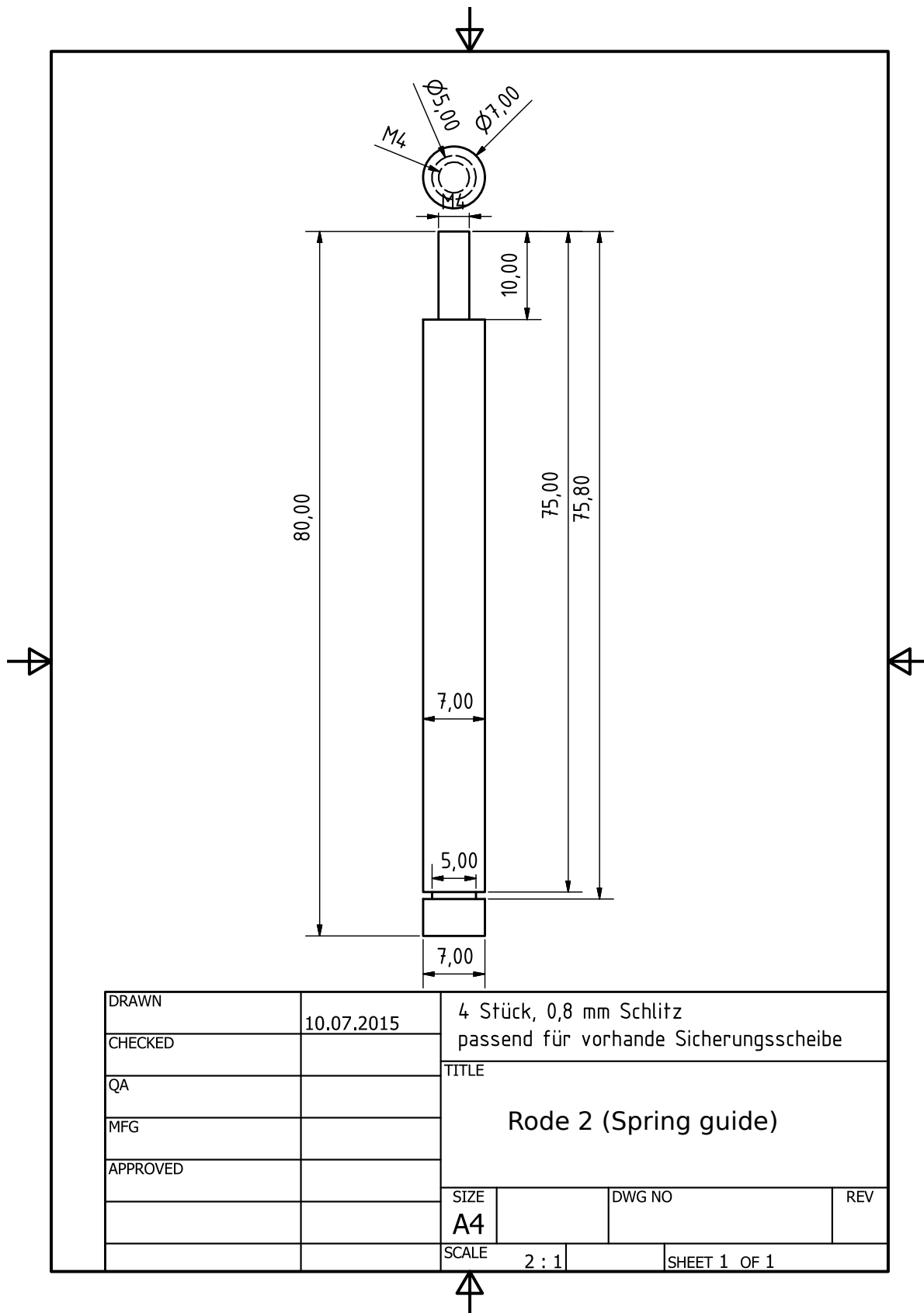




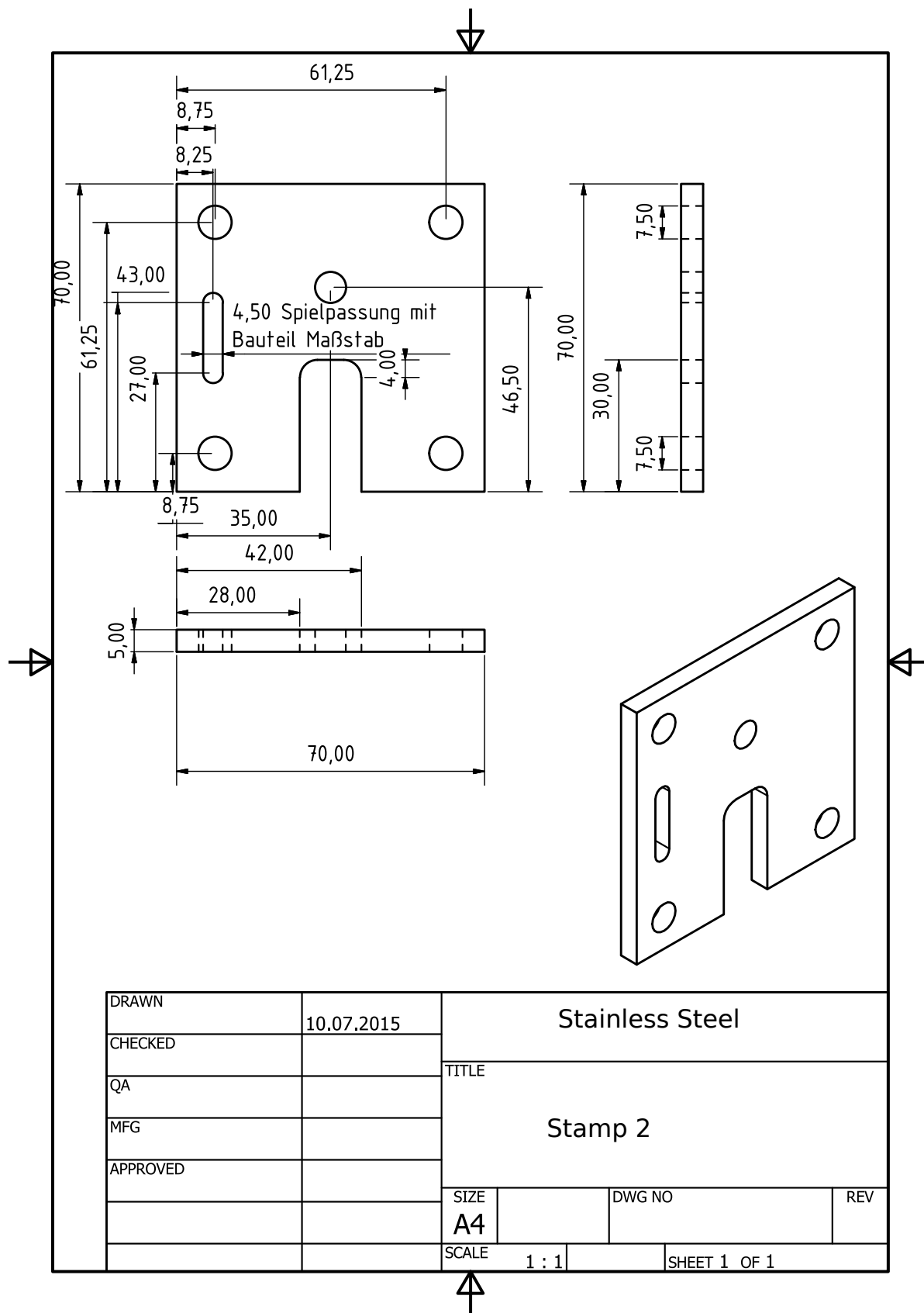


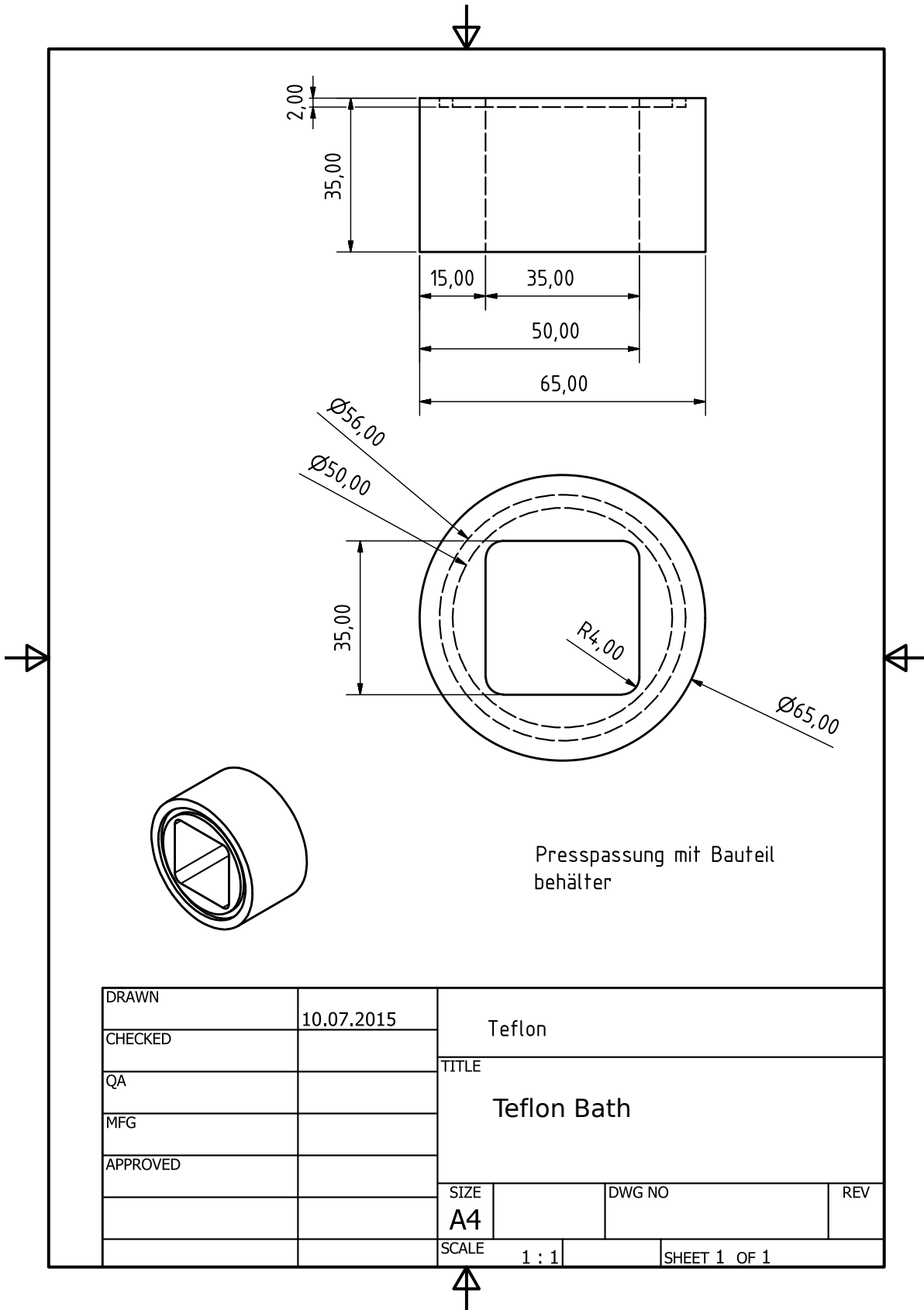


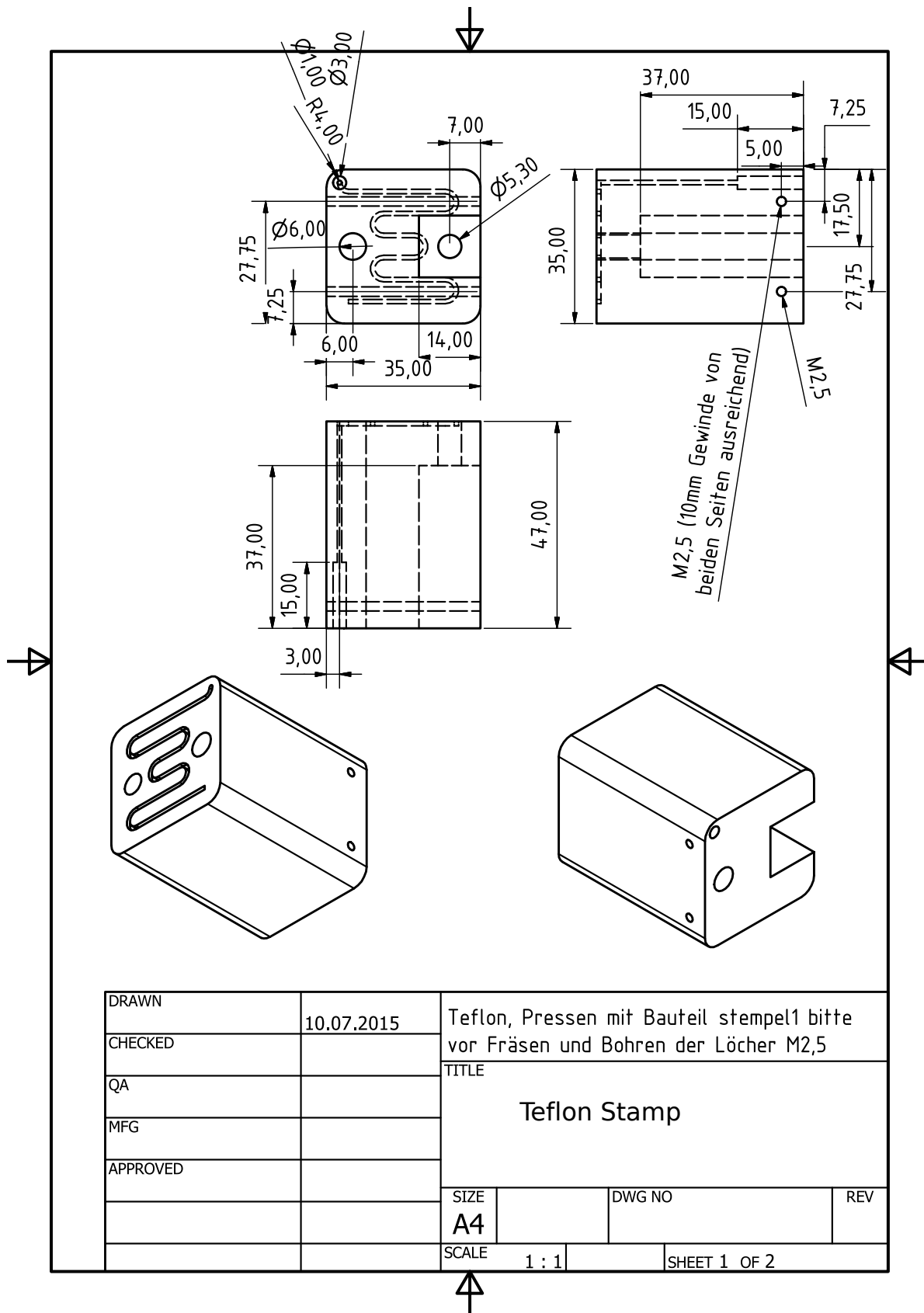






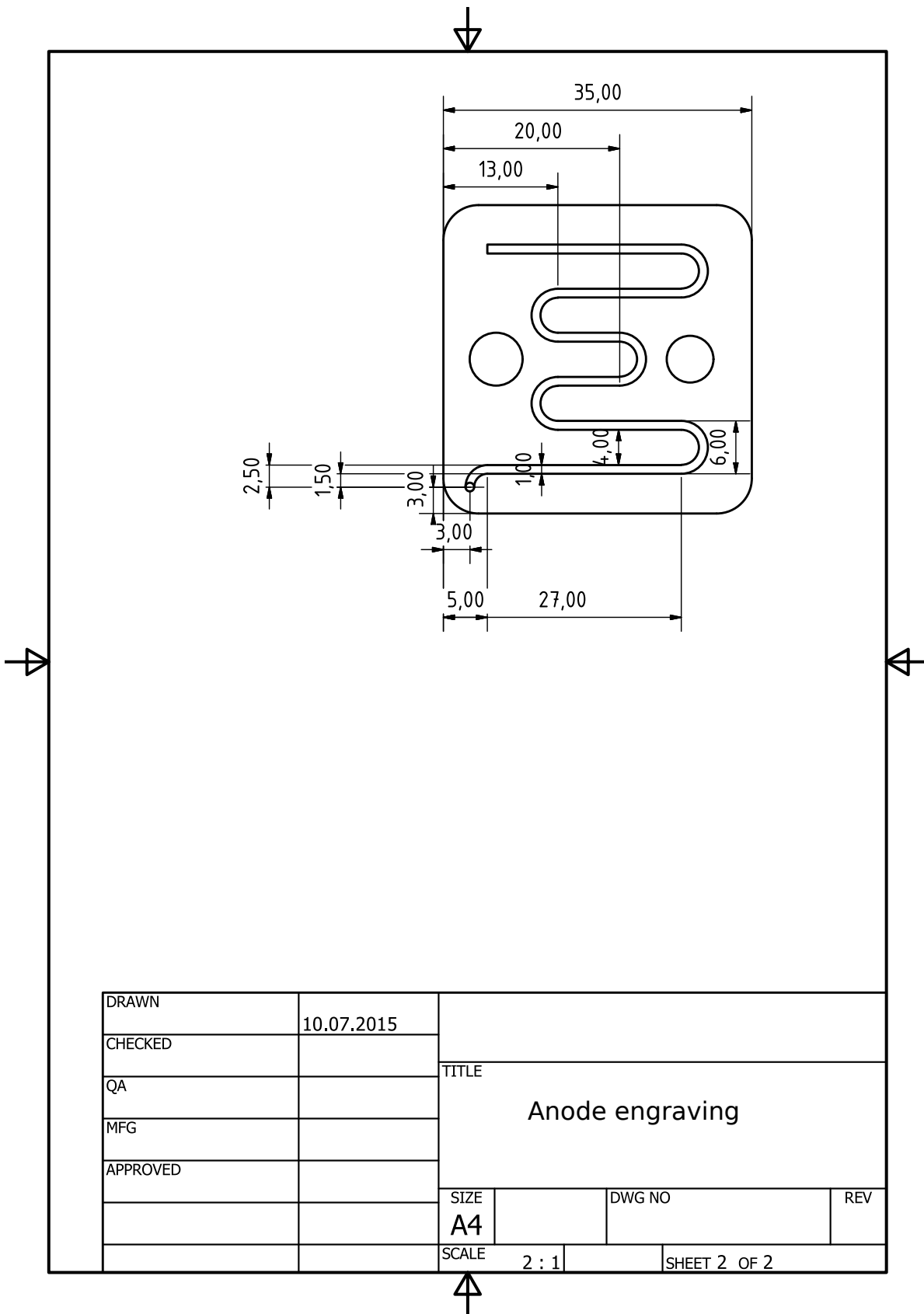


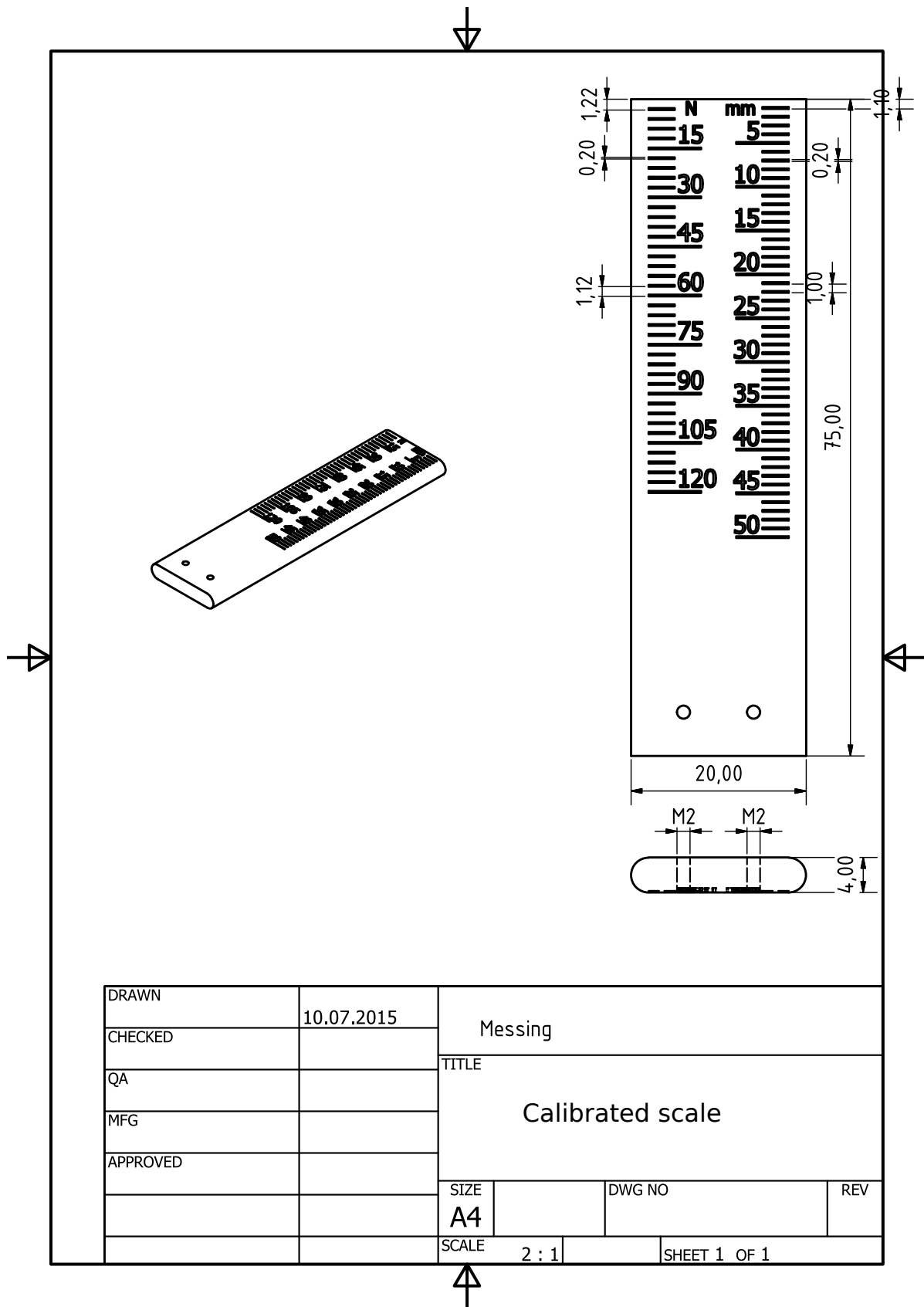




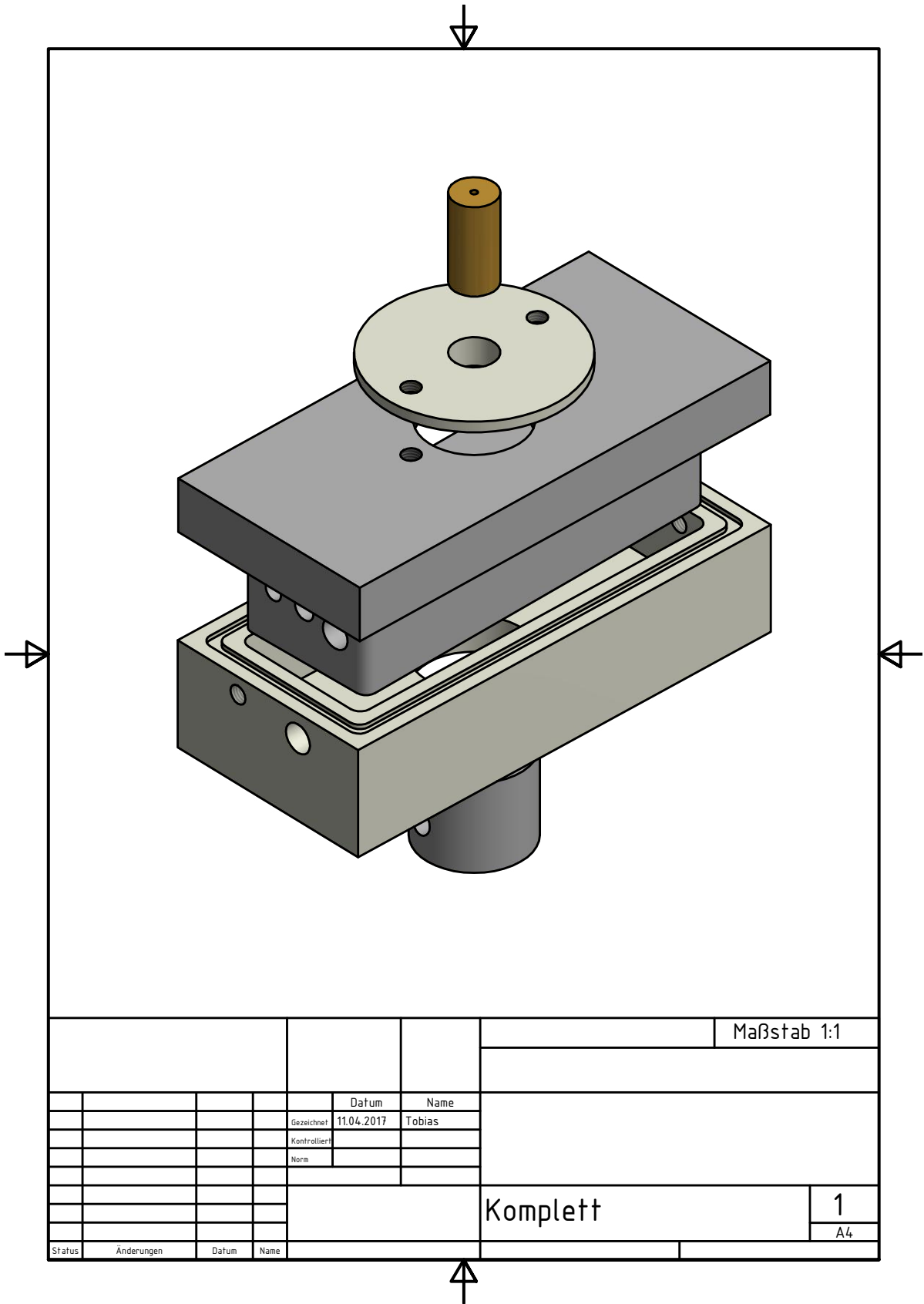
DRAWN	10.07.2015	Teflon, Pressen mit Bauteil stempel1 bitte vor Fräsen und Bohren der Löcher M2,5		
CHECKED		TITLE  <b>Teflon Stamp</b>		
QA				
MFG				
APPROVED				
		SIZE <b>A4</b>	DWG NO	REV
		SCALE 1 : 1	SHEET 1 OF 2	



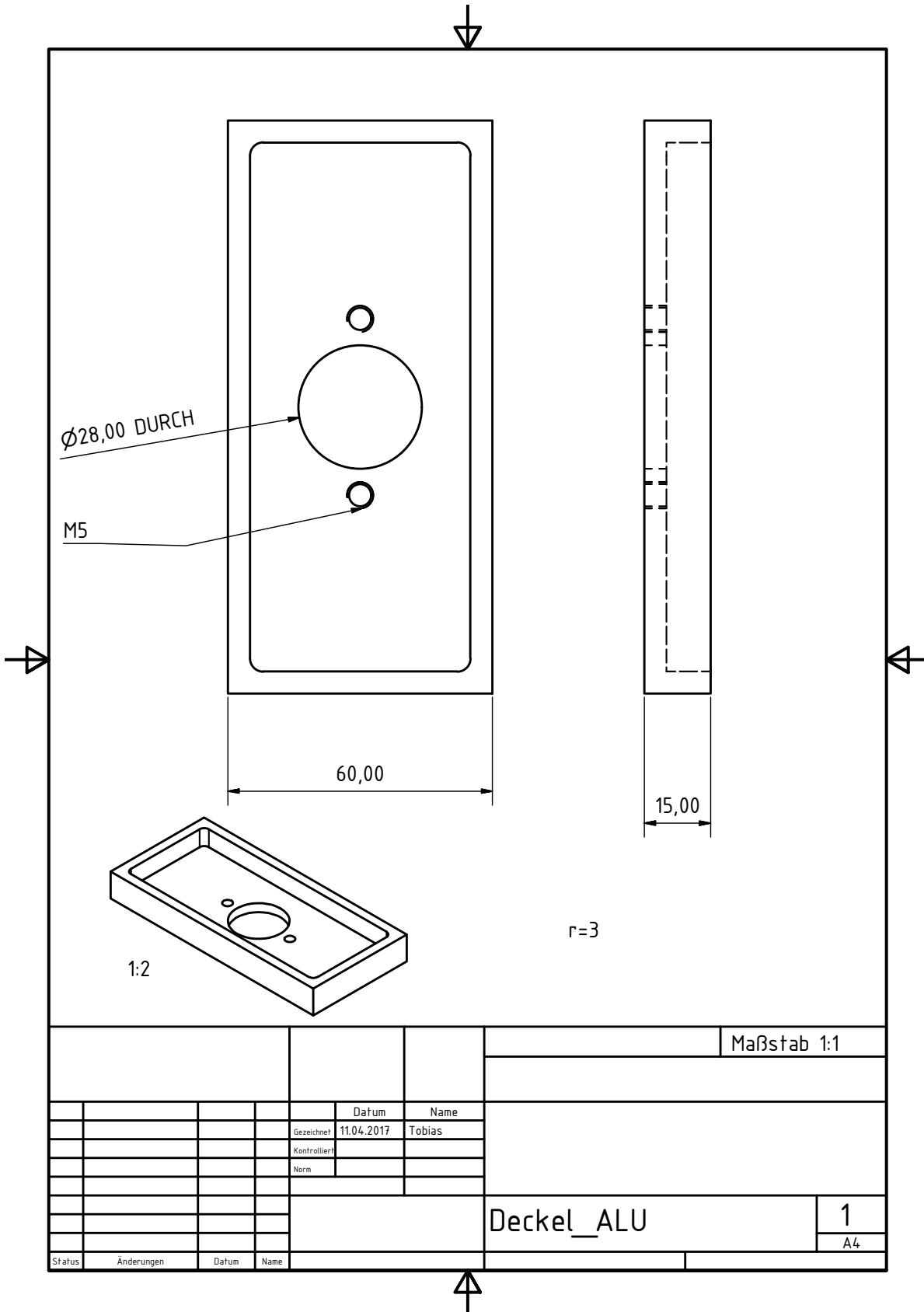




## C.2 Formic acid chamber

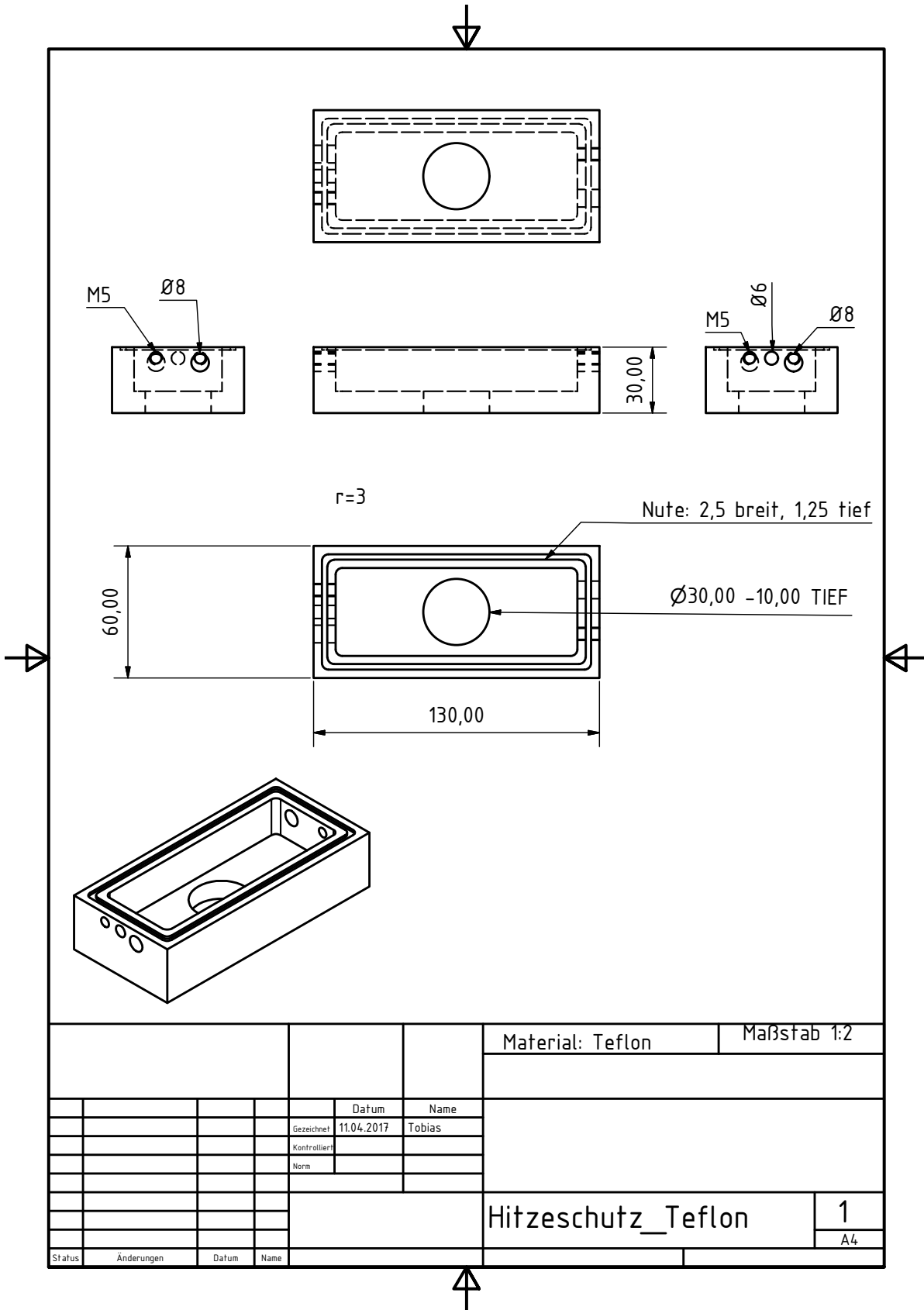


















# Farough Roustae

•  [www.linkedin.com/in/farough-roustaie](https://www.linkedin.com/in/farough-roustaie)

## Curriculum vitae

### CAREER HISTORY

---

#### NanoWired GmbH

06.2018–06.2022

- Scientific and technological expert of NanoWiring and KlettWelding
- Head of technological infrastructure
- Quality management

#### Co-founder of NanoWired GmbH

Since 01.2017

#### Research associate

*Microtechnology and electromechanical systems laboratory*

06.2013–06.2018

Institute of electromechanical design, Technische Universität Darmstadt, Germany

- Integration of metallic nano objects into microsystems

### EDUCATION & CERTIFICATIONS

---

#### Dr. -Ing.

*Microtechnology and electromechanical systems laboratory*

01.2014–06.2018

Institute of electromechanical design, Technische Universität Darmstadt, Germany

- **Doctoral thesis:** *Fabrication and integration of metallic nano and micro cones for on-chip electron field emitters.* In this thesis, the development and fabrication of cylindrical and conical metallic micro and nano-objects and their integration in 3D complex microsystems and their applications and industrialization have been explored. (Defence at 15.06.2022)

#### Diplom-Ingenieur Univ.

*Nanostructure Technology, Department of Physics and Astronomy*

10.2005–08.2012

Julius-Maximilians-Universität of Würzburg, Germany

- Design and fabrication of Gate-defined structures with GaAlAs-GaAs heterostructures by optical and electron-beam lithography in cleanroom.
- **Diplom thesis:** *Heating channel optimization and thermoelectric measurement in quantum point contacts.* In the thesis properties of a heating methode, so-called heating channel technique, are studied. For this method a mesoscopic heating channel is shaped through building up a potential barrier in a high mobility 2 dimensional electron gas (2DEG). At low temperatures of a few kelvin, the thermoelectric properties of the nanostructures in the absence of phonons are investigated.

#### Bachelor of Science

*Electronics, Electrical Engineering Department*

1998–2004

Azad University of Karaj, Iran

#### High school

*Shahid Rajaie High School, Karaj, Iran*

1994–1998

## Primary school

*Shahid Sanati School, Bandarabbas, Iran*

1986–1993

## AWARDS RECOGNITIONS

<b>IMPACT, Taiwan:</b> Best paper award	2021
<b>IMPACT, Taiwan:</b> Best paper award	2020
<b>Hermes industrial award, Germany:</b> Place 1	2019
<b>Step award , Germany:</b> Place 1	2018
<b>Science4life competition, Germany:</b> Place 1	2016
<b>TU-Ideen Wettbewerb, Germany:</b> Place 1	2015
<b>The national intelligent robotic mouse , Iran:</b> Place 1 with maze solving robot	2005
<b>The national intelligent robotic mouse , Iran:</b> Place 1 with fire fighter robot	2004

Mannheim, 05.08.2022